Oxygen isotope systematics of ordinary chondrite chondrules: insights into the inner solar system planetary reservoir

Leonardo Baeza

February 2019

A thesis submitted for the degree of Master of Philosophy

of the Australian National University

DECLARATION

This thesis consists of a study carried out at the Australian National University. I certify that this thesis is my own work except where otherwise acknowledged and has not been accepted for the award of any other degree or diploma at any university.

Leonardo Baeza

Acknowledgements

In these few lines I would like to thank all the people that have made this thesis possible and all the people who have supported me during this enjoyable process. In particular, my parents, who gave me the opportunity to explore different arts from the very beginning.

To my friends in Chile and Australia, family, RSES administrative and technical staff, friends from work, uni, particularly Morgan, Geoff, Suzette, Gianluca, Antonio, Pat, Melanie, Joëlle, Lianne, Michael, James, Johanna, Mari, and Rose.

I am especially grateful to Trevor who gave me the opportunity to study these ancient rocks and has been of great support, both on personal and academic levels. To Janaina for her help, feedback, and great vibes, to Guil for his help at the very beginning of my MPhil, and Yuri, for his scientific support and criticism. Also thankful to the two Peters and Dave from the SHRIMP group, and Bob for EPMA assistance. In addition, I would also like to thank the Chilean Government and its educational institution, CONICYT, for granting me with their international scholarship scheme, Becas Chile.

Finally, the most important ones, my wife Tutú, who made this crazy idea of playing with meteorites a family project, and my children, Vasco and Mila, who remind me every day about the essential things in life.

ABSTRACT

Chondrules are fundamental objects from which important insights in the conditions of the solar protoplanetary disk can be inferred. In this regard, oxygen isotope composition of chondrules have played a key role tracking the physicochemical environment under which their formation occurred. It has been proposed that chondrite asteroids accreted specific chondrule groups or 'chondrule populations' in terms of oxygen isotopes but this hypothesis has never been statistically assessed. Systematic in situ measurements of oxygen isotope composition of chondrule olivine from ordinary chondrites (H, L, and LL groups) by SHRIMP-SI and a robust statistical evaluation allowed us to conclude for the first time that the different ordinary chondrite parent bodies sampled the same main population of chondrules in their accretion location. This population is characterised by a mean of $\Delta^{17}O = 0.74 \pm 0.10‰$ ($\sigma_{95\%}$) with a variability of 0.53‰ ($\sigma_{95\%}$). Ordinary chondrite chondrules were then formed in the same gaseous oxygen isotope reservoir or region of the protoplanetary disk. This population is formed by chondrules with different chemical composition (Type I and Type II) indicating that their formation region was chemically differentiated and form a chemical continuum rather than two separated classes. Our results together with literature data lead us to propose an oxygen isotope gradient of the protoplanetary disk ambient gas under which these and other astrophysical objects (e.g. refractory inclusions) were formed, ^{16}O-richer closer to the Sun and ^{16}O-poorer at longer radial distances. Ultimately, we suggest a change in the paradigm related to the oxygen isotope reservoirs of the solar system, particularly the so-called planetary reservoir. It is proposed that the gaseous oxygen isotope planetary reservoir is a discrete reservoir enriched in SiO_{gas} molecules and other rock-forming elements present since the earliest stages of the solar system evolution possibly reflecting the average oxygen isotope composition of the primordial dust of the solar nebula. The mean composition of the planetary reservoir is $\delta^{18}O = 4.64 \pm 0.15‰$ ($\sigma_{95\%}$) and $\delta^{17}O = 3.03 \pm 0.10‰$ ($\sigma_{95\%}$), with variabilities of 0.97‰ and 0.52‰ ($\sigma_{95\%}$), respectively.

TABLE OF CONTENTS

Acknowledgements v
Abstract vi
1. INTRODUCTION 1
1.1. Problem presentation 2
2. Background 8
2.1. Oxygen Isotopes 8
2.2. Chondrites 13
2.3. Refractory inclusions 14
2.4. Chondrules 15
2.5. Matrix 20
2.6. Ordinary chondrites 20
3. SAMPLES AND ANALYTICAL METHODS 25
3.1. Samples 25
3.2. Optical Microscopy and Scanning Electron Microscopy 29
3.3. Electron Microprobe Analysis 29
3.4. Sensitive High Resolution Ion Microprobe Stable Isotopes (SHRIMP-SI) 30
3.5. Data Reduction 36
4. RESULTS 40
4.1. Matrix effect 40
4.2. Chondrule petrography and olivine chemical compositions 42
4.3. Oxygen Isotopes 54
4.3.1. Data analysis 54
4.3.2. Oxygen isotope compositions 58
4.3.3. Oxygen isotope composition and chondrule olivine Type 67
5. DISCUSSION 73
5.1. Matrix Effect 73
5.2. Chondrule size 74
5.3. Sample reclassification 76
5.4. Ordinary chondrites chondrule main population 78
5.5. ‘Statistical outliers’: insights into inner solar system spatially separated oxygen isotope gaseous reservoirs 100
5.6. ^{16}O-rich chondrule olivine: low mixing of dust from distinct oxygen reservoirs 109

5.7. Ordinary chondrites bulk composition: insights into terrestrial planet formation 122
5.8. Type I vs. Type II chondrules: physicochemical conditions of the ambient gas 129
5.9. The oxygen isotope planetary reservoir of the inner solar system..... 138
6. Conclusions..... 149
References..... 153
Appendix..... 172

LIST OF FIGURES

Figure 1.1 Oxygen isotope compositions of bulk individual chondrules from ordinary chondrites 5
Figure 2.1. Oxygen isotope composition of major chondrite classes and ranges of bulk chondrules 9
Figure 2.2. Oxygen isotope composition of the solar system materials 10
Figure 2.3. Photodissociation and self-shielding model in a molecular cloud. 12
Figure 2.4. Meteorite classification scheme 14
Figure 3.1. Transmitted light image of the UOCs used on this study..... 28
Figure 3.2. Representative BSE images of chondrules..... 30
Figure 3.3. Schematic diagram of the SHRIMP-SI. 31
Figure 3.4. SHRIMP-SI multiple collector configuration used for oxygen isotope analysis 33
Figure 3.5. Typical mass spectra of the oxygen mass region. 34
Figure 3.6. Acceptable range of MSWD values as a function of sample size at the 95% confidence level 39
Figure 4.1. Calibration line of the weighted mean of SHRIMP-SI analysis and LFMS values between Fo73 and Fo100..... 40
Figure 4.2. Bias of the weighted mean of SHRIMP-SI analysis and LFMS values for each synthetic olivine..... 42
Figure 4.3. Representative chondrule textures 43
Figure 4.4. Boxplot representation of apparent chondrule size 44
Figure 4.5. Major and minor element compositions of chondrule olivine from all samples..... 46
Figure 4.6. Major and minor element compositions of chondrule olivine from H samples..... 47
Figure 4.7. Major and minor element compositions of chondrule olivine from L samples 49
Figure 4.8. Major and minor element compositions of chondrule olivine from LL samples..... 50
Figure 4.9. Histograms of chondrule olivine Fa mol% content..... 52
Figure 4.10. Histograms of chondrule olivine Cr_2O_3 wt% 53
Figure 4.11. Oxygen isotope ratios of chondrule olivine grouped per H, L, and LL samples 54
Figure 4.12. MSWD range of acceptable values per session of the reference material 57
Figure 4.13. Triple oxygen plot and probability density function $\delta^{18}O$ and $\delta^{17}O$ of chondrule olivine..... 58
Figure 4.14. $\Delta^{17}O$ chondrule olivine histograms of H, L, and LL samples 60
Figure 4.15. Empirical cumulative distribution function of chondrule olivine $\Delta^{17}O$ ratios 61
Figure 4.16. Whisker-boxplot diagrams of chondrule olivine $\Delta^{17}O$ ratios..... 62
Figure 4.17. Whisker-boxplot diagrams and empirical cumulative distribution function of $\Delta^{17}O$ ratios of averaged chondrule per sample 65
Figure 4.18. Oxygen isotope ratios of chondrule olivine from H samples..... 68
Figure 4.19. Oxygen isotope ratios of chondrule olivine from L samples. 69
Figure 4.20. Oxygen isotope ratios of chondrule olivine from LL samples..... 71
Figure 5.1. Matrix effect correction..... 74
Figure 5.2. Chondrite classification scheme based on the Cr^2O^3 content of FeO-rich olivine.... 77
Figure 5.3. $\Delta^{17}O$ chondrule olivine histograms of H, L, and LL samples 85
Figure 5.4. $\Delta^{17}O$ averaged chondrule olivine histograms of H, L, and LL samples..... 86
Figure 5.5. Population assessment of $\Delta^{17}O$ averaged chondrule olivine per sample..... 89

Figure 5.6. Whisker-boxplot diagrams and empirical cumulative distribution function of $\Delta^{17}O$ ratios of averaged chondrule per H, L, and LL chondrites 90
Figure 5.7. $\Delta^{17}O$ histograms and PDFs of averaged chondrule olivine per H, L, and LL chondrites. 92
Figure 5.8. Population assessment of $\Delta^{17}O$ averaged chondrule olivine per H, L, and LL chondrites 93
Figure 5.9. Histograms and PDFs of $\Delta^{17}O$ ratios of all averaged chondrule olivine data..... 96
Figure 5.10. Ordinary chondrites main chondrule population assessment 97
Figure 5.11. $\Delta^{17}O$ ratios for all chondrule olivines 99
Figure 5.12. $\Delta^{17}O$ chondrule distribution of the statistical outliers..... 102
Figure 5.13. $\Delta^{17}O$ whisker-boxplot diagrams of the main chondrule population and the statistical outliers 103
Figure 5.14. ^{16}O-rich chondrule olivines relative to the major trend in WSG95300 110
Figure 5.15. ^{16}O-rich chondrule olivines relative to the major trend in QUE93030..... 113
Figure 5.16. ^{16}O-rich chondrule olivines relative to the major trend in ALHA77299 115
Figure 5.17. ^{16}O-rich chondrule olivines relative to the major trend in GRO06054..... 116
Figure 5.19. ^{16}O-rich chondrule olivine relative to the major trend in DOM10556 117
Figure 5.20. ^{16}O-rich chondrule olivine relative to the major trend in MIL05050 118
Figure 5.21. ^{16}O-rich chondrule olivine relative to the major trend in LAR06279..... 119
Figure 5.22. ^{16}O-rich chondrule olivine relative to the major trend in LAR12034..... 120
Figure 5.23. Schematic view of oygen isotope reservoirs 121
Figure 5.24. $\Delta^{17}O$ sample distribution of Type I and Type II chondrule olivine of the main chondrule population. 130
Figure 5.25. Minor element composition versus FeO (wt%) of chondrule olivine from the most pristine samples..... 131
Figure 5.26. Triple oxygen isotope of chondrule olivine considering Fa (mol%) content 134
Figure 5.27. Physical model of a protoplanetary disk surrounding a typical T-Tauri star 135
Figure 5.28. Abundances of H_2O molecules in the gas phase of a T-Tauri star protoplanetary disk 137
Figure 5.29. Planetary reservoir triple oxygen isotope plot..... 141
Figure 5.30. Oxygen isotopic compositions of FUN CAIs..... 142
Figure 5.31. Triple oxygen isotope model for gas-melt interactions between chondrule precursors and the ambient gas for carbonaceous chondrite chondrules..... 143
Figure 5.32. Triple oxygen isotope model for gas-melt interactions between chondrule precursors and the planetary reservoir for enstatite chondrite chondrules 145

LIST OF TABLES

Table 3.1. Unequilibrated Ordinary Chondrite samples and their general characteristics. 26
Table 3.2 Analytical conditions of SHRIMP-SI 34
Table 4.1. Oxygen isotope ratios of secondary standards 41
Table 4.2. LMFS oxygen isotope values of secondary standards and bias between SHRIMP-SI and LFMS. 41
Table 4.3. Summary of SHRIMP-SI oxygen isotope ratios and uncertainties 55
Table 4.4. Main statistics of $\Delta^{17}O$ ratios from chondrule olivine spot data 63
Table 4.5. Main statistics of $\Delta^{17}O$ ratios from chondrule olivine spot data of the prospective main population 64
Table 4.6. Main statistics of $\Delta^{17}O$ ratios from averaged chondrule olivine data 66
Table 4.7. Main statistics of $\Delta^{17}O$ ratios from averaged chondrule olivine data of the prospective main population 66
Table 5.1 Two sample Kolmogorov-Smirnov test of all $\Delta^{17}O$ chondrule olivine data 80
Table 5.2. Two sample Kolmogorov-Smirnov test of all $\Delta^{17}O$ averaged chondrule olivine data. 81
Table 5.3. Two sample Kolmogorov-Smirnov test of $\Delta^{17}O$ chondrule olivine data of the prospective main chondrule populations 82
Table 5.4. Two sample Kolmogorov-Smirnov test of $\Delta^{17}O$ averaged chondrule olivine data of the prospective main chondrule population 83
Table 5.5. $\Delta^{17}O$ averaged chondrule olivine statistics of the main chondrule population per sample 87
Table 5.6. $\Delta^{17}O$ averaged chondrule olivine statistics of the main chondrule population per H, L, and LL chondrites 94
Table 5.7. $\Delta^{17}O$ averaged chondrule olivine statistics of the prospective chondrule population of H, L, and LL chondrites before statistical assessment 94

1. INTRODUCTION

The solar system formed ~4567 Ma ago (Amelin & Ireland, 2013) as a result of the contraction of a dense molecular cloud within the interstellar space of the Milky Way. These gas and dust clouds are principally made of hydrogen and helium but also contain all the other chemical elements that were synthesized by red giants and other evolved stars prior to and during their final explosions as novae and supernovae. As the age of the universe has been estimated to be ~13.7 billion years old (Spergel et al., 2003), the Sun corresponds to a second generation star composed of matter that was accumulated in its galactic neighborhood incorporating 9 billion years of galactic evolution (Ireland, 2012). Typical atoms, molecules and compounds forming the solar nebula were diatomic hydrogen (H_2), helium (He), carbon monoxide (CO), carbon dioxide (CO_2), water (H_2O), complex organic molecules, oxides of metals (e.g. CaO, MgO, FeO) which formed small solid particles together with other presolar dust components (Faure & Mensing, 2007). Volatile compounds like H_2O and CO form small solid ice particles at molecular cloud temperatures (10-20 K).

The contraction of the solar nebula caused most of its mass to be concentrated and to spiral in to form the protosun. A result of this contraction is that the solar nebula suffers a huge volume decrease which is compensated by an increase in the rotational rate of the protosun and led to some portions of the remaining gas and dust to be positioned in a perpendicular plane to the star rotational axis thereby forming a protoplanetary disk.

The heat radiated by the protosun at the center of the disk and the high-temperature (up to 2000 K) transient heating events (e.g. x winds, shock waves, lightning, current sheets, planetesimal collisions, etc.) caused thermal processing –evaporation, condensation, and melting– of the primitive molecular cloud matter. In general, the ambient temperature of the disk decreased radially from the protosun. The sublimation of the ice particles and the less refractory dust and the survival of the most refractory components triggered a depletion of volatile elements in the inner solar system. The formation of the first solids of the solar system would have started from this new gas (Grossman, 1972). Beyond the bounds of the snow line, which some models located it at about 5 AU early in disk

evolution (Ciesla & Cuzzi, 2006), at approximately the radius of Jupiter's current orbit, the temperature of the protoplanetary disk remained cold enough to allow water ice to survive. At further radial distances, in addition to water, other ices were condensed (e.g. CO, CO_2, and methane). The different compounds available at distinct distances, broadly dependent on the background thermal gradient, were the ingredients that accreted into planetesimals, and subsequently, the distinctive planets that are seen today.

These chaotic processes, which have been briefly mentioned and simplified, explain in part the architecture of the solar system (e.g. Walsh et al., 2011). Since the early history of the solar system cannot be seen directly, meteorites represent the material from which the necessary information is obtained in order to do so. Specifically, chondrites, which are primitive rocks coming from parental bodies that avoided planet formation contain components and features that have recorded different periods and processes of the solar system history since their origin in the nebula until their arrival on Earth.

1.1. Problem presentation

Chondrites are primitive remnants of solar system formation. Some of their components formed during the birth of the solar system. They did not experience melting and igneous differentiation and therefore yield the most pristine clues to the origin of the solar nebula. These rocks incorporate material from a wide variety of sources and can be described as a cosmic breccia composed of three main components: 1) chondrules, 2) refractory inclusions, and 3) fine-grained matrix (Scott & Krot, 2014).

Chondrite primary chemical and oxygen isotopic compositions reveal that the precursor matter from where they were formed was heterogeneous. Secondary processes produced after accretion on their parent bodies (thermal metamorphism and aqueous alteration) left textural and mineralogical properties that can be correlated within members of chondrite groups. Tertiary variations, post-dating metamorphism, such as shock metamorphic features are also present in many of them (Hutchison, 2004).

Based on these characteristics a classification scheme has been developed and allows subdivision into 15 groups, which comprise mainly the carbonaceous, ordinary, and enstatite chondrites classes.

Triple oxygen isotope measurements (^{16}O, ^{17}O, and ^{18}O) have played a key role on the evolution of meteoritics since the discovery of large and ubiquitous oxygen isotopic anomalies in refractory inclusions within carbonaceous chondrites (Clayton et al. 1973). This discovery changed the way of understanding the solar nebula and removed the idea that asteroids, inner planets, and meteorites were originated from a hot, gaseous, and homogeneous nebula (Scott & Krot, 2014). In fact, whole rock chondrite groups have their own oxygen isotopic compositions suggesting that different chondrites derive from nebular material with different oxygen isotopic compositions. Moreover, based on the analysis of refractory inclusions, chondrules, and matrix minerals, it is considered that the early solar system oxygen isotope distribution was quite heterogeneous (e.g. Clayton et al., 1973; Clayton et al., 1991; Kita et al., 2010; Libourel & Chaussidon, 2011; Nagashima et al., 2015; Schrader et al., 2013; Scott & Krot, 2001; Tenner et al., 2013). Hence, the study of oxygen isotopes in meteorites reveals that each type of meteorite and their components might have been formed and/or processed in a different reservoir or region of the solar nebula yet the nature of the processes responsible for these heterogeneities or how these oxygen isotope reservoirs were produced remain open (e.g. Clayton, 2002; Yurimoto & Kuramoto, 2004; Lyons & Young, 2005).

Chondrules, together with refractory inclusions, are among the first solids formed in the protoplanetary disk (Amelin et al., 2010; Kita & Ushikubo, 2012; Ushikubo et al., 2013; Connelly et al., 2012; Bollard et al., 2017). They are reasonable big objects (mm-sized spherules) believed to have been once-free molten droplets formed by flash heating of solid precursors aggregates in the solar nebula that cooled relatively quickly. They are mainly composed of ferromagnesian silicate minerals (olivine and low-Ca pyroxene) set in a feldspathic glass or microcrystalline matrix or mesostasis. Despite their ubiquity in the majority of chondrites, chondrule formation mechanisms remain enigmatic (Johnson et al., 2015; Sanders & Scott, 2012; Salmeron & Ireland, 2012; Ruzicka, 2012; Desch et al., 2005; Desch & Connolly, 2002; Desch, et al., 2012; McNally et al., 2013; Morris et al., 2016).

Chondrules in primitive chondrites recorded the conditions while interacting with the ambient gas during their formation in the solar nebula. They retain information of their precursors and document the exchange between the melt and the gas during their passage

through the protoplanetary disk. Oxygen isotope ratios studies on chondrules have been of importance in tracing these interactions (e.g. Clayton et al., 1991; Kita et al., 2010; Libourel & Chaussidon, 2011; Nagashima et al., 2015; Schrader et al., 2013; Scott & Krot 2001; Tenner et al., 2013).

Early research on bulk chondrule oxygen isotopes compositions (e.g. Clayton et al., 1984; Clayton et al., 1991; Clayton, 1993) showed differences and similarities among chondrules from different chondrite groups. Recently, yet mainly in carbonaceous chondrites, high-precision secondary ion mass spectrometry (SIMS) analysis of chondrule phenocrysts has revealed oxygen isotopic heterogeneities at a micron scale (e.g. Rudraswami et al., 2011; Libourel & Chaussidon, 2011; Ushikubo et al., 2012; Tenner et al., 2013, 2015, 2017; Schrader et al., 2014; Hertwig et al., 2017). It appears that chondrites accreted specific chondrule groups or 'chondrule populations' of the solar nebula in terms of oxygen isotopes, reflecting the oxygen isotope reservoir under which they were thermally processed.

Despite the fact that ordinary chondrites (OCs) are the most common chondritic meteorites currently falling to Earth, are the most abundant in our collections, have been widely studied, and as for other chondritic meteorites, chondrules within OCs are the most significant components, oxygen isotope measurements of chondrule phenocrysts are still scarce.

While whole rock oxygen isotopic composition of OCs are similar, but resolvable, for H, L, and LL iron groups (Clayton et al., 1991); the range of oxygen isotope compositions of chondrules contained in them are similar among the three groups, show large scatter, and show no grouping corresponding to the classification of the host meteorite (Figure 1.1). OC chondrules, therefore, appear to be derived from a single population of chondrules in the solar nebula (Clayton et al., 1991) although the opposite has also been hypothesized (Metzler et al., 2017). As such, what might be causing the differences in whole rock oxygen-isotopic composition within OC is not clear yet.

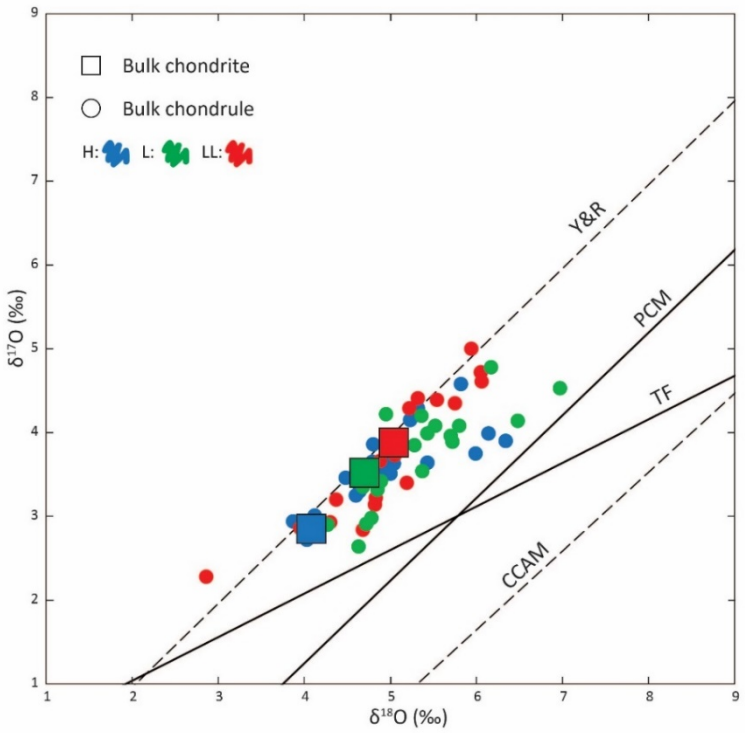

Figure 1.1 Oxygen isotope compositions of bulk individual chondrules from ordinary chondrites (H: blue, L: green, LL: red circles). The squares show the mean compositions of H, L, and LL (H: blue, L: green, LL: red squares). There is no correlation between chondrule composition and parent chondrite composition, which may indicate that all ordinary chondrite chondrules sample the same population in the solar nebula. The Y&R, PCM, TF, and CCAM lines are shown for reference (source Clayton et al., 1991).

During the residence on their asteroidal parent bodies, OCs were modified by geological processes (aqueous alteration and thermal metamorphism). Depending on the degree of thermal metamorphism they can be assigned to different petrologic types (Van Schmus & Wood, 1967). The sequence type 3 to type 6 represents an increasing degree of chemical equilibration and textural recrystallization (Krot et al., 2014). The least metamorphosed OCs (type 3), are more likely to reflect solar nebula characteristics and are known as unequilibrated ordinary chondrites (UOCs). Type 4 to 6 show progressively more metamorphic features and homogenization and are the chemically equilibrated ordinary chondrites (EOCs). Chondrules from UOCs are considered to best preserve the original textural, chemical, and isotopic signature at the time of chondrule formation.

Previous studies of oxygen isotope compositions by SIMS have been done on UOCs but only in a few dozens of chondrules and mainly associated with the LL group (e.g. Russell et al., 2000; Saxton et al., 1998; Sears & Lyon, 1998; Sears et al., 1998; Huss et al., 2005;

Kita et al., 2010; Kita et al., 2008; Libourel & Chaussidon, 2011; Pack et al., 2004; Ruzicka et al., 2007; Symes et al., 1998).

The principal aim of this research is to address what is controlling the oxygen isotope composition of a set of nine UOCs samples (three H, three L, and three LL). This question will be tackled through systematic in situ measurements of oxygen isotopic composition of chondrule olivine using the capabilities of the Sensitive High-Resolution Ion Micro Probe specialized on Stable Isotopes (SHRIMP-SI). The plan is to obtain information from as many chondrules as possible per sample. In this way, chondrules will be seen as statistical populations instead of individual objects. This statistical treatment is important since 'chondrule populations' in terms of oxygen isotopes have been suggested but, to the best of our knowledge, never been statistically assessed.

A big advantage of in situ measurements, besides its non-destructive nature, and particularly the SHRIMP-SI, is that the instrument configuration and analytical conditions allow for long sessions which provide a large number of observations (bigger population numbers) in a reasonable amount of time. Second, the data assessment protocol used for oxygen isotope analysis provides values of precision, accuracy, and reproducibility in oxygen isotope compositions to actually evaluate populations in a statistically robust manner. Finally, its high spatial resolution permits avoidance of secondary processes that are known to occur and change primordial oxygen isotope compositions in other chondrule phases (e.g. Kita et al., 2010; Bridges & Ireland, 2015). The chondrule olivine oxygen isotope analyses will be complemented with chemical, mineralogical and petrological data, allowing a more complete characterization of chondrule provenance in the protoplanetary disk.

By assessing chondrule populations in OCs, and chondrites in general, further insights could be obtained at different scales considering the context. For example, at an asteroidal scale if each chondrite group is thought to represent a distinct or multiple similar parent bodies (e.g. Vernazza et al., 2014) which sampled a variety of chondrules on its accretion location then finding one or more chondrule populations among them could provide evidence regarding what is controlling the oxygen isotope composition of asteroids.

Second, since chondrules are thought to be formed in highly localized environments or regions of the protoplanetary disk (e.g. Jones, 2012), then finding populations of chondrules with similar or different oxygen isotope ratios within chondrites could provide evidence about the isotopic and physicochemical structure of these regions, and the solar nebula itself. Moreover, it could offer clues on the dynamical processes operating within those regions, since chondrules and other objects could have been formed in one region but accreted at different orbital distances.

Finally, if chondrites are the building blocks from which planets are formed and planets are the byproduct of stellar formation then it could be possible to envision planet formation within the solar system as a general process since planets in other stellar systems could be responding to similar physicochemical conditions and processes.

2. BACKGROUND

2.1. Oxygen Isotopes

The Sun and planets formed from a protoplanetary disk of gas and dust, the solar nebula, which was the result of the gravitational collapse of a molecular cloud fragment ~4.6 billion years ago. The solar nebula was thought to be homogenous with respect to isotopic abundances of most elements which suggest considerable heating and mixing at the beginning of the solar system (Ireland, 2012). This view changed following the discovery by Clayton et al. (1973) of large and ubiquitous oxygen isotopic anomalies, compared to terrestrial material, in refractory inclusions within carbonaceous chondrites.

Oxygen is a unique chemical element in the solar system. It is the third most abundant element and a major constituent of both solid and gaseous states over a wide range of temperatures from volatile to refractory materials of the solar nebula, mainly CO, H2O, silicates, and oxides. Consequently, oxygen isotope abundance variations in meteorites and their components is an important tracer of the physicochemical conditions and processes that occurred in the protoplanetary disk for which a lifetime is thought to be ~3.8-4.5 Ma (H. Wang et al., 2017; Bollard et al., 2017).

The three stable isotopes ^{16}O, ^{17}O, and ^{18}O are produced by nucleosynthesis in stars, but by different nuclear processes in different stellar environments (Clayton, 2003). On Earth, the mean abundances of ^{16}O, ^{17}O, and ^{18}O are 99.76%, 0.04%, and 0.20%, respectively. Conventionally oxygen isotope compositions are reported as δ units, which are deviations in part per thousand or permil (‰) relative to the ratios $^{17}O/^{16}O$ and $^{18}O/^{16}O$ of the Vienna Standard Mean Ocean Water (VSMOW; Baertschi, 1976). The notation is as follows:

$$\delta^{17}O = 1000 \times [(^{17}O/^{16}O)_{unknown} / (^{17}O/^{16}O)_{VSMOW} - 1] ‰$$

$$\delta^{18}O = 1000 \times [(^{18}O/^{16}O)_{unknown} / (^{18}O/^{16}O)_{VSMOW} - 1] ‰$$

‘Unknown’ represent the isotope ratio of the unknown composition to be determined, and ‘VSMOW’ represent the ratio of standardization.

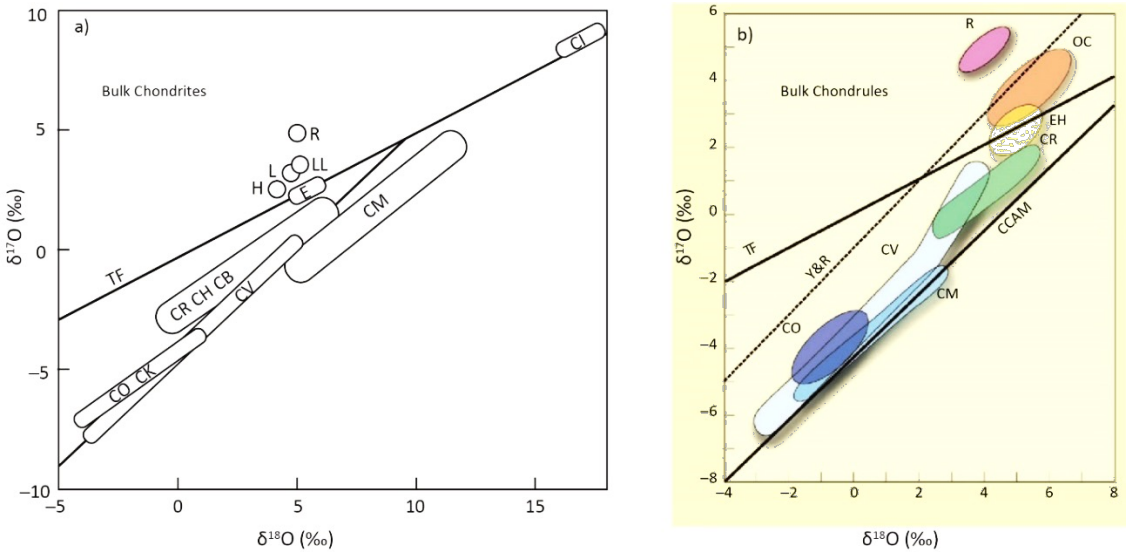

Figure 2.1. Schematic plot of oxygen three-isotopes: a) Locations and ranges of whole-rock composition of major chondrite classes (modified from Clayton, 2003). b) Locations and ranges of bulk chondrules composition in major chondrite classes (modified from Rubin, 2000). Terrestrial fractionation (TF), Young and Russel (1998), and carbonaceous chondrite anhydrous mineral (CCAM) lines are shown for reference.

Any mass-dependent reaction will increment or diminish the $^{18}O/^{16}O$ ratio by a fixed amount but will change the $^{17}O/^{16}O$ ratio by half that value. Therefore, the composition of nearly all terrestrial samples plot along a line of slope ~0.5, called the terrestrial fractionation (TF) line on the classic triple-oxygen isotope diagram of $\delta^{18}O$ vs. $\delta^{17}O$.

However, although mass-dependent fractionation occurs, the majority of extraterrestrial samples do not follow this pattern and they deviate from the TF line. Specifically, the major components of primitive chondrites (refractory inclusions, chondrules, and fine-grained matrix) plot along a line with slope close to 1 (Figures 1.1 and 2.1) indicating mass-independent fractionation processes that fractionates ^{16}O from ^{17}O and ^{18}O, prior to accretion of these bodies during the life-time of the protoplanetary disk (Yurimoto et al. 2007). Therefore, in the solar system, the predominant cosmochemical signature is based on ^{16}O isotope variability.

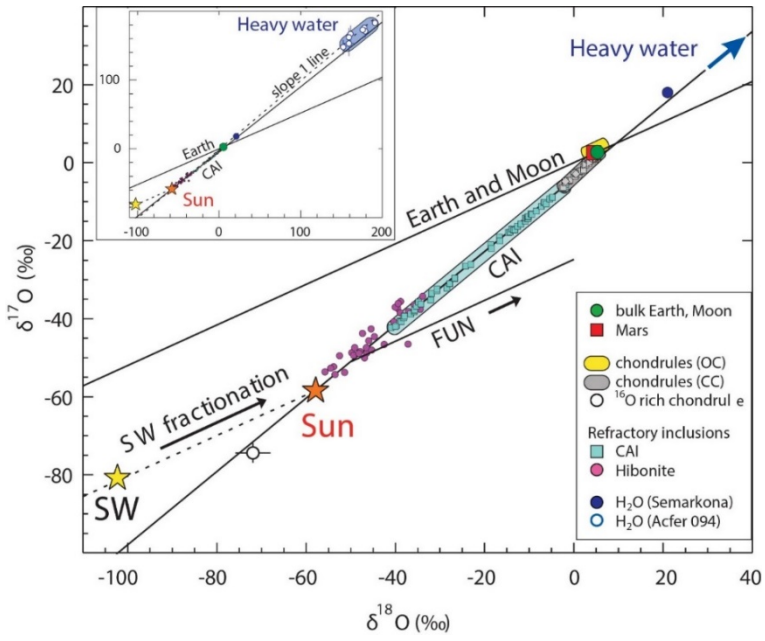

Figure 2.2. Triple-isotope plot showing data of a wide variety of chondrite components and the Sun. Almost all the data fall on a single mixing line with a slope of 1 (Obtained from McKeegan et al., 2011)

The degree of ^{16}O enrichment or depletion (distance) from the TF line is commonly calculated as:

$$\Delta^{17}O \sim \delta^{17}O - 0.52 \times \delta^{18}O$$

$\Delta^{17}O$ values are used to describe oxygen isotope heterogeneity that emphasizes the mass-independent oxygen isotope signature of the solar system and thereby represents the oxygen isotope reservoir of the measured object. By definition, any terrestrial sample will have a $\Delta^{17}O$ ratio of 0‰. Any ^{16}O-enriched material with respect to Earth will deviate towards negative $\Delta^{17}O$ values, and conversely, material depleted in ^{16}O (or enriched in ^{17}O and ^{18}O) will have positive $\Delta^{17}O$ ratios.

Current observation indicates two extreme reservoirs in the abundance of ^{16}O. The solar reservoir is ^{16}O-rich with $\Delta^{17}O \sim -28‰$ (McKeegan et al., 2011), while a nebular water reservoir is $^{17,18}O$-rich ($\Delta^{17}O \sim 80‰$; Sakamoto et al., 2007). These reservoirs have been identified in chondrite components. For instance, many refractory inclusions seem to have formed in a uniform ^{16}O-rich oxygen isotopic gas reservoir with a $\Delta^{17}O$ ratio of approximately -24‰ (e.g. Kööp et al., 2018; MacPherson, 2014) close to solar in composition. On the other hand, the nebula water reservoir has been measured in the matrix of chondrites (Choi et al., 1998; Sakamoto et al., 2007; Hashizume et al., 2011).

Additionally, ^{16}O-enriched compositions, relative to the Sun, have been observed in refractory inclusions and one chondrule with Δ^{17}O ratios as low as ~ -40‰ (Kobayashi et al., 2003; Krot et al., 2009; Gounelle et al., 2009). Similarly, $^{17, 18}$O enrichments have also been reported in lunar samples (Δ^{17}O ~27‰; Ireland et al., 2006). Most chondrules span within a Δ^{17}O range of -7‰ to 4‰, similar to bulk chondrites (Krot et al., 2009; Krot & Nagashima, 2017).

Solar system material with oxygen isotope compositions between these extreme reservoirs (solar and nebula water) have commonly been explained as representing mixing between these reservoirs, and/or evolution of these reservoirs (e.g. Cuzzi & Zahnle, 2004; Aléon, 2016). Primordial dust is assumed to be originally close to solar in oxygen isotope composition (e.g. Yurimoto & Kuramoto, 2004; Alexander et al., 2017), but was altered in the inner solar system. Specifically, thermal processing in such a mixture of reservoirs is used to explain the oxygen isotope composition of the Earth, Moon, Mars, differentiated asteroid meteorites, etc., which is similar among them (e.g. Clayton, 2003) and varies slightly around the terrestrial oxygen isotope composition. Some authors have called this composition the planetary reservoir (i.e. Ireland, 2012).

Initially, the early solar system oxygen isotope heterogeneities (^{16}O variability) were thought to be the result of a nucleosynthetic signature (Clayton et al., 1973). Current thinking is that these oxygen isotope end members are derived from the photochemical speciation and self-shielding of carbon monoxide in the solar system and/or in the molecular cloud from which the solar system was formed. This is an isotope-selective chemical process that has been seen to occur in cold dark molecular clouds (Yurimoto et al., 2006 and references therein) and consists of breaking bonds of carbon monoxide molecular isotopologues ($C^{16}O$, $C^{17}O$, and $C^{18}O$) by short wavelength (UV) photons. Since each molecule requires a different energy to be broken, when light travels through molecular clouds the photon wavelength that dissociates $C^{16}O$ is attenuated earlier in the surface layer of the molecular cloud (self-shielding) while the wavelengths required to dissociate $C^{17}O$ and $C^{18}O$ can reach further. This process results in a selective enrichment of atomic oxygen in ^{17}O and ^{18}O in the interior of molecular clouds which can react with hydrogen to form ^{16}O depleted water ice ($H_2{}^{17}O$ and $H_2{}^{18}O$) leaving behind a residual gas

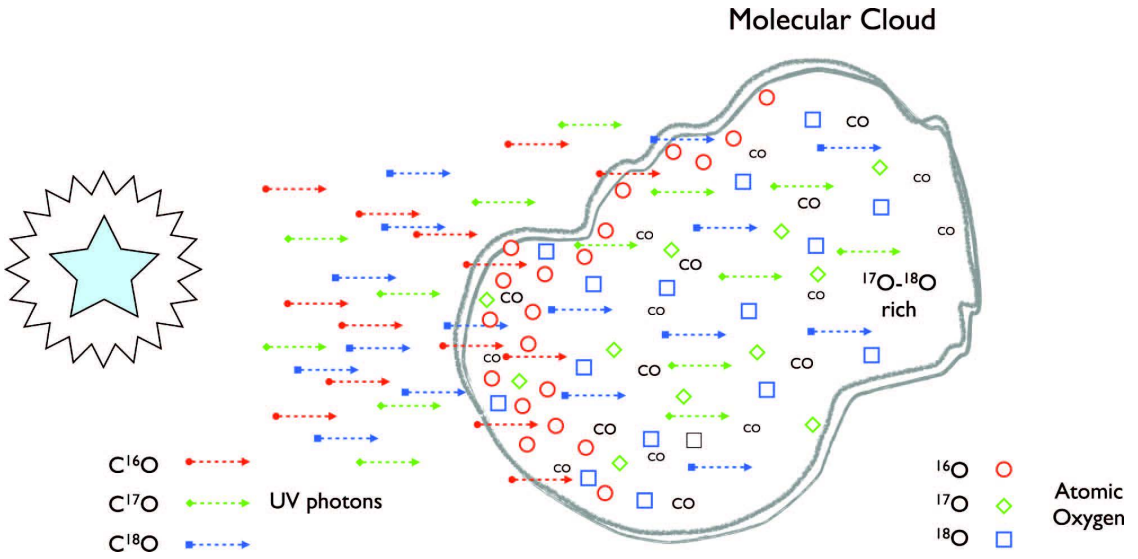

Figure 2.3. Schematic illustration of photodissociation and self-shielding in a molecular cloud (from Ireland, 2012).

enriched in $C^{16}O$ (Figure 2.3). While there is some general agreement on the mechanism, where this speciation took place is an unresolved problem in cosmochemistry (Clayton, 2002; Yurimoto & Kuramoto, 2004; Lyons & Young, 2005).

With this model in mind, the following scenario has been proposed. At the very beginning of the protoplanetary disk the H_2O/CO ratio of the inner disk was ^{16}O-rich or solar in composition, therefore, refractory inclusions and chondrules formed at that time are ^{16}O-rich. Subsequently and because ^{16}O-poor water ice dust particles that were beyond the snow line were drifting inwards the protosun and evaporating, the inner disk progressively became H_2O enriched and ^{16}O-depleted (^{17,18}O-rich). During this evolution step of the solar system, which may have lasted for ~5 Ma, most chondrules formed and refractory inclusions were melted or reprocessed at high temperatures (Krot et al., 2009) while some planetesimals where accreted and differentiated (Kruijer et al., 2014).

2.2. Chondrites

Meteorites are solids bodies of extraterrestrial material that survived entry through the atmosphere and arrived at the surface of the Earth from interplanetary space. Their sizes vary from particles smaller than a grain of sand (micrometeorites) to masses of many tons. Most of them are fragments of asteroids with perturbed orbits from the asteroid belt but some meteorites are from the surfaces of the Moon, Mars, and possibly comets.

Based on their bulk compositions and textures meteorites can be classified into two main categories, chondritic and non-chondritic meteorites. Chondritic meteorites are the most abundant. Non-chondritic meteorites are subdivided into achondrites, stony-irons, and iron meteorites (Figure 2.4). In one hand, non-chondritic meteorites experienced different degrees of melt extraction and differentiation. On the other hand, chondrites did not (Krot et al., 2014). This primitiveness makes chondrites important samples to track the evolution of the early solar system since some of their components were formed and/or processed when the Sun was experiencing rapid infall (class 0) through to an evolved (class I) protostar (Krot et al., 2009). Then some of their characteristics should be intimately related to the nebular gas present at the gaseous disk stage.

Chondritic meteorites are divided into 15 distinct groups based on their chemical, isotopic and mineralogical differences (carbonaceous, ordinary, enstatite, as well as other classes) and each group may represent one or a few similar asteroids or parental bodies (Vernazza et al., 2014). As their name suggests, ordinary chondrites are the most abundant chondrites in meteoritic collections. Despite the diverse origin of their components, chondrites can be described as rocks including three major constituents: refractory inclusions [Ca- and Al-rich inclusions (CAIs) and amoeboid olivine aggregates (AOAs)], chondrules, and fine-grained matrix (Scott & Krot, 2014)

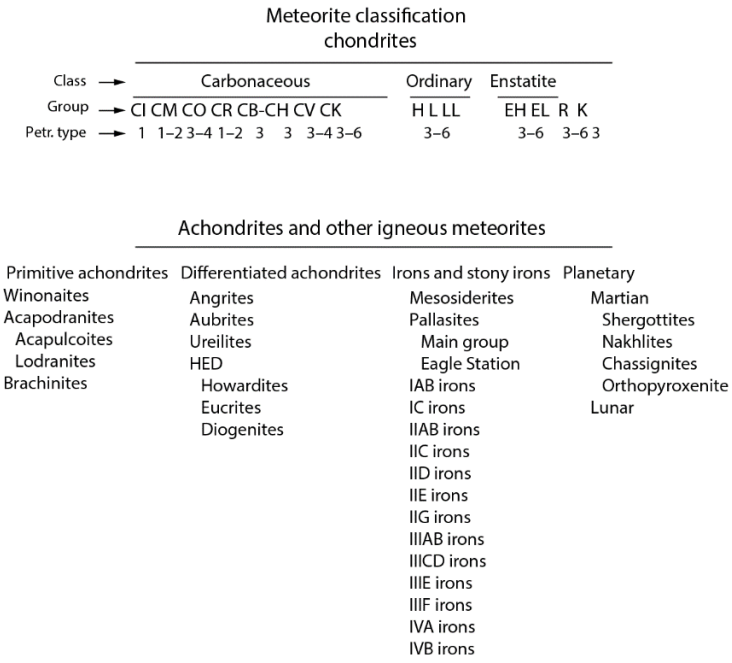

Figure 2.4. Classification of meteorites excluding ungrouped meteorites. Modified from Krot et al. (2014).

Even though they accreted together it is important to highlight that the individual components of a chondrite could have formed at different places and/or times in the protoplanetary disk.

2.3. Refractory inclusions

Refractory inclusions are mainly found within carbonaceous chondrites. CAIs are the oldest solids to have formed in the solar system approximately 4567 Ma ago (Amelin et al., 2010; Connelly et al., 2012). In meteoritics, they are regarded as representing the starting point (t_0) of the solar system. U-corrected-Pb-Pb absolute and ^{26}Al-^{26}Mg relative chronologies indicate that some CAIs were thermally processed from the very beginning of the protoplanetary disk and processing may have lasted up to 0.3 Ma after condensation of their precursors (Krot et al., 2017). Consequently, CAIs can be non-igneous, gas-solid condensates from the solar nebula, evaporative residuals of presolar grains or a mixture of both (Ireland & Fegley, 2000) and igneous (melted condensates) objects composed of Ca-, Al-, Ti-, Mg- oxides and silicates (corundum, hibonite, grossite, perovs.kite, melilite, spinel, Al–Ti-diopside, anorthite, and forsterite; MacPherson, 2014). These minerals are

predicted to be refractory condensates from a cooling gas of solar composition at ambient temperatures above ~ 1400 K, total pressures from 10^{-5} to 10^{-3} bar, and forming under extremely reducing conditions (log fO2 < IW-6; Ebel and Grossman, 2000; Grossman et al., 2008; Ireland and Fegley, 2000; MacPherson, 2014). CAIs range in size from submillimeter- to centimeter-sized clasts, their shapes ranging from subspherical to highly irregular objects surrounded by layered rims. The modal abundances of CAIs in different chondrite groups range from < 0.1 to ~ 3 vol % (Hezel et al., 2008).

AOAs are also refractory objects with fine grain size (5-20 μm,) irregular shapes, and sizes that range from 100 μm to 5 mm. Their mineralogy consists principally of forsterite and Fe, Ni- metal but also aluminous-diopside, spinel, anorthite, and melilite (Scott & Krot, 2014). AOAs also were formed at high temperatures (~ 1400 K) in a similar region to CAIs but appear to have avoided melting after aggregation.

The oxygen isotope compositions of CAIs and AOAs are heterogeneous depending on the type, the mineral phase measured, and the processes that affected them. Nevertheless, it is well known that they are commonly ^{16}O-rich relative to other components in chondrites such as chondrules and matrix (Scott & Krot, 2014). In general, the majority of CAIs from most chondrite types sampled the same ^{16}O-rich reservoir showing a composition of $\delta^{17,\,18}$O ~-50 ‰ to -60 ‰ (Δ^{17}O ~24 ‰; MacPherson, 2014). Both CAIs and AOAs are believed to have formed close to the Sun in a gas of solar composition by evaporation, condensation, and subsequent melting (MacPherson, 2014). After their formation, they were distributed throughout the solar nebula reaching multiple-astronomical-unit distances where they accreted into chondrites and other objects (Simon et al., 2016 and references therein).

2.4. Chondrules

One of the most intriguing features of chondrites are chondrules. Chondrules are the major components of chondrites –a name given to them because of the presence of chondrules within them– comprising up to 80% of their volume depending on the chondrite class.

These igneous-textured objects are half-mm-sized spherules (Friedrich et al., 2015) composed mainly of ferromagnesian silicate minerals (olivine and low-Ca pyroxene) set in a feldspathic glass or microcrystalline matrix or mesostasis. They are believed to have been once-molten free droplets formed by localized transient heating events of diverse solid precursor aggregates in different dust-rich region of the protoplanetary disk. Many of them also contain metallic Fe,Ni and sulfide grains. Solid isotopically diverse precursors include CAIs, AOAs, chondrules of earlier generations, fine-grained matrix-like material, and, probably, clasts of pre-existing thermally processed planetesimals (Krot et al., 2017).

Amelin et al. (2002) dated chondrules from carbonaceous chondrites (CR) precisely at 4564.7 ± 0.6 Ma using ^{207}Pb-^{206}Pb ages. Other results obtained by Amelin & Krot (2007) gave a weighted average of 4566.6 ± 1.0 Ma (CV). Connelly et al. (2012) reported ^{207}Pb-^{206}Pb ages that range from 4567.32 ± 0.42 Ma to 4564.71 ± 0.30 Ma from carbonaceous (CR and CV) and OC (L) chondrules. Recently, Bollard et al. (2017) shown Pb isotopic ages for a few chondrules from CR and L chondrites ranging from ~0 to ~4 My after CAIs. The above suggests that chondrule formation began contemporaneously with CAIs formation, and lasted for ~4 My afterward. However, the contemporaneous formation of chondrules and refractory inclusions is debatable and is not supported by short-lived radionuclide chronometers such as ^{26}Al-^{26}Mg and ^{182}Hf-^{182}W, which indicate that most chondrules formed ~1-3 My after CAIs (e.g. Kita et al., 2013; Budde et al., 2016a).

Chondrule size is an important physical parameter since each chemical group of chondrites possesses a specific size-frequency distribution of chondrules (Friedrich et al., 2015). Moreover, chondrule size is a constraint to chondrule formation models and mass transport models in the protoplanetary disk (Salmeron & Ireland, 2012; Jacquet, 2014a, 2014b; Friedrich et al., 2015). Friedrich et al. (2015) suggest a definition of chondrules as "half-mm-sized" spherules since a large number of chondrites have chondrule mean diameters of 500 µm. However, microchondrules with sizes 10-100 µm and macrocondrules > 5 mm can also be found in chondrites (see Friedrich et al., 2015).

Two main textures are used to divide chondrules: porphyritic (P), if they have optically resolvable minerals which are composed of large phenocrysts of olivine and/or pyroxene set in a glassy or fine-grained matrix; and nonporphyritic which include cryptocrystalline

(CC), radial pyroxene (RP), and barred-olivine (BO) textures (Scott & Krot, 2014). The relative abundances between olivine and pyroxene allow further classification of porphyritic chondrules as porphyritic olivine (PO), porphyritic pyroxene (PP), and porphyritic olivine/pyroxene (POP). In general, the distribution of chondrule textural types mentioned above is known to vary significantly among chondrite classes while minor differences are expected between chondrite groups within each class (Jones, 2012).

A direct implication of chondrule texture is the inferred thermal history. Briefly, porphyritic chondrules are thought to have crystallized from melts that have been heated to near-liquidus temperatures and have many seed nuclei after incomplete melting of the precursor material. On the other hand, non-porphyritic chondrules crystallized from melts that were superheated above their liquidus for a sufficient period of time to destroy all solids that could act as nuclei (Scott & Krot, 2014 and references therein). In more detail, chondrule precursors were heated at 104-106 K/h (Tachibana & Huss, 2005), reached peak temperatures in the range of 1650-1850K, and cooled at 100-1000 K/h (Desch & Connolly, 2002). Specifically, Desch & Connolly (2002) have suggested cooling rates of 5-300 °C/h, 500-3000 °C/h, and 5-100 °C/h for radial, barred, and porphyritic texture chondrules, respectively.

Chondrules are further classified into compositional types I and II based on the FeO content of their olivine and pyroxene crystals calculated as FeO/MgO+FeO mol%. Type I are referred to as FeO-poor or magnesian chondrules with fayalite (Fa) and ferrosilite (Fs) being <10 mol%, while Type II is FeO-rich or ferrous in composition with Fa and Fs >10 mol%. This number has been often used as an oxygen fugacity proxy of the chondrule formation environment for unequilibrated chondrites. In this regard and based on metal-silicate phase equilibria (e.g. Ebel & Grossman, 2000) Type I chondrules formed at more reducing conditions (log fO_2: IW -6 to IW -2) than Type II (log fO_2: IW -2 to IW; IM=iron-wustite buffer). The wide range of olivine Fa content from chondrules of different chondrite groups could imply variability in oxygen fugacity during their formation, moreover, the differences between Type I and Type II could be controlled by the original oxygen fugacity of the chondrule precursor range and/or the oxidation state of the region where chondrules were formed (Jones, 2012). Type I and Type II chondrule proportions also differ among chondrite classes. More than 95 % of chondrules in carbonaceous

chondrites are Type I (Scott & Krot, 2014) whereas Type I and Type II chondrules appears to occur in similar amounts in OCs (e.g. 56% vs. 46%, respectively; Hezel et al., 2018).

Generally, Type I chondrules have some Fe,Ni metal inclusions and are depleted in moderately volatile elements (e.g. Mn, Na, K, etc) and richer in refractory elements (e.g. Ca, Al, etc) compared to chondritic compositions; Type IIs have overall higher total iron content, are poorer in metal and have moderately volatile composition closer to chondritic (Scott & Krot, 2014).

Geological processes occurred on chondrite parental bodies that could have modified the original FeO content of chondrules. In fact, FeO can be mobilized during aqueous alteration and/or thermal metamorphism in olivines (Huss et al., 2006). As an example, highly unequilibrated OCs show a wide range of Fa contents but with increasing degree of thermal metamorphism this range becomes increasingly uniform and compositions tend to cluster around a uniform value for equilibrated ordinary chondrites of the same group (Huss et al., 2006). This equilibration implies that any zoning profile in chondrule olivine will disappear as a result of FeO diffusion from the matrix to forsterite olivine via grain boundaries and/or cracks (McCoy et al., 1991).

Relict grains also occur within chondrules. The common presence of these relict grains, composed mainly of olivine but also pyroxene that did not crystalize in situ during the last chondrule-forming episode, suggests that chondrules were subject to several melting or re-melting events (Ruzicka, 2012; Jones, 2012). There are two types of relict olivine grains: (1) forsteritic and (2) dusty olivine relicts. Forsteritic relicts are commonly observed in Type II chondrules and less common in Type I chondrules. They crystallized from more magnesian melts than the surrounding normal olivine. Dusty olivine relicts are common in Type I chondrules. They crystallized from melts that were more ferrous than surrounding chondrule phenocrysts and subsequently underwent reduction to form their characteristic finely exsolved iron metal, probably during the host chondrule formation (Ruzicka, 2012; Jones, 2012). Ruzicka, (2012) points out the importance of the presence of relict grains as it implies the mixing of chondrule components at subchondrule scale. He highlights that the mixing process could have been physical (e.g. collision of xenocrystic grains with individual melts) or thermochemical, with partial remelting of

chondrules occurring under different conditions such as temperature, oxygen fugacity, or system composition than that which produced early formed relict grains. More evidence of multistage melting includes coarse-grained igneous rims around chondrules and independent compound chondrules.

In general, bulk oxygen-isotope compositions of ferromagnesian chondrules are ^{16}O-depleted relative to refractory inclusions. They show a smaller and intermediate range of Δ^{17}O mainly from -7 ‰ to 4 ‰ (Krot & Nagashima, 2017). This discrepancy suggests that refractory inclusions and chondrules formed in gas reservoirs with different isotopic compositions, ^{16}O-rich and ^{16}O-poor, respectively. Heterogeneity is also present at micrometer scale within chondrule phenocrysts and glassy mesostasis/plagioclase of different chondrite groups invoking parental body processes (e.g. Kita et al., 2010; Rudraswami et al., 2011; Bridges & Ireland, 2015) yet some relict ^{16}O-rich olivine, compared to host olivine in porphyritic chondrules indicates a heterogeneity related to the chondrule formation process itself (Kita et al., 2010; Rudraswami et al., 2011; Tenner et al., 2013, 2015, 2017; Weisberg et al., 2011; Nagashima et al., 2015; Schrader et al., 2013, 2014, 2017).

Two main scenarios have been suggested to explain chondrule formation: 1) nebular scenarios such as shock waves (Desch et al., 2005; Morris & Desch, 2010), winds (Shu, et al., 1996; Salmeron & Ireland, 2012), magnetic reconnection flares (Cameron, 1995), magnetohydrodynamic turbulence (McNally et al. 2013), gas-liquid condensation (Varela et al., 2006), etc.; and 2) planetary scenarios based on e.g. planetesimal splash model (Sanders & Scott, 2012) or impact-generated plume environments (Symes et al., 1998; Fedkin & Grossman, 2013; Johnson et al., 2015), etc. The existence of a wide range of mechanisms of widely disparate nature shows that chondrule formation is a big problem yet to be resolved in cosmochemistry.

In general, any chondrule formation theory should explain, at least, the following basic chondrule properties (Salmeron & Ireland, 2012 and references therein): size (~0.1–1 mm), amount of mass processed considering the volume they represent in chondrites, low initial ambient temperature (< 400 K), rapid heating of precursors to peak temperatures (~1800 K), rapid cooling (~10 – 1000 K/h), formation of compound chondrules, dusty

rims around chondrules, the apparent chondrule-matrix chemical complementarity, and a broadly unfractionated chondrite chemistry.

2.5. Matrix

Scott et al. (1984) defined matrix as the fine-grained material (<5 μm) that hosts larger, optically identifiable, high-temperature objects (chondrules, refractory inclusions, and other components) in chondrites. Variations in matrix texture and composition are often related to parent body alteration (e.g. aqueous alteration and thermal metamorphism) forming e.g. serpentines, Fe-Mg-rich clays, and other phyllosilicates. In the rare chondrites that have avoided this alteration, matrices are composed of crystalline Mg-rich silicates (mostly olivine and pyroxene), amorphous silicate, Fe-Ni metal, refractory solar nebula grains, sulfides, and rock fragments. Other important constituents are presolar grains, carbon and organic phases (Scott & Krot, 2014). Although, as a whole, the matrix from primitive chondrites can be seen as material that experienced low temperatures (ca. 300 – 400 K) they are in fact a diverse mixture of high-temperature material and low-temperature material. The volume of chondrite matrices ranges from 5 to 50 vol. %, however, no matter the proportion, it appears that matrix and chondrules have a complementary chemical composition that characterizes the distinct chondrite types (Hezel & Palme, 2007; Bland et al., 2005).

In general, matrices have a near-chondritic composition but are richer in FeO than chondrules and have refractory abundances that deviate more from bulk chondrite values (Scott & Krot, 2014). In general, bulk oxygen isotopic compositions of matrix covers ranges similar to that for chondrules (Krot et al., 2009).

2.6. Ordinary chondrites

OCs are the most common meteorites falling to Earth. They can be differentiated from other chondrites, and also among them, using three main primary classification parameters: bulk chemical composition, bulk oxygen isotope composition, and oxidation state. OCs are classified as H, L, and LL iron groups, whose distinctions are related to the

bulk abundances of iron; where H means high total iron content; L, low iron content; and LL, low metallic iron relative to total iron, as well as low total iron content (Krot et al., 2014). Chondrules within OCs are their most significant constituent and could form up to 80% of their volume.

OCs have been modified by geological processes in asteroids. Aqueous and hydrothermal alteration, impacts, and thermal metamorphism are the main processes involved in the modification of chondritic material in asteroids (Scott & Krot, 2014). Modification of OCs due to thermal metamorphism is of special interest. Van Schmus & Wood (1967) introduced a classification scheme that, as mentioned before, provided a guide to assess the degree of thermal metamorphism experienced by OCs and depending on this scheme they can be assigned to different petrologic (or petrographic) types (types 3 to 6). Type 3 OCs are divided into subtypes 3.0-3.9 depending on their characteristics and there is evidence that chondrule mesostasis, CAIs, and matrix in the lowest subtypes were affected by hydrous fluids and they have promoted equilibration and alteration on these domains. Fluids were lost from parent bodies with increasing metamorphism. Type 4 to 6 OCs are thought to represent an isochemical metamorphic sequence (Scott & Krot, 2014).

Additionally, type 1 and type 2 are petrologic types accounting for the degree of aqueous alteration experienced by chondrites with type 1 being more altered than type 2 (Scott & Krot, 2014). This classification is associated to carbonaceous chondrites and there are not known OCs of any of these types.

Whole rock oxygen-isotopic composition of H, L, and LL groups are similar but each of them plots to their own region above the TF line on the triple-oxygen diagram with $\Delta^{17}O$ values being 0.73±0.18 ‰ (2SD), 1.07±0.18 ‰ (2SD), and 1.26±0.24 ‰ (2SD), respectively. On the other hand, bulk oxygen isotope ratios of chondrules contained in OCs plot above the TF line show a similar range (smaller compare to chondrules from carbonaceous chondrites) but randomly distributed compositions among the three groups, without any systematic difference, and no grouping corresponding to the classification of the host meteorite. These oxygen isotope signatures suggest that OC chondrules were derived from a single population in the solar nebula which was apart from carbonaceous and enstatite chondrites (Figure 1.1; Clayton et al., 1991).

Clayton et al. (1991) proposed that the OC differences in whole-rock composition may be the result of a size sorting effect considering that their mean sizes increase as follow: H < L < LL, while oxygen isotopic ratios decrease with chondrule size. As a general conclusion, they proposed that oxygen isotope compositions of chondrules in ordinary, enstatite and carbonaceous chondrites were the result of an exchange between ^{16}O-rich solid precursor and ^{16}O-poor nebular gas of different composition arguing a temporal evolution of the gas.

Subsequent bulk chondrule work made by Ash et al. (1998) showed no correlation between bulk chondrule isotope composition and chondrule size from Tieschitz (H/L3.6). In the same line Bridges et al. (1998, 1999) studied individual chondrules accounting sizes, chemical and mineralogical compositions, and oxygen isotope compositions from Chainpur (LL3.4), Parnallee (LL3.6), and Bo Xian (LL3.9). They found an inverse correlation between size and δ^{18}O in Chainpur and argued that this variation might reflect a more extensive exchange of smaller chondrules with surroundings ^{17}O- and ^{18}O-rich material due to their larger surface/volume ratio, particularly a ^{16}O-poor fluid water in the parent body. Recently, Metzler & Pack, (2016) measuring bulk chondrule compositions found an inverse size vs. δ^{18}O correlation from NWA 5205 (LL3.7). On the contrary, Clayton et al. (1991) and Metzler et al. (2017) reported a direct correlation between size and δ^{18}O bulk composition in Dhajala (H3.8) and Weston (H4), and NWA 2465 (H4), respectively. Metzler et al. (2017) speculated that the mixing line of UOCs (slope 0.63-0.77) was obtained principally due to exchange between molten chondrules and ^{16}O-poor nebula gas. Finally, Metzler et al. (2017) suggested that if the UOC mixing line was acquired by the interaction among chondrule melts and nebular gas, and if smaller chondrules are more likely to exchange with their surroundings, then chondrules from LL and H chondrites interacted with different reservoirs, namely that the H-reservoir was ^{16}O-rich relative to LL-reservoir which means that chondrules from OCs did not sample the same population of chondrules in terms of oxygen isotope reservoirs.

Early SIMS oxygen isotope analysis of olivine within OC chondrules were measured by (Sears et al., 1998; Saxton et al., 1998; Russell et al., 2000; Pack et al., 2004). In general, they reported ^{16}O-rich forsteritic grains with different oxygen isotope composition compared to bulk chondrules analyzed previously. In particular, Russell et al., 2000

measured mineral phases in Al-rich chondrules from Sharps (H3.4), Inman (L3.4), Quinyambie (L3.4), and Chainpur (LL3.4) and found a correlation of oxygen isotope ratios with chondrule textures with porphyritic chondrules being ^{16}O-enriched compared to barred and radial chondrules. They explained these variations concluding that partially melted chondrules retain some ^{16}O-rich relict grains while completely melted chondrules interacted more extensively with the ^{16}O-depleted nebular gas.

Ruzicka et al. (2007) reported SIMS oxygen isotope compositions from olivine grains in chondrules from Sahara-97210 (LL3.2), Wells (LL3.3), and Chainpur (LL3.4). They concluded that there were two groups of olivine based on their isotopic compositions: 1) ^{16}O-rich forsterite and Mg-rich olivine present as relict grains in Type II chondrules (Δ^{17}O ~ -8 to -4‰), and 2) less ^{16}O-enriched which included non-relict or normal ferrous olivine grains from Type II chondrules, normal Mg-rich olivine grains in Type I chondrules, dusty olivine relict grains in Type I chondrules, and Mg-rich olivine relicts in a Type I and Type II chondrule (Δ^{17}O ~ -3 to 4‰). They hypothesized a temporal evolution in the oxygen isotope composition of the gas where chondrules formed, from a ^{16}O-rich to ^{16}O-depleted, and that an earlier chondrule forming event produced Type I chondrules and isolated forsterites in carbonaceous chondrites, and provided forsteritic grains that were added to OCs as relict grains in chondrules and as isolated grains. The later chondrule formation events produced both Type I and Type II chondrules in OCs under diverse redox and thermal settings.

Libourel & Chaussidon (2011) reported that the Semarkona ordinary chondrite contains three different populations of Mg-rich olivines with Δ^{17}O showing well-defined peaks at -2.7‰, 0.3‰, and 2.7‰. They proposed that Mg-rich olivines from OC, CV, CR, and R chondrites are indistinguishable based on both chemical and oxygen isotopic compositions suggesting the same provenance and likely to represent debris of broken differentiated planetesimals.

Kita et al. (2010) reported SIMS oxygen isotope analysis from different phases of 36 chondrules from OC Semarkona (LL3.01), Bishunpur (LL3.15), and Krymka (LL3.2) showing a wide range of isotopic composition in Type I chondrules and a more compact cluster in Type II chondrules (Δ^{17}O ~0.54 ‰). They found an apparent mass-fractionation effect in Type I chondrules hypothetically occurring at low levels of dust enrichment (100

times solar) where evaporation and recondensation of solids may explain the isotopic fractionation between molten chondrule which correlates with bulk Mg/Si fractionation. On the other hand, Type II were explained as having water ice within their precursors and they interacted with a dust enriched environment (1000-10000 times solar) and, contrary to Type I chondrules, as evaporation and recondensation of major oxides was suppressed by dust enrichment, oxygen isotopic fractionation was negligible. Furthermore, they considered that oxygen isotope composition within Type II chondrules may have equilibrated by exchanging water vapor in the nebular gas. Additionally, based on olivine and pyroxene data they suggested that chondrule precursors in OCs were made of both ^{16}O-poor and ^{16}O-rich ($\Delta^{17}O \geq 1.6$ ‰ and $\Delta^{17}O$ as low as -9 ‰, respectively) the latter being common to chondrules in carbonaceous chondrites.

Finally, Bridges & Ireland (2015) and Kita et al. (2010) reported enrichments in the heavy oxygen isotopes of chondrule mesostasis from Semarkona (LL3.01), as compared to coexisting phenocrysts, indicating that oxygen isotope compositions in glass exchanged with a ^{16}O-poor aqueous fluid in the LL parent body during low thermal metamorphism.

3. SAMPLES AND ANALYTICAL METHODS

A combination of optical microscopy, backscattered electron (BSE) imaging, and energy-dispersive X-ray spectroscopy (EDS) was used to choose the best spots to be analyzed by further techniques. After these surveys, representative grains were selected for quantitative wavelength dispersive spectroscopy (WDS) electron microprobe analysis (EPMA). Petrographic and microprobe data were used to target subsequent secondary ion mass spectrometry (SIMS) analysis, obtained using the Sensitive High-Resolution Ion Microprobe for Stable Isotopes (SHRIMP-SI). In general, EPMA data were collected at the same site as succeeding SHRIMP-SI analysis. The spots sites were preferentially done on single phases, avoiding cracks and weathered areas. BSE images of all spots can be found in Electronic Annex 1.

3.1. Samples

The 9 samples chosen for this study are UOCs as they show minor effects of parental body processes which allow their primitive characteristics to be studied. On the other hand, they are all finds, which mean that they have been affected by terrestrial weathering to some extent. The meteorite sections were requested from the Antarctic Meteorite Collection (NASA) and comprise existing polished circular thin sections (30 um thick, 25 mm diameter). Table 3.1 shows the general characteristics of the samples obtained from both the *Meteoritical Bulletin Database* and the *Astromaterials Acquisition & Curation Office*. Weathering grades (A, B, C, and "e" for evaporates) are as reported in the *Meteoritical Bulletin Database*.

Table 3.1. Unequilibrated Ordinary Chondrite samples and their general characteristics.

Sample	Finding Location	Dimensions (cm)	Weight (g)	Group	Type	Weathering	Fayalite (mol%)	Ferrosilite (mol%)
WSG95300,25	Mount Wisting	14.0x10.0x9.0	2733.0	H	3.3	A/B	1-21	2-17
QUE 93030,2	Queen Alexandra Range	9.2x7.0x7.4	896.9	H	3.6	B/C	6-20	11-17
ALHA 77299,5	Allan Hills	9.5x5.5x3.5	260.7	H	3.7	A	11-21	15-20
MIL 05050,8	Miller Range	8.5x5.5x4.0	253.3	L	3.6	B	6-25	3-17
GRO 06054,19	Grosvenor Mountains	12.5 x 8.0 x 5.0	1319.4	L	3.6	A	4-28	4-23
DOM 10556,5	Dominion Range	5.0 x 4.8 x 3.0	119.9	L	3.6	A/Be	18-38	3
LAR 12034,7	Larkman Nunataks	14.2 x 9.0 x 4.0	930.6	LL	3.8	A/B	25-34	12-24
LAR 06279,7	Larkman Nunataks	9.5 x 6.5 x 4.0	729.8	LL	3.8	B	14-40	6-19
LAR 06301,12	Larkman Nunataks	11.5x6.5x6.0	803.6	LL	3.8	B	11-33	6-34

The following brief petrographic descriptions correspond to descriptions made by the NASA Meteorite Working Group (Johnson Space Center, Houston, USA):

WSG95300 has been classified as an H3.3 chondrite. The section is described as a section essentially unweathered and shows abundant chondrules (reaching up to 1.8 mm diameter), chondrule fragments, and mineral grains set in a dark matrix holding moderate amounts of Fe,Ni alloys, and troilite. EPMA analysis show variable compositions of olivine and pyroxene domains.

The QUE93030 polished-thin section corresponds to an H3.6 chondrite. The section is strongly weathered. Abundant chondrules (up to 1.5 mm across), chondrule fragments, and mineral grains are observed within a dark brown to black matrix, which contains abundant Fe,Ni alloys, and troilite in lesser amounts. The compositions of olivine and pyroxene are variable.

The meteorite ALHA77299 is classified as an H3.7 chondrite. The section has been described as having a closely-packed mass of chondrules (up to 1.5 mm diameter) and minerals set in a relatively small amount of matrix with interstitial Fe,Ni, and troilite. Moderate weathering can be recognized on the sample. Both olivine and pyroxene show variable compositions.

The sample MIL05050 has been classified as an L3.6 chondrite exhibiting well-defined chondrules (up to 1.5 mm) set in a black matrix of fine-grained silicates, troilite, and Fe,Ni alloys. The compositions of olivine and pyroxene are variable.

The section named GRO06054 has been classified as an L3.6 chondrite. Well-defined chondrules (up to 3mm) have been observed within a black matrix of silicates, troilite, and Fe,Ni. Low weathering and shock effects are present in the sample. Olivine and pyroxene compositions are variable.

The sample DOM10556 has been classified as an L3.6 chondrite. Various large and well-defined chondrules (up to 1 cm) are set in a black matrix of silicates, troilite, and Fe,Ni. Mild weathering and weak shock effects were observed as well. Olivine and pyroxene are unequilibrated and have heterogeneous compositions.

The meteorite LAR06279 is an LL3.8 chondrite. The section exhibit chondrules up to 1.5 mm across, chondrule fragments, occasional igneous clasts, within a matrix of fine-grained silicates, Fe,Ni alloys, and troilite. Weak shock effects have been observed. Olivine and pyroxene compositions are heterogeneous.

Sample LAR06301 has been classified as an LL3.8 chondrite. Several sharply-defined chondrules (up to 1.5 mm diameter) and rare melt clasts are set in a dark matrix. Fe,Ni metal, and troilite have been observed, as well as minor shock effects products. Olivine and pyroxene compositions are heterogeneous.

LAR12034 has been classified as an LL3.8 chondrite. Like the above samples, this section includes sharply-defined chondrules (up to 2mm) within a matrix of fine-grained silicates. Mild weathering products are present. Olivine and pyroxene compositions are heterogeneous.

However, during the course of this work, samples GRO06054, DOM10556, and MIL05050 were reclassified as L3.05, L3.1, and L3.1 (Discussion Chapter).

A general view of the samples is shown below in Figure 3.1.

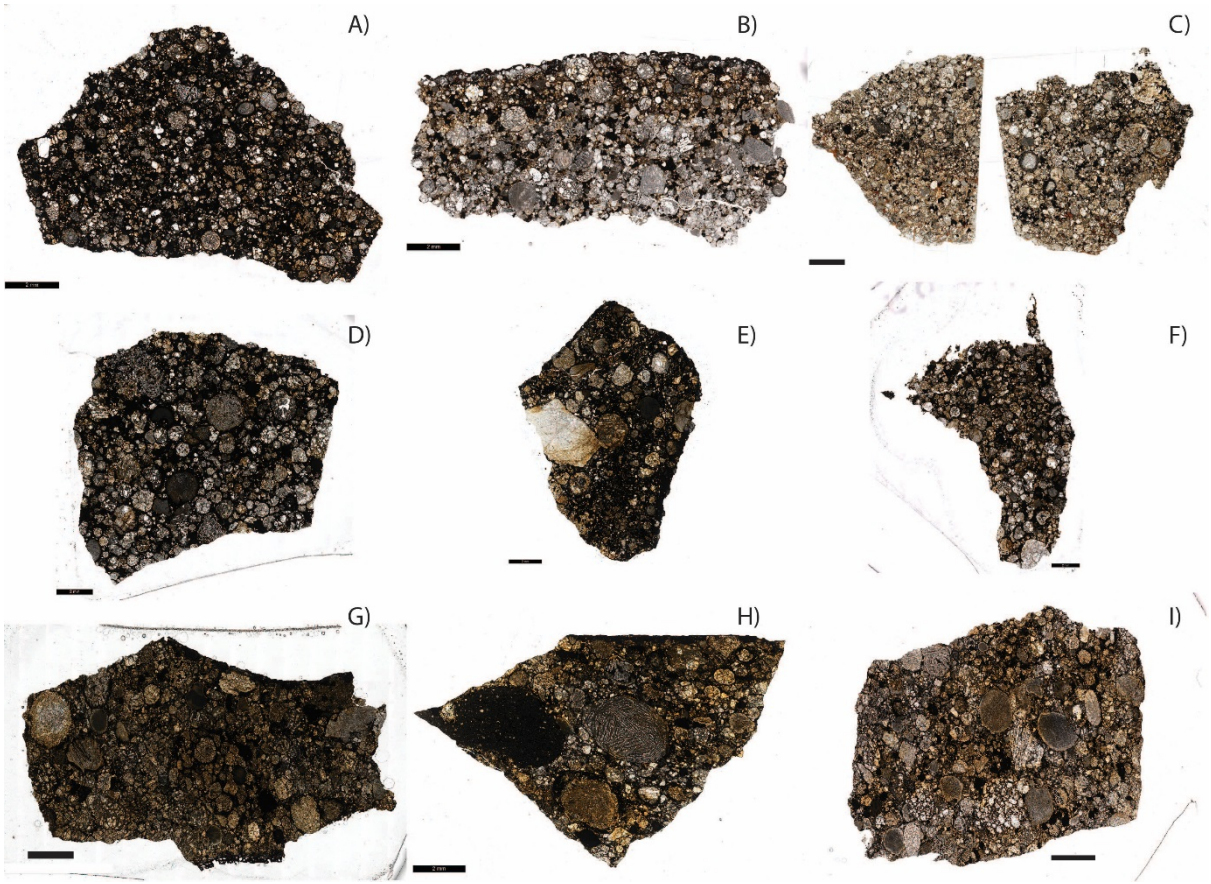

Figure 3.1. Transmitted light image of the UOCs used on this study. A) WSG95300, B) QUE93030, C) ALHA77299, D) GRO06054, E) DOM10556, F) MIL05050, G) LAR06279, H) LAR06301, and I) LAR12034. Scale bars are 2 mm.

3.2. Optical Microscopy and Scanning Electron Microscopy

General petrography observations of the 9 thin-polished sections were obtained using an automated Leica D6000 microscope in reflected and transmitted light at the Research School of Earth Sciences (RSES, Figure 3.1).

Further petrographic observations were acquired by a BSE imaging survey performed using a JEOL JSM-6610A SEM at the RSES, to identify and image suitable spots within chondrules and matrix for additional EPMA and SIMS analysis. The samples were coated with carbon prior to examination. Examples of representative chondrules can be observed in Figure 3.2.

In some cases, in order to identify phases within chondrules, EDS analyses were carried out. Operating conditions were a 15kV accelerating voltage and a beam current of 10 nA at a 10 to 12 mm working distance.

3.3. Electron Microprobe Analysis

Representative spots were selected for quantitative WDS electron microprobe analysis (EPMA) using the Cameca SX100 at the RSES, to characterize major- and minor-element compositions of olivine. The data were obtained in 13 sessions with measurements performed at 15kV accelerating voltage and a beam current of 20 nA and a 15 μm diameter defocused beam. Counting times were 30s on peak and 15s on the background. Natural and synthetic standards were used for quantitative analysis bracketing every 15-20 measurements of unknowns. Particularly, the San Carlos olivine standard material was used to generate a calibration line in order to correct an analytical drift observed during sessions for the major compounds (SiO_2, MgO, and FeO). This correction was applied to unknowns.

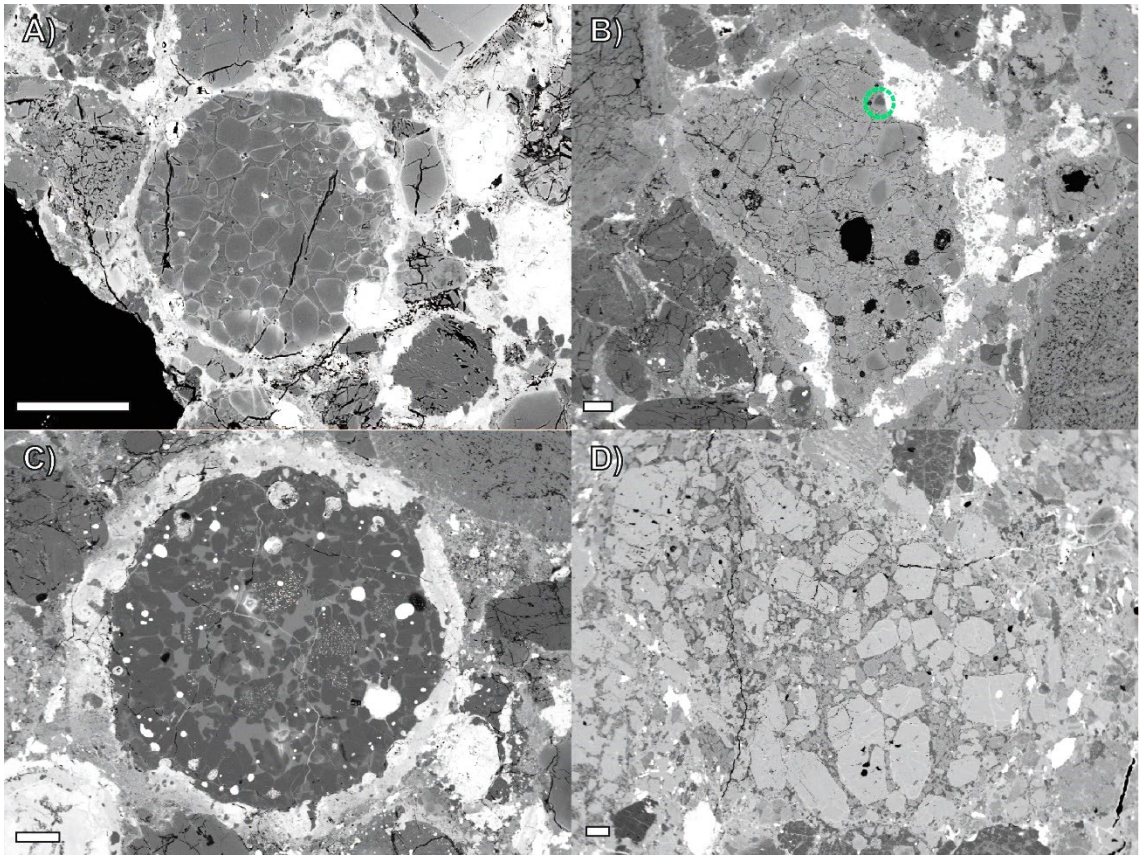

Figure 3.2. BSE images of 4 chondrules. A) FeO-rich (Type II) PO chondrule (CH069) from WSG95300. Euhedral olivines are st in a glassy mesostasis. Olivines show a ferrous-enriched edge (light grey). B) FeO-rich (Type II) PO chondrule (CH354) from GRO06054. Relict FeO-poor olivines are present (e.g. dashed green circle). C) FeO-poor (Type I) POP chondrule (CH334) from GRO06054. Olivines are set in a glassy mesostasis and Fe,Ni metal blebs can be identified. Some metal has been replaced by weathering products. Note the "dusty" relict olivines in the core of this chondrule. D) FeO-rich (Type II) POP chondrule (CH621) from LAR06279. This chondrule appears to be chemically equilibrated. Note the coarser-grain matrix surrounding it product of thermal metamorphism. Scale bars are 100 μm.

3.4. Sensitive High-Resolution Ion Microprobe Stable Isotopes (SHRIMP-SI)

Oxygen isotope measurements of selected chondrule olivine samples were performed in-situ using the SHRIMP-SI at RSES. SHRIMP-SI is an instrument similar to SHRIMP-II but designed and optimized to perform light element stable-isotope analysis (Ireland et al., 2008). Detailed differences and similarities between SHRIMP-II and SHRIMP-SI can be found in Ireland et al. (2014) and Ávila et al. (In Review). A schematic view of the instrument can be observed in Figure 3.3.

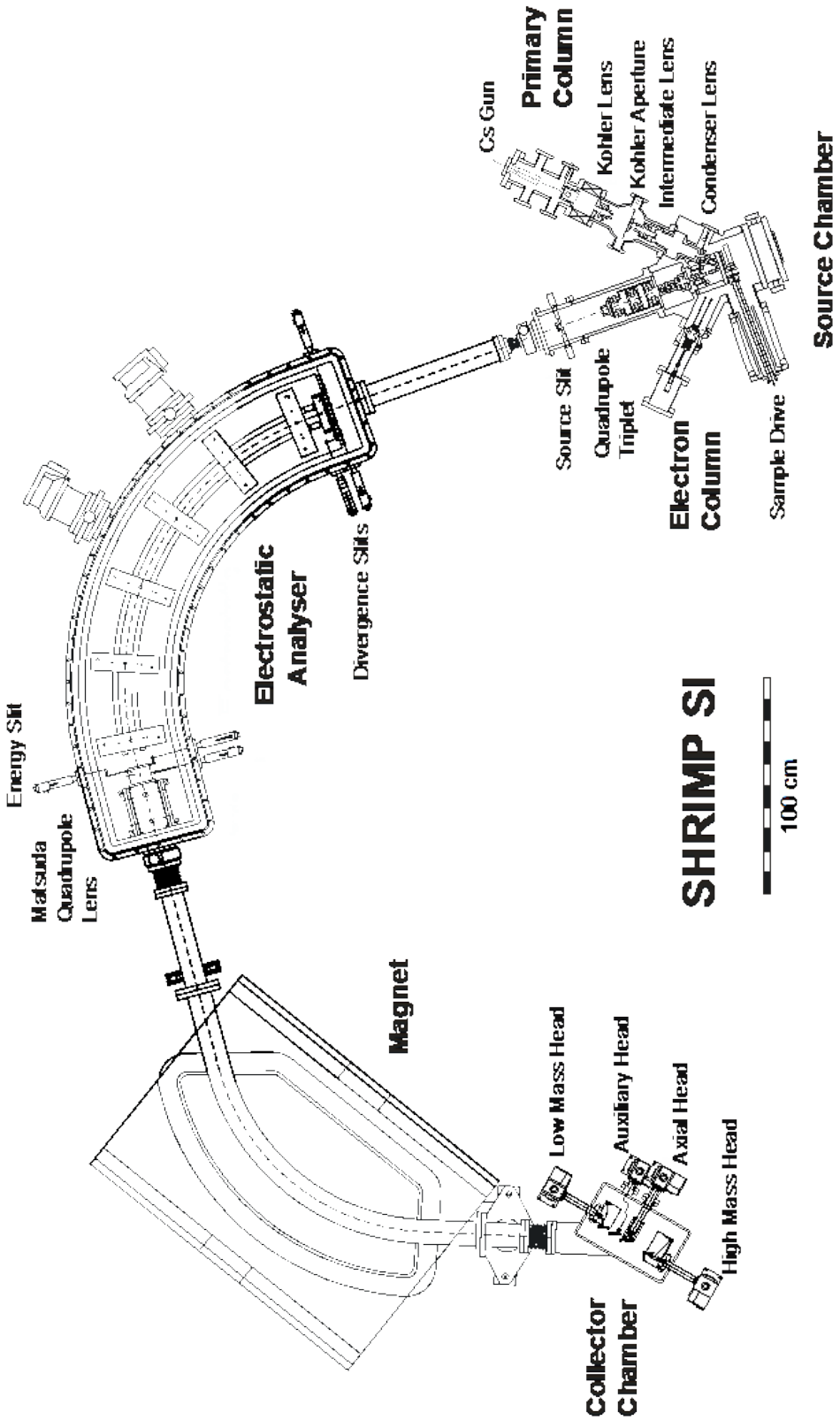

Figure 3.3. Schematic diagram of the SHRIMP-SI. Image obtained from Turner et al. (2015).

Prior to analysis, thin sections were gently polished by hand with a 1 μm diamond paste to remove the carbon coat used for SEM and EPMA analysis. Subsequently, the samples were cleaned with detergent and ethanol in an ultrasonic bath and coated with a 40 nm film of aluminium prior to SHRIMP-SI analysis. The use of aluminium instead of carbon or gold is because it has better conductivity than carbon and is lighter than gold. Aluminium can be removed easily by a 30 min warm water ultrasonic bath as previously checked with a basalt epoxy mount, or washed out using detergent. Aluminium allows better results to be obtained without jeopardizing highly precious samples in view that there is no need to repolish the sections to remove the metal coating. After at least one day in the vacuum oven (60°C), the samples were loaded into steel holders for insertion into SHRIMP-SI. Steel holders are designed to avoid edge effects related to proximity to the steel holder as shown by Ickert et al. (2008).

First, the source chamber was pumped down to a base pressure which is about 5 x 10^{-9} mbar, but common pressure with epoxy mounts is 1.0 x 10^{-8} mbar (Ávila et al., In Review).

A Cs+ ion beam produced in a Kimball Physics IGS-4 ion gun was accelerated up to 15 keV with an intensity of 1-2 nA and focused to sputter a ~ 20 x 30μm spot (under Köhler illumination) on the sample. To neutralize positive charge build-up on the sample surface, electrons were delivered to the target focused to a spot of ca. 200 μm diameter using an electron gun potential set to -2.0 kV. During measurements, the electron-induced secondary ion emission (EISIE, Ickert et al., 2008) was monitored and subtracted from the total counts.

The resulting negative secondary ions, after their initial acceleration due to the difference between sample voltage (-10 kV) and the first extraction plate voltage (-9.2 kV), were accelerated to real ground by the extraction lens. The beam transmission is maximized through the source slit, which was set to 20 μm, by the standard quadrupole-triplet lens system used on other SHRIMP models (Ireland et al., 2008).

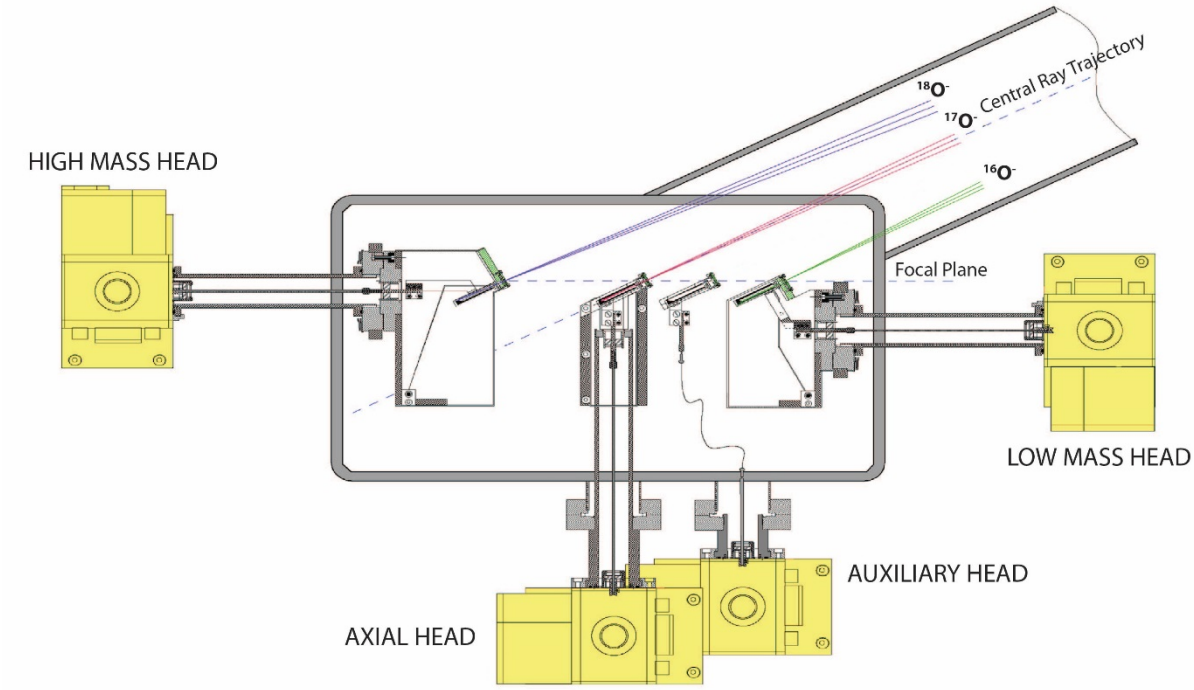

Figure 3.4. SHRIMP-SI multiple collector configuration used for 3-isotope oxygen analysis. The $^{18}O^-$, $^{17}O^-$, and $^{16}O^-$ ions can be observed being focused into high-mass (HM) head, axial (AA) head, and low-mass (LM) head. Modified from Ireland et al., 2014.

The secondary mass analyzer consists of an electrostatic analyzer (ESA, turning radius of 1270 mm), an electrostatic quadrupole lens, and a magnet (turning radius of 1000 mm). The secondary ions are focused according to mass into the collector slits located in the multiple collector chamber (Figure 3.4). The collector slit widths for the oxygen isotope measurements of $^{16}O^-$, $^{17}O^-$, and $^{18}O^-$ were set at 300 µm, 120 µm, and 300 µm, generating a mass resolution of ca. 2000, 5000, and 2000, respectively. The highest resolution of the axial detector is required to resolve potential isobaric interference of $^{16}OH^-$ on $^{17}O^-$. Representative peak shapes are shown in Figure 3.5.

For this work, the head detectors were equipped with Faraday cups for simultaneous detection. Measurements were performed in a static multicollector mode with the electrometers for $^{16}O^-$ and $^{18}O^-$ set to 10^{11} Ω (50V range) and 10^{12} Ω (5V), respectively, and in charge mode for $^{17}O^-$ (5V).

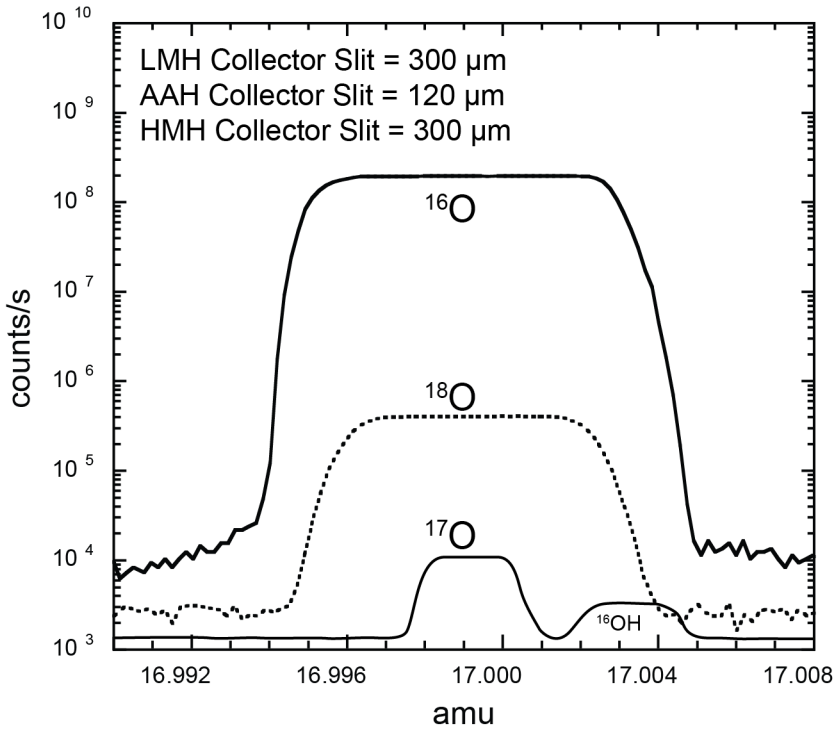

Figure 3.5. Typical mass spectra of the oxygen mass region. Collector slit widths were set at 300µm for $^{16}O^-$, 120µm for $^{17}O^-$ and 300µm for $^{18}O^-$.

Table 3.2 Analytical conditions of SHRIMP-SI

Component	Value
Primary beam	1-2 nA
Source slit	20 µm
LM (^{16}O) collector slit	300 µm
AA (^{17}O) collector slit	120 µm
HM (^{18}O) collector slit	300 µm
LM electrometer (resistor, range)	10^{11}Ω, 50 V
AA electrometer (mode, range)	Charge mode, 5 V
HM electrometer (resistor, range)	10^{12}Ω, 5 V
Electron Gun energy	-2 kV

Each analysis took approximately 11min which can be divided into 120s of pre-sputtering, ~100s of automated steering of secondary ions, ~5s of automated centring of the secondary ions in the collector slits, 60s of EISIE counts which consisted of 3 measurements of 20s count time at the beginning, middle, and end of each analysis, and 400s of data collection, which was divided into 2 sets of 10 scans, with each scan comprising 20s. Table 3.2 summarises the analytical conditions.

The data were collected over 11 sessions, and San Carlos olivine standard was run as the primary reference material. Oxygen isotopic ratios for San Carlos olivine were obtained previously by Laser Fluorination Mass Spectrometry (LFMS, $\delta^{17}O$=2.705‰, and $\delta^{18}O$=5.208‰; McKibbin et al., 2016). San Carlos olivine was used to monitor instrumental mass fractionation (IMF), and to assess the precision, accuracy, and reproducibility of oxygen-isotope measurements of each session.

Olivine in this study ranges in magnesium composition from ~Fo58 to ~Fo100 (Fo= molar Mg/[Mg+Fe] x 100). One session was dedicated to tracking systematics errors induced by matrix effects using 3 synthetic olivines (~Fo50, ~Fo60, and ~Fo70), for which oxygen isotopes compositions were obtained previously by LFMS (McKibbin et al., 2016). The offset of $\delta^{17}O$ and $\delta^{18}O$ when comparing SHRIMP-SI with the LFMS results were obtained for the 3 olivine samples and a calibration line was calculated to correct the compositional induced differences among the unknowns with Fo numbers between Fo50 and Fo73. A second calibration line obtained by Scicchitano (2018), who investigated matrix effects of olivine in the range of Fo73 and Fo100, was used to correct matrix effect of the unknowns within that compositional range.

After SHRIMP-SI runs, analysis sites and craters of unknowns were examined and documented using a JEOL JSM-6610A SEM at RSES.

3.5. Data Reduction

Data reduction of the measurements was accomplished with POXI MC Labview software (an in-house RSES-ANU data-reduction program).

To evaluate chondrule populations within OCs, some concepts and methodologies that are well known and widely used in Earth Science for assessment populations are applied in this investigation, particularly those used on the assessment and characterization of age and provenance of zircons, e.g. the weighted mean (Wendt & Carl, 1991; Schoene et al., 2013; Spencer et al., 2016; Ávila et al., In Review).

In this regard, the population assessment has been done using the $\Delta^{17}O$ ratios since it does not suffer instrumental mass-fractionation effects, represents the mass-independent fractionation variability of the solar system materials, and is used as a value of the oxygen isotope reservoir in which solids were thermally processed in the protoplanetary disk.

Although a full description of the data assessment protocol used for oxygen isotope analysis of zircons can be found in Ávila et al. (In Review) a summary is given below. A similar assessment is used here for chondrule olivine.

Briefly, the aim of the SHRIMP-SI data assessment protocol is to provide a value and its uncertainty which reflects the oxygen isotope composition of each olivine spot, dependent on analytical set up, and the fidelity of the measurement based on the scatter associated with repeated measurements (reproducibility) of the reference material (San Carlos olivine). Therefore, it combines within-spot measurement uncertainties (internal error component) and the uncertainty intrinsic to the reference material (external error component). For each session, data is normalized to the reference material and then the uncertainties are calculated for both the spot and the sample when analyses are pooled.

In this work, the standard deviation (SD) is used as an estimate of variability (reproducibility) of the population from which the sample was obtained both for the reference material and the unknowns, and is reported at the 2σ level. On the other hand, the standard error (SE) of the mean is used to represent the precision or uncertainty of the estimated mean (mean ± SE) which is calculated by the expression $SE = SD/\sqrt{n}$, with SD being the standard deviation and n the size of the sample. Since inferences about

populations are being made on the basis of the information contained in a sample, standard deviations and standard errors (e.g. single spot or sample) are estimated at 95% confidence intervals ($\sigma_{95\%}$) applying a two-sided 95% confidence distribution with n-1 degrees of freedom Student-t value.

The internal error of a spot analysis is calculated by combining the 2 subsets of oxygen isotope ratios, and each subset represents a mean value of 10 acquisitions with an associated standard error (SE). The distribution of the subset analysis (10 scans) is statistically assessed and up to two outliers are rejected if suitable. A weighted mean is calculated for each subset and the internal error is expressed as the error of the weighted mean.

The external error of a spot analysis has two components. The internal error components explained above and an external error component. The external error component is calculated by assessing the reproducibility or variability (SD) of the normalizing reference material which is measured under the same analytical conditions as the unknowns. From Ávila et al. (In Review) an appropriate external precision (error) of any spot can be calculated as the following:

$$\sigma_{ext\_spot} = \sqrt{\sigma^2_{int\_spot} + SD^2_{RM}}$$

Therefore, the external spot error (σ_{ext_spot}) is the quadratic sum of the internal spot precision (σ_{int_spot}) and the standard deviation on the repeated analyses of the reference material (SD_{RM}). In this study, the external error of each spot has been calculated using the same formula and San Carlos olivine as reference material.

The internal error of a sample (SE of the mean) is calculated by the weighted mean of the pooled spot analyses using the external error of each spot. For San Carlos olivine any point lying beyond ±2.5σ of the mean is rejected as an outlier, since the sample is obtained from a nominally homogeneous reference material which is expected to come from a population with a Gaussian distribution.

The external error of the sample (unknown) is calculated by adding in quadrature the internal error of the weighted mean of the reference material and the unknown (pooled),

which are both based on the SE of the mean, and the error of the laser fluorination uncertainty (S. McKibbin, *pers. comm*.).

For chondrule olivine from OCs the assumption that a sample is drawn from a single population is neither trivial nor obvious since chondrule olivine relict grains and chondrules with the same oxygen isotope signatures as carbonaceous chondrite chondrules have been observed (e.g. Kita et al., 2010; Ruzicka et al., 2007). In chapter 4, to identify possible populations classic statistical treatments are applied to chondrule olivine (unknowns) data e.g. histograms, box and whisker, and cumulative density function in order to visualize the variation of the sample distribution without any a priori assumptions on their dispersion. After exploratory analysis, statistical 'outliers' are detected at the 95% confidence interval of the whole sample and subsequently removed.

The pooled data for both the reference material and unknowns are assessed by the mean squared of weighted deviates (MSWD) or reduced chi-squared statistic test, which is commonly used to assess the robustness of analytical uncertainties. When measurements of the same chondrite were obtained in different SHRIMP-SI sessions, data is previously merged and statistically evaluated for populations.

For the unknown measurements this data treatment is done for both individual chondrule olivine data and chondrule olivine average data. In this regard, for chondrules with more than one measurement the chondrule average data was calculated considering petrographic and isotopic aspects. If obvious petrographic characteristics, e.g. forsterite rich or dusty relict grains were observed, the oxygen isotope compositions of these grains were not used to calculate the average composition of the chondrule. If clear petrographic characteristics did not exist then olivine outliers per chondrule were recognized if they were statistically resolvable using the external error ($\sigma_{95\%}$) of each olivine spot. These calculations are provided in Table 5, Electronic Annex 2.

As discussed below, it is assumed that the $\Delta^{17}O$ composition of chondrule olivine obtained in this study is representative of the chondrule, even for chondrules where only one spot was measured since it has already been shown that, excluding relict grains, most chondrules are internally homogeneous within SIMS oxygen isotopes uncertainties (Kita et al., 2016 and references therein).

For this investigation, the MSWD is particularly significant because is not only used to assess analytical uncertainties but to define chondrule populations themselves. In this regard, a useful metric used in this study is the expression $1 \pm 2\sqrt{2/f}$ where f is the degrees of freedom (n – 1) (Wendt & Carl, 1991). This expression shows the range of acceptable MSWD values (95% confidence interval); related to the number of analyses used to calculate the weighted mean of a sample drawn from a population (Figure 3.6).

Concisely, an MSWD value greater than $1 + 2\sqrt{2/f}$ reflects that either the uncertainties were underestimated or that the variability represents the natural variation of the material being measured. In contrast, MSWD values lower than $1 - 2\sqrt{2/f}$ suggest that the analytical uncertainties have been overestimated or that the weighted average uncertainty has not captured the actual variation in the data which could lead to the unjustified rejection of individual measurements. Therefore, if the MSWD value does not violate the $1 \pm 2\sqrt{2/f}$ rule then there is a >95% probability that the weighted mean is appropriate and the sample forms a single population.

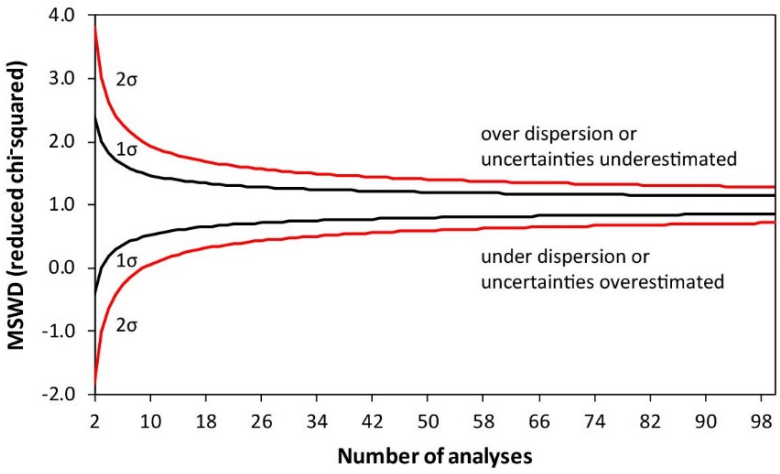

Figure 3.6. Acceptable range of MSWD values as a function of sample size at the 95% confidence level. Calculated using the $\sqrt{2/f}$ rule of Wendt and Carl (1991).

4. RESULTS

4.1. Matrix effect

Olivine in this research varies in magnesium composition from ~Fo_{58} to ~Fo_{100}. To correct for systematic errors produced by matrix effects between this range two calibration lines were used. The first one was calculated during the course of these research using 3 synthetic olivines (~Fo_{50}, ~Fo_{60}, and ~Fo_{70}) and used to correct the compositional induced differences among the unknowns with Fo numbers between Fo_{50} and Fo_{73}. A second calibration line provided by Scicchitano (2018) was used to correct matrix effect of the unknowns within Fo_{73} to Fo_{100} (Figure 4.1).

During the SHRIMP-SI session utilized to investigate matrix effects, San Carlos olivine (~Fo90) was used as the primary standard to correct for instrumental mass-fractionation. The variability (SD) of the primary standard on this session was 0.39‰ for $\delta^{17}O$, 0.31‰ for $\delta^{18}O$, and 0.32‰ for $\Delta^{17}O$ at 95% level of confidence. The weighted means and internal errors of the reference material are 2.73 ± 0.09‰ for $\delta^{17}O$, 5.23 ± 0.07‰ for $\delta^{18}O$, and 0.02 ± 0.08‰ for $\Delta^{17}O$.

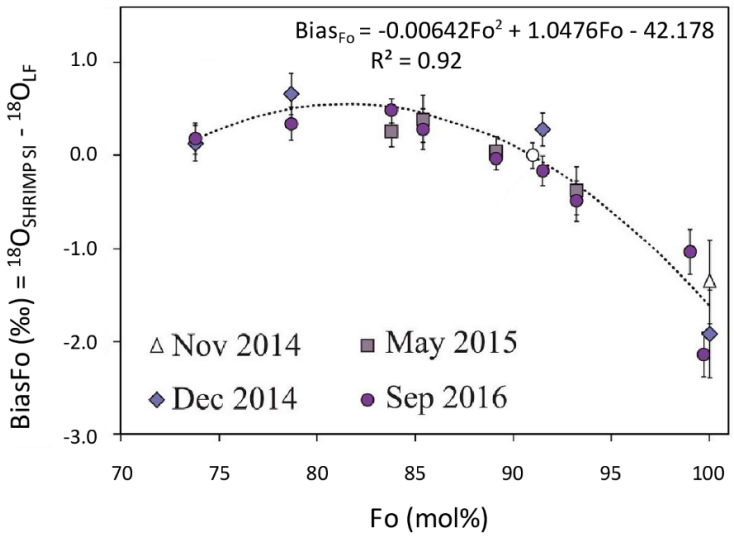

Figure 4.1. Calibration line of the weighted mean of SHRIMP-SI analysis and LFMS values between Fo73 and Fo100 after Scicchitano (2018).Open symbol corresponds to San Carlos olivine. Uncertainties are 2SE ($\sigma_{95\%}$).

After error propagation based on the reference material reproducibility, the weighted mean uncertainties of the synthetic olivines Mi32 (Fo_{50}), Mi6 (Fo_{60}), and Mi31 (Fo_{70}) are better than 0.2‰ at the 95% confidence interval. These results are shown in table 4.1.

LFMS oxygen isotope ratios and the bias of SHRIMP-SI relative to LFMS results are shown in Table 4.2. The matrix-effect bias is the difference between the weighted mean of SHRIMP-SI $\delta^{17}O$, $\delta^{18}O$, and $\Delta^{17}O$ analysis for each mineral and their respective LFMS values (Figure 4.2). From these results, the uniformity of $\Delta^{17}O$ ratios for synthetic olivines within uncertainties is clear.

On the other hand, Mi32, Mi6, and Mi31 present a bias in both $\delta^{17}O$ and $\delta^{18}O$ towards lighter compositions when measured with SHRIMP-SI. The matrix effect increases with the FeO olivine content and follows a positive linear correlation when plotting the bias versus Mg olivine composition (Figure 4.2). The secondary reference material pooled data are resolvable within uncertainties from San Carlos olivine for $\delta^{17}O$ and $\delta^{18}O$ when considering the external error of the samples weighted mean.

Table 4.1. Oxygen isotope ratios of secondary standards measured by SHRIMP-SI using San Carlos olivine as the primary reference material.

Sample	Fo molar	$\delta^{17}O$ (‰)	± External error (tσ)	$\delta^{18}O$ (‰)	± External error (tσ)	$\Delta^{17}O$ (‰)	± External error (tσ)
Mi32	50	6.91	0.16	13.27	0.13	0.01	0.14
Mi6	60	6.51	0.16	12.56	0.13	-0.02	0.14
Mi31	70	7.52	0.16	14.53	0.13	-0.01	0.14

Table 4.2. LMFS oxygen isotope values of secondary standards and bias between SHRIMP-SI and LFMS.

Sample	Fo molar	$\delta^{17}O$ (‰)	$\delta^{17}O$ Bias (‰)	$\delta^{18}O$ (‰)	$\delta^{18}O$ Bias (‰)	$\Delta^{17}O$ (‰)	$\Delta^{17}O$ Bias (‰)
Mi32	50	7.46	-0.54	14.52	-1.25	-0.09	0.10
Mi6	60	7.07	-0.56	13.67	-1.11	-0.04	0.01
Mi31	70	7.77	-0.25	15.12	-0.59	-0.09	0.09

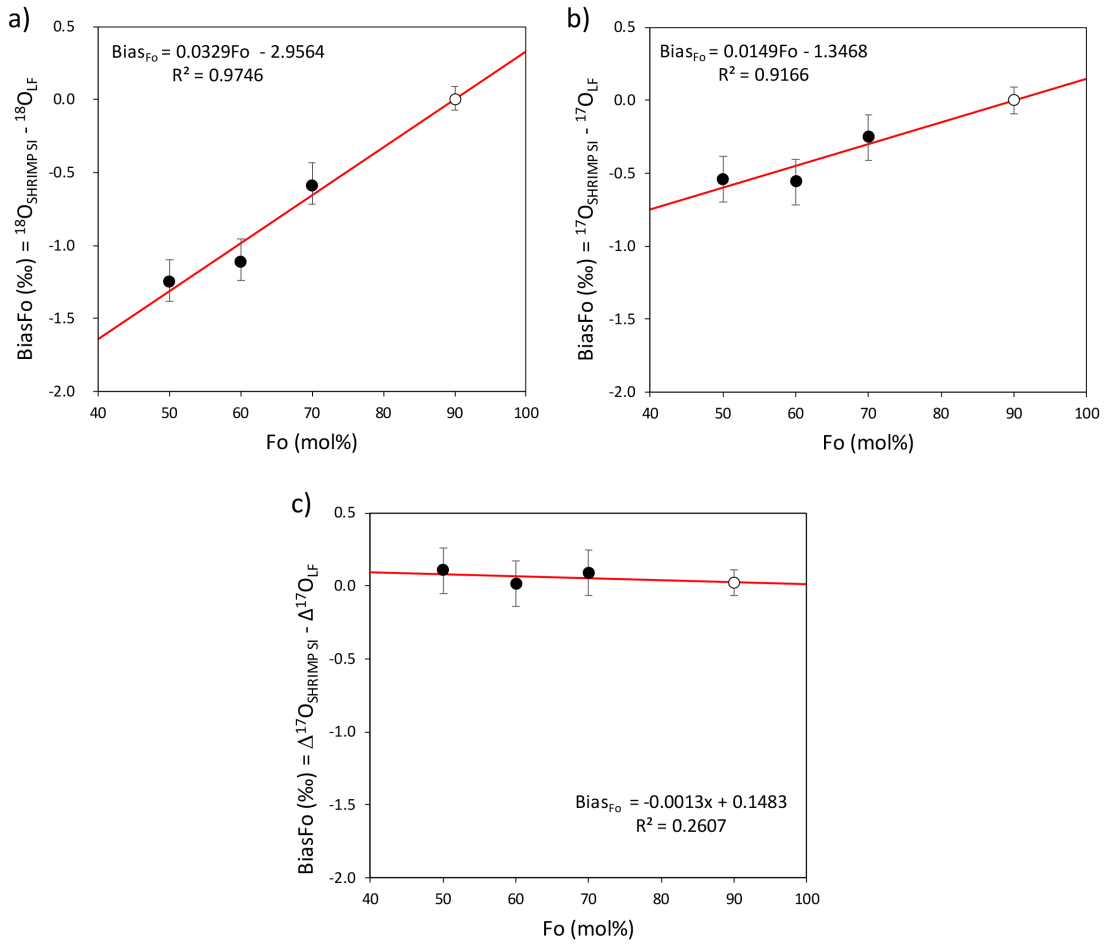

Figure 4.2. Bias of the weighted mean of SHRIMP-SI analysis and LFMS values for each synthetic olivine. Closed symbols are the synthetic olivines (Mi32, Mi6, and Mi36). Open symbol corresponds to San Carlos olivine. Uncertainties are 2SE ($\sigma_{95\%}$).

4.2. Chondrule petrography and olivine chemical compositions

A total of 620 chondrules or chondrule fragments were analyzed for major and minor elements in olivine in this study. The majority of chondrules have porphyritic textures (~97%, 598 chondrules), although chondrules with barred olivine (BO) texture (~3%, 20 chondrules), four Al-rich, and one radial pyroxene (RP) chondrule were also measured. Further division has been obtained by the proportion of olivine and pyroxene within chondrules; PO (>80% olivine), POP (20-80% olivine), and PP (<20% olivine). PO chondrules represent ~53%, POP chondrule proportion is ~34%, and PP chondrules are ~10% of the total. Selected BSE images of representative chondrules are shown in Figure 4.3.

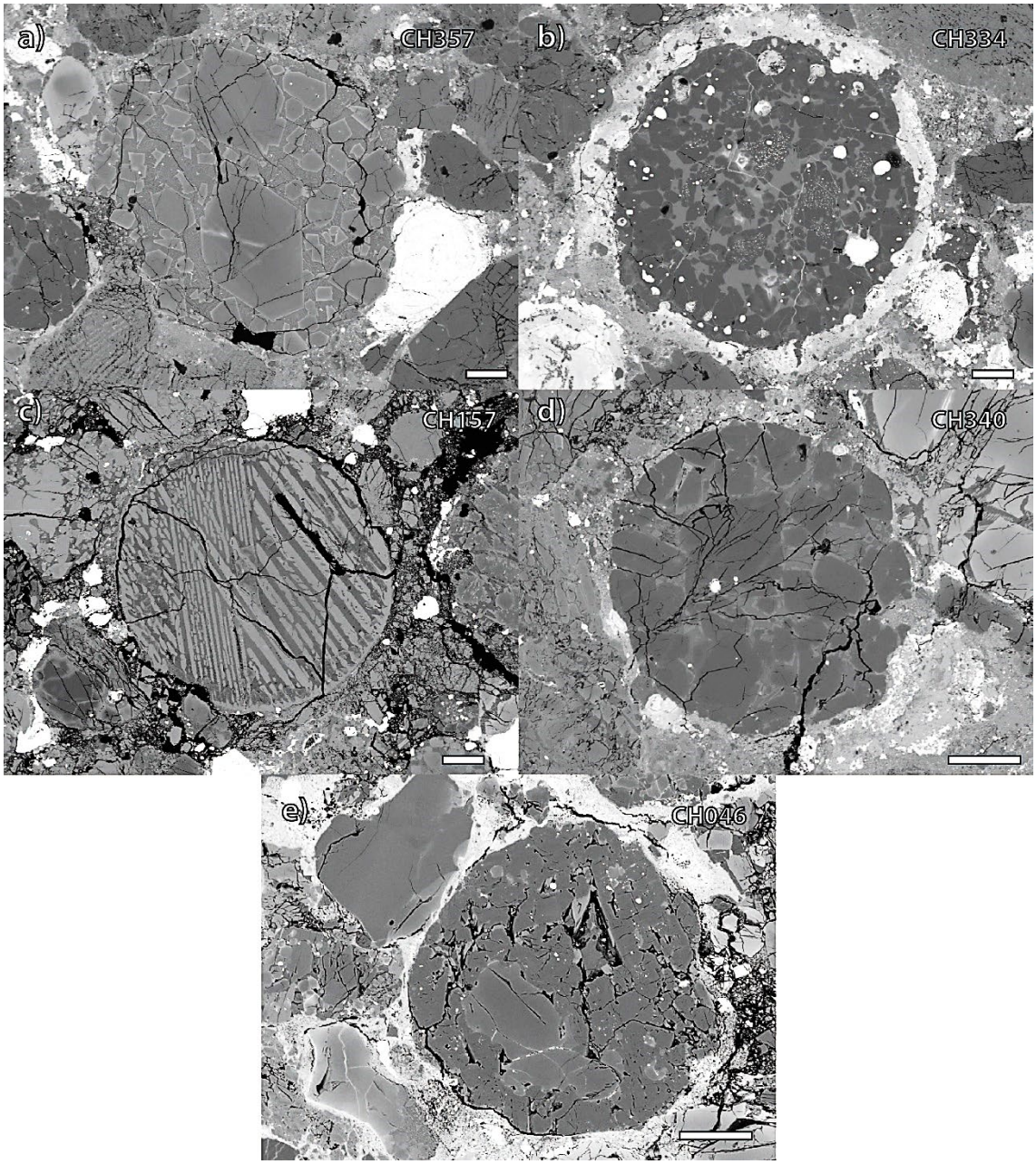

Figure 4.3. BSE images of 5 chondrules showing different textures and types. a) Type PO chondrule. Euhedral olivines are set in a mesostasis with microcrystallites. Olivines show a ferrous edge (light grey). b) Type I POP chondrule. Olivines are set in a glassy mesostasis and Fe,Ni-metal blebs can be identified. An incipient low-Ca pyroxene rim is noted. "Dusty" relict olivines in the core of this chondrule are present c) Type II BO chondrule. Olivine blades have two crystallization orientation and a rim of olivine surround the chondrule. d) Type I PO chondrule presenting a glassy mesostasis. e) Type I PP chondrule. A couple of olivine crystals are poikilitically enclosed by low-Ca pyroxene. Scale bars are 100 μm.

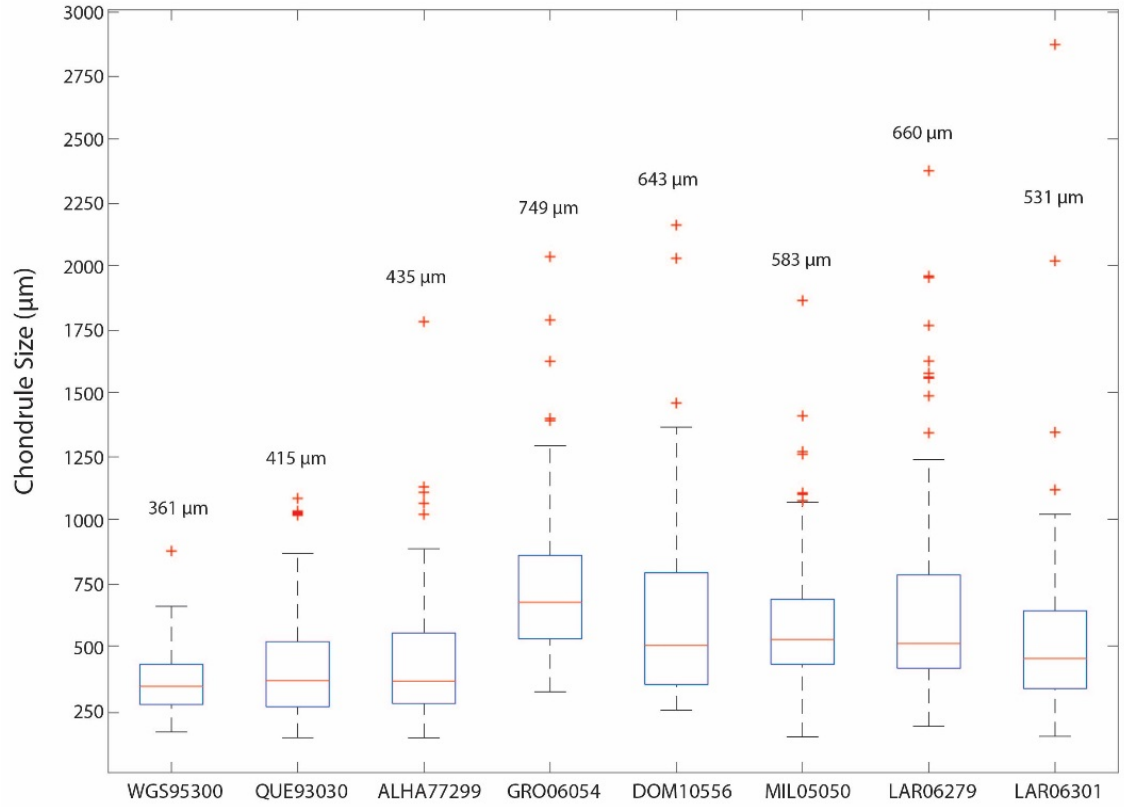

Figure 4.4. Boxplot representation of apparent chondrule size of each sample. The numbers above each boxplot are the apparent chondrule size mean.

Chondrule size distribution varies on the different samples (Figure 4.4). H chondrites share a similar chondrule mean size ranging from ~361 to ~435 µm, reaching a maximum value of ~1750 µm in ALHA77299. L samples chondrules show an unusually high mean size mean in GRO06054 (~749 µm) and smaller values in DOM10556 and MIL05050 (~643 and ~583 µm, respectively) compare to recent recommended mean size chondrules from L chondrites (500 µm). Chondrules from LL chondrites share a similar chondrule size range, from ~100 to ~2300 µm, approximately, and mean values around ~600 µm. Interestingly, based on the whisker-boxplots shape, it appears that OCs chondrules studied here have sample distribution with longer tails toward bigger chondrule sizes.

Major and minor element composition of 1371 olivines were measured, 505 from H group samples, 451 from L samples, and 415 from LL iron group samples. EPMA data per chondrule olivine can be found in table 1, Electronic Annex 2.

General chemical trends are recognised for chondrules from H, L, and LL samples. A positive correlation between FeO and MnO is a common feature among the samples and 2 clusters are recognized between ~16-20wt% FeO and ~0.4-0.5wt% MnO, for H UOCs, and ~25-30wt% FeO and ~0.4-0.5wt% MnO, for LL olivines (Figure 4.5). A positive correlation is observed between Cr_2O_3 and FeO until ~2wt% FeO, after this value the correlation disappears and Cr_2O_3 seems to be randomly distributed with many grains containing between the detection limit (~0.05wt%) and 0.7wt%. However, L samples tend to have higher Cr_2O_3 ranges than H and LL. Similar to the MnO trend, 2 clusters are obvious for both H and LL samples with Cr_2O_3 varying among ~0-1wt% and FeO abundances at ~16-20wt% and ~25-30wt% (Figure 4.5). An inverse correlation is observed between CaO and FeO abundances. In detail, up to ~5wt% FeO, a CaO decrease is noticeable. Past this value, the correlations vanish and a general increasing pattern emerges. Again, 2 olivine groups are visible around ~0.0 wt% CaO for H and LL chemical groups (Figure 4.5). In contrast to H and LL chondrites, samples belonging to the L group chondrites do not show any compositional clustering or grouping.

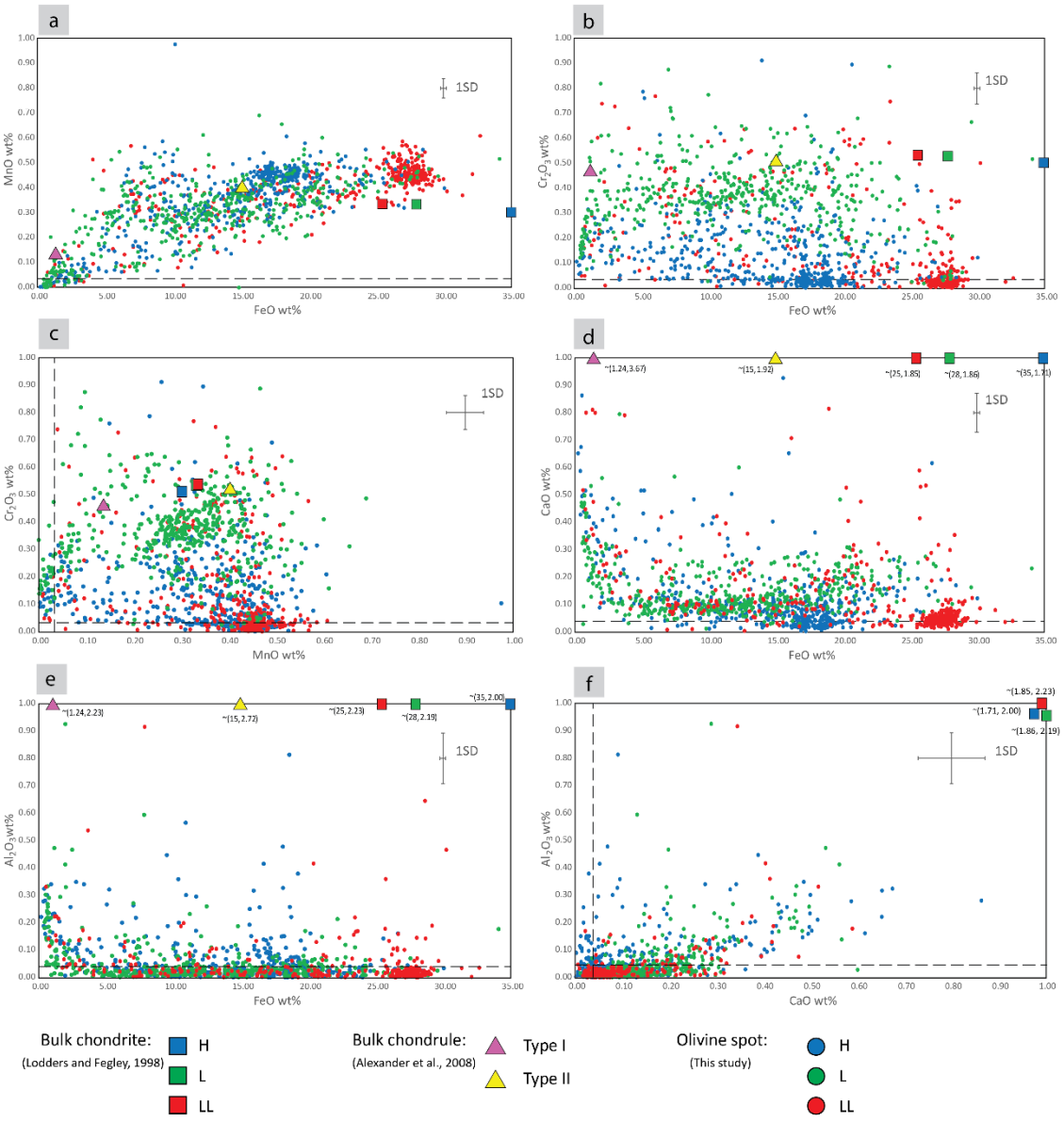

Figure 4.5. Major and minor element compositions of chondrule olivine grouped per chondrite group (H, L, and LL). Bulk chondrite and bulk chondrule, Type I and Type II, values are shown for reference. Two clear clusters are present for chondrule olivine from H and LL samples. Dashed lines represent the detection limit of the chemical compound being plotted. Representative errors are shown as 1SD.

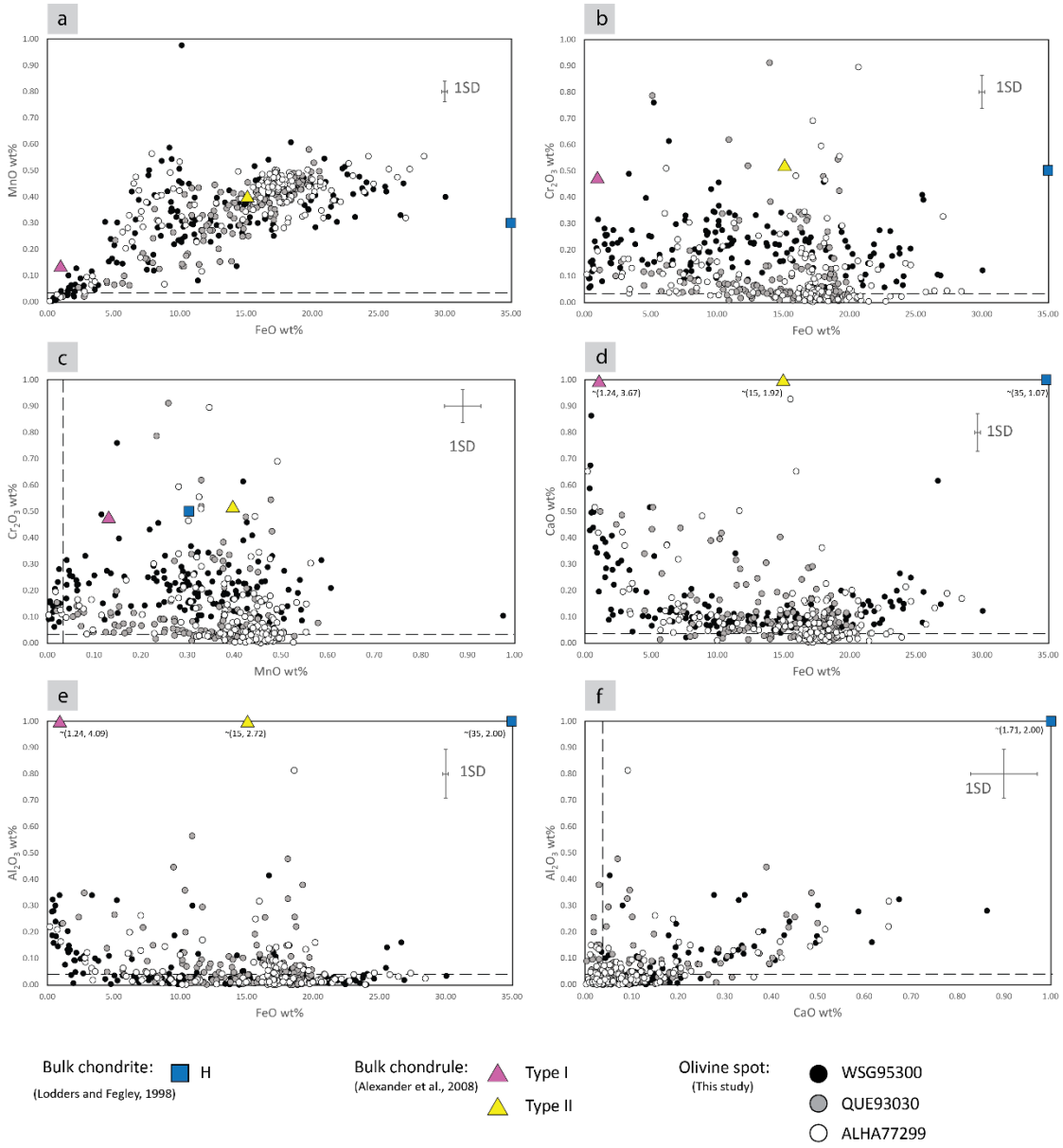

Figure 4.6. Major and minor element compositions of chondrule olivine from H samples. Bulk chondrite and bulk chondrule, Type I and Type II, values are shown for reference. Dashed lines represent the detection limit of the chemical compound being plotted. Representative errors are shown as 1SD.

In more detail, figure 4.6 shows the chemical trends of chondrule olivine from H-group samples. QUE93030 (H3.6) and ALHA77299 (H3.7) define the cluster for Cr_2O_3, MnO, and CaO abundances vs. FeO. WSG95300 (H3.3) is the exception and describe the general patterns of MnO, Cr_2O_3, and CaO vs. FeO mentioned in the previous paragraph. Additionally, wt% Cr_2O_3 in WSG95300 is higher compare to QUE93030 and ALHA77299, shows an increase up to ~2wt% FeO and then scatters to a broader range

(~0.05-0.5wt%). Even though Al_2O_3 compositions are mainly below detection limit it behaves similarly to CaO between 0-5wt% FeO.

Figure 4.7 shows the chemical trends of chondrule olivine in the L iron group samples. GRO06054 (L3.05), DOM10556 (L3.1), and MIL05050 (L3.1) compositional patterns are very similar among them, matching the general tendencies noted before but no clustering is present. In detail, the MnO vs. FeO correlation seems to be steeper between 0-3wt% FeO and less sharp after (Figure 4.7a). Cr_2O_3 vs. FeO positive correlation also changes after ~2wt% FeO, with Cr_2O_3 abundances fluctuating among ~0.05 and ~0.7wt% (Figure 4.7b). CaO and Al_2O_3 behave similarly with respect to FeO displaying a negative from 0 to ~2wt% FeO. Then, CaO seems to correlate positively and Al_2O_3 falls below the detection limit (Figure 4.7d and 4.7e).

LAR06279 (LL3.8), LAR06301 (LL3.8), and LAR12034 (LL3.8) follow similar compositional patterns (Figure 4.8). The correlation between MnO and FeO is evident but the distinction before and after ~2wt% FeO, as shown by L samples, is not clear. A cluster is identified at ~0.45wt% MnO and ~28wt% FeO (Figure 4.8a). Similar to L samples, Cr_2O_3 tendency against FeO can be separated before and after ~2wt% FeO. A compositional cluster is observable for Cr_2O_3 around ~0.05wt% and ~28wt% FeO (Figure 4.8b). The CaO vs. FeO negative correlation exists when FeO values are between the range 0-5wt%. After that, no clear pattern remains, however a group of olivine plots around 0.05wt% CaO and 28wt% FeO (Figure 4.8d and 4.8e).

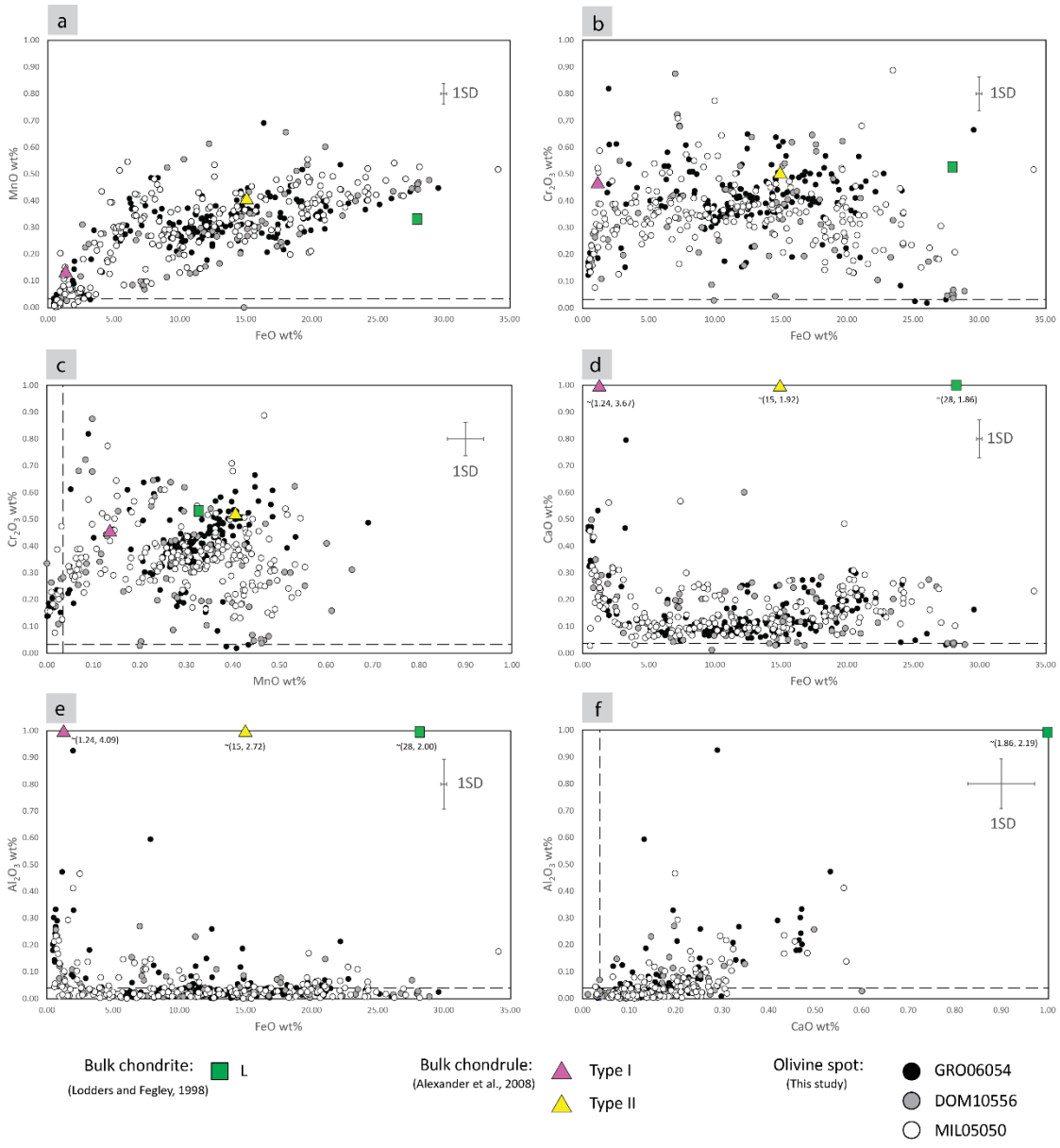

Figure 4.7. Major and minor element compositions of chondrule olivine from L samples. Bulk chondrite and bulk chondrule, Type I and Type II, values are shown for reference. Dashed lines represent the detection limit of the chemical compound being plotted. Representative errors are shown as 1SD.

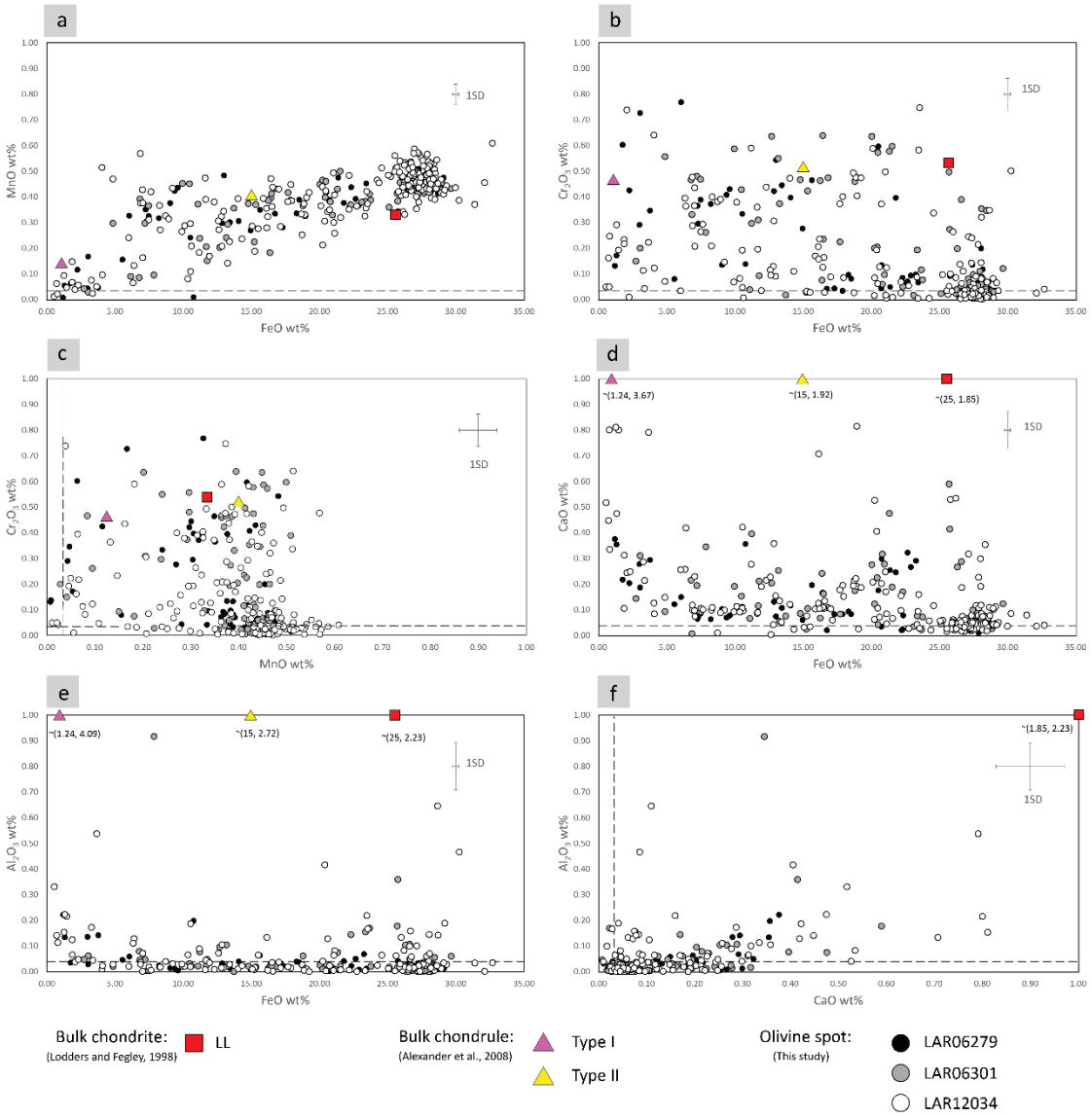

Figure 4.8. Major and minor element compositions of chondrule olivine from LL samples. Bulk chondrite and bulk chondrule, Type I and Type II, values are shown for reference. Dashed lines represent the detection limit of the chemical compound being plotted. Representative errors are shown as 1SD.

Figure 4.9 shows histograms of Fa mol% contents of olivines in all the samples including the whole range of FeO composition. Among H group samples, WSG95300 appears to be the most heterogeneous with Fa content ranging from ~Fa0 to Fa34 mol%, showing two modes around ~Fa0 and Fa10 mol%. QUE93030 distribution is narrower including values between ~Fa1 and Fa23 mol% and having a clear peak between ~Fa19 and Fa20 mol% (Figure 4.9a and 4.9b). Chondrule olivine within ALHA77299 encompasses a distribution from ~Fa0 up to Fa32 mol% holding a clear population enclosed by ~Fa17 and Fa20 mol% (Figure 4.9c). The mean Fa mol% composition for WSG95300, QUE93030, and ALHA77299 are Fa13, Fa16, and Fa17, respectively. In general, L chondrite chondrules exhibit heterogeneous olivine Fa content ranging from ~Fa0 to Fa34. A couple of peaks are noted within GRO06054 around Fa0 and Fa12. DOM10556 shows several populations close to Fa0, Fa6, Fa10, Fa15, and Fa30. MIL05050 have different modes around Fa0, Fa5, Fa10, Fa15, and Fa20, and a single olivine with ~Fa40 (Figure 4.9d, 4.9e, and 4.9f). The mean Fa abundances for GRO06054, DOM10556, and MIL05050 are Fa13, Fa14, and Fa12, respectively. Samples from the LL chemical group share similar histogram distributions between ~Fa0 and Fa35 showing a distinct population from ~Fa29 to Fa32 mol%. The highest FeO content of olivine is found in LAR12034 reaching up to ~Fa42 mol% (Figure 4.9g, 4.9h, and 4.9i). LAR06279, LAR06301, and LAR12034 mean Fa values are Fa22, Fa25, and Fa24, respectively.

Type I olivines (Fa < 10mol%) are more abundant in WSG95300 compared to QUE93030 and ALHA77299 Fa distribution. Comparable to WSG95300, Type I chondrule olivine from L chondrites (GRO06054, DOM10556, and MIL05050) are an important proportion of the analyzed olivines as shown in figure 18d, 18e, and 18f. In contrast, Type I olivine from LL samples do not represent significant populations within them (Figure 4.9g, 4.9h, and 4.9i).

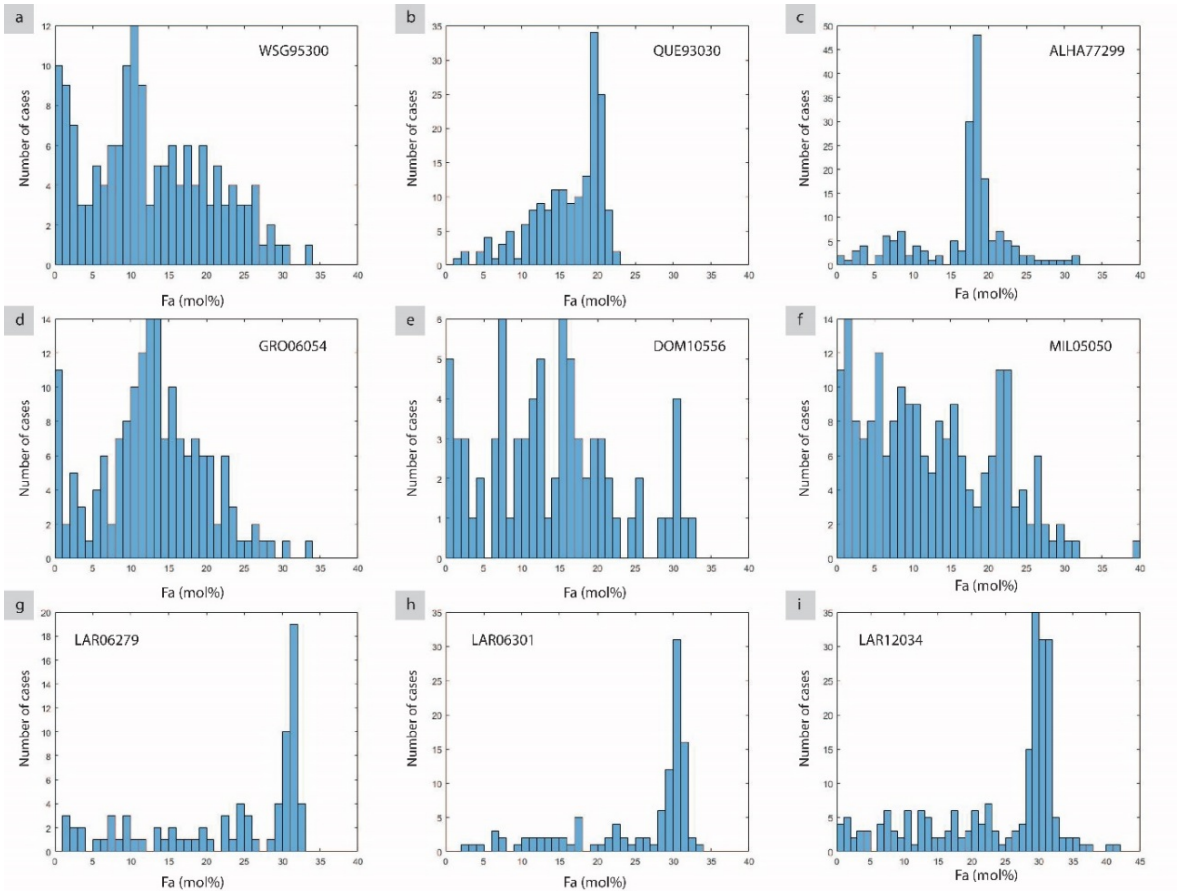

Figure 4.9. Histograms of chondrule olivine FeO content (Fa mol%).

Type II olivines (Fa > 10mol%) in all chondrites studied show a large compositional range and different distributions. However, the mean Fa composition of Type IIA or PO (>80% olivine chondrule modal abundance) chondrules tends to be similar in the samples. Hence WSG95300, QUE93030, and ALHA77299 have a Fa mean content of Fa18, Fa18, and Fa19, respectively. GRO06054, DOM10556, and MIL05050 show a Fa mean of Fa17, Fa20, and Fa18, respectively, and the LL samples have a mean Fa composition close to Fa27.

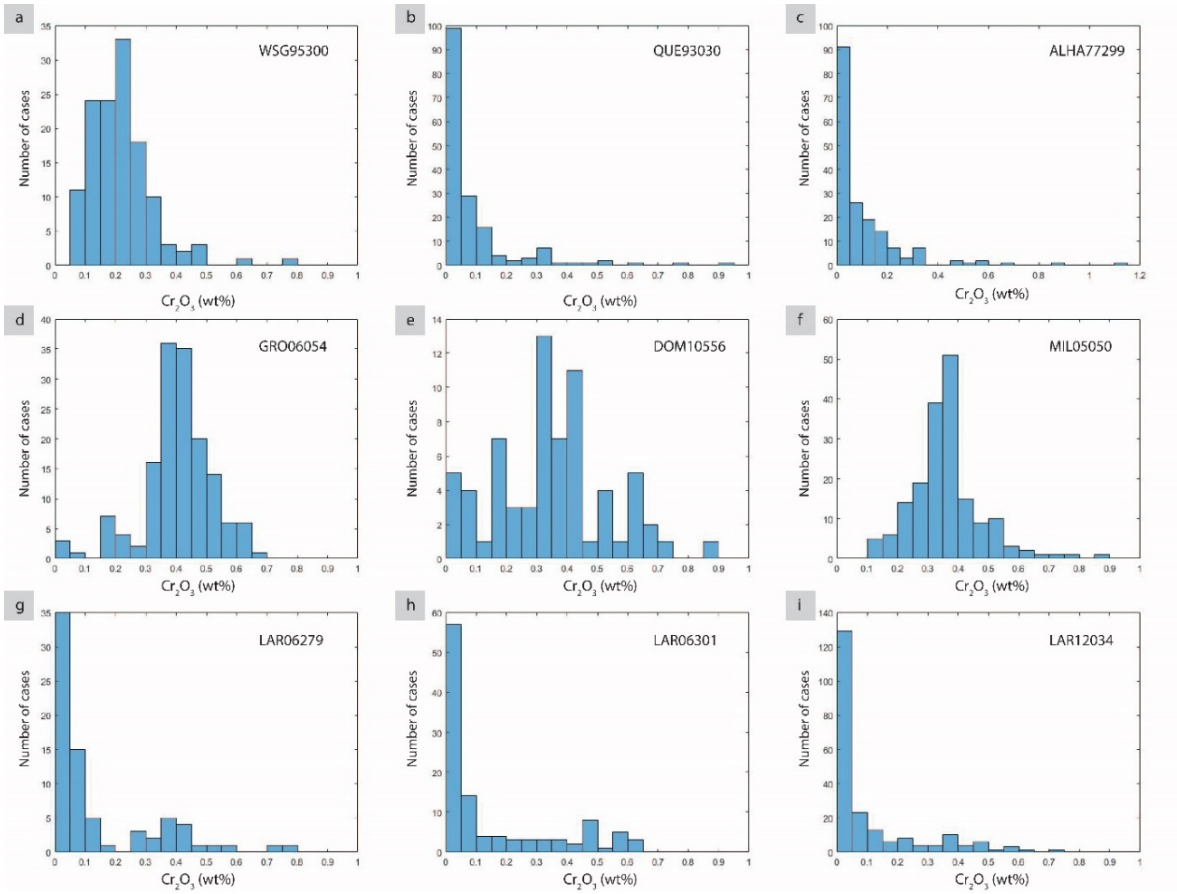

Figure 4.10. Histograms of chondrule olivine Cr_2O_3 composition. Similar distributions with a strong mode around 0.5 wt% are observed for QUE93030, ALHA77299, LAR06279, LAR06301, and LAR12034.

A very sensitive indicator of thermal metamorphism in UOCs is the Cr2O3 abundance of olivine with FeO compositions above 2 wt% (Grossman & Brearley, 2005). Figure 4.10 shows the distribution of Cr2O3 in olivine with >2 wt% FeO for all samples studied here. L chondrites, GRO06054, DOM10556, and MIL05050, have similar and broad distribution mostly between 0.2 and 0.7 wt% Cr2O3 (Figure 4.10d, 4.10e, and 4.10f). WSG95300 histogram is comparable to the former but with the mode shifted towards lower values of Cr2O3, from ~0.1 to 0.5 wt% (figure 17a). The rest of the samples exhibit a strong mode between 0 and 0.2 wt% with a tail pointing to higher values (Figure 4.10 b, 4.10c, 4.10g, 4.10h, and 4.10i).

4.3. Oxygen Isotopes

4.3.1. Data analysis

A total of 421 oxygen isotope analyses from the reference material, San Carlos olivine, were carried out over 11 analytical sessions. At the same time, a total of 764 individual oxygen isotope analyses from olivine were obtained from 549 chondrules. 99 olivines from 67 chondrules were measured in WSG95300, 108 grains from 77 chondrules were analysed in QUE93030, 82 olivine grains from 63 chondrules in ALHA77299, 104 olivines from 53 chondrules in GRO06054, 48 spots from 2 chondrules in DOM10556, 114 olivines from 83 chondrules in MIL05050, 50 olivines from 41 chondrules in LAR06279, 74 olivines from 60 chondrules in LAR06301, and 96 grains from 79 chondrules in LAR12034. These results are summarized per session in table 4.3 and figure 4.11. Full analytical tables can be found in table 2 of the Electronic Annex 2.

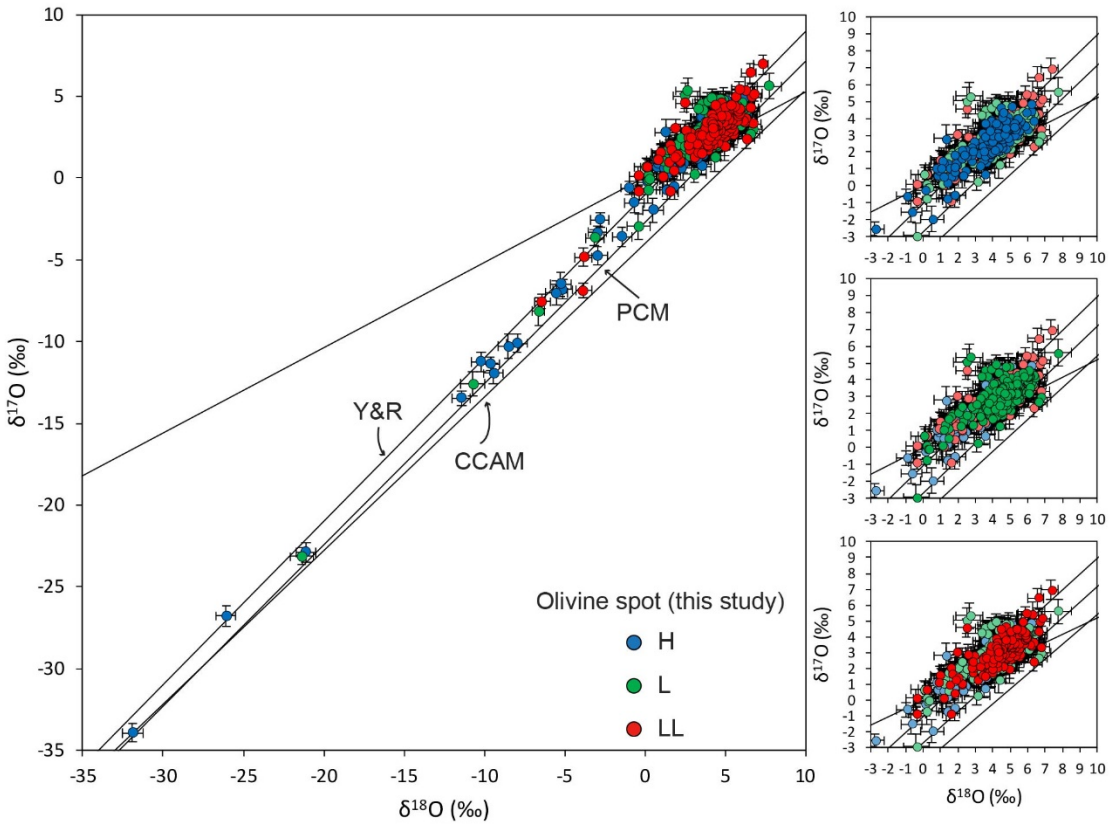

Figure 4.11. Oxygen isotope ratios of chondrule olivine grouped per OC group (H, L, and LL). The insert shows the detail for chondrule olivine from H, L, and LL chondrites. Most of the measurements plot above the TF line. CCAM, PCM, and Y&R lines are shown for reference.

Table 4.3. Summary of SHRIMP-SI oxygen isotope ratios and uncertainties. In red and green are MSWD values that fall out and within the acceptable range to form a single population.

Session/Sample			Weighted mean	± Internal $error_{sample}$ (ts)	± External $error_{sample}$ (ts)	Standard deviation (ts)	MSWD	no.	no. outliers	Internal $error_{spot}$ average (ts)	External $error_{spot}$ average (ts)	Skewness
Session 1												
San Carlos	$\delta^{17}O$	(‰)	2.71	0.11	-	0.69	0.77	52	1	0.37	0.79	-
olivine	$\delta^{18}O$	(‰)	5.21	0.11	-	0.74	0.97	52	1	0.11	0.75	-
	$\Delta^{17}O$	(‰)	0.00	0.09	-	0.59	0.81	52	1	0.28	0.66	-
GRO06054	$\delta^{17}O$	(‰)	2.87	0.08	0.13	3.78	23.81	104	0	0.37	0.79	-5.58
L3.05	$\delta^{18}O$	(‰)	4.43	0.07	0.13	3.95	28.22	104	0	0.11	0.75	-4.70
	$\Delta^{17}O$	(‰)	0.58	0.06	0.10	2.08	9.91	104	0	0.28	0.66	-3.39
Session 2												
San Carlos	$\delta^{17}O$	(‰)	2.70	0.08	-	0.42	0.85	30	1	0.15	0.45	-
olivine	$\delta^{18}O$	(‰)	5.21	0.11	-	0.55	0.90	30	1	0.14	0.57	-
	$\Delta^{17}O$	(‰)	-0.01	0.06	-	0.23	0.56	30	1	0.20	0.30	-
DOM10556	$\delta^{17}O$	(‰)	2.57	0.07	0.11	2.17	20.84	48	0	0.16	0.45	-4.09
L3.1	$\delta^{18}O$	(‰)	3.74	0.08	0.13	2.91	25.61	48	0	0.14	0.57	-2.08
	$\Delta^{17}O$	(‰)	0.63	0.04	0.06	1.36	17.2	48	0	0.20	0.31	-0.72
Session 3												
San Carlos	$\delta^{17}O$	(‰)	2.71	0.17	-	0.75	0.72	26	2	0.40	0.85	-
olivine	$\delta^{18}O$	(‰)	5.21	0.08	-	0.37	0.87	26	2	0.11	0.38	-
	$\Delta^{17}O$	(‰)	0.00	0.15	-	0.69	0.79	26	2	0.27	0.75	-
MIL05050	$\delta^{17}O$	(‰)	2.83	0.12	0.19	3.46	16.26	54	0	0.40	0.85	-4.98
L3.1	$\delta^{18}O$	(‰)	4.20	0.05	0.09	3.74	96.45	54	0	0.11	0.38	-4.03
	$\Delta^{17}O$	(‰)	0.66	0.10	0.17	1.96	7.03	54	0	0.29	0.75	-3.06
Session 4												
San Carlos	$\delta^{17}O$	(‰)	2.70	0.09	-	0.51	0.89	33	1	0.15	0.53	-
olivine	$\delta^{18}O$	(‰)	5.21	0.13	-	0.73	0.93	33	1	0.14	0.74	-
	$\Delta^{17}O$	(‰)	-0.01	0.05	-	0.23	0.55	33	1	0.20	0.31	-
MIL05050	$\delta^{17}O$	(‰)	2.56	0.07	0.11	7.06	183.33	60	0	0.15	0.53	-6.80
L3.1	$\delta^{18}O$	(‰)	3.96	0.10	0.16	7.09	91.54	60	0	0.14	0.74	-6.44
	$\Delta^{17}O$	(‰)	0.46	0.04	0.06	3.59	168.88	60	0	0.20	0.31	-5.89
Session 5												
San Carlos	$\delta^{17}O$	(‰)	2.71	0.06	-	0.39	0.86	49	2	0.15	0.42	-
olivine	$\delta^{18}O$	(‰)	5.21	0.08	-	0.55	0.94	49	2	0.14	0.56	-
	$\Delta^{17}O$	(‰)	0.01	0.05	-	0.30	0.62	49	2	0.21	0.37	-
WSG95300	$\delta^{17}O$	(‰)	2.39	0.04	0.07	4.81	129.23	99	0	0.15	0.42	-4.98
H3.3	$\delta^{18}O$	(‰)	3.57	0.06	0.10	4.98	78.89	99	0	0.14	0.56	-4.14
	$\Delta^{17}O$	(‰)	0.54	0.04	0.06	2.38	39.02	99	0	0.21	0.37	-5.07
Session 6												
San Carlos	$\delta^{17}O$	(‰)	2.71	0.08	-	0.44	0.58	61	1	0.38	0.58	-
olivine	$\delta^{18}O$	(‰)	5.21	0.08	-	0.60	0.97	61	1	0.12	0.61	-
	$\Delta^{17}O$	(‰)	0.00	0.05	-	0.31	0.58	61	1	0.26	0.41	-
QUE93030	$\delta^{17}O$	(‰)	1.44	0.06	0.08	11.43	391.04	108	0	0.38	0.58	-4.34
H3.6	$\delta^{18}O$	(‰)	2.72	0.06	0.10	11.30	346.08	108	0	0.12	0.61	-4.33
	$\Delta^{17}O$	(‰)	-0.05	0.04	0.06	5.62	215.64	108	0	0.26	0.41	-4.21
Session 7												
San Carlos	$\delta^{17}O$	(‰)	2.74	0.12	-	0.72	0.86	40	0	0.21	0.75	-
olivine	$\delta^{18}O$	(‰)	5.21	0.10	-	0.65	0.94	40	0	0.13	0.66	-
	$\Delta^{17}O$	(‰)	0.05	0.10	-	0.57	0.69	40	0	0.32	0.66	-
ALHA77299	$\delta^{17}O$	(‰)	2.29	0.08	0.14	4.58	37.36	82	0	0.24	0.76	-3.69
H3.7	$\delta^{18}O$	(‰)	3.56	0.07	0.12	4.57	48.49	82	0	0.13	0.66	-3.37
	$\Delta^{17}O$	(‰)	0.45	0.07	0.11	2.39	13.52	82	0	0.30	0.65	-3.06
Session 8												
San Carlos	$\delta^{17}O$	(‰)	2.70	0.09	-	0.52	0.84	36	1	0.20	0.56	-
olivine	$\delta^{18}O$	(‰)	5.21	0.09	-	0.52	0.91	36	1	0.13	0.54	-
	$\Delta^{17}O$	(‰)	-0.01	0.08	-	0.41	0.71	36	1	0.27	0.49	-
LAR06279	$\delta^{17}O$	(‰)	2.86	0.07	0.11	2.51	19.97	59	0	0.20	0.56	-4.19
LL3.8	$\delta^{18}O$	(‰)	4.20	0.07	0.11	3.25	36.40	59	0	0.12	0.54	-2.63
	$\Delta^{17}O$	(‰)	0.67	0.06	0.09	1.51	9.82	59	0	0.27	0.50	-1.05
Session 9												
San Carlos	$\delta^{17}O$	(‰)	2.71	0.14	-	0.48	0.57	20	1	0.37	0.61	-
olivine	$\delta^{18}O$	(‰)	5.21	0.09	-	0.35	0.83	20	1	0.12	0.37	-
	$\Delta^{17}O$	(‰)	0.00	0.12	-	0.46	0.66	20	1	0.29	0.54	-
LAR06301	$\delta^{17}O$	(‰)	3.14	0.11	0.16	2.92	22.56	31	0	0.36	0.61	0.54
LL3.8	$\delta^{18}O$	(‰)	4.42	0.07	0.11	2.75	52.78	31	0	0.11	0.37	-0.58
	$\Delta^{17}O$	(‰)	0.82	0.10	0.15	1.80	10.08	31	0	0.27	0.53	1.04
Session 10												
San Carlos	$\delta^{17}O$	(‰)	2.70	0.16	-	0.74	0.73	28	1	0.40	0.85	-
olivine	$\delta^{18}O$	(‰)	5.21	0.11	-	0.57	0.91	28	1	0.11	0.58	-
	$\Delta^{17}O$	(‰)	-0.01	0.17	-	0.80	0.84	28	1	0.31	0.86	-
LAR06301	$\delta^{17}O$	(‰)	3.29	0.13	0.19	1.88	4.99	43	0	0.38	0.84	-0.84
LL3.8	$\delta^{18}O$	(‰)	4.80	0.09	0.14	1.77	9.19	43	0	0.10	0.58	-0.43
	$\Delta^{17}O$	(‰)	0.80	0.13	0.20	1.40	2.61	43	0	0.28	0.85	-0.61
Session 11												
San Carlos	$\delta^{17}O$	(‰)	2.70	0.07	-	0.41	0.88	46	2	0.14	0.44	-
olivine	$\delta^{18}O$	(‰)	5.21	0.08	-	0.50	0.91	46	2	0.14	0.52	-
	$\Delta^{17}O$	(‰)	-0.01	0.05	-	0.26	0.60	46	2	0.21	0.33	-
LAR12034	$\delta^{17}O$	(‰)	2.66	0.05	0.08	3.52	62.93	96	0	0.16	0.45	-3.79
LL3.8	$\delta^{18}O$	(‰)	4.11	0.05	0.09	3.66	51.02	96	0	0.14	0.52	-3.14
	$\Delta^{17}O$	(‰)	0.53	0.03	0.05	1.86	29.22	96	0	0.22	0.34	-3.42

For the analyses of olivine reference material, only 13 spots lying more than 2.5σ from the mean were rejected from a sample of 421, which corresponds to approximately 3% of the entire population. No more than 2 spots where rejected per session. The reference material analyses are pooled and population statistics are evaluated including the external precision per spot to obtain the internal error based on the weighted mean of the pooled sample (see Chapter 3).

The internal precision of the reference material pooling ranges from 0.06 to 0.17‰ ($\sigma_{95\%}$) for $\delta^{17}O$, 0.08 to 0.13‰ ($\sigma_{95\%}$) for $\delta^{18}O$ and 0.05 to 0.17‰ ($\sigma_{95\%}$) for $\Delta^{17}O$, with a mean of 0.11‰, 0.10‰, and 0.09‰ for $\delta^{17}O$, $\delta^{18}O$, and $\Delta^{17}O$, respectively. Except for session 6, where the chondrite QUE93030 (H3.6) was measured, the weighted mean of $\delta^{17}O$, $\delta^{18}O$, and $\Delta^{17}O$ for the pooled samples of reference material and their MSWD value varies in the range of values that do not violate the $1 \pm 2\sqrt{2/f}$ rule at the 95% confidence interval (Table 4.3; figure 4.12). Even though session 6 has MSWD values outside the acceptable range in $\delta^{17}O$ and $\Delta^{17}O$ they are still very close to it (Figure 4.12). A value of 0.58 for both $\delta^{17}O$ and $\Delta^{17}O$ would indicate that the errors have been overestimated. In this regard, session 6 has particularly high internal error per spot averages for $\delta^{17}O$ (± 0.38‰, $\sigma_{95\%}$) and $\Delta^{17}O$ (± 0.26‰, $\sigma_{95\%}$) probably reflecting the true analytical uncertainty, which has been observed to be underestimated when performing SIMS analyses (Ávila et al., In Review). Therefore, when propagating errors using the reproducibility of 0.44‰ and 0.31‰ for $\delta^{17}O$ and $\Delta^{17}O$, respectively, to large external errors are obtained for quite a small variability. One option would be to add an external component for the external error of $\delta^{17}O$ and $\Delta^{17}O$ as $(0.5xSD_{RM})^2$ instead of SD_{RM}^2 (Chapter 3). However, since the MSWD values are marginally away from the acceptable range and to maintain the same methodology as in other SHRIMP-SI sessions it is chosen not to change the previously calculated external error of session 6.

The internal precision of the weighted means of pooled San Carlos olivine for $\delta^{17}O$, $\delta^{18}O$, and $\Delta^{17}O$ in every session are in agreement with the laser fluorination values of 2.71 ± 0.07‰ (2σ), 5.21 ± 0.07‰ (2σ) and -0.05 ± 0.07‰ (2σ), respectively.

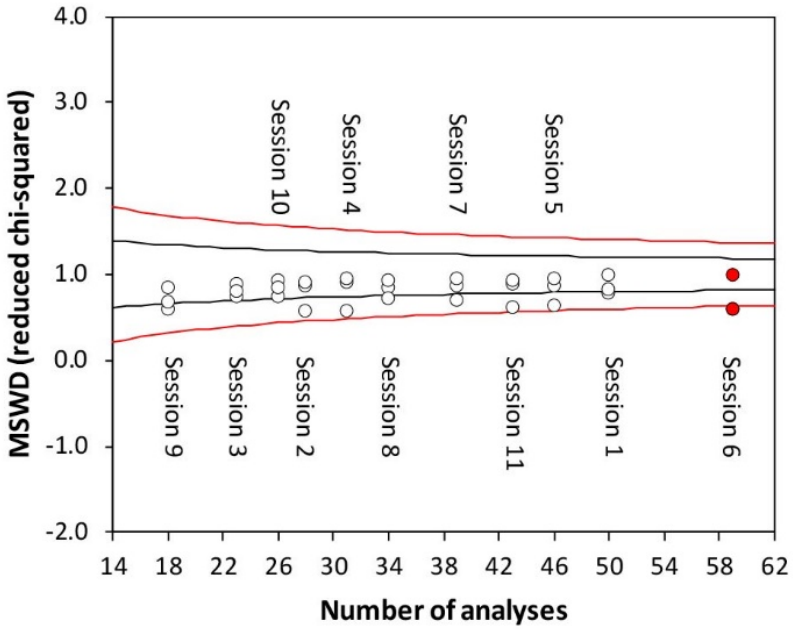

Figure 4.12. MSWD range of acceptable values per session of the reference material. Red circles highlight session 6 which does not meet this requirement for $\delta^{17}O$ and $\Delta^{17}O$.

For chondrule olivine (unknowns), table 4.3 shows that the external error average per olivine spot ranges from 0.42 to 0.85‰ ($\sigma_{95\%}$) for $\delta^{17}O$, 0.37 to 0.75‰ ($\sigma_{95\%}$) for $\delta^{18}O$, and 0.31 to 0.85‰ ($\sigma_{95\%}$) for $\Delta^{17}O$, having an average of 0.62‰, 0.57‰, and 0.52‰ for $\delta^{17}O$, $\delta^{18}O$, and $\Delta^{17}O$, respectively. It is also noticeable from table 4.3 that the MSWD values for the oxygen isotope ratios, considering the whole sample per chondrite, is out of the 95% confidence interval range of acceptable values. Therefore, a single chondrule population representing the same oxygen isotope gas reservoir of the protoplanetary disk cannot be statistically assumed a priori for the samples studied in this work when all data is taken into account. This is consistent with the skewness of the unknowns' oxygen isotope sample distributions which are generally negative, meaning that the tail towards lighter oxygen isotope compositions (^{16}O-richer) is a feature to take into account in populations of chondrules from OCs.

The weighted mean of $\delta^{17}O$, $\delta^{18}O$, and $\Delta^{17}O$ for the unknowns varies from session to session (table 4.3). For $\delta^{17}O$ it ranges from 1.44‰ in QUE93030 (session 6) to 3.29‰ in LAR06031 (session 10). $\delta^{18}O$ covers a range from 2.72‰ in QUE93030 (session 6) to 4.80‰ in LAR06031 (session10). For $\Delta^{17}O$ ratios, it ranges from -0.05‰ in QUE93030 to 0.82‰ in LAR06301 (session 9) although most of them are between 0.45‰ and

0.80‰. The external precision of the unknowns weighted means using all olivine data ranges from smaller than 0.10‰ ($\sigma_{95\%}$) up to 0.20‰ ($\sigma_{95\%}$) in $\delta^{17}O$, $\delta^{18}O$, and $\Delta^{17}O$ (table 4.3).

4.3.2. Oxygen isotope compositions

Overall, the oxygen isotope compositions of chondrule olivine from UOCs show the mass-independent cosmochemical signature of the solar system material, as can be noted in the triple-oxygen isotope diagram (Figure 4.11), with data points plotting along the Y&R and PCM lines. However, the majority of the measurements fall very close the TF line. This is quite clear when the chondrule olivine histograms and PDFs of $\delta^{17}O$ and $\delta^{18}O$ are visualized on the top and right margins, respectively, from figure 4.13.

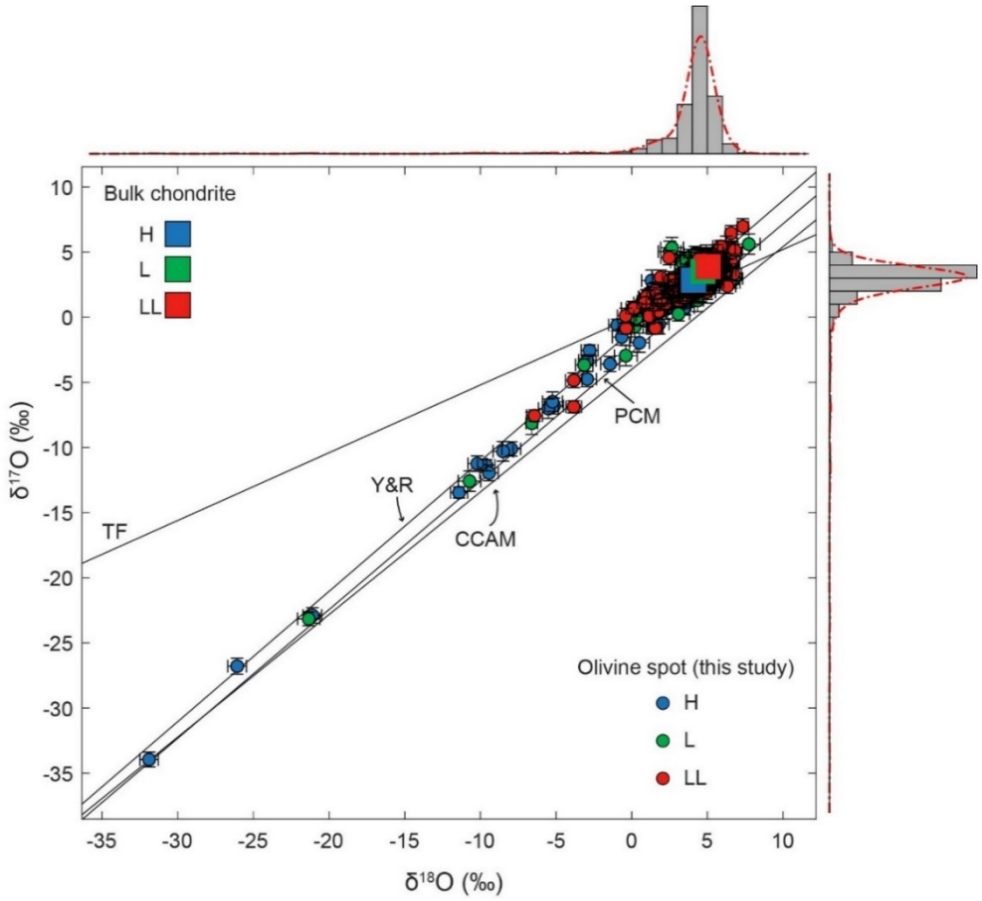

Figure 4.13. Oxygen isotope ratios of chondrule olivine grouped per OC group (H, L, and LL). PDF of $\delta^{18}O$ and $\delta^{17}O$ are shown above and to the right of the triple-oxygen plot, respectively are shown. TF, CCAM, PCM, and Y&R lines are shown for reference. Bulk equilibrated OCs compositions are from Clayton et al., 1991.

In general, despite the chondrite group (H, L or LL), oxygen isotope ratios ranges of chondrule olivine within this trend are broadly between ~-1‰ and ~7‰ for $\delta^{17}O$ and from ~-1‰ to ~8‰ for $\delta^{18}O$ (Figure 4.11). Exceptions to this tendency are olivine grains with relatively ^{16}O-richer compositions which plot below the TF line among Y&R, PCM, and CCAM lines ($\Delta^{17}O < -2‰$). These signatures are commonly observed in carbonaceous chondrite chondrules (Kita et al., 2017 and references therein). In detail, chondrule olivine with ^{16}O-richer ratios compare to the main cloud of data were measured from chondrules CH027 and CH084 in WSG95300, CH130, CH139, CH162, CH169, CH170, CH181, and CH207 in QUE93030, from CH285, CH305, CH312, and CH315 in ALHA77299, from olivine within chondrules CH354 and CH368 in GRO06054, from chondrule CHextra9 in DOM10556, chondrules CH487, CH528, and CH547 in MIL05050, chondrule CH596 in LAR06279, and from CH862 and CH869 in LAR12034. The most extreme oxygen isotope ratios are $\delta^{17}O$~ -34‰ and $\delta^{18}O$~ -32‰ ($\Delta^{17}O$~ -17‰) obtained from chondrule CH207 which plot on the PCM line (Figure 4.13). On the other hand, a couple of points from GRO06054, LAR06279, and LAR06301 that plot towards higher $\delta^{17}O$ and $\delta^{18}O$ ($\Delta^{17}O > 3‰$), values that have been regarded as a characteristic of Rumuruti chondrite chondrules (e.g. Greenwood et al., 2000), are also away from the general cluster of data (Figure 4.13). The nature of these distinct olivine grains will be discussed in chapter 5.

The triple-oxygen data is shown in figure 4.14 which displays chondrule olivine histograms and PDFs of $\Delta^{17}O$ values. In this regard, approximately 96% of chondrule olivines measured here show quite a symmetric $\Delta^{17}O$ ratio distribution between -2‰ and 3‰ with a clear and similar peak among samples close to ~0-2‰. An emerging single chondrule population can be graphically envisioned from figure 4.14 where the densest part of each chondrite chondrule olivine sample approaches a bell-shaped distribution. However, as mentioned above, variability towards lower and higher $\Delta^{17}O$ values is small but distinguishable.

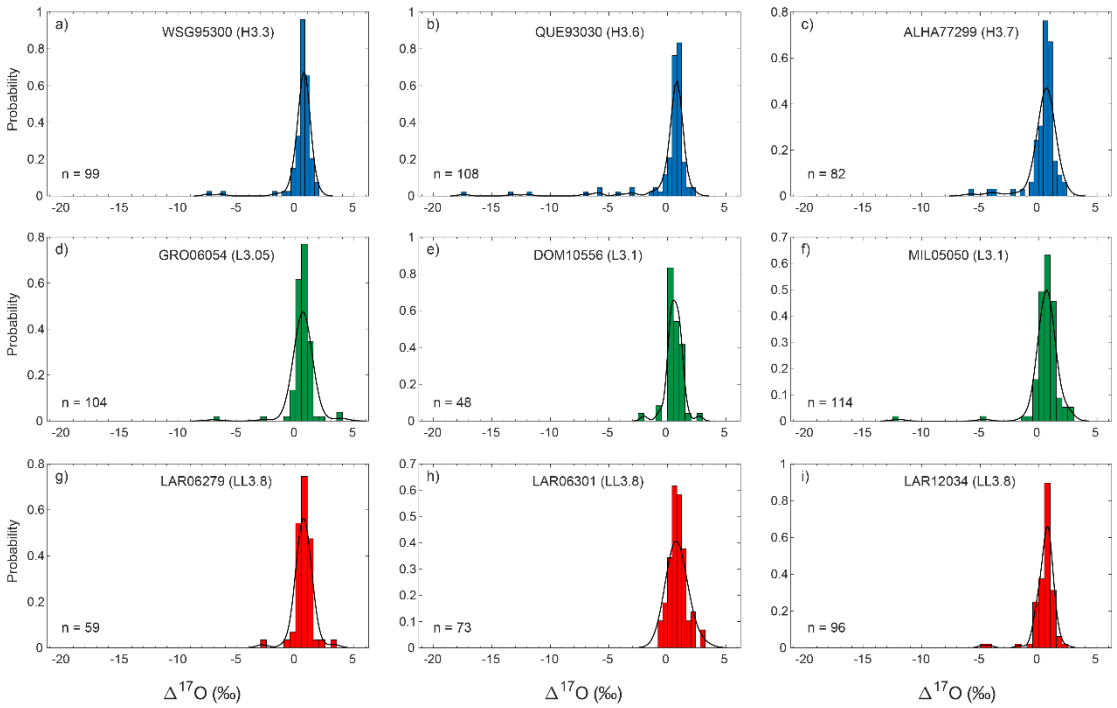

Figure 4.14. $\Delta^{17}O$ chondrule olivine histograms of H, L, and LL samples. Most of the measurements define a clear major population between $\Delta^{17}O$ ratios -2‰ and 2‰. PDFs are shown for each sample distribution.

In the same line, figure 4.15 shows the empirical cumulative distribution function of $\Delta^{17}O$ ratios for each sample. Similar to histograms, it is apparent from this figure that the majority of the samples are distributed from 0‰ to 2‰. On this matter, and considering the average external spot errors per SHRIMP-SI session (±0.3–0.9‰; table 4.3) it appears that the chondrule olivine $\Delta^{17}O$ distribution of each chondrite was obtained from the same continuous distribution.

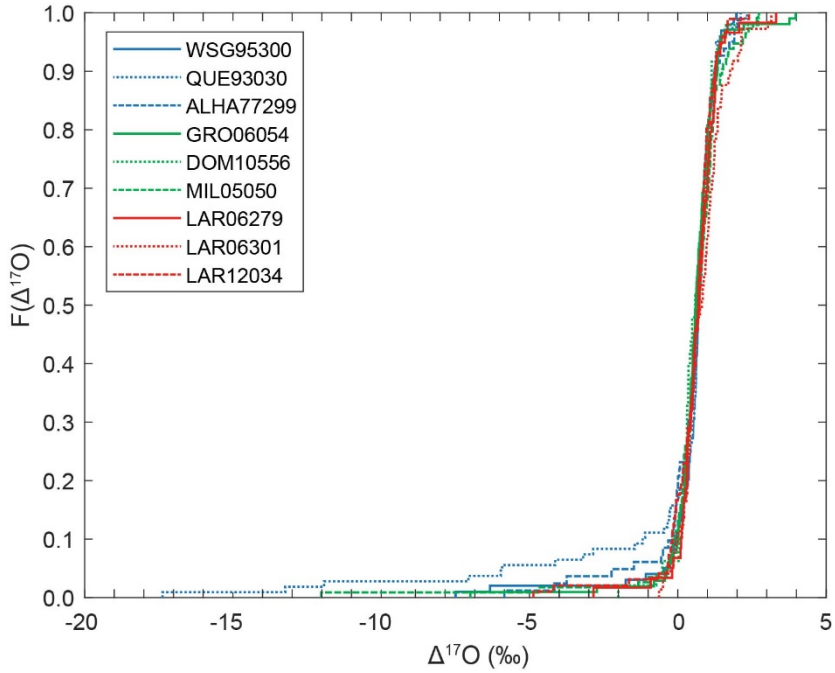

Figure 4.15. $\Delta^{17}O$ ratios empirical cumulative distribution function of chondrule olivine per chondrite investigated in this study.

Figure 4.16 depicts the $\Delta^{17}O$ composition of chondrule olivine from the H, L, and LL chondrites investigated as simple whisker boxplot diagrams with statistical outliers defined at the 95% confidence interval (Chapter 3). The medians of each sample are graphically represented by the horizontal red line inside the boxplot and a notch is included to visualize their significance at the 95% level. It is evident that medians between samples are statistically indistinguishable and varying around a $\Delta^{17}O$ value close to 0.7‰. Following this line, the interquartile range from each chondrite sample is also very similar among them varying from 0.53 in WSG95300 to 0.85 in MIL05050.

In more detail, the $\Delta^{17}O$ ratios in the boxplot diagrams show that chondrule olivine subsample data ($\sigma_{95\%}$) for each chondrite, graphically represented by the observations within the whiskers of each boxplot, have a consistently similar and quite symmetric sample distribution which varies from 0.06‰ to 1.30‰ in WSG95300, 0.02‰ to 1.36‰ in QUE93030, -0.19‰ to 1.35‰ in ALHA77299, -0.04‰ to 1.42‰ in GRO06054, 0.03‰ to 1.46‰ in DOM10556, -0.37‰ to 1.70‰ in MIL05050, -0.19‰ to 1.42‰ in LAR06279, -0.26‰ to 1.84‰ in LAR06301, -0.14‰ to 1.31‰ in LAR12034. Table 4.4 shows a summary of the main statistics per chondrite sample (olivine spot). In this table,

as mentioned in Chapter 3, the weighted mean, uncertainties, and standard deviation are calculated at the 95% significance interval ($\sigma_{95\%}$).

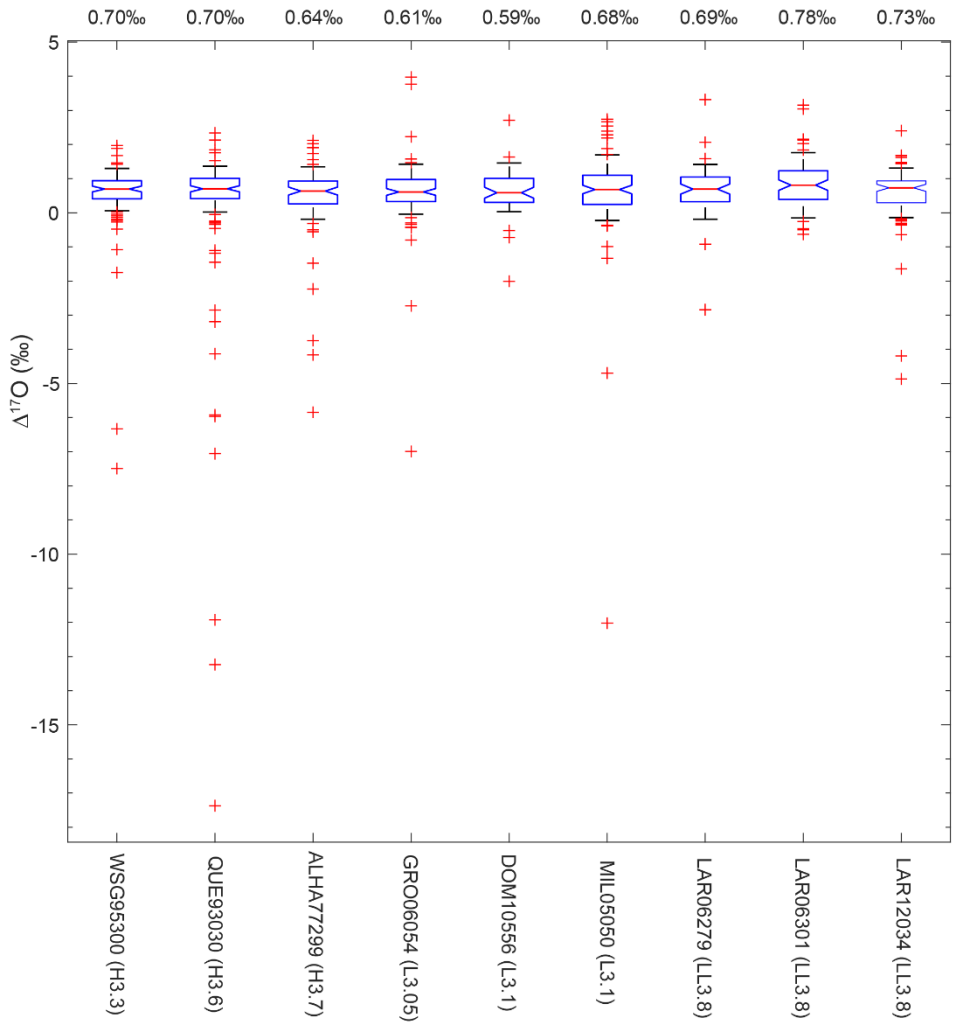

Figure 4.16. Whisker-boxplot diagrams of chondrule olivine $\Delta^{17}O$ ratios per chondrite. Whiskers are defined at the 95% confidence interval. The medians correspond to the red line within the boxplot and their values are displayed above the graph for each meteorite. Medians are statistically undistinguishable at the 95% confidence interval.

Table 4.4. Main statistics on chondrule olivine spot $\Delta^{17}O$ ratios data of the investigated samples. MSWD values in red are outside the range of acceptable values for one population ($\sigma_{95\%}$).

Chondrite Sample		Weighted mean	± External $error_{sample}$ (ts)	Standard deviation (ts)	no.	Median	Min	Max	Iqr	Skewness	MSWD
WSG95300 (H3.3)	$\Delta^{17}O$ (‰)	0.54	0.06	2.38	99	0.70	-7.49	1.97	0.53	-5.07	38.02
QUE93030 (H3.6)	$\Delta^{17}O$ (‰)	-0.05	0.06	5.62	108	0.70	-17.37	2.34	0.59	-4.21	215.64
ALHA77299 (H3.7)	$\Delta^{17}O$ (‰)	0.45	0.11	2.39	82	0.64	-5.85	2.12	0.67	-3.06	13.52
GRO06054 (L3.05)	$\Delta^{17}O$ (‰)	0.58	0.10	2.08	104	0.61	-6.99	3.97	0.64	-3.39	9.91
DOM10556 (L3.1)	$\Delta^{17}O$ (‰)	0.63	0.06	1.36	48	0.59	-2.01	2.71	0.70	-0.72	17.20
MIL05050 (L3.1)	$\Delta^{17}O$ (‰)	0.49	0.10	2.89	114	0.68	-12.02	2.74	0.85	-6.11	91.59
LAR06279 (LL3.8)	$\Delta^{17}O$ (‰)	0.67	0.09	1.51	59	0.69	-2.84	3.31	0.72	-1.05	9.82
LAR06301 (LL3.8)	$\Delta^{17}O$ (‰)	0.83	0.15	1.46	74	0.78	-1.43	3.16	0.84	0.37	5.37
LAR12034 (LL3.8)	$\Delta^{17}O$ (‰)	0.53	0.05	1.86	96	0.73	-4.87	2.40	0.64	-3.42	29.22

If the focus of the statistical analysis is now centered on the pooled chondrule olivine data defined here to range within the values of the box plot whiskers (Figure 4.16), some noticeable similarities and differences are observed.

For instance, the weighted mean of $\Delta^{17}O$ of these subsamples are different to whole chondrule olivine data (Tables 4.4 and 4.5). Precisely, 0.73 ±0.06‰ for WSG95300 (H3.3), 0.78 ±0.06‰ for QUE93030 (H3.6), 0.63 ±0.12‰ for ALHA77299 (H3.7), 0.65 ±0.11‰ for GRO06054 (L3.05), 0.65 ±0.07‰ for DOM10556 (L3.1), 0.65 ±0.10‰ for MIL05050 (L3.1), 0.67 ±0.07‰ for LAR06279 (LL3.8), 0.72 ±0.15‰ for LAR06301 (LL3.8), and 0.67 ±0.06‰ for LAR12034 (LL3.8). Therefore, the weighted means among the subsamples are statistically the same at the 95% confidence range. The weighted mean of all means per chondrule olivine is 0.70 ±0.03‰.

Similarly, the medians of each subsample are basically the same to the medians of the whole olivine spot results (Tables 4.4 and 4.5), always ranging close to $\Delta^{17}O$ ~0.7‰. This is an expected result considering the lower density (poorer statistics) of the oxygen isotope olivine data towards the tails of the samples. However, when comparing the medians and weighted means of each subsample it is evident that they are statistically the same, again suggesting that they were drawn from a single population.

Table 4.5. Main statistics on chondrule olivine spot $\Delta^{17}O$ ratios data of the investigated sub samples. MSWD values in red and green are outside and within the range of acceptable values for one population ($\sigma_{95\%}$), respectively.

Chondrite Sample		Weighted mean	± External $error_{sample}$ (ts)	Standard deviation (ts)	no.	no. outliers	Median	Min	Max	Iqr	Skewness	MSWD
WSG95300 (H3.3)	$\Delta^{17}O$ (‰)	0.73	0.06	0.58	99	17	0.72	0.06	1.30	0.36	-0.08	2.68
QUE93030 (H3.6)	$\Delta^{17}O$ (‰)	0.78	0.06	0.60	108	23	0.80	0.02	1.36	0.42	-0.25	2.23
ALHA77299 (H3.7)	$\Delta^{17}O$ (‰)	0.63	0.12	0.78	82	15	0.64	-0.19	1.35	0.51	-0.41	1.42
GRO06054 (L3.05)	$\Delta^{17}O$ (‰)	0.65	0.11	0.73	104	13	0.62	-0.04	1.42	0.54	0.17	1.27
DOM10556 (L3.1)	$\Delta^{17}O$ (‰)	0.65	0.07	0.76	48	5	0.59	0.03	1.46	0.67	0.18	6.32
MIL05050 (L3.1)	$\Delta^{17}O$ (‰)	0.65	0.10	0.91	114	14	0.67	-0.23	1.70	0.68	-0.04	5.61
LAR06279 (LL3.8)	$\Delta^{17}O$ (‰)	0.67	0.10	0.81	59	5	0.68	-0.19	1.42	0.68	-0.06	2.59
LAR06301 (LL3.8)	$\Delta^{17}O$ (‰)	0.72	0.15	0.93	74	10	0.70	-0.26	1.84	0.72	0.11	2.12
LAR12034 (LL3.8)	$\Delta^{17}O$ (‰)	0.67	0.06	0.72	96	18	0.74	-0.14	1.31	0.47	-0.46	4.68

Additionally, as briefly mentioned above, the skewness of each subsample is closer to zero implying that they hold more symmetric distributions when comparing to whole sample skewness, again suggesting that the probability distributions are close to being Gaussian.

In this line, as expected, when reducing the statistical analysis to each meteorite chondrule olivine subsample, MSWD values are closer to the accepted range that define that one sample was drawn from a single population at the 95% significance interval (Tables 4.4 and 4.5). Specifically, $\Delta^{17}O$ ratios per olivine spot of chondrite GRO06054 (L3.05) has an MSWD value within this range, meaning that they were obtained from a single chondrule olivine population represented by the weighted mean of the sample, $\Delta^{17}O$= 0.65 ±0.11‰ ($\sigma_{95\%}$).

The previous exploratory and statistical analysis were also investigated for $\Delta^{17}O$ chondrule olivine average. Once more, the medians among OCs samples are statistically the same at the 95% significance interval and their empirical cumulative distribution function are very similar and distributing primarily among 0‰ and 2‰ (Figure 4.17).

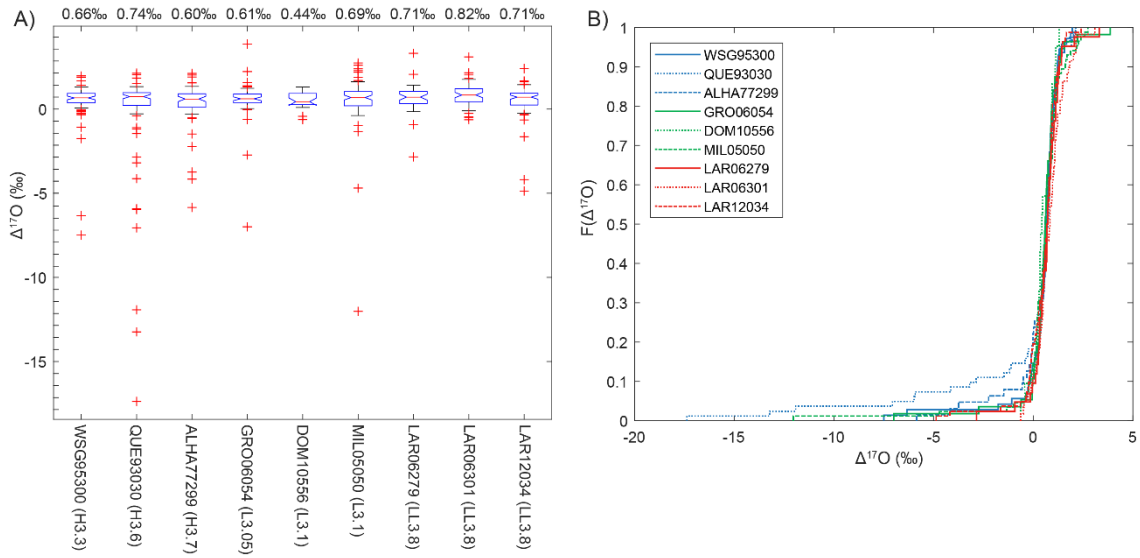

Figure 4.17. A) Whisker-boxplot diagrams of averaged chondrule olivine $\Delta^{17}O$ ratios per chondrite. Whiskers are defined at the 95% confidence interval. The medians correspond to the red line within the boxplot and their values are displayed above the graph for each meteorite. Medians are statistically undistinguishable at the 95% confidence interval. B) $\Delta^{17}O$ ratios empirical cumulative distribution function of averaged chondrule olivine per chondrite investigated in this study.

In the case of per chondrule averaged olivine data, the $\Delta^{17}O$ weighted mean and external error of pooled samples ($\sigma_{95\%}$) are 0.72 ±0.07‰ for WSG95300 (H3.3), 0.73 ±0.06‰ for QUE93030 (H3.6), 0.62 ±0.13‰ for ALHA77299 (H3.7), 0.59 ±0.13‰ for GRO06054 (L3.05), 0.63 ±0.08‰ for DOM10556 (L3.1), 0.59 ±0.10‰ for MIL05050 (L3.1), 0.70 ±0.11‰ for LAR06279 (LL3.8), 0.77 ±0.16‰ for LAR06301 (LL3.8), and 0.64 ±0.06‰ for LAR12034 (LL3.8). The weighted means per chondrule are again indistinguishable from each other. The weighted mean of all the means per chondrule is 0.67 ±0.03‰, statistically the same compared to the weighted mean of per spot chondrule olivine data (0.70 ±0.03‰).

Moreover, the weighted means and medians of the averaged olivine subsample are again essentially the same (Tables 4.6 and 4.7), and the skewness and MSWD values both improve towards values reflecting a more symmetric distribution and sampling of a single population, respectively. The previous is comparable to what occurs when analyzing individual spot measurements. Particularly, $\Delta^{17}O$ ratios per averaged chondrule olivine of meteorite GRO06054 (L3.05) has an MSWD value within the range for accepting one population at the 95% significance (green MSWD value in table 4.7). Therefore, this chondrule population is characterized by a weighted mean of $\Delta^{17}O$= 0.59±0.13‰.

Table 4.6. Main statistics on averaged chondrule olivine $\Delta^{17}O$ ratios data of the investigated subsamples. MSWD values in red are outside the range of acceptable values for one population ($\sigma_{95\%}$).

Chondrite Sample		Weighted mean	± External $error_{sample}$ (ts)	Standard deviation (ts)	no.	Median	Min	Max	Iqr	Skewness	MSWD
WSG95300 (H3.3)	$\Delta^{17}O$ (‰)	0.47	0.06	2.77	71	0.66	-7.49	1.97	0.56	-4.33	52.52
QUE93030 (H3.6)	$\Delta^{17}O$ (‰)	-0.30	0.06	6.38	82	0.74	-17.37	2.13	0.75	-3.57	276.34
ALHA77299 (H3.7)	$\Delta^{17}O$ (‰)	0.35	0.12	2.65	63	0.60	-5.85	2.12	0.80	-2.76	16.40
GRO06054 (L3.05)	$\Delta^{17}O$ (‰)	0.52	0.14	2.57	56	0.61	-6.99	3.87	0.53	-3.58	14.75
DOM10556 (L3.1)	$\Delta^{17}O$ (‰)	0.53	0.08	1.05	21	0.44	-0.62	1.31	0.66	-0.51	10.86
MIL05050 (L3.1)	$\Delta^{17}O$ (‰)	0.33	0.10	3.26	86	0.69	-12.02	2.74	0.84	-5.53	116.33
LAR06279 (LL3.8)	$\Delta^{17}O$ (‰)	0.68	0.11	1.72	42	0.71	-2.84	3.31	0.73	-1.04	12.56
LAR06301 (LL3.8)	$\Delta^{17}O$ (‰)	0.80	0.15	1.43	60	0.82	-1.47	3.10	0.79	0.05	5.51
LAR12034 (LL3.8)	$\Delta^{17}O$ (‰)	0.51	0.06	1.98	82	0.71	-4.87	2.40	0.70	-3.25	32.89

Table 4.7. Main statistics on averaged chondrule olivine spot $\Delta^{17}O$ ratios data of the investigated subsamples. MSWD values in red and green are outside and within the range of acceptable values for one population ($\sigma_{95\%}$), respectively.

Chondrite Sample		Weighted mean	± External $error_{sample}$ (ts)	Standard deviation (ts)	no.	no. outliers	Median	Min	Max	Iqr	Skewness	MSWD
WSG95300 (H3.3)	$\Delta^{17}O$ (‰)	0.72	0.07	0.61	71	14	0.71	0.06	1.30	0.39	-0.02	2.89
QUE93030 (H3.6)	$\Delta^{17}O$ (‰)	0.73	0.06	0.72	82	17	0.80	-0.28	1.33	0.42	-0.72	3.22
ALHA77299 (H3.7)	$\Delta^{17}O$ (‰)	0.62	0.13	0.82	63	11	0.65	-0.32	1.35	0.46	-0.43	1.57
GRO06054 (L3.05)	$\Delta^{17}O$ (‰)	0.59	0.13	0.61	56	10	0.60	-0.04	1.23	0.49	-0.15	0.84
DOM10556 (L3.1)	$\Delta^{17}O$ (‰)	0.63	0.08	0.79	21	2	0.48	0.09	1.31	0.63	0.24	6.32
MIL05050 (L3.1)	$\Delta^{17}O$ (‰)	0.59	0.10	0.93	86	11	0.66	-0.38	1.63	0.77	-0.14	5.23
LAR06279 (LL3.8)	$\Delta^{17}O$ (‰)	0.70	0.11	0.82	42	4	0.71	-0.15	1.43	0.60	-0.07	2.58
LAR06301 (LL3.8)	$\Delta^{17}O$ (‰)	0.77	0.16	0.92	60	11	0.81	-0.11	1.76	0.62	0.09	1.91
LAR12034 (LL3.8)	$\Delta^{17}O$ (‰)	0.64	0.06	0.86	82	10	0.73	-0.24	1.45	0.58	-0.42	6.43

The results presented above suggest as a first approximation that, within uncertainties, OCs accreted the same 'main chondrule population', corresponding to the sub sample data, which is represented by an estimated weighted mean close to $\Delta^{17}O$ ~0.7‰.

4.3.3. Oxygen isotope composition and chondrule olivine Type

In more detail, as reviewed in Chapter 2, chondrules are chemically classified as Type I and Type II depending on the iron content of their mineral phases, here olivine. In this work, oxygen isotope ratios of individual olivine show differences among Type I and Type II, yet overlapping occurs. This data is displayed per olivine grain since bulk chondrule composition was not obtained. However, major, minor, and trace elements from olivine mimic the behavior of bulk Type I and Type II chondrule composition (Ruzicka, 2012). Therefore, olivine chemical data will be used as a proxy to evaluate bulk chondrule chemical processes.

WSG95300 (H3.3) exhibits a tight Type II chondrule olivine dominated cluster at $\delta^{17}O$ ~3.0‰ and $\delta^{18}O$ ~4.5‰, respectively. Differently, Type I olivine shows more variability on Type I olivine, from $\delta^{18}O$ ~-11‰ to $\delta^{18}O$ ~6‰ and ~-13‰ to ~-5‰ (Figure 4.18a and 4.18b).

Type II chondrule olivine grains from QUE93030 (H3.6) show the widest range among this sample, with $\delta^{18}O$ values from ~-32‰ to ~6‰ and $\delta^{17}O$ ratios from ~-34‰ to ~5‰. Type I olivine grains possess a narrower composition with a range of $\delta^{18}O$ values from ~-10‰ to ~5‰ and $\delta^{17}O$ ratios from ~-11‰ to ~4‰. A cluster dominated by Type II olivine is observed close to $\delta^{18}O$ ~5.0‰ and $\delta^{17}O$ ~3.5‰ (Figure 4.18c and 4.18d).

In ALHA77299 (H3.7), the variability among Type I and Type II olivine is similar. Type I olivine ranges from ~-9‰ to ~6‰ in $\delta^{18}O$ and ~-10‰ to ~4‰ in $\delta^{17}O$. Type II chondrule olivine from -6‰ to 5‰ in $\delta^{18}O$ and ~-7‰ to ~4‰ in $\delta^{17}O$. A similar cluster characterized by Type II grains is observed close to $\delta^{18}O$ ~4.5‰ and $\delta^{17}O$ ~3.5‰ (Figure 4.18e and 4.18f).

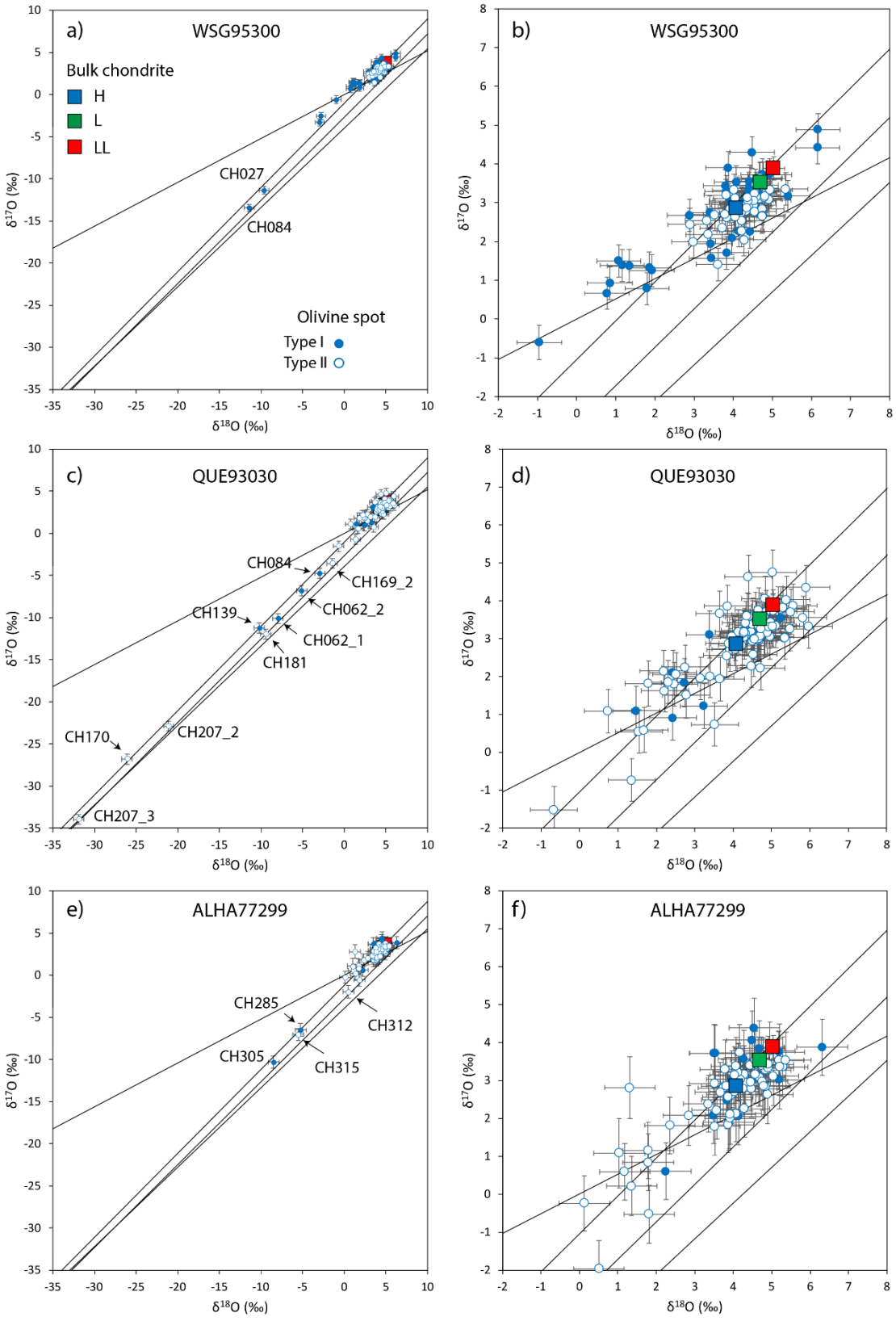

Figure 4.18. Oxygen isotope ratios of chondrule olivine from H samples. Lines are as in figure 1.1.

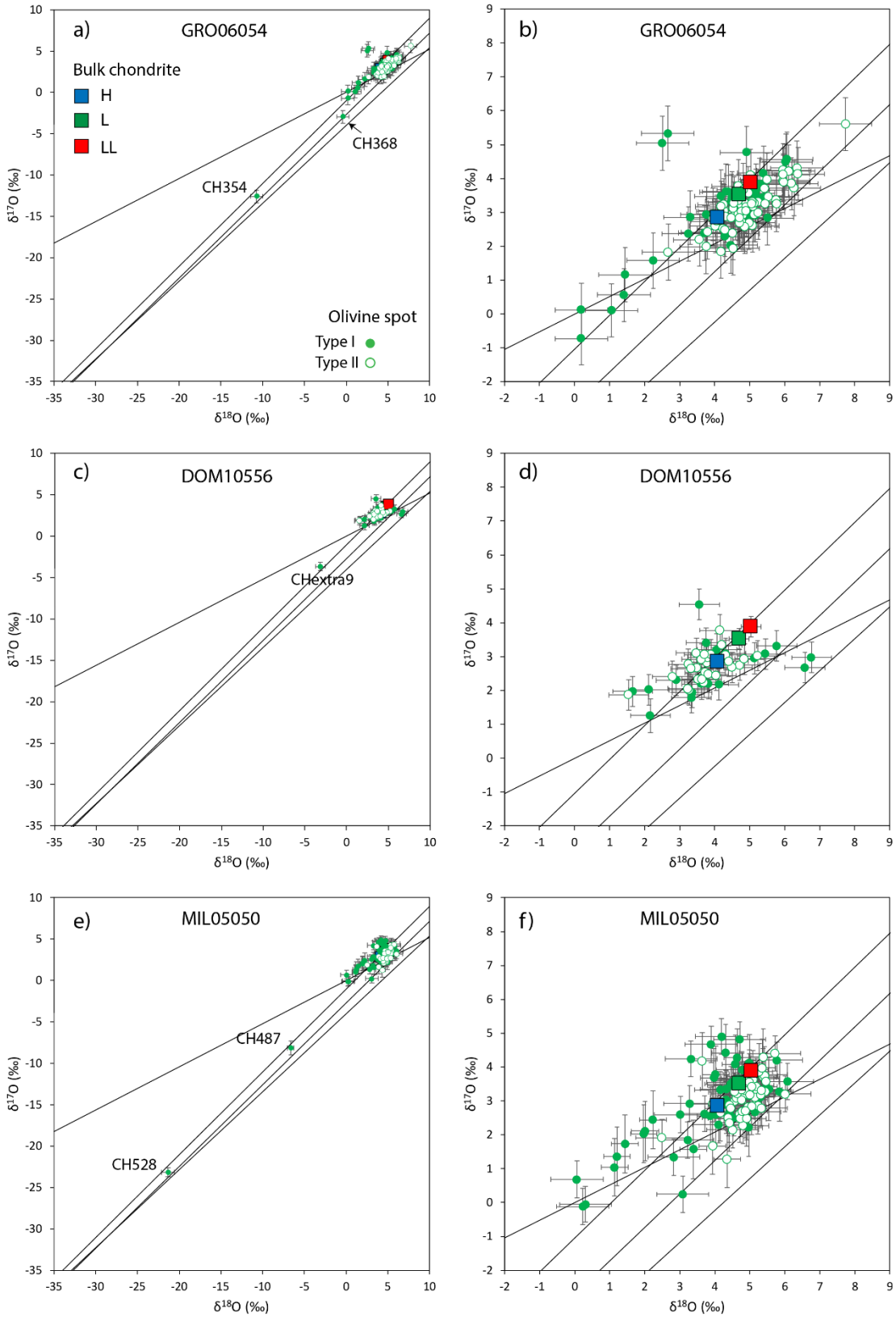

Figure 4.19. Oxygen isotope ratios of chondrule olivine from L samples. Lines are as in figure 1.1.

GRO06054 (L3.05) chondrule olivine show a similar variability compare to WSG95300 and ALHA77299. Type I data show a range of $\delta^{18}O$ ratios from ~-11‰ to ~5‰ and $\delta^{17}O$ from ~-13‰ to ~5‰. In contrast, Type II olivine grains mainly cluster close to $\delta^{17}O$ ~3‰ and $\delta^{18}O$ ~5‰ (Figure 4.19a and 4.19b).

Type I data from MIL05050 (L3.1) vary from ~-21‰ to ~6‰ in $\delta^{18}O$ and ~-23‰ to ~5‰ in $\delta^{17}O$ while Type II olivines tend to plot close to the same cluster as GRO06054 at $\delta^{17}O$ ~3‰ and $\delta^{18}O$ ~5‰ (Figure 4.19e and 4.19f).

Type I olivine from DOM10556 (L3.1) range from $\delta^{18}O$ ~-3‰ to ~7‰ and $\delta^{17}O$ ~-4‰ to ~5‰ while Type II chondrule olivine display variability from ~1‰ to ~7‰ in $\delta^{18}O$ and ~1‰ to ~5‰ in $\delta^{17}O$. However, an incipient cluster at $\delta^{17}O$ ~3.5‰ and $\delta^{18}O$ ~4.5‰ can be recognized (Figure 4.19c and 4.19d).

LAR06279 (LL3.8) is dominated by Type II chondrule olivine which varies from ~-4‰ to ~7‰ in $\delta^{18}O$ and ~-5‰ to ~4‰ in $\delta^{17}O$. On the other hand, Type I olivine grains range from 2‰ to ~5‰ in $\delta^{18}O$ and ~2‰ to ~5‰ in $\delta^{17}O$. Similar to previous samples a Type II chondrule olivine dominated cluster can be observed $\delta^{18}O$ ~5‰ and $\delta^{17}O$ ~3‰ (Figure 4.20a and 4.20b).

LAR06301 (LL3.8) is also dominated by Type II olivine which shows a range of $\delta^{18}O$ ratios from ~1‰ to ~7‰ and $\delta^{17}O$ ratios from ~0‰ to ~7‰. Present but less clear compared to the other samples, a Type II grain dominated cluster appears close to $\delta^{18}O$ ~5‰ and $\delta^{17}O$ ~3‰ (Figure 4.20c). Whereas Type I data range from ~2‰ to ~5‰ in $\delta^{18}O$ and ~0‰ to ~5‰ in $\delta^{17}O$.

Type I chondrule olivine from LAR12034 (LL3.8) ranges from ~-6‰ to ~6‰ in $\delta^{18}O$ and ~-8‰ to ~4‰ in $\delta^{17}O$ while Type II olivine covers $\delta^{18}O$ ratios from ~-4‰ to ~7‰ and ~-7‰ to ~5‰ in $\delta^{17}O$. The same Type II dominated cluster is well-defined close to $\delta^{18}O$ ~5‰ and $\delta^{17}O$ ~3‰ (Figure 4.20a and 4.20b).

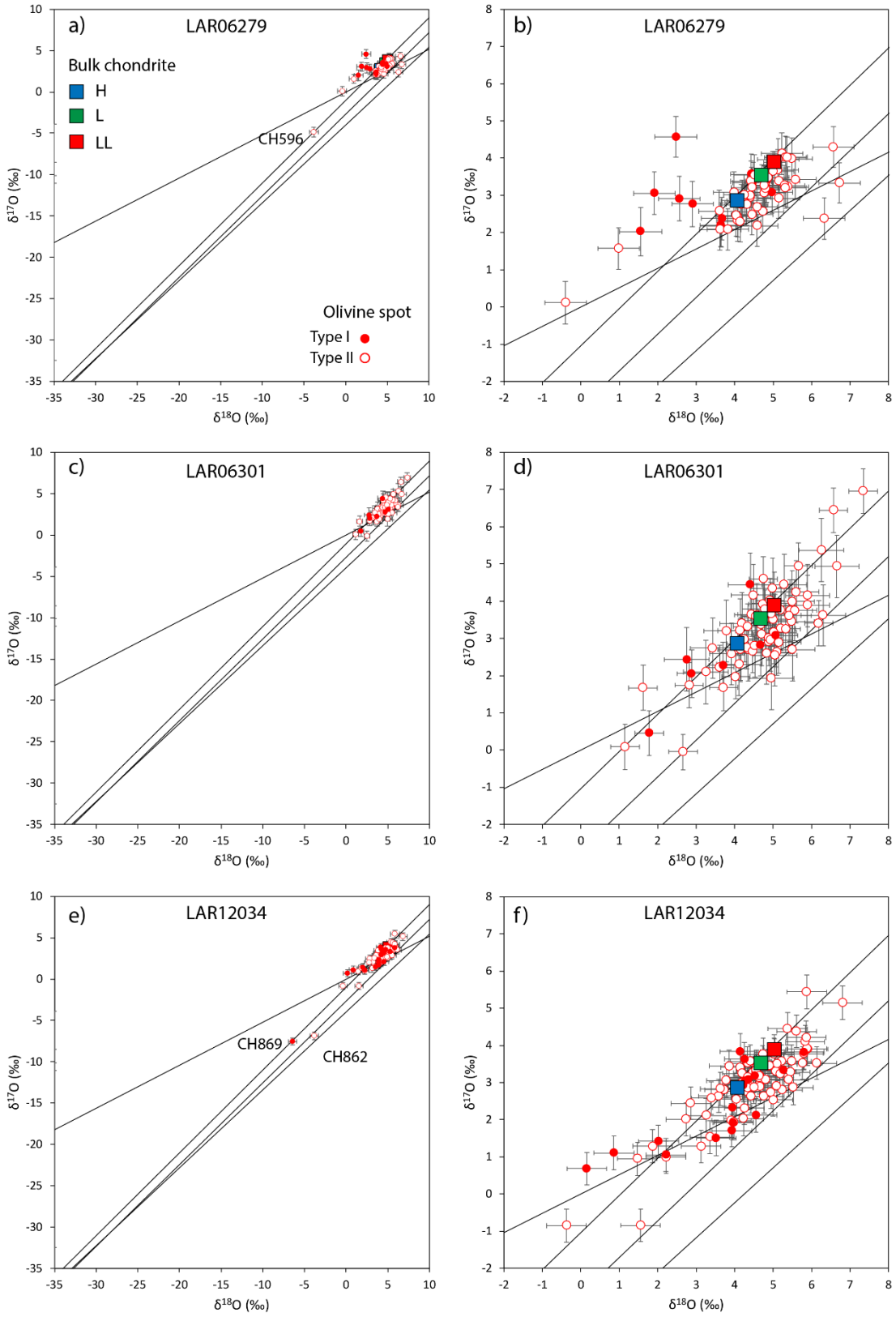

Figure 4.20. Oxygen isotope ratios of chondrule olivine from LL samples. Lines are as in figure 1.1.

It is important to highlight here that taking into consideration the petrologic type of QUE93030 (H3.6), ALHA77299 (H3.7), LAR06279 (LL3.8), LAR06301 (LL3.8), and LAR12034 (LL3.8), and the possibility that the Fa mol% composition of olivines might have been affected by thermal metamorphism in the parent body (Chapter 2), Type I and Type II olivine distinctions mentioned above are only descriptive for these samples. On the other hand, chondrite samples from a lower petrologic type WSG95300 (H3.3), GRO06054 (L3.05), DOM10556 (L3.1), and MIL05050 (L3.1) contain chondrules which represent a more primitive chemical signature, associated to solar nebula processes.

5. DISCUSSION

5.1. Matrix Effect

After correction of San Carlos olivine for an overall IMF, the remaining matrix effect bias towards FeO-richer olivine standards is small but resolvable in both $\delta^{17}O$ and $\delta^{18}O$ considering the internal error of the primary standard (0.07‰ for $\delta^{17}O$ and 0.09‰ for $\delta^{18}O$) and the external error of the synthetic olivines which, is better than 0.20‰ at the 95% confidence interval. The range of FeO olivine composition of this study covers mainly from Fa0 to Fa30mol% with an IMF effect of ~0.5‰ for $\delta^{18}O$. The richest olivine FeO composition measured was ~Fa40 with an offset of ~1‰.

Even though the IMF effect on the range of olivine compositions of this study is small, the high quality of the reproducibility on the primary standard allows us to resolve this bias. The correction was calculated by fitting an order one polynomial equation when plotting olivine composition vs. bias between LF and SHRIMP-SI oxygen isotope measurements. An example of non-corrected and corrected data is depicted in figure 5.1 where the relatively small IMF effects of SHRIMP-SI can be observed graphically. In any case, further work is required to understand and evaluate the reproducibility of IMF effects of SHRIMP-SI on the whole FeO olivine compositional range. By this means, IMF effects could be calibrated to high accuracy.

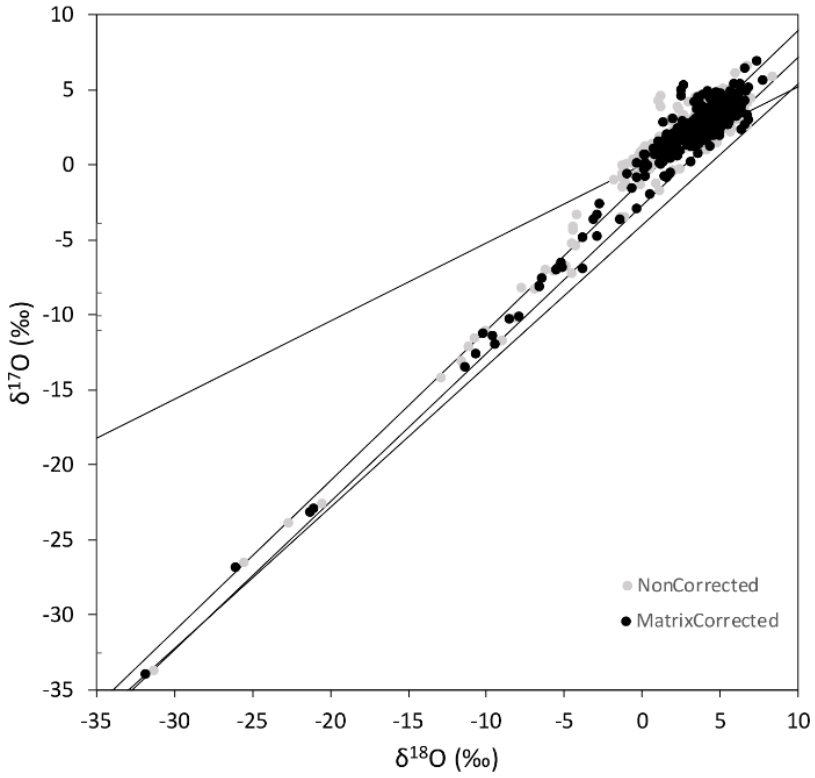

Figure 5.1. Triple-oxygen isotope plot of corrected and non-corrected chondrule olivine. Referential lines are as in figure 1.1.

5.2. Chondrule size

Chondrule size is an important physical property. It has been used to classify chondrites on to chemical groups since each of them possesses a specific chondrule size distribution. Moreover, if one see chondrules as astrophysical objects then chondrule size is significant for the understanding and development of models of chondrule formation and mass transport in the protoplanetary disk (Friedrich et al., 2015; Jacquet, 2014a, 2014b; Salmeron & Ireland, 2012).

In general, the ordinary chondrite chondrule size of this study agrees with their classification scheme which put them in an increasing apparent mean size from H to L to LL iron groups (Scott & Krot, 2014). The mean values of chondrules from H and LL samples are very close to the proposed values (~450 μm, ~500 μm, and ~550 μm, for H, L, and LL, respectively; Friedrich et al., 2015). On the other hand, chondrules from the L samples show particularly high mean sizes (~749 μm, ~643 μm, and ~583 μm; figure 4.4)

but the size frequency distribution, size range (~100 μm to ~1900 μm), and the median are similar to the typical observed in L chondrites (Friedrich et al., 2015).

Rubin (2010) argues that the chondrule size distribution in chondrites is controlled by dust abundance and the number of remelting events in different chondrule-forming regions and that the size sorting occurred during accretion of chondrites. (Jones, 2012) also suggests that even though size-sorting does not appear to be the major control on the distribution of chondrule textural types it could account for the similar size range of chondrules in each group. Jacquet (2014a) proposed that chondrule size is correlated to the size of the precursor suggesting that the chondrule-melting process(es) did not modify significantly the mass of the precursor. The size distribution among OCs could be a mixture of factors and/or conditions.

It is well known that Type I chondrules are significantly smaller than Type II chondrules (Jones, 2012) and that chondrule size increases with respect to H, L, and LL groups. Additionally, the chondrule ratio Type I/Type II appears to decrease from H to L, to LL groups suggesting that Type I chondrules are present in higher abundances in H chondrites (Zanda et al., 2006). Then, taking into account that Type I chondrules formed under more reducing conditions compare to Type II chondrules it could be possible that H, L, and LL chondrites accreted chondrules that represent a transition from smaller and more reduced chondrules towards bigger and more oxidized chondrules from H to L, to LL chondrite groups. If this is the case, these populations could also represent the transition of chondrule formation from smaller to bigger precursors which could be correlated to the dust enrichment of the chondrule formation region (Jacquet, 2014b; Rubin, 2010).

5.3. Sample reclassification

A significant characteristic among chondrule olivine measured in this study is the clustering observed for Cr_2O_3 (~0-1wt%), MnO (~0.4-0.5wt%), and CaO (~0-1wt%) when plotted against FeOwt% for QUE93030 (H3.6), ALHA77299 (H3.7), LAR06279 (LL3.8), LAR06301 (LL3.8), and LAR12034 (LL3.8) samples (Figures 4.6, 4.7 and 4.8).

The variability of Fa mol% composition of these clusters corresponds to the range observed in olivines from equilibrated H and LL OCs, 16-21mol% and 26-33mol%, respectively. The above suggests chondrule olivine chemical equilibration due to thermal metamorphism (Huss et al., 2006) for these chondrule olivine clusters, consistent with their host chondrites previous classification.

In this regard, a sensitive indicator of thermal metamorphism is the Cr_2O_3wt% content of olivine with FeO compositions above 2wt% (Grossman & Brearley, 2005). Interestingly, neither of the expected Cr_2O_3 compositional features for higher chondrite compositional types are observed in GRO06054, DOM10556, and MIL05050 which has been classified as L3.8 (Meteoritical Bulletin). On the contrary, the Cr_2O_3wt% compositional trend of these meteorites suggests that they did not suffer an important degree of thermal metamorphism.

Bonal et al., (2016) using Raman spectroscopy of matrix polyaromatic carbonaceous matter, classified GRO06054 and MIL05050 as L3.05 and L3.1, respectively, consistent with the Cr_2O_3wt% olivine systematics presented in Chapter 3. They also classified LAR06279 as an LL3.05-3.1 which does not correlate with the equilibrated Cr_2O_3 olivine compositions of the present study (Figure 4.10g). In this respect since many OCs are breccias (Bischoff et al., 2006), it is possible that the matrix analyzed in (Bonal et al., 2016) represents material from a lower type lithology and that the material investigated in this work is from a more thermally metamorphosed region. Additionally, meteorite DOM10556 has been reclassified here as an L3.1 based on the chondrule olivine mean and standard deviation of Cr_2O_3wt% (Figure 5.2; Grossman & Brearley, 2005).

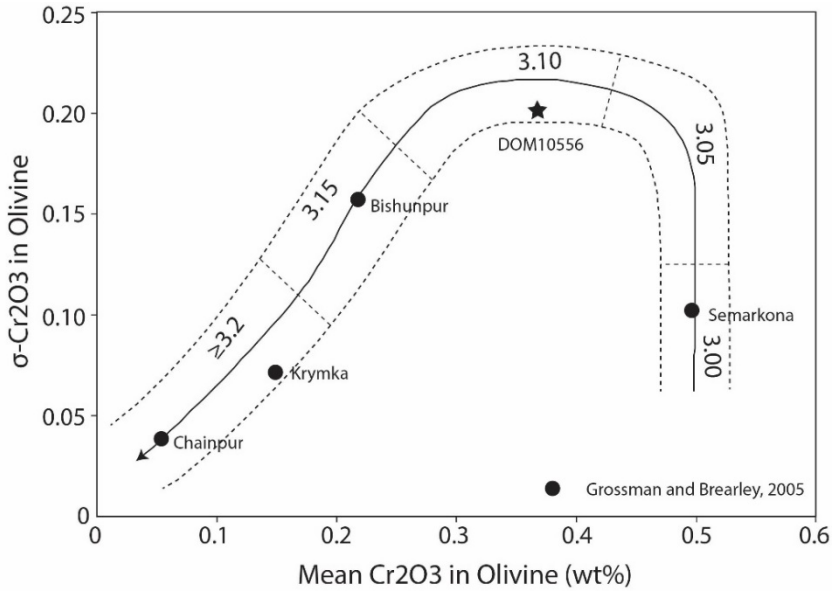

Figure 5.2. Plot of the mean versus the standard deviation of the Cr2O3 content of FeO-rich olivine. The star symbol is the sample from this study. Other data obtained from Grossman and Brearley (2005).

Although not all chondrules were affected by thermal metamorphism to the same extent, and general chemical patterns can still be recognized using all samples, the more pristine samples are chondrule olivines from WSG95300 (H3.3), GRO06054 (L3.05), DOM10556 (L3.1), and MIL05050 (L3.1). These reflect the chemical exchange among chondrule precursors and the solar nebula.

In the case of oxygen isotope diffusion due to parent body processes, it has been shown that chondrule mesostasis (glass and/or plagioclase) oxygen isotope ratios differ from those of coexisting olivine and pyroxene in weakly and mildly thermal altered UOCs and carbonaceous chondrites (Kita et al., 2010; Bridges & Ireland, 2015; Tenner et al., 2017). The difference in oxygen isotope composition among chondrule phases occurs because plagioclase is more susceptible to exchange during thermal metamorphism compared to olivine and pyroxene. Experimental data on plagioclase and feldspathic-glass self-diffusion rates are orders of magnitude faster than those of olivine and pyroxene and oxygen can diffuse 10 μm^2 per million years at 200-400°C (Giletti et al., 1978; Ryerson et al., 1989). In contrast, olivine grains require sustained temperatures above 700-800°C to observe appreciable oxygen diffusion.

Therefore, assuming that the peak metamorphic temperature was ~600°C for UOCs, although it might be lower (Bonal et al., 2016; Huss et al., 2006), then chondrule olivine

primary oxygen isotope signatures for UOCs should be resistant to disturbance by thermal metamorphism, or having little change. Supporting this hypothesis, McDougal et al. (2017) showed that oxygen isotope systematics of chondrule olivine from type 4 OCs are heterogeneous having similar ranges to type 3 chondrites. They concluded that the peak metamorphic temperatures of type 4 chondrites were not enough to equilibrate the oxygen isotope ratios in olivine and pyroxene. Additionally, they showed that chondrule olivine equilibration of oxygen isotopes is noticeable in type 5 and type 6 equilibrated OCs. Given these results, the oxygen isotope ratios of chondrule olivine investigated here should not be substantially affected by thermal metamorphism; they probably represent the primitive signature attained during chondrule formation which is indicative of the oxygen isotope reservoir or region of the protoplanetary disk where thermal processing of chondrule precursors occurred.

5.4. Ordinary chondrites chondrule main population

First of all, for the sake of clarity, the term reservoir will be used considering only the $\Delta^{17}O$ value which is commonly used to describe the oxygen isotope variability due to mass-independent fractionation processes. This parameter emphasizes the cosmochemical characteristics of solar system materials and reflects the region of the solar nebula where chondrules and/or chondrule precursors acquired their oxygen isotope signature.

In general, $\Delta^{17}O$ ratios do not vary largely among different phases within the same chondrule and are internally homogenous within SIMS uncertainties (e.g. Table 5, Electronic Annex 2; Chaussidon et al, 2008; Kita et al., 2010; Weisberg et al., 2011; Ushikubo et al., 2012; Tenner et al., 2013, 2015, 2017; Nagashima et al., 2015; Miller et al., 2017; Schrader et al., 2017). The main exceptions are relict grains that survived the last chondrule formation heating event which show large oxygen isotopic disequilibrium with the minerals formed from the melt (Jones, 2012), and, as mentioned before, feldspathic mesostasis that can be affected by parental body processes. Therefore, the $\Delta^{17}O$ composition of chondrule olivine obtained in this study will be utilized as a proxy for bulk chondrule composition.

As mentioned in Chapter 1, and based on bulk oxygen isotope composition of individual chondrules from OCs of the different chemical groups (H, L, and LL), it has been argued that chondrules could represent a single population or various populations in the solar nebula representing one or various solid or gaseous reservoirs (Clayton et al., 1991; Metzler et al., 2017). However, neither of these options have been statistically assessed in the past.

It was shown in Chapter 4 that in the $\delta^{18}O$ vs. $\delta^{17}O$ diagram the majority of chondrule olivine grains plot above the TF line clustering between the Y&R and PCM lines (Figure 4.11), representing a first-order characteristic of chondrules from OCs. On this subject, this distinctive feature observed in the triple-oxygen plot can be visualized even clearly when using the $\Delta^{17}O$ ratios of chondrule olivine, depicted in figure 4.13 exhibiting chondrule olivine histograms and PDFs of each chondrite sample.

Although some variability towards higher and lower $\Delta^{17}O$ ratios is observed among olivine, these values appear to be an anomaly rather than the norm considering the amount of data acquired. In fact, close to 96% of chondrule olivine has $\Delta^{17}O$ values ranging from -2.5‰ to 3‰ essentially forming a unimodal (bell-shaped) distribution between these values no matter the host chondrite type (H, L, or LL). This suggests that OCs accreted one 'main chondrule population', in agreement with Clayton et al. (1991).

However, as mentioned earlier, this evident peak on the sample distributions needs to be statistically assessed to be meaningful. In this regard, some clues were already noted in Chapter 3. Briefly:

1) all OCs investigated here share statistically the same median for $\Delta^{17}O$ (~0.7‰) at the 95% significance, per olivine spot or per averaged chondrule olivine, either when the whole sample is considered or when the subsample is pooled from the data;

2) when each chondrite subsamples are sorted out, chondrule olivine weighted mean $\Delta^{17}O$ values are the same within uncertainties (~0.7‰) and indistinguishable from their medians, these results are in conformity with Kita et al., (2010), who based on SIMS olivine and pyroxene phenocrysts measurements from unequilibrated LL chondrites, reported comparable chondrule average $\Delta^{17}O$ ratios (~0.6‰);

3) the empirical cumulative distribution function, histograms, PDFs and whisker boxplot diagrams of $\Delta^{17}O$ ratios for each chondrite show that most of the chondrule olivine distribution is condensed within 0‰ and 2‰;

4) Indicators of symmetry (e.g. skewness) of each sample show a significant improvement towards values closer to zero when the subsample is evaluated compared to the whole sample; and

5) the MSWD values, which provides a measure of goodness of fit represented by the weighted mean of the prospect chondrule population, also change towards values closer to the range of a single population acceptability.

Therefore, the exploratory analysis together with the statistics of each chondrite are strong evidence that support the hypothesis that OCs sampled the same chondrule population in terms of oxygen isotopes in their accretion location.

Having this hypothesis in mind, an important question to be resolved here is to evaluate if these chondrules were either obtained from the same continuous distribution or not. In this regard, a non-parametric two-sample Kolmogorov-Smirnov test which returns a test decision for the null hypothesis that two samples share the same continuous distribution at the 95% confidence level was performed for all the possible combinations both for spot olivine and averaged olivine per chondrule data. Tables 5.1 and 5.2 show the statistical test results for olivine spot and averaged chondrule, respectively.

Table 5.1 Two sample Kolmogorov-Smirnov test of all $\Delta^{17}O$ chondrule olivine data. 0: samples come from the same continuous distribution; 1: samples come from different distributions.

Sample/Group		WSG95300 H	QUE93030 H	ALHA77299 H	GRO06054 L	DOM10556 L	MIL05050 L	LAR06279 LL	LAR06301 LL	LAR12034 LL
WSG95300	H	-	0	0	0	0	0	0	0	0
QUE93030	H	-	-	0	0	0	0	0	0	0
ALHA77299	H	-	-	-	0	0	0	0	0	0
GRO06054	L	-	-	-	-	0	0	0	0	0
DOM10556	L	-	-	-	-	-	0	0	0	0
MIL05050	L	-	-	-	-	-	-	0	0	0
LAR06279	LL	-	-	-	-	-	-	-	0	0
LAR06301	LL	-	-	-	-	-	-	-	-	0
LAR12034	LL	-	-	-	-	-	-	-	-	-

Table 5.2. Two sample Kolmogorov-Smirnov test of all $\Delta^{17}O$ averaged chondrule olivine data. 0: samples come from the same continuous distribution; 1: samples come from different distributions.

Sample/Group		WSG95300 H	QUE93030 H	ALHA77299 H	GRO06054 L	DOM10556 L	MIL05050 L	LAR06279 LL	LAR06301 LL	LAR12034 LL
WSG95300	H	-	0	0	0	0	0	0	0	0
QUE93030	H	-	-	0	0	0	0	0	0	0
ALHA77299	H	-	-	-	0	0	0	0	0	0
GRO06054	L	-	-	-	-	0	0	0	0	0
DOM10556	L	-	-	-	-	-	0	0	0	0
MIL05050	L	-	-	-	-	-	-	0	0	0
LAR06279	LL	-	-	-	-	-	-	-	0	0
LAR06301	LL	-	-	-	-	-	-	-	-	0
LAR12034	LL	-	-	-	-	-	-	-	-	-

The results of the statistical test between samples show that all combinations are consistent with the acceptance of the null hypothesis that the pairs of samples being evaluated come from the same continuous distribution. This is true for olivine data and for averaged chondrule olivine data. Therefore, since OCs accreted chondrules drawn from the same sample distribution in terms of $\Delta^{17}O$ ratios and this distribution has a clear main population the question now is how to statistically define the borders of this population.

Once again, a glimpse to this answer was already given during the exploratory analysis in Chapter 3 when the chondrule olivine spot and averaged chondrule $\Delta^{17}O$ data from each chondrite was pooled. This data can be visualized from the whiskers boxplots because the whiskers were set to represent the 95% interval of the sample distribution. In more detail, for chondrule olivine spot data, the lower and upper whiskers are 0.06‰ and 1.30‰ in WSG95300 (H3.3), 0.02‰ and 1.36‰ in QUE93030 (H3.6), -0.19‰ and 1.35‰ in ALHA77299 (H3.7), -0.04‰ and 1.42‰ in GRO06054 (L3.05), 0.03‰ and 1.46‰ in DOM10556 (L3.1), -0.37‰ and 1.70‰ in MIL05050 (L3.1), -0.19‰ and 1.42‰ in LAR06279 (LL3.8), -0.26‰ and 1.84‰ in LAR06301 (LL3.8), -0.14‰ and 1.31‰ in LAR12034 (LL3.8), respectively, which are the first approach to the lower and upper limits of the 'main chondrule population' per chondrite.

In order to evaluate each chondrite subsample, a good starting point is to consider them as samples themselves since they represent the norm rather than the exception of the whole sample distribution. By doing so, 'normal' results will provide the strongest piece of evidence to evaluate chondrules from OCs. Additionally, although for the statistical analysis we consider all $\Delta^{17}O$ values, it has been shown that $\Delta^{17}O$ below -2‰ in OC

chondrules are usually related to relict grains that acquired their oxygen isotope signature in a region of the protoplanetary disk common to carbonaceous chondrite chondrules (Kita et al., 2016, 2017).

The above is then consistent with having a subsample representing the 'main chondrule population'. Therefore, the same statistical test (Kolmogorov-Smirnov) was performed for the 'main chondrule population' using both per spot and averaged data. Table 5.4 and table 5.5 show the results of these tests from where it can be observed that in the majority of the tested chondrite pairs the null hypothesis is accepted, that the 'main populations' being evaluated come from the same continuous distribution at the 95% confidence interval.

Interestingly, the number of rejections of the null hypothesis is higher when comparing spot data (7 of 43) to averaged data (1 of 43), although one could argue that this is an expected result since the two-sample Kolmogorov-Smirnov test evaluates the difference between the cumulative density functions (CDFs) of the distributions of the two samples, then averaging the olivine spots in chondrules with more than one observation, diminishes the intrinsic variability associated with per spot data, resulting in more similar CDFs.

Table 5.3. Two sample Kolmogorov-Smirnov test of the 'main population' $\Delta^{17}O$ chondrule olivine data. 0: samples come from the same continuous distribution; 1: samples come from different distributions.

Sample/Group		WSG95300 H	QUE93030 H	ALHA77299 H	GRO06054 L	DOM10556 L	MIL05050 L	LAR06279 LL	LAR06301 LL	LAR12034 LL
WSG95300	H	-	0	0	1	1	0	0	0	0
QUE93030	H	-	-	0	1	1	1	1	1	0
ALHA77299	H	-	-	-	0	0	0	0	0	0
GRO06054	L	-	-	-	-	0	0	0	0	0
DOM10556	L	-	-	-	-	-	0	0	0	0
MIL05050	L	-	-	-	-	-	-	0	0	0
LAR06279	LL	-	-	-	-	-	-	-	0	0
LAR06301	LL	-	-	-	-	-	-	-	-	0
LAR12034	LL	-	-	-	-	-	-	-	-	-

Table 5.4. Two sample Kolmorogov-Smirnov test of the 'main population' $\Delta^{17}O$ averaged chondrule olivine data. 0: samples come from the same continuous distribution; 1: samples come from different distributions.

Sample/Group		WSG95300 H	QUE93030 H	ALHA77299 H	GRO06054 L	DOM10556 L	MIL05050 L	LAR06279 LL	LAR06301 LL	LAR12034 LL
WSG95300	**H**	-	0	0	0	0	0	0	0	0
QUE93030	**H**	-	-	0	1	0	0	0	0	0
ALHA77299	**H**	-	-	-	0	0	0	0	0	0
GRO06054	**L**	-	-	-	-	0	0	0	0	0
DOM10556	**L**	-	-	-	-	-	0	0	0	0
MIL05050	**L**	-	-	-	-	-	-	0	0	0
LAR06279	**LL**	-	-	-	-	-	-	-	0	0
LAR06301	**LL**	-	-	-	-	-	-	-	-	0
LAR12034	**LL**	-	-	-	-	-	-	-	-	-

In more detail, the basic statistics of each chondrite 'main population' can be found in tables 4.5 and 4.7 from Chapter 4. Broadly, considering the olivine spot data, the $\Delta^{17}O$ ratios of the 'population' range from -0.26‰ to 1.84‰, their standards deviations ($\sigma_{95\%}$) from 0.58‰ to 0.93‰, the medians from 0.59‰ to 0.80‰, weighted means from 0.63‰ to 0.78‰, skewness from -0.41 to 0.18, and MSWDs with one value within the acceptable range (MSWD=1.27, GRO06054), meaning that the sample obtained from GRO06054 was drawn from a single population ($\sigma_{95\%}$). All the rest of MSWD values are away from the upper end of the envelope, therefore that samples do not represent a single population.

The outcome of this analysis is the same when the averaged chondrule olivine data is investigated (Table 4.7). Briefly, considering averaged chondrule olivine data, $\Delta^{17}O$ compositions vary from -0.38‰ to 1.76‰, standards deviations ($\sigma_{95\%}$) from 0.61‰ to 0.93‰, medians from 0.48‰ to 0.81‰, weighted means from 0.59‰ to 0.77‰, skewness from -0.43 to 0.24, and MSWDs with one value within the acceptable range (MSWD=0.84, GRO06054).

Figure 5.3 shows the 'main chondrule population' in detail, for chondrule olivine data. In general, the shape of the samples PDF (black continuous line), which is drawn considering uncertainties, shows more or less symmetric unimodal sample distributions. To the naked eye, it appears that chondrule olivine sample distribution from GRO06054 is the most similar to a Gaussian distribution. The exception to this unimodality is sample DOM10556 which shows two peaks (Figure 5.3e). In this regard, the thin section of sample DOM10556 had fewer chondrules than the rest of the samples. Additionally, DOM10556 is the sample with less observations (n=43) of this study, therefore some bias and poorer statistics are expected from this chondrite. The same occurs, when the figure is plotted using the averaged olivine data per chondrule (Figure 5.4).

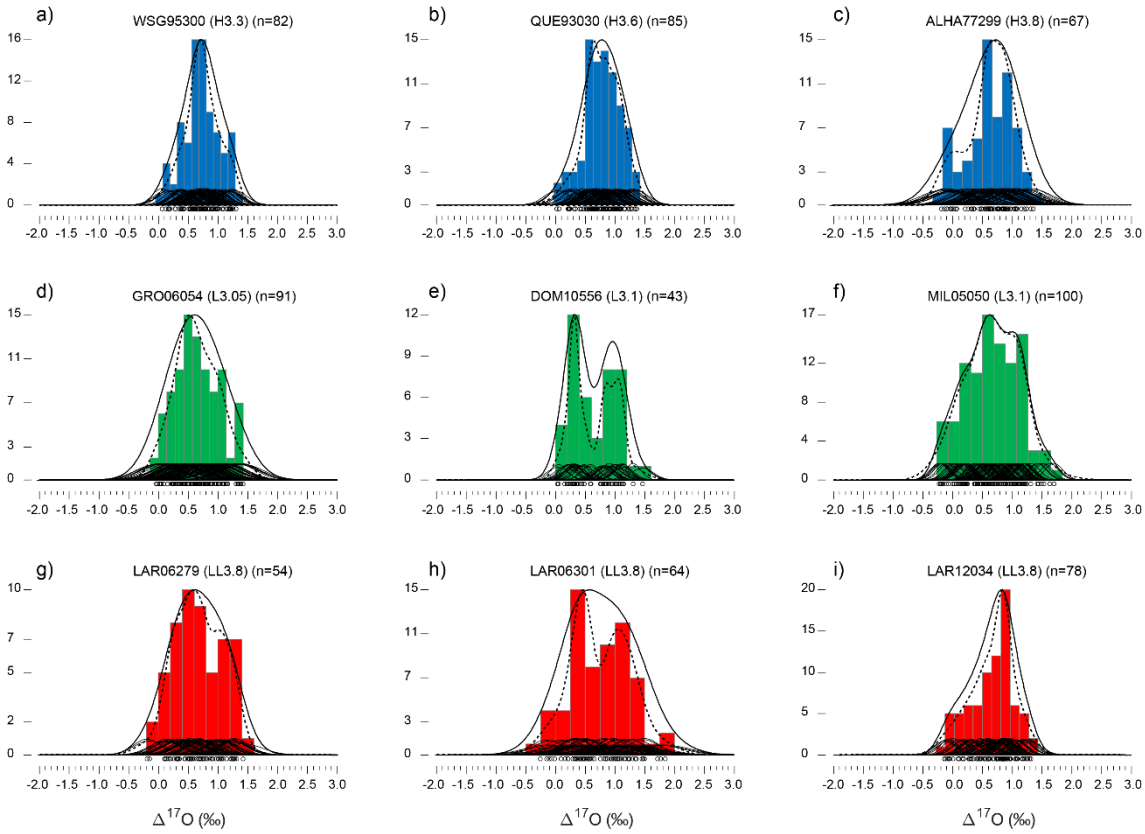

Figure 5.3. $\Delta^{17}O$ chondrule olivine histograms of H, L, and LL samples. Continuous black line: PDF; dashed-black line: KDE. The cloud of curves on the bottom of each plot are the normal distribution of each observation considering the external error ($\sigma_{95\%}$).

In addition to the PDFs, a kernel density estimation (KDE) was also calculated for the sample distribution of the data using the software DensityPlotter (Vermeesch, 2012). Similar to PDF, KDE also involves summing a set of Gaussian distributions (each datum) but does not explicitly take into account the analytical uncertainties (Figure 5.3 and 5.4). This tool was suggested to be a more robust way of visualizing zircon detrital age distributions (Vermeesch, 2012). Therefore, using the KDE of chondrule olivine $\Delta^{17}O$ distribution is an interesting way of exploring the data, considering that chondrites are sedimentary cosmic rocks.

In this regard, each sample appears to be less smooth and more tightly distributed when the KDE is considered (Figures 5.3c, 5.3e and 5.3h) suggesting that within the 'chondrule main population' range more than one mode exists. This effect is, in general, accentuated when averaged chondrule olivine is explored (Figure 5.4), probably due to a smaller sample size. It appears that the KDE approach highlights the fact that the samples with

two clear peaks have a lack of observations with $\Delta^{17}O$ composition between these peaks, which is otherwise obscured by the PDF of those samples.

At any rate, in contrast to detrital zircon data which usually display PDFs with a high number of peaks, making the visualization and provenance assessment of populations more difficult, OC chondrule oxygen data forms in general one clear peak suggesting that the 'main population of chondrules' incorporated in their parental bodies where thermally processed in the same region of the protoplanetary disk with little 'contamination' from other sources of the solar nebula.

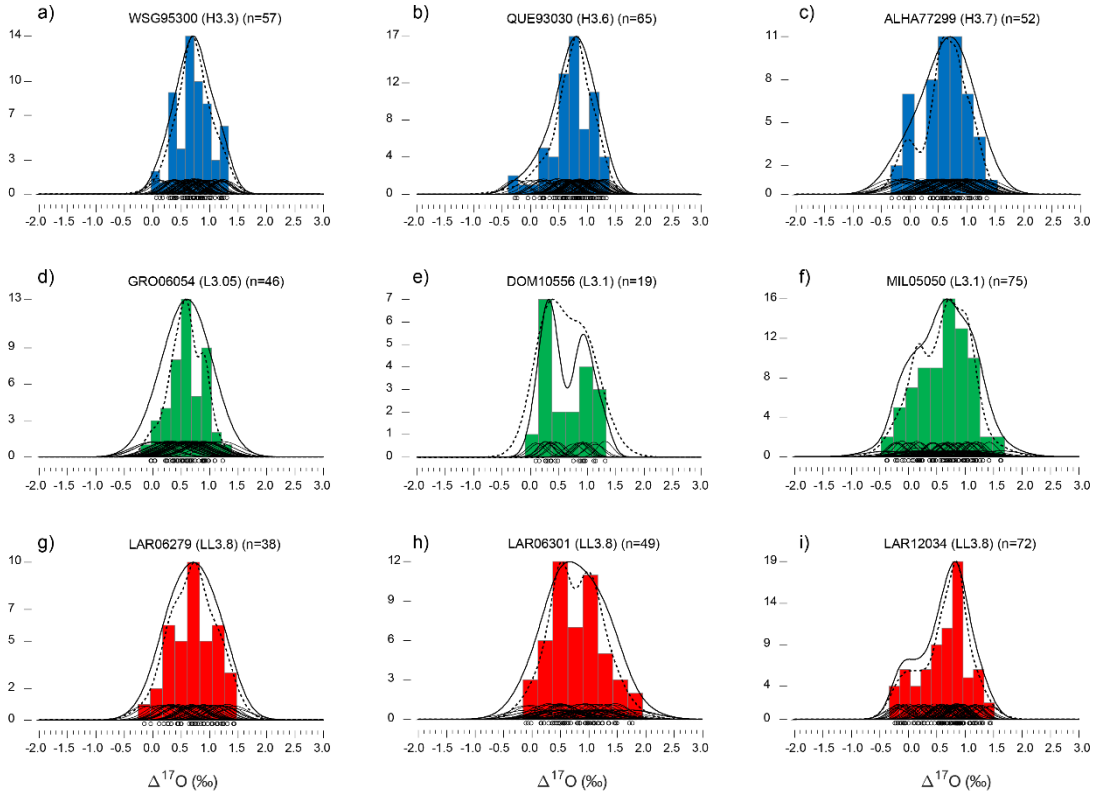

Figure 5.4. $\Delta^{17}O$ averaged chondrule olivine histograms of H, L, and LL samples. Continuous black line: PDF; dashed-black line: KDE (see text). The cloud of curves on the bottom of each plot are the normal distribution of each averaged chondrule olivine observation considering the external error ($\sigma_{95\%}$).

However, since the goal is to constrain the borders of this apparent chondrule population per chondrite and the preferred method to statistically characterize it is the weighted mean, each OC 'main population' is assessed for the weighted mean at the 95% confidence interval. From here, in order to obtain an oxygen isotope composition representative of the chondrule population, the averaged chondrule olivine data will be used for the following analysis (see Chapter 3).

When the analysis of the weighted mean is done, the MSWD values of all but one sample (LAR06279) fall within the range of acceptable values to represent a single population, ergo the 'main chondrule population' per chondrite (Table 5.5). This data treatment can be graphically observed in figure 5.5 where the blue bars correspond to chondrules from H chondrites, green bars to L chondrites, and red bars to LL chondrites. Purple bars represent the values away from the weighted mean which have been rejected from the model to define OCs 'main chondrule population'. Individual uncertainties are external errors and the error of the weighted means are internal errors of the pooled unknown sample. All errors are displayed at the 95% confidence interval.

Table 5.5. Main averaged chondrule olivine population border assessment of $\Delta^{17}O$ ratios at the 95% representative interval. MSWD values in green and red fall inside and outside the range of acceptable values for one population, respectively ($\sigma_{95\%}$); no. is the size of the whole averaged chondrule olivine sample while no. outliers is the number of $\Delta^{17}O$ values that were not considered to calculate the limits of the main population.

Chondrite Sample		Weighted mean	± External $error_{sample}$ (ts)	Standard deviation (ts)	no.	no. outliers	MSWD
WSG95300 (H3.3)	**$\Delta^{17}O$ (‰)**	0.67	0.07	0.41	71	26	**1.28**
QUE93030 (H3.6)	**$\Delta^{17}O$ (‰)**	0.82	0.06	0.44	82	30	**1.16**
ALHA77299 (H3.7)	**$\Delta^{17}O$ (‰)**	0.69	0.13	0.70	63	15	**1.11**
GRO06054 (L3.05)	**$\Delta^{17}O$ (‰)**	0.59	0.13	0.61	56	10	**0.84**
DOM10556 (L3.1)	**$\Delta^{17}O$ (‰)**	0.34	0.10	0.39	21	10	**1.22**
MIL05050 (L3.1)	**$\Delta^{17}O$ (‰)**	0.65	0.11	0.64	86	33	**1.06**
LAR06279 (LL3.8)	**$\Delta^{17}O$ (‰)**	0.72	0.11	0.67	42	9	**1.71**
LAR06301 (LL3.8)	**$\Delta^{17}O$ (‰)**	0.75	0.16	0.80	60	16	**1.28**
LAR12034 (LL3.8)	**$\Delta^{17}O$ (‰)**	0.79	0.06	0.38	82	36	**1.24**

Two options are possible to explain the MSWD value of chondrite LAR06301. One is that the $\Delta^{17}O$ errors have been underestimated, although this is unlikely since the average external error of the session where this chondrite was measured is ±0.5‰ which is close to the average between the most and least precise sessions (±0.6‰). The other is that after the systematic data treatment given to all chondrites studied here, the oxygen isotope variability of chondrules from this chondrite does not show the signature of the prospective 'main chondrule population', therefore representing more than one population of chondrules.

The idea of asteroids sampling different chondrule populations on their accretion location might not be a surprise given that models predict radial and vertical migration and mixing of dust of different sizes (including chondrules) throughout the disk (e.g. Testi et al., 2014). What is strikingly remarkable is to see such a clear 'population' in ordinary chondrites. In this line, there are some reasons to believe that despite the MSWD value of LAR06279, this chondrite still accreted one 'main chondrule population'. Firstly, the MSWD value is still very close to the accepted range around unity; secondly, it was previously tested that the sample distribution using all data of each chondrite are statistically the same among them; and thirdly, this was also demonstrated when the 'main chondrule population' data was assessed via the two-sample Kolmogorov-Smirnov test. Given this argument, in this research, it is preferred to consider that LAR06279 accreted the same 'main chondrule population', just like the other OCs investigated.

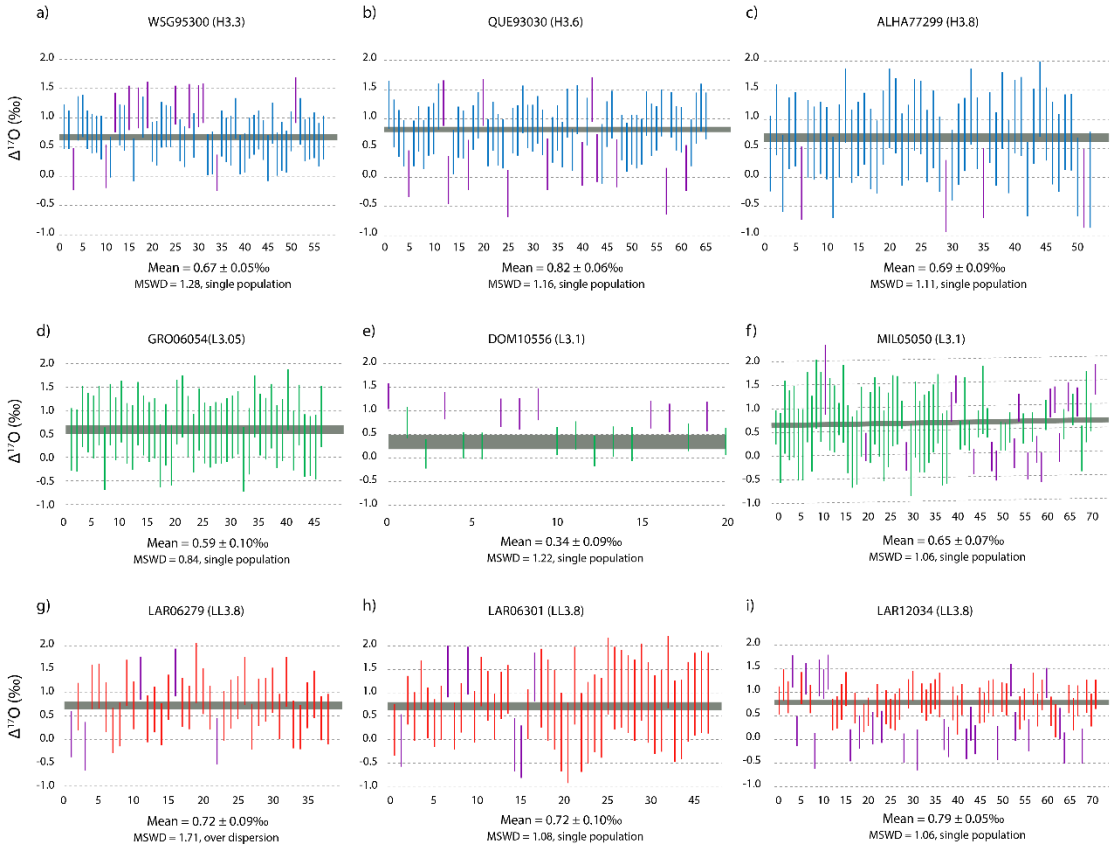

Figure 5.5. $\Delta^{17}O$ averaged chondrule olivine weighted mean assessment for H, L, and LL samples of this research. Value are sorted by spot name. Each bar represents the $\Delta^{17}O$ chondrule value with its associated external error ($\sigma_{95\%}$). Purple bars represent the rejected values to define OCs 'main chondrule population'. The grey band of each plot represents the value of the weighted mean considering the internal error of the pooled sample ($\sigma_{95\%}$).

Another result that needs to be argued when assessing the $\Delta^{17}O$ border values of the 'main chondrule population' is the weighted mean of DOM10556 (Table 5.5) which is lower and resolvable from the others. Specifically, the $\Delta^{17}O$ weighted mean and respective external errors of chondrules are 0.67 ± 0.07‰ for WSG95300, 0.82 ± 0.06‰ for QUE93030, 0.69 ± 0.13‰ for ALHA77299, 0.59 ± 0.13‰ for GRO06054, 0.34 ± 0.10‰ for DOM10556, 0.65 ± 0.11‰ for MIL05050, 0.72 ± 0.11‰ for LAR06279, 0.75 ± 0.16‰ for LAR06301, and 0.79 ± 0.06‰ for LAR12034.

It appears that the lack of chondrules with $\Delta^{17}O$ ratios between the two peaks of this sample causes the weighted mean to be defined around the sharpest mode ($\Delta^{17}O$ ~0.3‰) when the 'main chondrule population' of DOM10556 is evaluated. However, prior to this assessment, its weighted mean is 0.63 ± 0.07‰, the same within uncertainties as for the

other chondrites investigated here. Second, is important to repeat that this sample has poorer statistics based on the number of chondrules analyzed (n = 21). In addition, it was shown that the 'main chondrule population' of the chondrite samples were drawn from the same sample distribution (most of them with MSWD values within the acceptable envelope) suggesting that chondrules from DOM10556 belong to the same 'main chondrule population'. In this regard, based on the central limit theorem of statistics, if more chondrules were available to be measured in DOM10556 this problem would probably not have existed.

A logic step on the analysis is to compare the 'main chondrule population' per chondrite type H, L, and LL. In order to do this, three datasets are created merging $\Delta^{17}O$ ratios from averaged chondrule olivine data per chondrite type and the same standard routine described above was applied to them. Similar to the previous exploratory analysis, boxplot and whiskers diagrams and the empirical cumulative density function reveals that most data is distributed from ~0‰ to ~1.5‰ (Figure 5.6a and 5.6b). In more detail, the prospective 'main chondrule population' per OC type is graphically represented by the whiskers of each boxplot, and varies from -0.10‰ to 1.35‰ in H chondrites, -0.23‰ to 1.42‰ in L chondrites, and from -0.22‰ to 1.49‰ in LL chondrites.

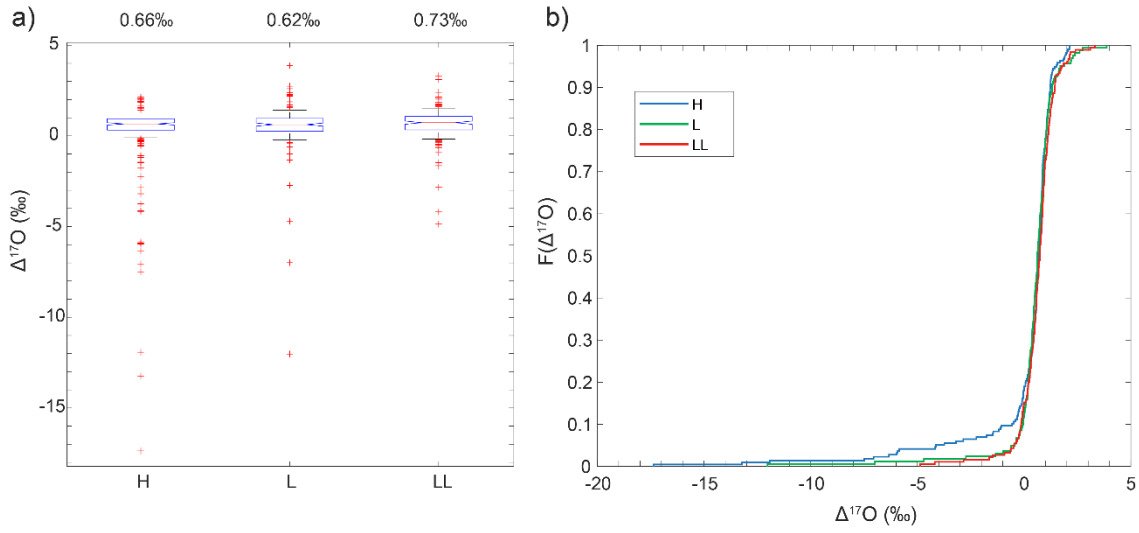

Figure 5.6. a) Whisker-boxplot diagrams of averaged chondrule olivine $\Delta^{17}O$ ratios per H, L, and LL chondrites. Whiskers are defined at the 95% confidence interval. The medians correspond to the red line within the boxplot and their values are displayed above the graph for chondrite type. Medians are statistically undistinguishable at the 95% confidence interval. b) Empirical cumulative distribution function of $\Delta^{17}O$ ratios from averaged chondrule olivine per chondrite type.

From figure 5.6a is also evident that the medians for chondrules from H, L, and LL chondrites are statistically the same at the 95% confidence interval and have $\Delta^{17}O$ values of 0.66‰, 0.62‰, and 0.73‰, respectively.

The sample distribution of H, L, and LL sub data sets are, as expected, practically the same when histograms and PDFs of $\Delta^{17}O$ values are displayed (Figure 5.7). However, PDFs of H, L, and LL data sets are smother than PDFs per chondrite since the size of the samples from which the PDFs were drawn are bigger in numbers with 172 observations for H chondrites, 140 for L, and 157 data points for LL chondrite type. Particularly, when the prospective 'main population' is pooled from each data set the similitude between the PDFs of chondrules from H, L, and LL chondrites is quite evident (Figures 5.7b, 5.7d, and 5.7f).

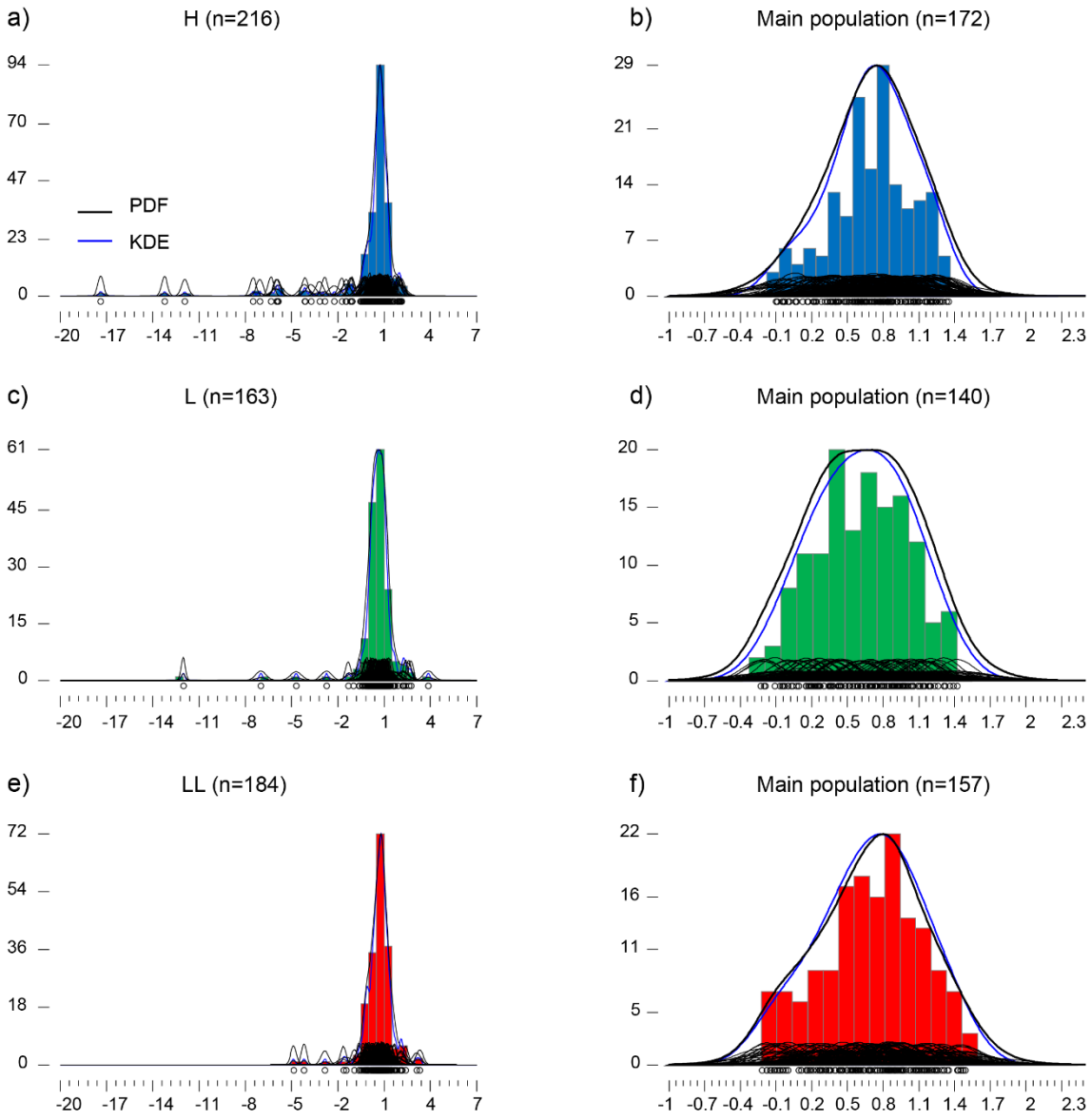

Figure 5.7. $\Delta^{17}O$ histograms of averaged chondrule olivine per H, L, and LL chondrites. a), c), and e) shows all data per chondrite type; b), d), and f) shows the prospective main population per chondrite type. Black line: PDF; blue line: KDE. The cloud of curves on the bottom of each plot are the normal distribution of each observation considering their external error ($\sigma_{95\%}$).

As previously done for the data per chondrite, the two-sample Kolmogorov-Smirnov test is also applied for the H, L, and LL averaged chondrule olivine sub datasets to evaluate if they come from the same sample distribution. The results of the test fail to reject for all combinations the hypothesis that chondrules from H, L, and LL chondrites have the same continuous distribution in terms of $\Delta^{17}O$ values.

Finally, when the 'main chondrule population' of H, L, and LL datasets is assessed at the 95% confidence interval by the weighted mean all MSWD values fall within the envelope

of acceptable values. Therefore, it is possible to conclude that they form a single chondrule population. Figure 5.8 shows this data treatment where blue, green, and red bars correspond to chondrules from H, L, and LL chondrites, respectively. Purple bars represent the values away from the weighted mean which have been rejected from the model to define the 'main chondrule population' of chondrite types.

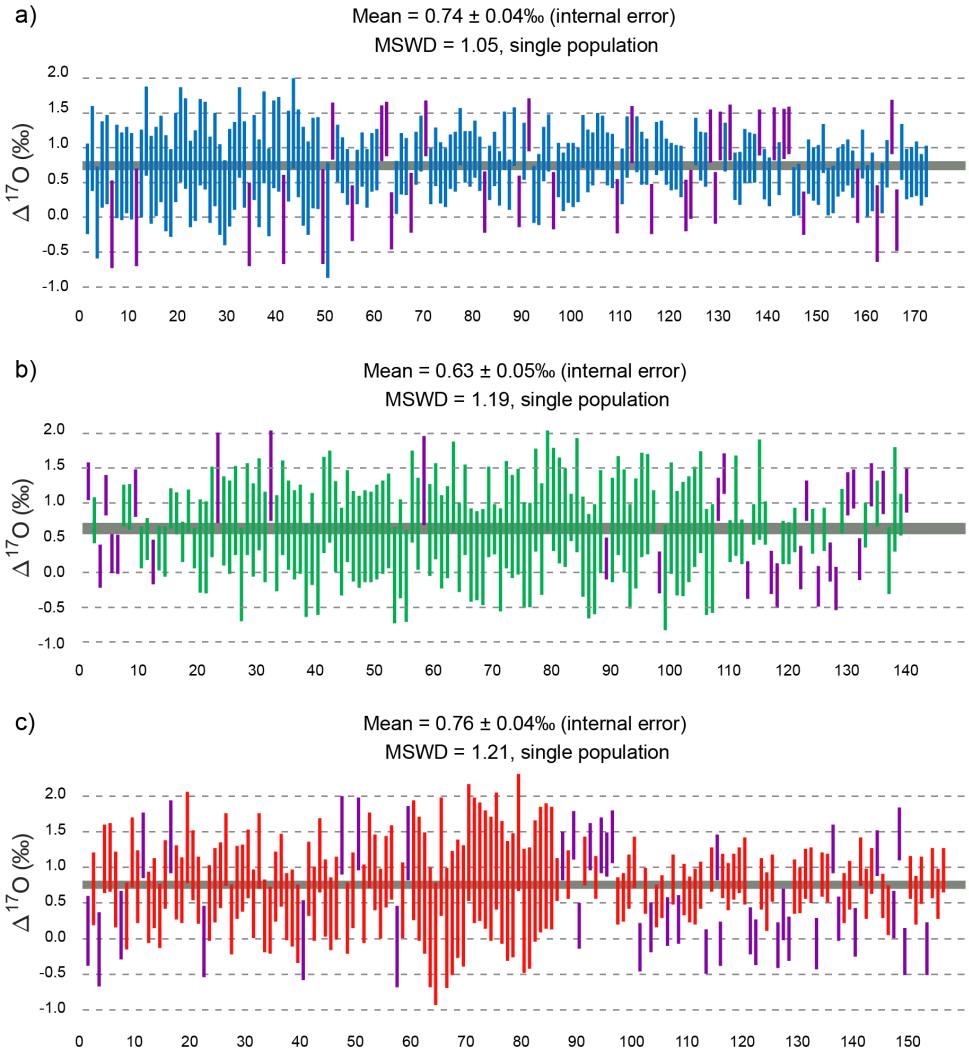

Figure 5.8. $\Delta^{17}O$ averaged chondrule olivine weighted mean assessment per H, L, and LL chondrite types. Each bar represents the $\Delta^{17}O$ chondrule value with its associated external error ($\sigma_{95\%}$). Purple bars represent the rejected values to define the 'main chondrule population' per chondrite type. The grey band of each plot represents the value of the weighted mean considering the internal error of the pooled sample ($\sigma_{95\%}$).

Table 5.6. Main averaged chondrule population $\Delta^{17}O$ ratios assessment per chondrite groups. MSWD values in green fall inside the range of acceptable values for one population ($\sigma_{95\%}$); no. is the size of the whole averaged chondrule olivine sample while no. outliers is the number of $\Delta^{17}O$ values that where not considered to calculate the limits of the main population.

Chondrite Group		Weighted mean	± External error$_{sample}$ (ts)	Standard deviation (ts)	no.	no. outliers	MSWD
H	$\Delta^{17}O$ (‰)	0.74	0.07	0.48	172	34	1.05
L	$\Delta^{17}O$ (‰)	0.63	0.09	0.62	140	28	1.19
LL	$\Delta^{17}O$ (‰)	0.76	0.10	0.56	157	39	1.21

The $\Delta^{17}O$ weighted mean and the external errors of the H, L, and LL pooled chondrules are 0.74 ± 0.07‰ for H, 0.63 ± 0.09‰ for L, and 0.76 ± 0.10‰ for LL chondrites, therefore statistically undistinguishable per chondrite group. The external errors were calculated summing in quadrature the internal error of the pooled unknown samples, the uncertainty of the laser fluorination measurements, and the average of the internal errors of pooled San Carlos olivine obtained during SHRIMP-SI sessions where the unknowns of H, L, and LL chondrites where analyzed, respectively. Table 5.6 shows the values that define the main chondrule population per chondrite group at the 95% significance interval ($\sigma_{95\%}$).

Table 5.7 shows the same values as in table 5.6 but taking into consideration the prospective 'main population' previous to border assessment. From it, it can be noted that the boundary rejections do not bias the means, which are the same within uncertainties, and only affects the tails of the distribution as can be distinguished from their 2SD ($\sigma_{95\%}$) which are ~0.2‰ larger.

Table 5.7. Main chondrule population $\Delta^{17}O$ ratios before assessment per chondrite groups. MSWD values in red fall outside the range of acceptable values for one population ($\sigma_{95\%}$); no. is the size of the whole averaged chondrule olivine sample.

Chondrite Group		Weighted mean	± External error$_{sample}$ (ts)	Standard deviation (ts)	no.	no. outliers	MSWD
H	$\Delta^{17}O$ (‰)	0.72	0.07	0.68	172	0	2.38
L	$\Delta^{17}O$ (‰)	0.61	0.09	0.77	140	0	3.83
LL	$\Delta^{17}O$ (‰)	0.68	0.09	0.83	157	0	3.97

Therefore, taking into consideration the exploratory analysis and the systematic statistical assessment applied to the data, it has been statistically proven for the first time that OCs accreted the same main population of chondrules in terms of oxygen isotopes ($\Delta^{17}O$), in agreement with the assertion by Clayton et al. (1991). However, as argued in the next section, less frequent subpopulations of chondrules were also sampled by OCs which yield insights into the oxygen isotope reservoirs of the inner solar system neighborhood.

Nevertheless, in order to better constrain this chondrule population, and consequently, the dominant oxygen isotope gas reservoir or region to which chondrules from OCs exchanged within the protoplanetary disk during their formation, the data of each sample were merged into one database containing all $\Delta^{17}O$ values. This allows us to exploit the sample size on behalf of finer statistics for the chondrule population. The new dataset accounts for n=563 observations and its sample distribution can be observed in figure 5.9a. It is worth mentioning that this data merging could have been done earlier in the discussion after it was proven by the two-sample Smirnov-Kolmogorov test that chondrule oxygen isotope compositions from each OC studied in this research come from the same continuous sample distribution. However, it was preferred to do it step by step, sample by sample, to emphasize the methodology.

The same standard routine described above was applied to the merged averaged chondrule olivine data in order to detect statistical outliers at the 95% confidence interval and, consequently, delimiting as a first approximation the $\Delta^{17}O$ boundaries of the main chondrule population without making any assumptions on the sample distribution. This process provides a new pooled dataset having a sample size of n= 474 which ranges from $\Delta^{17}O$ -0.23‰ to 1.56‰. Figure 5.9b shows the sample distribution of the prospect main chondrule population which is remarkably bell-shaped.

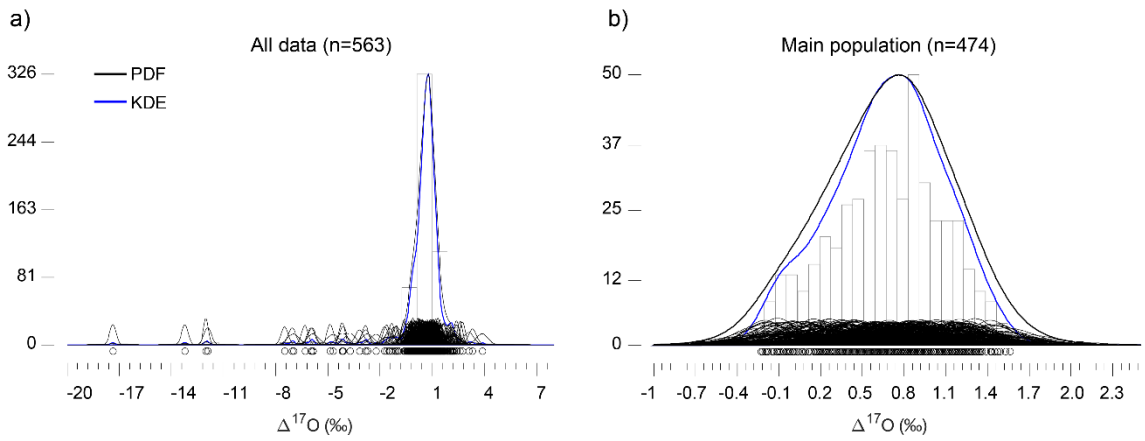

Figure 5.9. $\Delta^{17}O$ chondrule olivine histograms of all averaged olivine from H, L, and LL chondrites together. a) All data are shown; b) main population prostpect. Black line: PDF; blue line: KDE. The cloud of curves on the bottom of each plot are the normal distribution of each observation considering their external error ($\sigma_{95\%}$).

The pooled main chondrule population mean is then estimated via the weighted mean at the 95% confidence interval which can be visualized in figure 5.10a.

After the rejection of statistical outliers, the MSWD statistic is 1.08, within the acceptable envelope, allowing us to infer that the sample was drawn from a single population (Figure 5.10a). Therefore, the definitive pooled main chondrule population from OCs accounts for 360 chondrules and is characterized by a $\Delta^{17}O$ weighted mean of 0.74 ± 0.08‰ (external error, $\sigma_{95\%}$) with a variability of 0.53‰ (2SD, $\sigma_{95\%}$; figure 5.10b). The external error of the sample was calculated summing in quadrature the internal error of the unknown pooled sample (±0.02‰), the uncertainty of the laser fluorination (±0.002‰), and the average internal error of San Carlos olivine (±0.08‰) calculated from the eleven SHRIMP-SI sessions (Table 4.3).

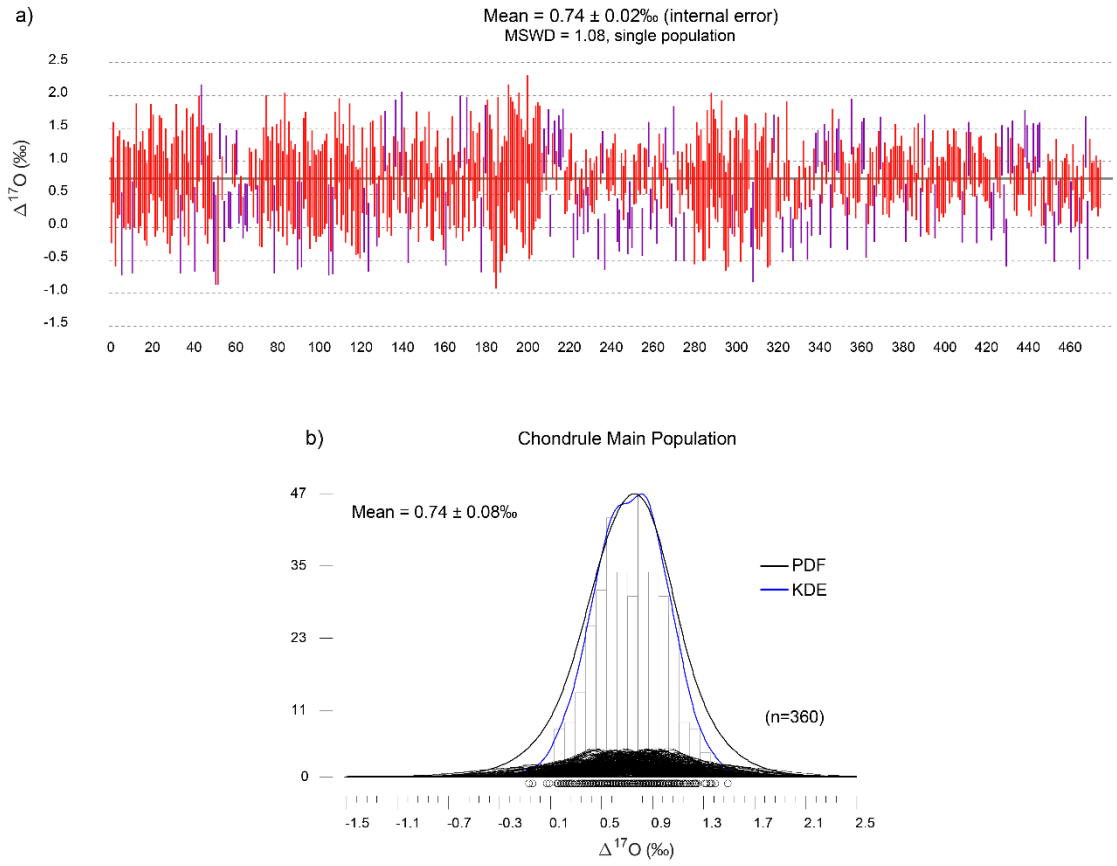

Figure 5.10. a) $\Delta^{17}O$ averaged chondrule olivine weighted mean assessment all samples together. Each bar represents the $\Delta^{17}O$ chondrule value with its associated external error ($\sigma_{95\%}$). Red bars are used to calculate the mean. Purple bars represent the rejected values to define OCs 'main chondrule population'. The grey band of each plot represents the value of the weighted mean considering the internal error of the pooled sample ($\sigma_{95\%}$). b) Definitive chondrule main population.

It is stated then that OCs accreted a majority of chondrules that exchanged with a gas reservoir dominated by an oxygen isotope composition of $\Delta^{17}O$ ~0.7‰. Another line of evidence that supports this interpretation is the oxygen isotope ratios of barred olivine (BO) chondrules since they are thought to represent the composition of the ambient nebular gas with which they exchanged (e.g. Schrader et al., 2014 and references therein) because of almost complete melting of their precursors (e.g. Hewins et al., 2005; Jones, 2012). In this regard, the range of $\Delta^{17}O$ ratios of olivine from clear BO chondrules studied here covers a range from ~-0.6‰ to ~3.2‰ and the average is $\Delta^{17}O$ = 0.73 ± 0.21‰ (n=20) is the same as previously defined for the main population.

Figure 5.11 allows us to visualize all chondrule olivine $\Delta^{17}O$ values of this study. The grey band represents the variability of the population and the black band the mean and its external error, both at the 95% confidence interval. From this figure it is quite evident that H, L, and LL chondrite chondrules interacted with quite a discrete oxygen isotope reservoir. On this subject, if the $\Delta^{17}O$ main chondrule population defined here is compared to the average $\Delta^{17}O$ ratio calculated from chondrule within type 3 to type 4 OCs reported by Clayton et al. (1991), which is approximately 1.0‰, it is apparent that the shift towards higher oxygen isotope ratios of their bulk chondrule compositions could be related to secondary processes occurred in their parent bodies, for instance aqueous alteration affecting chondrule glasses in the case of highly unequilibrated type 3 samples (Kita et al., 2010; Bridges & Ireland, 2015), thermal metamorphism for type 4 samples, and/or possible contamination from matrix portions that were not removed before analysis. The latter is proposed since average SIMS oxygen isotope compositions of chondrules from UOCs reported by Kita et al., (2010) are statistically the same as the results presented here.

The consequences of having such a range of $\Delta^{17}O$ chondrule composition in OCs is relevant considering the predictive power of such a sample distribution. A brief example, if Pb-Pb dates are accurate and some OC chondrules are as old as refractory inclusions (Connelly et al., 2012; Bollard et al., 2017) then knowing the oxygen isotopic ratios of those chondrules would give a time frame to understand the different oxygen isotopic gas reservoirs of the protoplanetary disk at its earliest stage.

From the results presented here and the literature it is highly probable that those chondrules would have had $\Delta^{17}O$ ratios within the range of the main population defined here or at least between ~-2.0‰ to ~3.0‰, which would imply that ^{16}O-rich and ^{16}O-poor distinct oxygen isotope reservoirs existed at the same time but where spatially separated at the earliest stage of the solar nebula. These spatially separated reservoirs have already been suggested considering refractory inclusions but not {Citation}chondrules to the best of our knowledge (e,g. Krot et al., 2010; Aléon, 2016; Kööp et al., 2016; Simon et al., 2016).

Moreover, Bollard et al. (2017) reported the oldest ages associated to type II chondrules, being as old as 4567.61 ± 0.54 My which considering the most precise age of the solar system 4.567.30 ± 0.16 My (Connelly et al., 2012) means that, given uncertainties, type II chondrules could have started forming ~70,000 years after refractory inclusions. This would constitute a very short time to achieve the necessary conditions to oxidize iron Fe^0 to Fe^{2+} for posterior incorporation in olivine according to current models (e.g. Grossman et al., 2008, 2012). More implications about the main chondrule population and its statistical 'outliers' will be portrayed and discussed in the following sections.

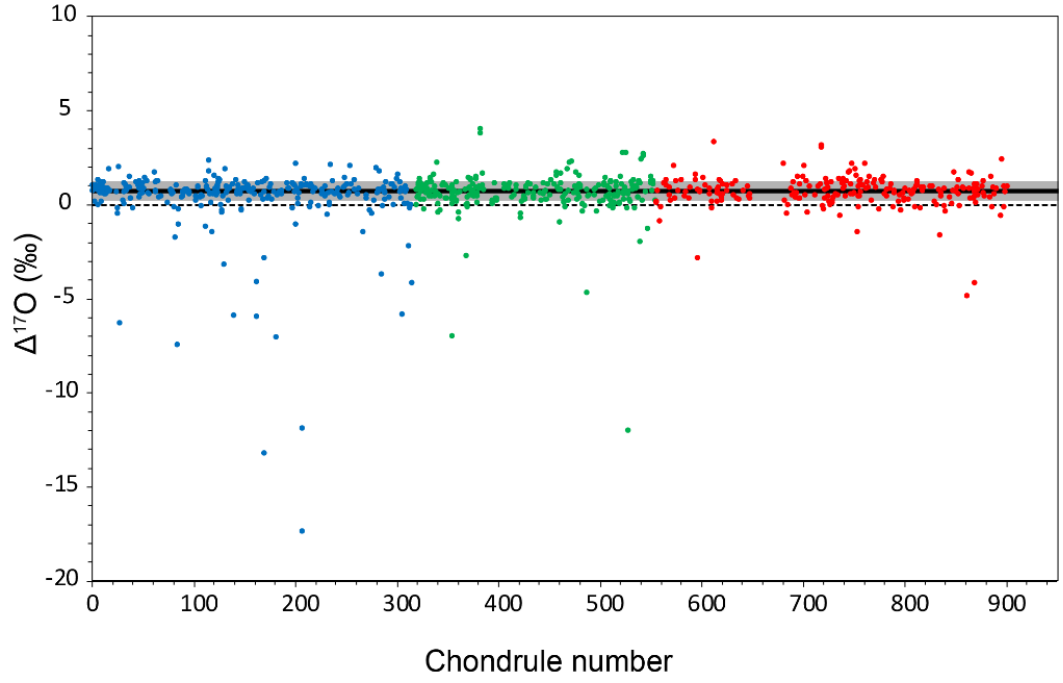

Figure 5.11. Plot of $\Delta^{17}O$ values for all measured chondrule olivine. Data is organized by chondrule number. The $\Delta^{17}O$ mean of the main population is shown as a black bar ($\sigma_{95\%}$). Grey rectangle represent the variability of the population (2SD, $\sigma_{95\%}$) and dashed line is Earth's $\Delta^{17}O$ reservoir. Individual errors are omitted for clarity. The gap in LL samples are olivines from chondrules that were not measured for oxygen isotopes.

5.5. 'Statistical outliers': insights into inner solar system spatially separated oxygen isotope gaseous reservoirs

It was demonstrated in section 5.4 that OCs accreted one main chondrule population in terms of oxygen isotope composition. Focusing on the most common occurrence of chondrule composition allows making strong inferences and conclusions considering the numbers, emphasizing the general picture. However, as briefly mentioned above, variability towards higher and lower $\Delta^{17}O$ compositions of chondrules is observed, despite the fact that is less frequent. The values away from the main chondrule population have been classified as statistical outliers but this is somehow misleading. Such 'statistical outliers' provide the details associated with the context of the main population.

On one hand, OC chondrules and their frequency of occurrence (probability) could be representing that chondrules and/or chondrule precursors with lower probabilities were formed in more distant oxygen isotope reservoirs with different characteristics compared to the main chondrule population's reservoir and/or in the same region but under completely different conditions. On the other hand, chondrules with compositions closer to the main chondrule population (relatively higher probability) could be reflecting chondrule formation in either closer reservoirs and/or showing slight variations of the main chondrule population reservoir towards heavier (^{16}O-poorer) or lighter (^{16}O-richer) compositions.

For example, when evaluating all averaged chondrule olivine data set, the probability of having oxygen isotope ratios lower than $\Delta^{17}O$ -2.0‰, which are oxygen isotope ratios commonly observed in chondrules accreted by carbonaceous chondrite asteroids, is less than 10% which on the contrary means that close to 90% of the data is above this value. In the same line, the probability of having a chondrule with $\Delta^{17}O$ ratios between -2.0‰ and 3.0‰ is close to 93%. Finally, the probability of finding chondrules with values above 3.0‰ is about 6%.

It is worth mentioning that, when no more spots were measured, the data treatment has considered single olivine spots per chondrule as representative of the whole chondrule and that, although small in numbers, some of these olivines have signatures considered to be relicts representing other reservoirs of the protoplanetary disk (e.g. Kita et al., 2010),

if these possible relict grains are not taken into consideration in the statistical analysis, the probabilities of finding chondrules with the oxygen isotope composition of the main chondrule population in OCs would be even higher.

Nevertheless, the important question now is what is controlling the oxygen isotope composition of the different reservoirs. In this regard, since chondrules are thought to have formed in dust enriched regions of the protoplanetary disk (dust/gas ratios 50 to 10^6 times solar; e.g. Alexander et al., 2008; Grossman et al., 2008; Kita et al., 2010; Fedkin & Grossman, 2013; Tenner et al., 2015) the oxygen isotope reservoir of the ambient gas where chondrules were formed should be considered a mixture of gases which composition is controlled by the major oxygen carrier gas species: carbon monoxide (CO), vaporized dust (SiO), and vaporized water (H_2O), respectively (Clayton, 1993; Marrocchi & Chaussidon, 2015; Javoy et al., 2012; Di Rocco & Pack, 2015; Nagahara & Ozawa, 2012).

Therefore, the oxygen isotope reservoir under which chondrules of the main chondrule population was formed represents the right mixture of these gas species (to achieve $\Delta^{17}O$ ~0.7‰) and, assuming that the photochemical and self-shielding model is correct, deviations towards heavier and lighter compositions could be representing higher partial pressures of H_2O (^{16}O-poor) and CO (^{16}O-rich) species, respectively. This view is formed on the basis that the initial refractory dust in the solar nebula, having oxygen isotope compositions close to solar ($\Delta^{17}O$~ -24‰, e.g. Alexander et al., 2017), would have previously reacted with $^{17,18}O$-rich nebula water to achieve compositions close to a planetary reservoir (Ireland, 2012). Further, this new dust, in terms of oxygen isotope composition, or chondrule precursors present in local disk regions where chondrule formation occurs, would have an average oxygen isotope composition similar to the oxygen isotope composition of the ambient gas, as has been interpreted by some authors (e.g Chaumard et al., 2018; Kita et al., 2016; Tenner et al., 2017). This view provides an overall explanation on how oxygen isotope reservoirs can change. However, this paradigm will be explored further in section 5.9.

Having the above in mind, e.g. increasing the partial pressures of $C^{16}O$ would bring the reservoir towards lighter oxygen isotope compositions and the opposite would occur when adding $^{17, 18}O$-rich vapour water to the system, then it is reasonable to think that the

redox conditions would also change according to the change of the dominant gas species on the chondrule formation region. Therefore, chondrules from this research with lighter and heavier oxygen isotope compositions compared to the main chondrule population could have formed under more reducing and more oxidizing conditions, respectively.

In particular, it can be observed from figure 5.9b that previous to the definition of the main chondrule population boundaries the prospective population possess a left tail which is longer than the right one, consistent with the skewness of -0.2 of the sample and from the KDE on the same figure, which shows a small subpopulation around $\Delta^{17}O$ ~0‰. At the same time, even though a specific subpopulation is not as clear as the left tail, the right tail chondrules with heavier oxygen isotope compositions also exists. These left and right tail chondrules are rejected as statistical outliers of the main population which can be observed in figure 5.10a as lower and upper purple bars, respectively.

In order to highlight 'statistical outliers' and investigate these possible subpopulations of chondrules, a new dataset comprising only statistical outliers of the main chondrule population was compiled. This dataset can be observed in figure 5.12 where PDF and KDE are portrayed. From this figure, which shows all the statistical outliers, the previously mentioned left and right tails show a clear cut close to $\Delta^{17}O$ ~0‰.

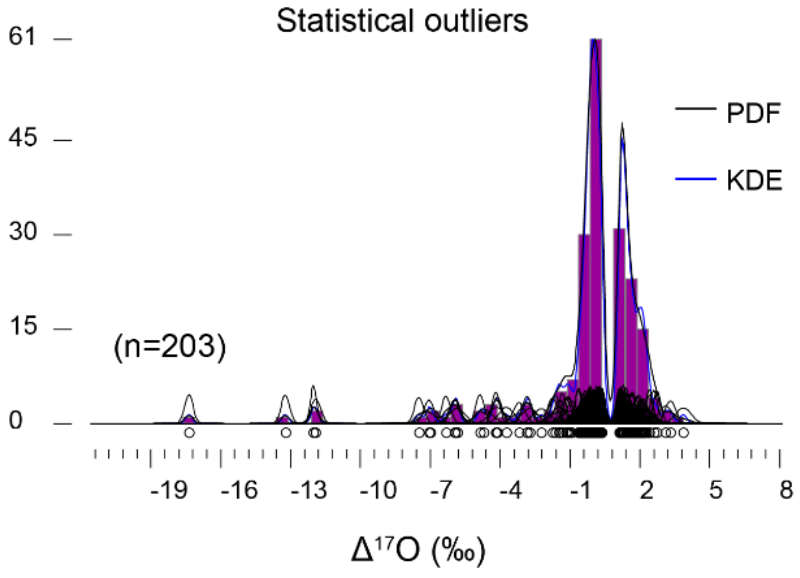

Figure 5.12. $\Delta^{17}O$ chondrule distribution of the statistical outliers of the main chondrule population. Black line: PDF; blue line: KDE. The cloud of curves on the bottom of each plot are the normal distribution of each observation considering their external error ($\sigma_{95\%}$).

In detail, the right tail varies from $\Delta^{17}O$ 1.11‰ to 3.87‰ although its distribution is mainly covering from 1.11‰ to 2.40‰ ($\sigma_{95\%}$), with a median of 1.46‰. On the other hand, the left tail ranges from -17.37‰ to 0.37‰, and the densest part of its distribution is between -1.65‰ to 0.37‰ ($\sigma_{95\%}$) with a median of -0.14‰. Figure 5.13 displays the left tail, the main chondrule population, and the right tail, from left to right, as box and whisker plots. The whiskers of each subsample were set at the 95% confidence interval and the medians are shown above the plot. Interestingly, the medians (red horizontal lines) are statistically different (at $\sigma_{95\%}$). Therefore, considering the analysis performed to define the main chondrule population of OCs, where the medians of each chondrite sample were consistently close to the final weighted mean, it is likely that the medians of the left and right tail subsamples represent the $\Delta^{17}O$ ratios of the subpopulations of chondrules accreted by OCs parent bodies, or at least a close value.

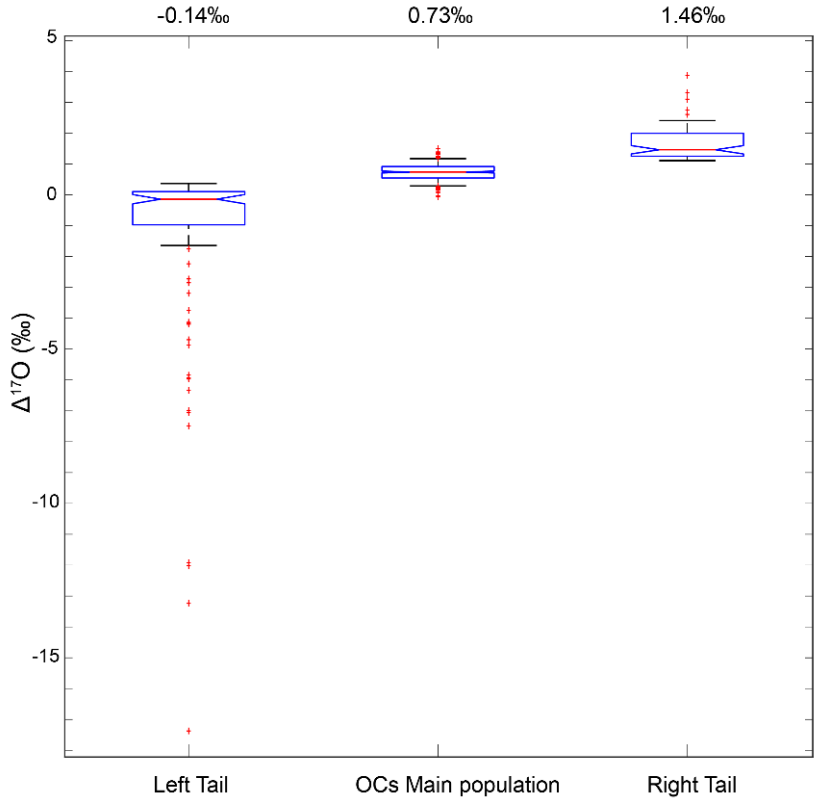

Figure 5.13. Whisker-boxplot diagrams of averaged chondrule olivine $\Delta^{17}O$ ratios of subsamples. Whiskers are defined at the 95% confidence interval. The medians correspond to the red line within the boxplot and their values are displayed above the graph for each subsample. Medians are statistically different at the 95% confidence interval.

In this regard, the value of the median of the left tail subsample is slightly lower than Earth-Moon and chondrules from enstatite chondrites oxygen isotope compositions since enstatite chondrites appear to have accreted a main chondrule population at $\Delta^{17}O$ ~0‰ (Clayton et al., 1984; Weisberg et al., 2011; Weisberg & Kimura, 2012). It is possible then that chondrule forming regions, ergo oxygen isotope gaseous reservoirs, of chondrules from OCs and enstatite chondrites were close to each other. If this is the case, the subpopulation of chondrules from OCs with oxygen signatures similar to chondrules from enstatite chondrites could be indicating the transition between these regions, with the enstatite chondrule formation region having an ambient gas mixture richer in CO, relative to OCs reservoir, and therefore, with lower oxygen fugacity.

On the other hand, if the $^{17,18}O$-richer median of the right tail statistical outliers ($\Delta^{17}O$ 1.46‰) is representing another subpopulation of chondrules accreted by OCs, the ambient gas of such a population would have an oxygen isotope reservoir defined by a mixture of the main oxygen carriers of the solar system with a higher presence of H_2O (^{16}O-poor), compare to OCs chondrule reservoir. In this regard, even though chondrules from Rumuruti chondrites have oxygen isotope compositions which are similar to the main chondrule population found within OCs (Greenwood et al., 2000; Miller et al., 2017; Kita et al., 2017), it might be possible that the right tail statistical outliers defined here represents chondrules from the chondrule formation region of Rumuruti chondrules. This option is quite interesting considering that Rumuruti chondrites are chemically related to OCs but whole-rock oxygen isotopes are higher, $\Delta^{17}O$ ~2.72‰ (Bischoff et al., 2011).

To test this hypotheses and investigate enstatite and Rumuruti chondrite chondrules but also carbonaceous chondrite chondrules at the population level, SHRIMP-SI measurements, and the same statistical assessment will be done in the near future in samples from other chondrite classes.

Following up, the same reasoning used above to propose possible subpopulations of chondrules and their oxygen isotope reservoir characteristics, can be invoked to understand the forming regions of chondrules and/or relict grains with lower probabilities in OCs which are relatively ^{16}O-richer ($< \Delta^{17}O = -2.0‰$).

In this regard, chondrules from carbonaceous chondrites appear to show clear populations with modes around $\Delta^{17}O$ ratios of -2.5‰ and -5.0‰ (Kita et al., 2017 and references therein). Therefore, the gaseous reservoir of their chondrule formation region was a mixture of oxygen-bearing species with higher partial pressures of ^{16}O-enriched CO, consequently having lighter oxygen isotope compositions.

The extreme member of this rationale are refractory inclusions which are thought to have been processed close to the Sun at high ambient temperatures (>1400K) under extremely reducing conditions (log fO2 < IW-6; Grossman et al., 2008), thus higher pressure of $C^{16}O$, in a gas of solar composition possibly during the first ~300,000 years of the solar system formation (Krot et al., 2017), although see Ushikubo et al. (2017). Therefore, refractory inclusions have, in general, ^{16}O-rich compositions ($\Delta^{17}O$ ~ -24‰) close to the solar reservoir ($\Delta^{17}O$ ~ -28‰; McKeegan et al., 2011), although ^{16}O-poor compositions close to the planetary reservoir have been observed (Krot et al., 2010; MacPherson, 2014; Aléon, 2016; Kööp et al., 2016; Simon et al., 2016).

Overall, having in mind the photochemical and self-shielding model, it appears that the most ^{16}O-rich signatures of the meteoritical record are associated with higher partial pressures of ^{16}O-enriched CO molecules compared to SiO and H_2O, but also to the physicochemical conditions, e.g. higher temperatures and lower oxygen fugacity of the ambient gas, and therefore the location where the thermal process occurs. If this is true, chondrules studied here (and chondrules in general) with the heaviest oxygen isotope compositions (up to $\Delta^{17}O$ ~3.9‰ in this research) were formed in cooler and more oxidising environments at further distances from the nascent Sun, under higher partial pressures of $^{17,18}O$-rich H_2O molecules, possibly closer to the snow line (water ice evaporation front) which, as discussed by Doyle et al. (2015), is thought to have been at 2−3 AU when the disk was just 2−4 My old (Ciesla & Cuzzi, 2006), close to the actual location of the main asteroid belt. In such a region, the proportion of water vapor is expected to be higher (Yurimoto et al., 2006) due to the inwardly drifting water-ice-rich material of the outer solar system, therefore increasing its local partial pressure.

Since refractory inclusions and chondrules are thought to have formed in local regions of the protoplanetary disk, the picture about oxygen isotope reservoirs introduced by this investigation is absolutely consistent with the localized formation of these astrophysical

objects, since it allows them to form under different conditions which are dependent on the thermal structure of the solar nebula.

The implications of such a concept are significant not only to understand the physicochemical conditions of the ambient gas where chondrule formation occurred but the dynamics affecting dust in the protoplanetary disk. In this regard, when dynamical models about radial and vertical migration and mixing of solids in the gaseous protoplanetary disk of the protosun are taken into consideration (e.g. Ciesla, 2008; Salmeron & Ireland, 2012; Jacquet, 2014b; Testi et al., 2014; Miyazaki & Korenaga, 2017), a more complete vision of the astrophysical context under which chondrules and planets are formed emerges.

In this regard, having such a sample distribution of chondrule oxygen isotope compositions in OCs (Figure 5.10a) perhaps means that if mixing of solids (chondrules and/or chondrule precursors) took place in the vicinities of the chondrule formation region of OCs this dust migration was probably governed by processes able to cause mixing at local scales which would be consistent with having most of chondrule olivine with $\Delta^{17}O$ ratios between -2.0‰ to 3.0‰ and a major chondrule population.

In addition, chondrule ages from OCs are in a few cases as old as refractory inclusions (Bollard et al., 2017), but mainly about ~1 to ~3 My younger (Krot et al., 2009; Villeneuve et al., 2009; Kita & Ushikubo, 2012; Kita et al., 2013; Ushikubo et al., 2013). Then, as briefly mentioned before, the oxygen isotope gas reservoir where they were thermally processed would have had to be present at least within ~70,000 years after refractory inclusions, considering uncertainties of the younger chondrule in Bollard et al. (2017) and the age of the solar system of Connelly et al. (2012), and lasted up to ~3 My after refractory inclusions since accretion of OCs is thought to have happened between ~2 to ~3 My after first solids formation (e.g. Doyle et al., 2015, 2016; Desch et al., 2017 and references therein). Therefore, OCs chondrules older than the accretion age of their parent bodies would have had to be somehow 'wandering' for a few million years in the protoplanetary disk before accretion occurred since chondrules with different ages have been found in OCs (Villeneuve et al., 2009; Kita et al., 2013; Bollard et al., 2017; Desch et al., 2017 and references therein).

Moreover, as mentioned before, carbonaceous chondrites contain mainly two population of chondrules characterised by oxygen isotopes signatures of $\Delta^{17}O$ -2.5‰ and -5.0‰, which based on the above rationale, perhaps were formed closer to the Sun relative to chondrules from OCs, in order to have lighter oxygen isotope compositions or earlier in time when the mixture of gases in the inner solar system due to the infalling molecular cloud was still not homogeneous and ^{16}O-richer, as it has been suggested (e.g. Ruzicka, 2012).

In this regard, it has been shown that several chondrules from OCs have ages which overlap with the ages of chondrules from carbonaceous chondrites (Krot et al., 2009; Ushikubo et al., 2013; Kita & Ushikubo, 2012). Also, it appears that a few chondrules from both ordinary and carbonaceous chondrites have ages as old as refractory inclusions (Bollard et al., 2017). Additionally, some refractory inclusions, particularly associated with the melilite phase among them, show oxygen isotope compositions thought to have been acquired in the solar nebula, with $\Delta^{17}O$ ratios close to terrestrial values (planetary reservoir; (Krot et al., 2010; MacPherson, 2014; Simon et al., 2016; Aléon, 2016).

The above imply that ^{16}O-rich reservoirs (solar) and ^{16}O-poor reservoirs (planetary) coexisted from the earliest stages of the solar nebula up to 2-3 My after first solids formation, as proposed by Ushikubo et al. (2017) who reported a ^{16}O-rich anorthite in one refractory inclusion having that range of ages (2-3 My). Consequently, chondrules from carbonaceous chondrites coeval with chondrules from OCs could have been formed relatively closer to the protosun than OCs chondrules.

Given the above, if enstatite chondrites and OCs accreted closer to the Sun than carbonaceous chondrites, as it is usually accepted (e.g. Morbidelli et al., 2012), then carbonaceous chondrite chondrules, as well as refractory inclusions, travelled longer distances to finally be captured in their accretion location suggesting that, in order to reach those orbital distances, their migration was the result of a more energetic mechanism(s), possible X- or disc- winds (Shu et al., 1996; Salmeron and Ireland, 2012).

The connotations of such an idea are relevant and in conflict to the current knowledge about the basic chondrule and chondrite properties. Specifically, the chemical and nucleosynthetic isotopic complementarity between chondrules and the matrix (Hezel &

Palme, 2007; Budde et al., 2016a; Budde et al., 2016b) and references therein), which suggests that they cannot have been spatially separated to a large degree and derive from a common reservoir of dust. Nucleosynthetic 'anomalies' (e.g. ε^{54}Cr, ε^{50}Ti, ε^{62}Ni, $\varepsilon^{182, 183}$W, ε^{100}Ru and $\varepsilon^{92, 94, 95, 97}$Mo) have been suggested to reveal a fundamental dichotomy in the origin of meteorites (chondrites, achondrites, irons, etc), classifying them as carbonaceous and non-carbonaceous (Warren, 2011). In this regard, some authors have attributed this dichotomy to formation in two spatially separated locations of the solar nebula, possibly by proto-Jupiter formation (e.g. Gerber et al., 2017; Scott et al. , 2018).

In this regard, from the literature, the nucleosynthetic complementarity, ergo genetic link between chondrules and matrix from carbonaceous chondrites, is clearer when considering siderophile elements (e.g. Olsen et al., 2016; Budde et al., 2016a). On one hand, Budde et al. (2016b) suggest that chondrules from CV chondrites are depleted in the presolar carrier enriched in s-process Mo and the matrix, enriched. They associated this carrier to a metal phase and suggested that the isotope variations of Mo and W, are linked with this carrier. On the other hand, Olsen et al. (2016) noted that overall the Cr isotopic composition of chondrules from CV and CR chondrites do not support a genetic link among chondrules and matrix within individual chondrite groups.

Therefore, in the picture of this research, the formation of chondrules from carbonaceous chondrites in a different environment to their accretion location and chondrule-matrix complementarity still holds when considering nucleosynthetic isotope siderophile elements which are more abundant in the matrix relative to chondrules.

These different lines of evidence contributes to strengthening the interpretation that oxygen isotope gaseous reservoirs of the protoplanetary disk coexisted and were spatially separated, possibly reflecting a radial (heliocentric) gradient characterized by the availability of the main oxygen carrier species (CO, H_2O, and SiO), and by inference temperature, on the different forming regions of refractory inclusions and chondrules.

5.6. ^{16}O-rich chondrule olivine: low mixing of dust from distinct oxygen reservoirs

This section treats in detail the possible relict nature of several chondrule olivines with distinct oxygen isotope compositions (^{16}O-rich) compared to the main chondrule population of OCs. Even though the probability of finding chondrules with oxygen isotope compositions lower than $\Delta^{17}O = -2.0‰$ is less than 10%, based on the results of this research, their presence is relevant to understand the variability of chondrule precursors present in the OCs chondrule-forming region and their association to distinctively different oxygen isotope reservoirs, commonly associated to other chondrite groups.

WSG95300

CH027 chondrule (Type I) appears to be a compound chondrule with a POP texture displaying olivine grains poikilitically enclosed by pyroxene and a couple of Fe,Ni-metal blebs. The analysed olivine is particularly big (~90x90µm) compare to other minerals, shows a resorption texture, a forsteritic composition (~Fa0), and a carbonaceous chondrule-like oxygen isotope ratio plotting between the Y&R and PCM lines ($\Delta^{17}O$ -6.3 ± 0.4‰; figure 5.14a; e.g. Tenner et al., 2017). The petrographic, chemical and isotopic composition suggests that spot 1 olivine is a relict olivine that did not melt during CH027 formation. However, this cannot be guaranteed since no more measurements were performed in this chondrule.

One grain was analyzed from CH084 (Type I) chondrule which presents a PO texture and one metal grain inclusion (Figure 5.14b). The olivine grain has an Mg-rich composition (~Fa0) and a $\Delta^{17}O$ composition of -7.5 ± 0.4‰ plotting between the Y&R and PCM lines ($\delta^{18}O$ of -11.4 ± 0.6‰, $\delta^{17}O$ of -13.5 ± 0.4‰). Despite the fact that a relict origin is not straightforward based on petrography and because no more oxygen analysis were obtained from other mineral grains it is clear that this olivine/chondrule acquired its isotopic signature in another reservoir of the protoplanetary disk, similar to some chondrules of the carbonaceous chondrite chondrule forming region (e.g. Chaumard et al., 2018).

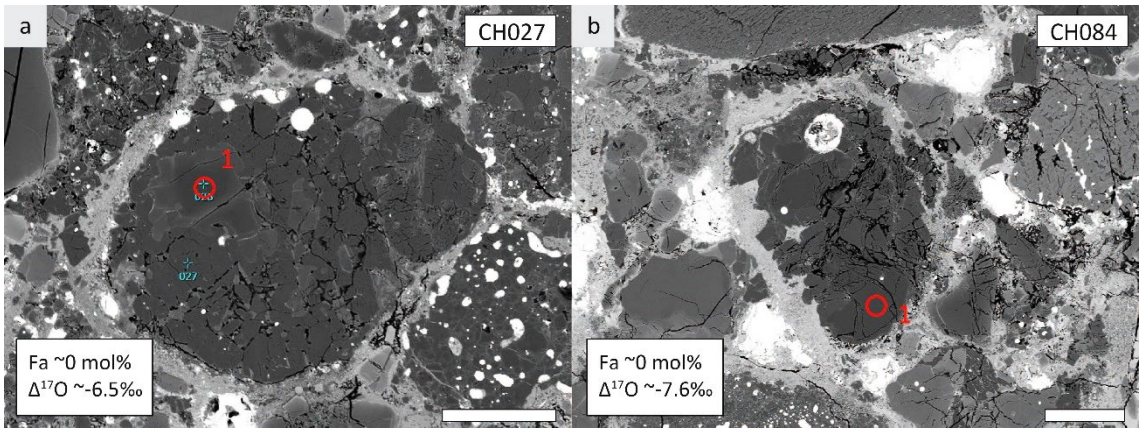

Figure 5.14. ^{16}O-rich chondrule olivines relative to the major trend in WSG95300. Scale bars are 100 µm.

QUE93030

Only one olivine grain (~150 x 100 µm2) was measured in chondrule CH130 which consists of a Type I olivine (Fa ~1mol%) core surrounded by a small fine-grained rim of Ca-poor pyroxene ± olivine and FeNi ± troilite. The olivine shows a complex zoning or sector growth profile (Figure 5.15a). The oxygen isotope data plot between the Y&R and PCM lines showing a $\Delta^{17}O$ of -3.2 ±0.5‰, similar to chondrules from carbonaceous chondrite chondrules (Figure 4.18c) (e.g. Ushikubo et al., 2012; Tenner et al., 2015).

Data from CH139 correspond to one measurement of a small and compact area of olivines from a PO chondrule with a Type I olivine composition of Fa ~5mol% (Figure 5.15b). The oxygen isotope data of this grain plots on the Y&R line with $\delta^{18}O$ and $\delta^{17}O$ ratios of -10.2 ±0.6‰ and -11.2 ±0.6‰, respectively ($\Delta^{17}O$ of -5.9 ±0.4‰, figure 4.18c) similar to oxygen isotope compositions of some carbonaceous chondrite chondrules (Chaumard et al., 2018 and references therein).

Two grains were analyzed from CH162 chondrule which presents a PP/POP texture (Figure 5.15c). Both olivines show Mg-rich cores, spot 1 and spot 2 being Fa ~7mol% and Fa ~5mol% (Type I), and with $\Delta^{17}O$ values of ~-6.0 ‰ and ~-4.1 ‰, respectively, similar to carbonaceous chondrite chondrules compositions (Kita et al., 2017 and references therein) and resolvable within uncertainties (±0.4‰) which talks about the heterogeneity of precursors for this chondrule. Considering, the FeO content, grain size,

and overgrowths of olivines plus the higher modal abundance of Ca-poor pyroxene on this chondrule, suggests that these ^{16}O-rich grains are relicts that did not melt during the last chondrule formation event.

CH169 consists of a POP chondrule with poikilitic olivine (figure 24d). Three data points were obtained in this chondrule. Spot 1, 2, and 3 show a Type II olivine composition (~Fa_{12}, ~Fa_{12}, and ~Fa_{18}, respectively). However, their oxygen isotope signatures are Δ^{17}O ~1.2‰, ~-2.9‰, and ~0.7‰, respectively. Spots 1 and 3 are unresolvable within uncertainties. On the other hand, spot 2 is resolvable at the 95% confidence interval and plots between the Y&R and PCM lines (Figure 5.15d). Therefore, spot 2 olivine is a relict grain a with a carbonaceous chondrule-like oxygen isotope composition which survived the last heating event in the OCs chondrule forming region.

Only one SHRIMP-SI measurement was planned in chondrule CH170, based on its texture (PO) and its FeO content (~Fa_{17}, Type II). Spot 1 shows a significant degree of ^{16}O-enrichment (Δ^{17}O ~-13.2‰) and plots on the Y&R line (δ^{18}O ~-26.1‰ and δ^{17}O ~-26.8‰) in the refractory inclusion region of the triple oxygen isotope diagram (Figure 5.15e; Clayton, 1993). Consequently, four more spots were measured (no EPMA data) showing Δ^{17}O values from ~-1 ‰ to ~0.5 ‰ plotting close to the TF line, indicating that spot 1 is a relict grain. To be rigorous the extra data obtained from this chondrule, with no associated EPMA analysis, were excluded from the statistical assessment since it is a biased sampling. To the best of our knowledge, this is the first time that chondrule olivine grains with an oxygen isotope similar to refractory inclusions have been observed in OC chondrules suggesting that, although their probability of occurrence is very low (<<< 1%) they were among chondrule precursors in the OCs chondrule forming region.

CH181 is a POP chondrule with minor inclusions of Fe,Ni-metal. Similar to CH170, one olivine was chosen to measure oxygen isotope ratios. Spot 1 olivine is a Type II grain (~Fa_{14}) and has ^{16}O-enriched oxygen isotope ratios (Δ^{17}O of -7.1 ±0.4‰, δ^{18}O of -9.4 ±0.6‰ and δ^{17}O of -12.0 ±0.6‰) plotting on the PCM line (Figure 5.15f) in the region of some carbonaceous chondrite chondrules olivines (e.g. Tenner et al., 2015, 2017). Two extra points were analyzed (no EPMA data) showing Δ^{17}O ~-5.6 ‰ and ~-0.7 ‰, resolvable within uncertainties (±0.4‰ for Δ^{17}O), which suggests mixing of precursors

from quite different reservoirs from carbonaceous chondrite chondrules to close to OC chondrules.

Chondrule CH207 exhibits a POP texture, with an olivine dominated core, Ca-poor pyroxene increasing towards the rim, and some FeNi-metal blebs. The two analyzed olivines have a ~Fa_{20} composition, within the range of equilibrated olivines in H chondrites, and the most ^{16}O-enriched oxygen isotope signature of all samples reaching $\Delta^{17}O$ values as low as -17.4 ±0.4‰ and -12.0 ±0.4‰ (Figure 5.15g), for spot 3 and 2, respectively. Given that no more data was obtained from this chondrule, it is not possible to assure the relict nature for these grains but that the chondrule was partially or completely formed from heterogeneous ^{16}O-rich precursors. These precursors were probably formed in the refractory inclusion (spot 3) and carbonaceous chondrite (spot 2) chondrule forming regions (e.g. Clayton, 1993).

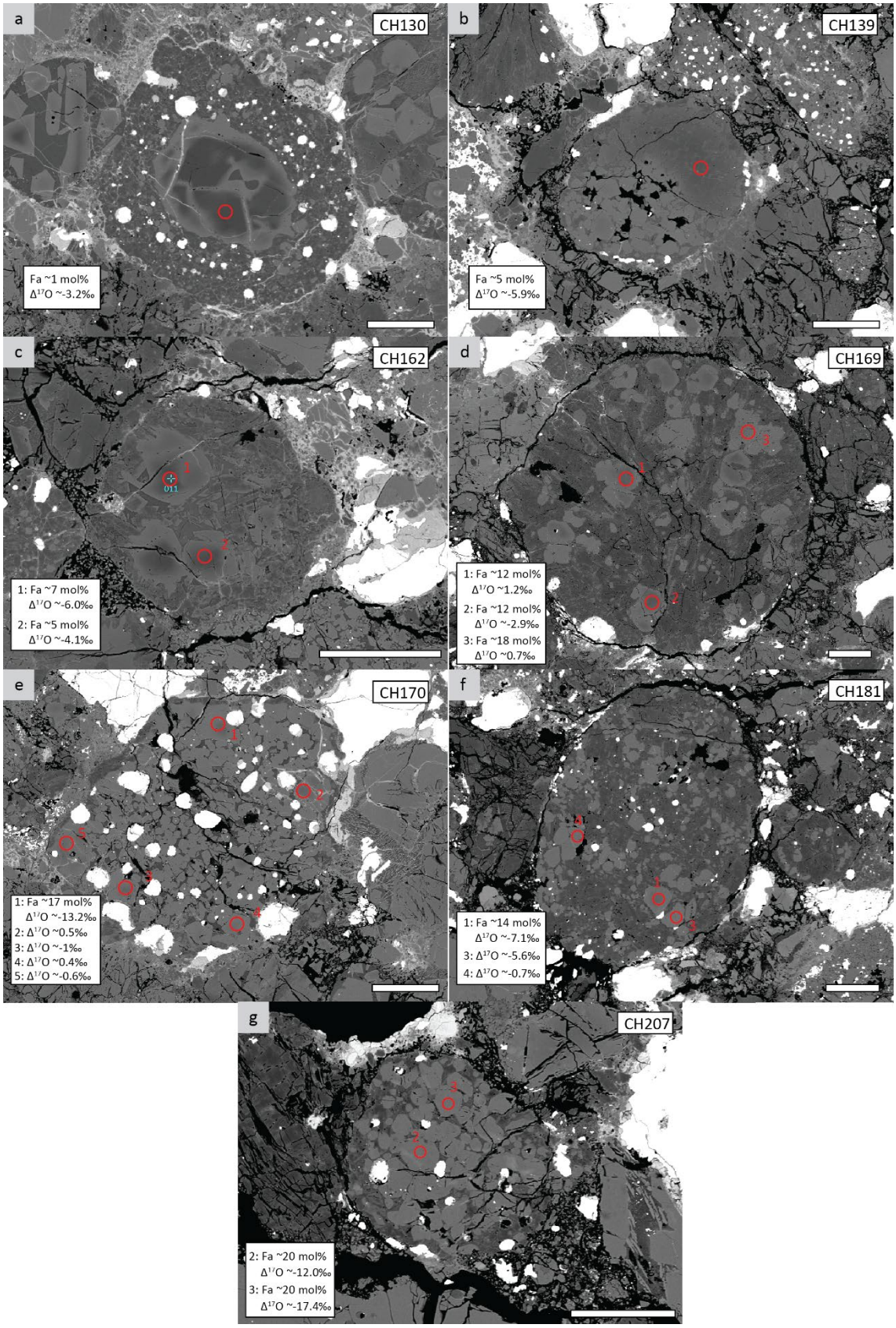

Figure 5.15. ^{16}O-rich chondrule olivines relative to the major trend in QUE93030. Scale bars are 100 µm.

ALHA77299

Chondrule CH285 has a porphyritic texture, formed by euhedral olivines and a glassy-microcrystalline mesostasis which is more abundant in the core of the chondrule. FeNi-metal ± troilite blebs are abundant and most olivines have a FeO-rich rim (Figure 5.16a). The olivine is of Type I composition (~Fa1) and its $\Delta^{17}O$ value is ~-3.0‰ plotting close to the Y&R line. No more analysis was possible due to the small grain-size minerals, and a relict origin is not straightforward. Based on its petrographic similarities to carbonaceous chondrite Type I chondrules (Jones, 2012), chondrule CH285 may have been formed in a carbonaceous chondrite chondrule environment and transported to the OC chondrule forming region.

CH305 correspond to a Type I chondrule with a PO texture which contains a small FeNi-metal inclusion (Figure 5.16b). The composition of the analyzed olivine is forsteritic (~Fa0) and has oxygen isotope ratios of 8.5±0.7‰‰ for $\delta^{18}O$ and -10.3 ±0.8‰for $\delta^{17}O$ plotting between the Y&R and PCM lines (Figure 4.18e, $\Delta^{17}O$ of -5.9 ±0.7‰) similar to chondrules found in carbonaceous chondrites (e.g. Tenner et al., 2015).

One grain was analyzed from CH312 chondrule which presents a PO texture. Olivine grains within this chondrule range in sizes from 25 by 25µm to 100 by 100µm which is the size of the measured olivine (Figure 5.16c). This chondrule appears to be chemically equilibrated which is consistent with the Type II composition (~Fa18) of the analyzed olivine. The oxygen isotope ratios of this grain are ~0.6‰ for $\delta^{18}O$ and ~-2.0‰ for $\delta^{17}O$ ($\Delta^{17}O$ ~-2.2) plotting close to the PCM line (Figure 4.18e). Given that no more data was obtained from this chondrule neither the relict nature of the olivine measured nor the whole chondrule ^{16}O-rich signature can be assumed. In either case, it can be stated that at least one of the chondrule precursors had a composition similar to carbonaceous chondrite chondrules during the last experienced chondrule forming event which, as mentioned earlier, could be a signal of a certain amount of mixing of precursors and/or chondrules between different oxygen isotope reservoirs.

CH315 chondrule is characterized by a POP texture. One grain was measured which has an Mg-number close to Fa18 (Figure 5.16d) corresponding to the Fa composition of equilibrated olivines in H chondrites. Its oxygen isotope ratios are $\delta^{18}O$ ~-5.5‰ and $\delta^{17}O$

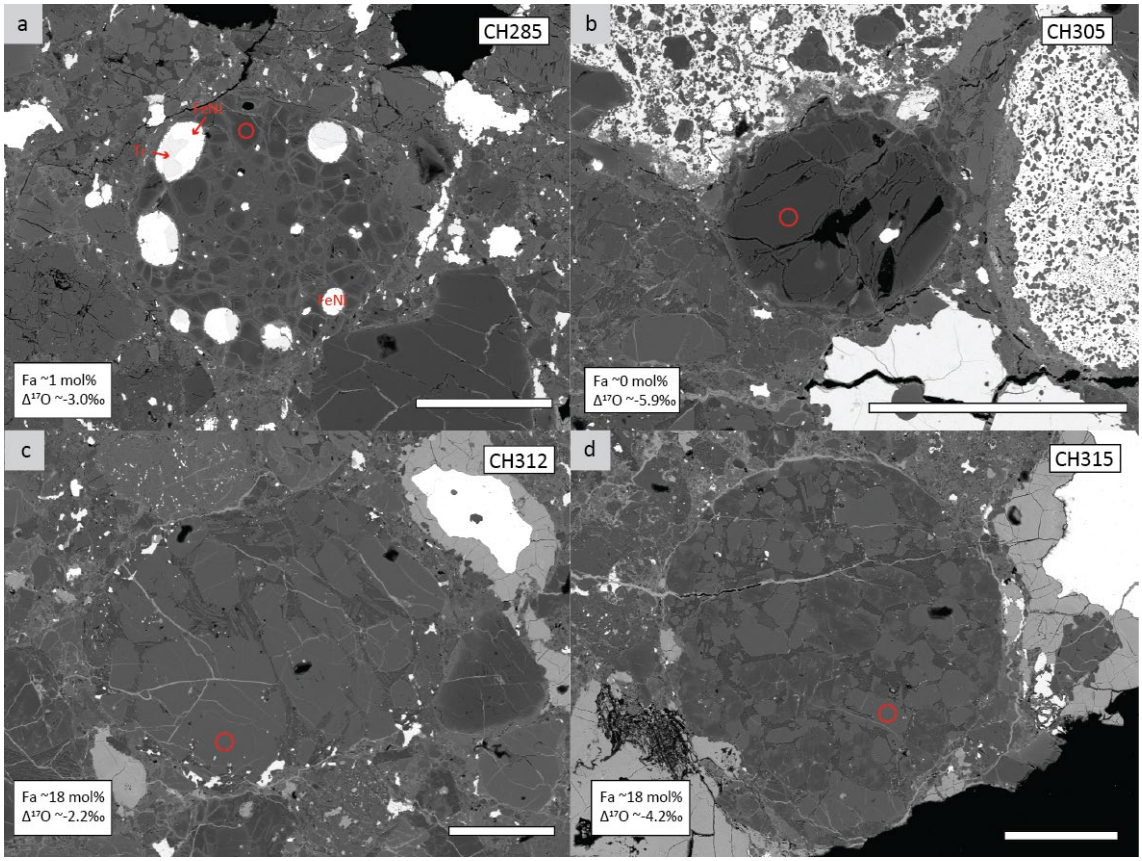

Figure 5.16. ^{16}O-rich chondrule olivines relative to the major trend in ALHA77299. Scale bars are 100 µm.

~-7.2‰ (Δ^{17}O of -4.2 ±0.6‰) plotting between the Y&R and PCM lines (Figure 4.18e). Similar to chondrule CH312, since no more measurements were taken from this chondrule, it can be said that at least one of the chondrule precursors had a composition similar to carbonaceous chondrite chondrules before chondrule formation (e.g. Kita et al., 2017 and references therein).

GRO06054

Two grains were analyzed from CH368 chondrule which presents a PO texture (Figure 5.17a). Spot 1 olivine has an Mg-rich core (~Fa3), two small FeNi-metal blebs, and Fe-richer overgrowths. On the other hand, spot 2 olivine shows sharp phase boundaries and Type II grain composition (~Fa_{90}). Moreover, spot 1 exhibits oxygen isotope ratios of $\delta^{18}O$ ~-0.4‰, $\delta^{17}O$ ~-3.0‰ and $\Delta^{17}O$ ~-2.7‰, plotting on the PCM line (Figure 4.19a), while spot 2 data is $\delta^{18}O$ ~5.1‰, $\delta^{17}O$ ~2.6‰ and $\Delta^{17}O$ ~0.0‰. Given the petrographic and isotopic observations, spot 1 olivine is identified as a relict grain sharing an oxygen isotope composition with chondrules from carbonaceous chondrites (e.g. Tenner et al., 2017).

CH354 chondrule (Type II) or olivine agglomerate object (Ruzicka et al., 2012) shows a PO texture, with different size closely packed olivine grains, surrounded by a rim of troilite which also occurs minimally inside the object (Figure 5.17b). Six olivines show Fa mol% compositions ranging from Fa_{15} to Fa_{22}, with nearly homogeneous $\Delta^{17}O$ values (~0.0 to 1.0‰), indistinguishable within per spot external uncertainties which have an average of ±0.66‰ in this SHRIMP-SI session. The exception is spot 9 olivine, which is Mg-rich (~Fa_3) and ^{16}O-enriched in oxygen isotope composition with ratios of $\delta^{18}O$ ~-10.7‰, $\delta^{17}O$ ~-12.6‰ ($\Delta^{17}O$ ~-7.0‰) plotting between the Y&R and PCM lines (Figure 4.19a), indicating its relict nature and suggesting this olivine acquired its ^{16}O-enriched composition in an oxygen isotope gas reservoir similar to what has been reported mainly for carbonaceous chondrite chondrules (Kita et al., 2017 and references therein)

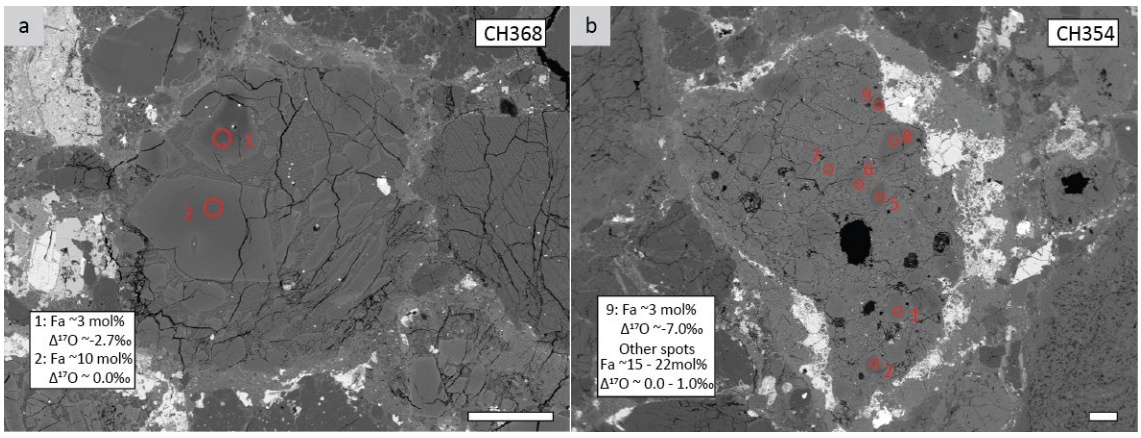

Figure 5.17. ^{16}O-rich chondrule olivines relative to the major trend in GRO06054. Scale bars are 100 µm.

DOM10556

Spot 1 was the only grain measured within CHextra9 (POP), presenting a FeO content of ~Fa1 and a $\Delta^{17}O$ ratio of -2.0 ±0.4‰ plotting close to the Y&R line ($\delta^{18}O$ of ~3.1‰ and $\delta^{17}O$ of ~3.7‰; figure 4.20c). From the BSE image in figure 5.19, is evident that the grain is a relict Mg-rich olivine surrounded by FeO-richer phenocrysts.

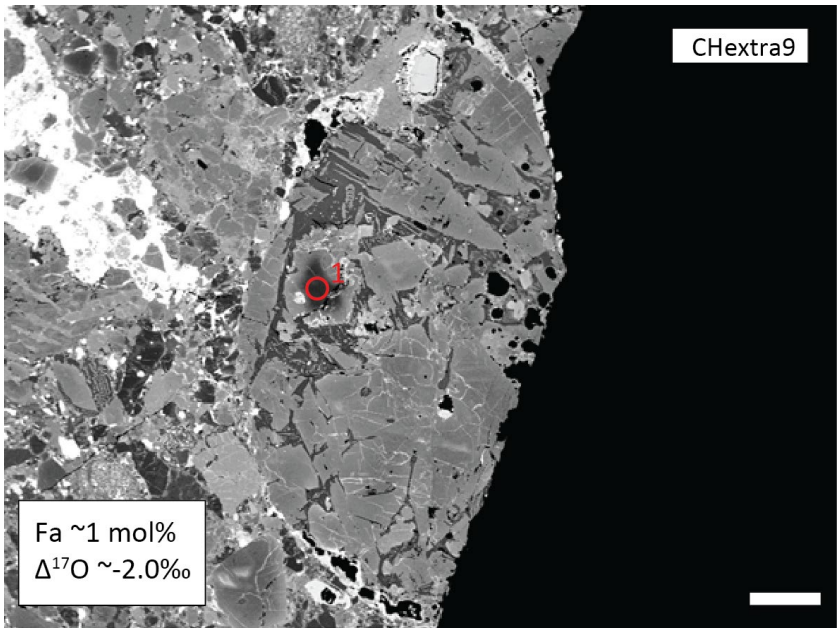

Figure 5.18. ^{16}O-rich chondrule olivine relative to the major trend in DOM10556. Scale bar is 100 µm.

MIL05050

Two grains were measured in CH487 (POP Type II) with olivine composition of ~Fa15 (spot 2) and ~Fa7 (spot 3), the latter showing an Mg-rich core and Fe-richer overgrowths (Figure 5.20a). $\Delta^{17}O$ values of spot 2 and 3 are ~0.8‰ and ~-4.7‰, respectively, resolvable within uncertainties (±0.7‰). Spot 3 plots within Y&R and PCM lines on the triple-oxygen isotope diagram while spot 2 plots on the Y&R line, within the cluster specified on the results (Figure 4.19e). Based on these petrographic, chemical, and isotopic characteristics, spot 2 is considered to be a relict grain which survived the last chondrule melting event maintaining its previous oxygen isotopic signature and perhaps reflecting some mixing among chondrule precursors from the carbonaceous chondrite chondrule forming region and the OCs chondrule forming region.

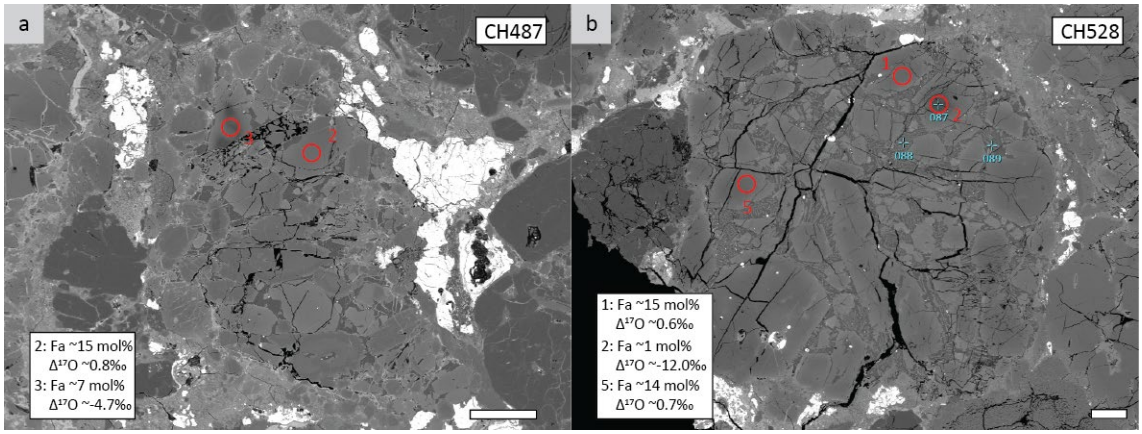

Figure 5.19. ^{16}O-rich chondrule olivine relative to the major trend in MIL05050. Scale bar is 100 µm.

CH528 chondrule is a big chondrule (900 x 900µm approximately) that has a PO texture and Type II composition showing clear olivine crystals embedded in a mesostasis with small pyroxene microcrystals (Figure 5.20b). Three measurements were performed in this chondrule. Spot 1 and 5 show a Fa mol% composition of Fa_{15} and Fa_{14} and $\Delta^{17}O$ ratios of ~0.6 and ~0.7‰, respectively, close to the main chondrule population mean. On the other hand, spot 2 depicts an Mg-rich olivine core (~Fa_1) that evolve to Fe-richer compositions towards the edge of the mineral. Spot 2 olivine oxygen isotope composition is ^{16}O-enriched with ratios of -21.4 ±0.7‰ in $\delta^{18}O$ and -23.2 ±0.5‰ in $\delta^{17}O$ ($\Delta^{17}O$ of -12.0 ±0.3‰) plotting between the Y&R and PCM lines (Figure 4.19e) in the limit between carbonaceous chondrite chondrules and refractory inclusions oxygen isotope regions (Clayton, 1993), indicating its relict origin.

LAR06279

^{16}O-rich isotope compositions were found in one chondrule from LAR06279. Chondrule CH596 is a Type II chondrule which appears to be chemically equilibrated due to thermal metamorphism on its parent body (Figure 5.21). Accordingly, the Fa mol% measured on the two analyzed olivines within this chondrule are ~Fa_{32} for both spot 1 and spot 2. However, their oxygen isotope ratios are different among them with spot 1 having 4.8 ±0.5‰ in $\delta^{18}O$ and 3.3 ±0.5‰ in $\delta^{17}O$ ($\Delta^{17}O$ of 0.8 ±0.5‰) and spot 2 having -3.8 ±0.5‰ in $\delta^{18}O$ and -4.8 ±0.5‰ in $\delta^{17}O$ ($\Delta^{17}O$ of -2.8 ±0.5‰) both plotting on the Y&R line (Figure 4.20a). Therefore, spot 2 is a relict olivine with an oxygen isotope signature typical of carbonaceous chondrite chondrules (e.g. Chaumard et al., 2018).

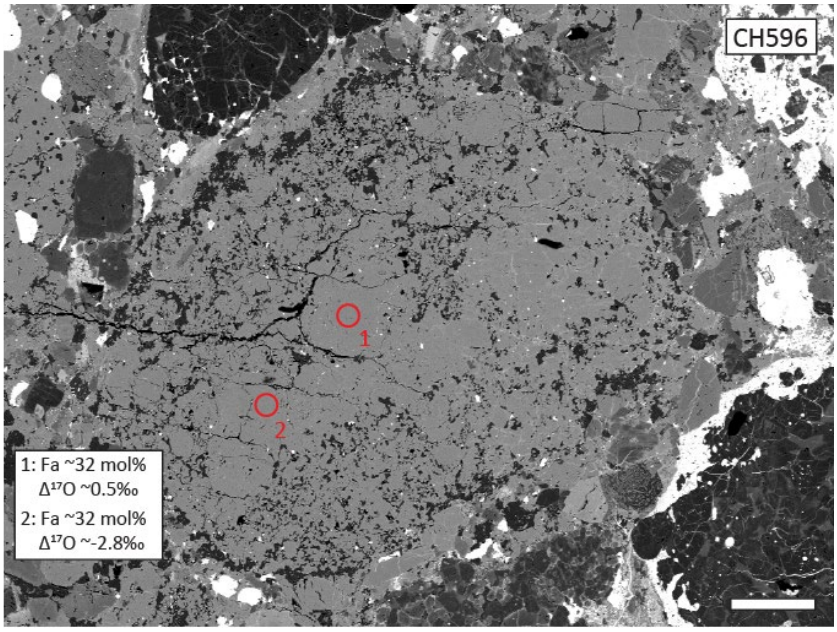

Figure 5.20. ^{16}O-rich chondrule olivine relative to the major trend in LAR06279. Scale bar is 100 µm.

LAR12034

Type II chondrule CH862 has a PO texture and appears to be chemically equilibrated. This is consistent with the Fa content of the olivine measured which is the range of equilibrated chondrule olivines in OCs (~Fa_{31}; figure 5.22a). However, its oxygen isotope composition shows that this grain was probably formed in a similar reservoir to some carbonaceous chondrite chondrules having ratios of -3.8 ±0.5‰ in $\delta^{18}O$ and -6.9 ±0.5‰ in $\delta^{17}O$ ($\Delta^{17}O$ of -4.9 ±0.4‰) plotting slightly to the left of the PCM line (Figure 4.20e).

Chondrule CH869 is a big chondrule (1.5 by 2.0 mm approximately) with PO texture and Type II composition (Figure 5.22b). Five olivines were measured for oxygen isotopes within this chondrule most of them with $\Delta^{17}O$ ratios that range from ~0.4 to ~1.1‰, indistinguishable within external errors (±0.4‰). Nevertheless, a relict grain was observed in this chondrule (spot 1) which is forsteritic in composition (~Fa_1) and has lighter oxygen isotope composition, similar to chondrules from carbonaceous chondrites, with ~-6.4‰ in $\delta^{18}O$ and ~-7.6‰ in $\delta^{17}O$ ($\Delta^{17}O$ of -4.2‰) plotting on the Y&R line (Figure 4.20e).

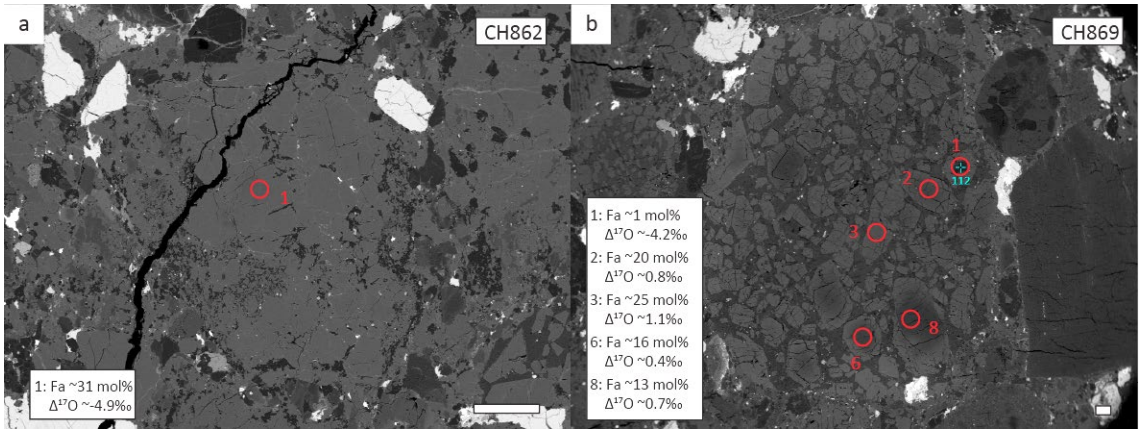

Figure 5.21. ^{16}O-rich chondrule olivine relative to the major trend in LAR12034. Scale bar is 100 µm.

To conclude this section, figure 5.23 shows schematically the distribution of chondrule olivine and the different reservoirs from where relicts and chondrules were probably transported from to finally accrete onto OCs asteroids. The light orange and yellow areas represent ranges which are typical of refractory inclusions and carbonaceous chondrite chondrules, respectively. Additionally, to the right this figure, a qualitative illustration of the possible thermal structure of the inner solar system and its implication on gaseous oxygen isotopes is provided.

As argued before, the probability of finding olivine relicts and/or chondrules with $\Delta^{17}O$ ratios < -2.0‰ is low (7%) indicating low dust mixing between OCs main reservoir and reservoirs distinctive of carbonaceous chondrite chondrules and refractory inclusions. This suggests a low degree of dust mixing between these reservoirs. In this regard, to the best of our knowledge, this is the first time that refractory inclusion-like compositions are found in chondrules from OCs. On the other hand, probabilities increase when $\Delta^{17}O$ ratios get closer to the main chondrule population of OCs implying that these chondrules were formed on the vicinity of the main population reservoir.

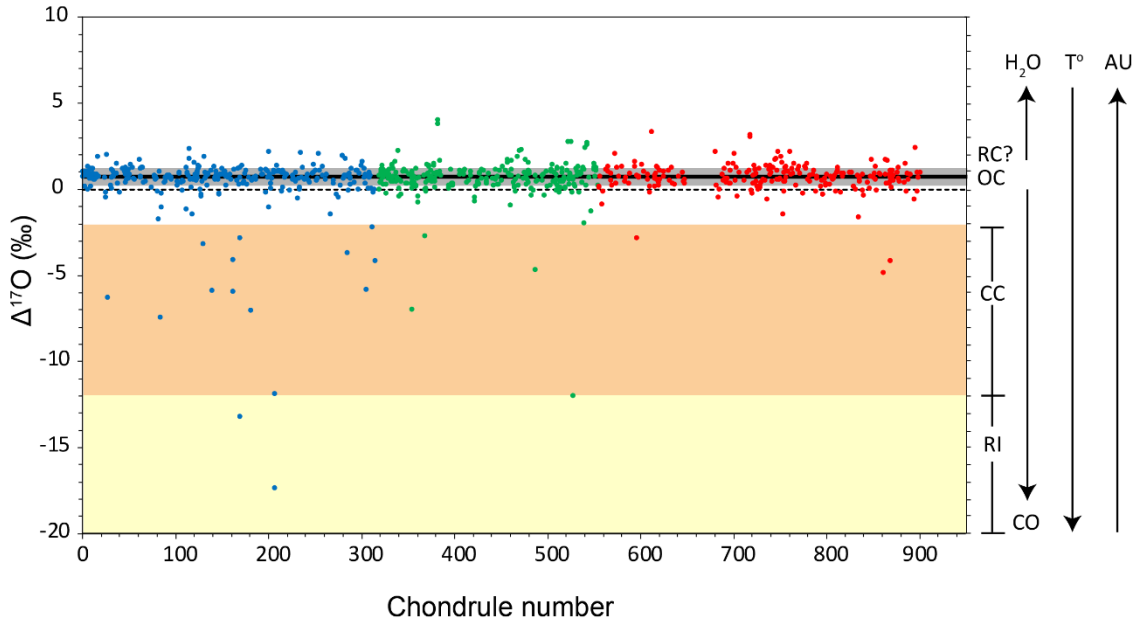

Figure 5.22. $\Delta^{17}O$ values of all measured chondrule olivine. Data is organized by chondrule number. The $\Delta^{17}O$ mean of the main population is shown as a black bar ($\sigma_{95\%}$). Grey rectangle represent the variability of the population (2SD, $\sigma_{95\%}$) and dashed line is Enstatite-Earth's $\Delta^{17}O$ reservoir. Individual spot errors are omitted for clarity. The gap in LL samples are olivines from chondrules that were not measured for oxygen isotopes. Arrows indicate a qualitative relative increment of the gas species H2O and CO, temperature, and heliocentric distance.

5.7. Ordinary chondrites bulk composition: insights into terrestrial planet formation

The mean oxygen isotope composition of equilibrated bulk H, L, and LL ordinary chondrite (EOCs) define different mass-fractionation lines or reservoirs with $\Delta^{17}O$ of 0.7 ± 0.2 ‰ (2SD), 1.1 ± 0.2 ‰ (2SD), 1.3 ± 0.2 ‰ (2SD), respectively, while bulk chondrite compositions of UOCs display on average $\Delta^{17}O$ ratios of 0.7 ± 0.1‰ (2SD), 1.0 ± 0.2‰ (2SD), and 1.1 ± 0.2‰ (2SD), for H, L, and LL, respectively (Clayton et al., 1991), slightly lower than equilibrated OCs. On the other hand, the mean oxygen isotope composition of chondrule olivine from H, L, and LL samples in this study are generally lower than bulk OC chondrites consistent with previous high-precision oxygen isotope SIMS measurements on LL samples (Kita et al., 2010).

Having the main chondrule population of OCs in mind ($\Delta^{17}O$ ~0.7‰) it appears that the shift towards heavier oxygen isotope compositions in UOCs and equilibrated bulk samples is controlled by the matrix fraction composition, as previously suggested by other authors (e.g. Kita et al., 2010; Bridges & Ireland, 2015; Sanders et al., 2017). Interestingly, this whole-rock variability augments in the order of H<L<LL which is correlated to the heliocentric distances commonly accepted for OCs accretion location (e.g. Desch et al., 2017) although the opposite has also been proposed (Vernazza et al., 2014).

Moreover, most chondrites also accreted ^{16}O-poor water and is very likely that minerals in the matrix and chondrule phases in chondrules, particularly mesostasis, exchanged with this ^{16}O-poor fluid (e.g. Sakamoto et al., 2007; Choi et al., 1998; Kita et al., 2010; Bridges & Ireland, 2015) on their parental bodies due to aqueous alteration. However, the average anhydrous composition of dust from the matrix is essentially unknown.

Nevertheless, since one main population of chondrules was accreted by OCs asteroids, the oxygen isotope composition of this ^{16}O-poor fluid could be estimated, considering that OCs are mainly a mixture of chondrules and matrix (Krot et al., 2014). Similar to Kita et al. (2010), one approach to answer this question is by assuming that the average composition of the bulk anhydrous dust of OCs is represented by the composition of the main chondrule population.

A mass-balance calculation can be used to obtain the $\Delta^{17}O$ value of water necessary to move OCs bulk composition towards higher values. In this regard, the proportions of chondrules is fixed to be 70% since it is the average vol% range of chondrules observed in OCs (Krot et al., 2014) and water bulk content was calculated to be ~1.8%, ~1.9%, and ~1.5% of the volume using the average water content of H, L, and LL UOCs, respectively (Jarosewich, 1990). The rest (matrix plus metal) is assumed to be anhydrous having a $\Delta^{17}O$ composition equal to the main chondrule population. Adopting whole-rock $\Delta^{17}O$ composition to be ~0.69‰, ~0.96‰, and ~1.08‰ for H, L, and LL UOCs (Clayton et al., 1991), respectively, the water accreted on the different parental bodies would have been characterized by $\Delta^{17}O$ values of ~0.1‰, ~14.4‰, and ~26.0‰, for H, L, and LL UOCs, respectively. Such ^{16}O-poor water oxygen isotope reservoirs can be obtained if the CO-photochemical self-shielding holds for the solar nebula. On this respect, the most extreme ^{16}O-poor composition has been observed in magnetite-sulfide (cosmic symplectite) assemblages in Acfer094 matrix, considered the least aqueously altered chondrite, with $\Delta^{17}O$ ~80‰ (Sakamoto et al., 2007).

Another approach would be to consider the oxygen isotopic value of aqueous altered mesostasis of chondrules in Semarkona (LL3.0), the least thermally metamorphosed OC. The highest mesostasis $\Delta^{17}O$ value measured by Kita et al. (2010) is ~5‰, which as pointed out by them, matches the mass-fractionation line defined by magnetite found in Semarkona's matrix (Choi et al., 1998). This magnetite is the product of aqueous alteration and oxidation of metallic iron in the LL parental body; Choi et al. (1998) estimated that the $\Delta^{17}O$ composition of the heavy H_2O oxidant would have been close to ~7‰, in order to achieve magnetite compositions.

At any rate, whatever the preferred approach, the point is to highlight that the shift in whole-rock composition has to be caused by some matrix component that was isotopically heavier than the bulk rock to complement for the lighter composition of the main chondrule population, and this component is probably heavy water. In this regard, SHRIMP-SI measurements on the matrix of the OCs investigated here and the same statistical assessment will be done in the near future to obtain a mean $\Delta^{17}O$ value for the matrix.

The oxygen isotope composition of EOCs is particularly interesting if one considers chondrites as the building blocks of the solar system from which planets formed (Wood, 1962) and that the isotopically equilibrated oxygen compositions of OCs could be seen as the parallel of the equilibrated or homogeneous composition of differentiated meteorites or even planets. In other terms, OCs sampled a batch of cosmic material on their accretion location that, once thermally and isotopically equilibrated, represents the average oxygen isotope reservoir of the parental asteroid.

Sanders et al. (2017) carried out a detailed characterization and discussion of some oxygen isotopic and chemical trends associated with EOCs that are pertinent to the argument here. These trends are as follow: 1) the mean whole-rock oxygen isotope composition of equilibrated H, L, and LL, fall close to a slope 1 line on the triple oxygen diagram (ECL line; Clayton et al., 1991); 2) a positive correlation between bulk rock $\Delta^{17}O$ and the Fa composition of chemically equilibrated olivine is observed from H to L to LL; and 3) a positive correlation in olivine between molar FeO/MgO and FeO/MnO for EOCs increasing from H to L to LL is observed.

For trend 2), Sanders et al. (2017) envision that the original ice water (high-$\Delta^{17}O$) was melted in a closed system in OCs parental bodies causing an early stage of low temperature (~100 °C) aqueous alteration that oxidised the iron metal within the matrix increasing both the FeO and $\Delta^{17}O$ content of the bulk average composition until full equilibrium is achieved. They also propose that adding FeO to the system would explain the redox correlation (trend 3) of EOCs. Finally, they hypothesised that having a closed system would have caused the bulk oxygen isotope composition of EOCs to remain near to the cosmochemical mass-independent slope-1 line of the solar system, therefore they pointed out that heavy H_2O was added in lower amounts to H chondrites, medium in L, and high in LL chondrites, if they sampled the same chondrule population, as indicated in this research.

The early aqueous alteration stage conceived by Sanders et al. (2017) has also been proposed by Bridges & Ireland (2015) who measured oxygen isotope composition of chondrule phases from LL3.0, LL3.2, and LL3.4 samples. They propose that LL3.0 chondrite chondrules recorded the early aqueous alteration, after which anhydrous thermal metamorphism partially equilibrated the isotopic compositions of chondrules

phases from LL3.0 to LL3.2 to LL3.4. Interestingly, McDougal et al. (2017) showed that oxygen isotope homogenization of chondrule phases is completed in type 5 and type 6 reaching chondrule compositions on the range of their host EOCs meteorite bulk-rock values.

Considering the previous discussion, it is remarkable that OCs sampled both high temperature (e.g. chondrules) and low-temperature (e.g. water ice) objects together at their accretion location. In this regard, it has been shown that H, L, and LL asteroids accreted at quite similar ages from ~2 to ~3 My after first solids formation (e.g. Henke et al., 2012; Sugiura & Fujiya, 2014; Doyle et al., 2015, 2016; Blackburn et al., 2017; Desch et al., 2017). At the same time, OCs have been usually associated to S-complex asteroids which dominate the inner asteroid belt (DeMeo & Carry, 2014) from ~2 to ~3 AU (e.g. Morbidelli et al., 2012) probably close to their current parent body location with orbital distances in the order H<L<LL (e. g. Desch et al., 2017). Although asteroid mixing could have occurred if Jupiter's migration actually happened (Walsh et al., 2011), it appears that overall, the bulk $\Delta^{17}O$ composition of EOCs is correlated with their heliocentric distance from the Sun as argued below.

As proposed by Sanders et al. (2017), it is possible that H chondrites accreted less isotopically heavy ice water than L and LL chondrites and that the amount of ice accreted by each OC group, similar to gaseous oxygen isotope reservoirs, is also dependant on the thermal structure of the protoplanetary disk. Therefore, the thermal structure of the protoplanetary disk might be affecting the availability of ice water on OCs formation location meaning that less H_2O was available in the H chondrite accretion zone compared to L and more extremely to LL accretion site. Moreover, if one assumes that H, L, and LL chondrite matrices were initially the same, then the bulk oxygen isotope composition of H, L, and LL equilibrated chondrites could be reflecting that, at least in terms of ice water, the matrix of H has been devolatilized more than for L and LL chondrites, in that order, once again according to the thermal profile. Similar concepts have been explored and modelled related to moderately volatile element depletion in chondritic meteorites (e.g. Ciesla, 2008).

Additionally, if the thermal structure is also important for the matrix composition of OCs (or any chondrite class), then it is possible that the higher amount of iron metal accreted

by H chondrites is also related to the thermal gradient of the solar nebula which, having in mind the oxygen isotope gaseous reservoir picture of section 5.5, would mean that the average redox conditions were more reducing at higher ambient temperatures (closer to the Sun), then a larger proportion of more reduced matrix component (iron metal) was probably sampled by H chondrites compare to L and LL chondrites. This idea holds with enstatite and Rumuruti chondrites which have more and less iron metal within their matrices, respectively, compared to OCs (Sanders et al., 2017 and references therein). The opposite occurs related to water, with more water accreted in Rumuruti chondrites and less water accreted in enstatite chondrites, relative to OCs. In this regard, in terms of metal, the end-member case, although at a planetary scale, is Mercury which accreted probably close to its current orbit (~0.4 AU) and has a large metal core (McCoy & Nittler, 2014).

The devolatilised matrix concept due to the thermal structure of the solar nebula presented above for H, L, and LL chondrites is very interesting to keep developing in the future since it appears to be controlling the oxygen isotope changes and the chemistry of bulk-rock samples (parent bodies). For instance, it is well known that objects in the solar system show some degree of volatile depletion (depleted in elements with a 50% condensation temperature, Tc, between 250K and 1250K) when compared to Ivuna chondrites (CI) which are thought to represent solar compositions (Lodders, 2003).

As pointed out by Shukolyukov & Lugmair (2000), it is expected that planetary objects formed closer to the Sun have more refractory compositions than objects forming at longer distances. Then, if terrestrial planets formed by a mechanism similar to OCs, then the feeding objects available into their accretion vicinity (e.g. dust matrix and chondrules) and their oxygen isotopic and chemical characteristics could be responding to the thermal structure of the protoplanetary disk. Is important to highlight here that the devolatilisation of the dust matrix for OCs, does not necessarily mean that it has been thermally processed but that thermal processing of dust in the solar nebula has caused a lower availability of primitive matrix on their accretion locations. The same concept applies to planet formation.

If this is the case, there is no need to invoke an initial CI composition and posterior devolatilisation for terrestrial planets or chondrites due to an incomplete condensation

from the solar nebula, or volatile loss by evaporation during accretion, or mixing of sharp primordial reservoirs consistent of a volatile-poor refractory and a volatile-rich CI-like components (Pringle et al., 2017 and references therein), since the primitive dust or residual dust available in their accretion zones would have already been chemically and isotopically (at least in terms of oxygen) fractionated or devolatilised.

In this line, considering that the oxygen isotope bulk compositions ($\Delta^{17}O$) of the Earth-Moon (1 AU) and Mars (~1.5 AU) are 0‰ and ~0.3‰ (Clayton, 1993), respectively, the previously recognized heliocentric gradient for OCs asteroids appears to be a broad characteristic of terrestrial planets. It would be predicted then that Venus and Mercury probably have oxygen isotope ratios ^{16}O-richer than Earth.

Moreover, having this gradient in mind, if howardites, eucrites, and diogenites (HED) achondrites come from 4 Vesta which orbits at 2.36 AU (Desch et al., 2017 and references therein), its whole-rock $\Delta^{17}O$ ratio of ~-0.24‰ (Greenwood et al., 2017) would indicate that 4 Vesta formed closer to the Sun than the Earth, therefore it might be an interloper due to giant planets migration (Walsh et al., 2011).

Fischer-Gödde & Kleine (2017) measured the ruthenium nucleosynthetic ($\varepsilon^{100}Ru$) composition in samples from Earth, enstatite chondrites, OCs, and carbonaceous chondrites and found that the $\varepsilon^{100}Ru$ compositions increase from Earth to enstatite chondrites to OCs to Rumuruti chondrites to carbonaceous chondrites. Therefore, they also propose a heliocentric gradient with material formed at greater heliocentric distances having larger Ru isotope 'anomalies'.

As with Mo isotopes (e.g. Budde et al., 2016b), Ru is also a siderophile element, then as pointed out in section 5.5, it is highly probable that what is causing the enrichment or depletion in chondrites is a metal carrier associated to their matrix instead of chondrules and/or refractory inclusions. Since overall matrix tends to increase from enstatite-ordinary chondrites to Rumuruti to carbonaceous chondrites, the heliocentric gradient associated to Ru isotope (and Mo) could be reflecting the amount of primitive matrix dust in the different chondrite groups (and planets), which could be dependent on the thermal structure of the disk.

In this view, appealing to Jupiter as the cause of the apparent nucleosynthetic isotope dichotomy of solar system materials (Gerber et al., 2017; Scott et al., 2018), is not necessarily required since the nucleosynthetic signatures of the different objects would be the natural consequence of the thermal processing of primordial solar nebula dust which is expected to be higher closer to the protosun. This is in agreement with Poole et al. (2017), who also favor the importance of the thermal profile to explain the Mo signature of a set of iron meteorites, although they did not involve Jupiter. If this is the case, it is possible that the missing nucleosynthetic signatures might be associated to a sample bias towards well classified-grouped samples of the meteoritical record and are yet to be discovered.

This hypothesis allows another important inference. It is well known that, in general, the amount of iron metal decreases from enstatite to ordinary to Rumuruti to carbonaceous chondrites which is inversely correlated to the nucleosynthetic heliocentric gradient mentioned above. Actually, a prediction of this gradient would be that Mercury is an end-member among terrestrial planets in Mo and Ru nucleosynthetic compositions meaning that accreted less metal carriers but, at the same time, the metal core of Mercury is ~40% of the planet, proportionally bigger than Earth core. Therefore, part of the terrestrial planets metal core and the metal in chondrites and iron meteorites might be indigenous to the solar system, probably a direct condensate of the solar nebula gas. Experimental work is in agreement to this interpretation since it appears that metal condensation is an efficient process under nonequilibrium conditions from a canonical solar nebula gas (Tachibana et al., 2011).

5.8. Type I vs. Type II chondrules: physicochemical conditions of the ambient gas

Since the most pristine UOC samples of this study are WSG95300 (H3.3), GRO06054 (L3.05), DOM10556 (L3.1), and MIL05050 (L3.1) their chondrule olivine chemistry and oxygen isotope composition are going to be used in this section to further discussion. The focus will be on the main chondrule population defined in section 5.4 and olivine chemical data will be used as a proxy to evaluate bulk chondrule chemical processes.

So far chondrules within OCs have been treated as a whole in order to discriminate populations among them in terms of oxygen isotope compositions.

This perspective highlights the general view related to oxygen reservoirs in the protoplanetary disk. However, the compositional Type I-Type II ferromagnesian chondrule dichotomy is an important and still actively debated problem in cosmochemistry (e.g. Jacquet et al., 2015; Friend et al., 2016; Jones, 2012).

As mentioned in chapter 2, Type I and Type II differentiates FeO-poor (Type I) from FeO-rich (Type II) chondrules based on the FeO content of their crystals, in this case, olivine, calculated as Fa=FeO/MgO+FeO mol% <10 mol% and >10 mol% for Type I and Type II, respectively. In general, this distinction means they were formed under different redox conditions in the solar nebula with Type I chondrules being formed under more reducing conditions than Type II, and lower and higher dust/gas ratios for Type I and Type II, respectively (e.g. Ebel & Grossman, 2000).

The estimated mean of the main chondrule population within OCs suggests that they were heated in an ambient gas with an oxygen isotopic composition of $\Delta^{17}O$ ~0.7‰. To explore this gaseous oxygen isotope reservoir pointing to its chemical characteristics we compile the Type I (n = 70) and Type II (n = 162) chondrule olivine oxygen data of the most pristine samples from the main chondrule population. The PDFs of Type I and Type II chondrule olivine is shown in figure 5.24.

From figure 5.24 it can be noted that the $\Delta^{17}O$ sample distribution of Type I olivines is less homogeneous than Type II, which shows a clear peak centered close to 0.7‰. In detail, Type I data have a $\Delta^{17}O$ mean of 0.74 ± 0.10‰ (external error, $\sigma_{95\%}$) and a

variability of 0.64‰ ($\sigma_{95\%}$) while Type II olivine has a mean of 0.66 ± 0.08‰ (external error, $\sigma_{95\%}$) with a variability of 0.50‰ ($\sigma_{95\%}$). These results are very similar to Kita et al. (2010) who calculated average $\Delta^{17}O$ compositions of ~0.7‰ and ~0.5‰ for Type I and Type II chondrules, respectively, in LL chondrites. Although Type I mean is slightly higher than Type II olivine, they are statistically the same within external uncertainties. However, Type I variability is larger than Type II olivine, in fact, Type I chondrule olivine is delimiting the borders of the main population's PDF.

These results suggest that the redox and chemical chondrule 'endmembers' within OCs main chondrule population were overall formed in the same oxygen isotope gaseous reservoir of the solar nebula and that this ambient gas was somehow chemically fractionated to account for the two compositional type of chondrules.

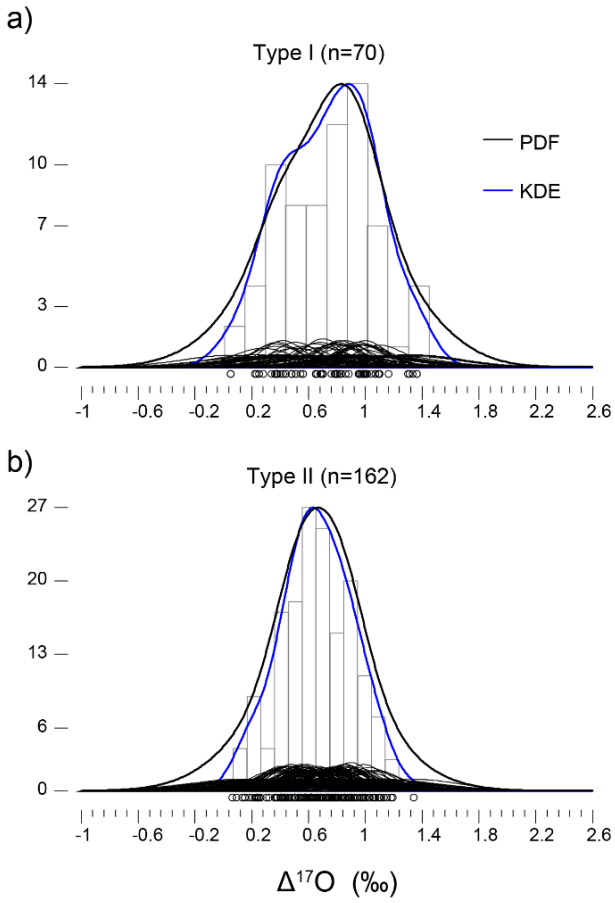

Figure 5.23. $\Delta^{17}O$ sample distribution of a) Type I and b) Type II chondrule olivine of the main chondrule population.

In detail, Type I chondrule olivine within the main chondrule population presents a range of Fa numbers from ~Fa1 to ~Fa10 averaging ~Fa5. Additionally, the average of CaO, Cr_2O_3, and MnO are 0.18wt%, 0.33wt%, and 0.21wt%. On the other hand, Type II chondrule olivine presents a range of iron composition from ~Fa10 to ~Fa34 with an average of ~Fa17, and CaO, Cr_2O_3, and MnO mean compositions of 0.12wt%, 0.34wt%, and 0.34wt%, respectively. These compositions are consistent with the literature from which is well known that Type I chondrules are generally depleted in moderately volatile elements ($704K<t_c<1290K$; e.g. Mn, Na, K, etc) and enriched in refractory elements ($t_c>1360K$; e.g. Ca, Ti, Al, etc) while Type II have less refractory compositions and moderately volatile compositions closer to chondritic (Hewins, 1997; Ruzicka, 2012).

The general olivine chemical trends shown in the results chapter are shown here for the most pristine chondrites of this research (Figure 5.25). From this figure, although average compositions were given above, it appears that some of the aforementioned chemical characteristics represent a gradient from Type I to Type II chondrules.

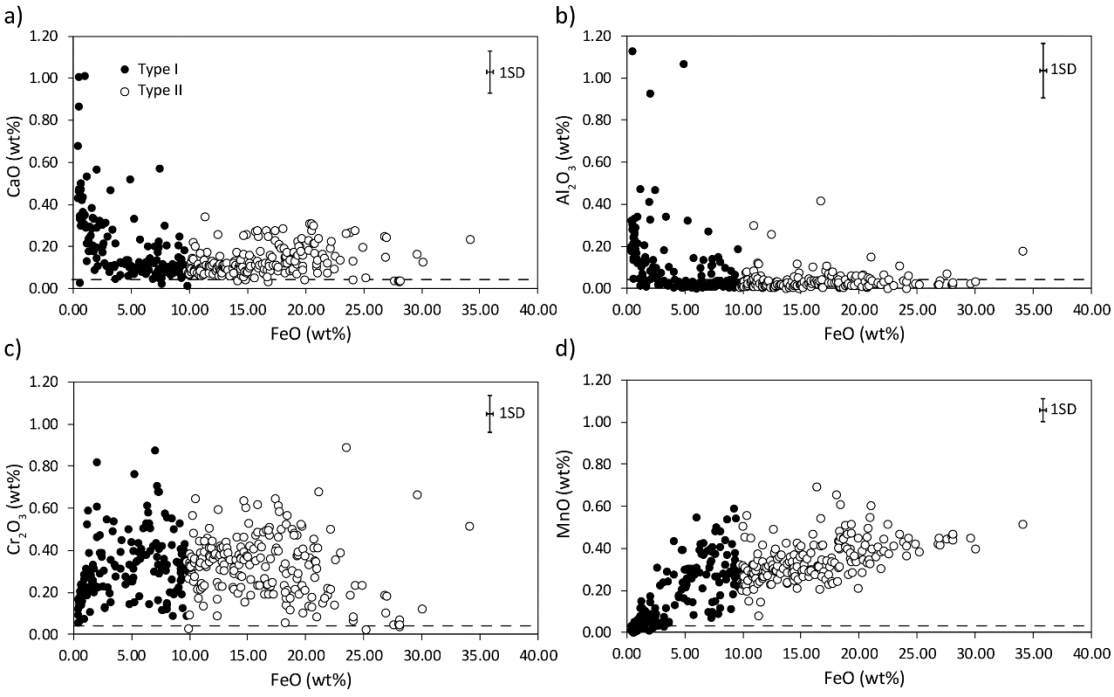

Figure 5.24. a) CaO, b) Al_2O_3, c) Cr_2O_3, and d) MnO minor element composition versus FeO (wt%) of chondrule olivine from the most pristine samples. Dashed lines represent the detection limit of the chemical compound being plotted. Representative errors are shown as 1SD.

Particularly, Type II chondrules appear to have formed as a closed system for Na (Alexander et al., 2008; Jacquet et al., 2015). This chemical composition suggests that chondrules, in general, were formed in regions with high dust/gas ratios far from canonical solar nebula values since temperatures high enough to melt olivine precursors are needed but, at the same time, high partial pressures of moderately volatile elements or moderately volatile rock-forming elements, as pointed out by Salmeron & Ireland (2012), to account for their composition.

In this regard, it has been calculated that the dust/gas ratios to form Type I chondrules covers a range from 50x to 300x solar and Type II from 1000x to 10^6x with different amounts of H_2O ice as precursors, both dust and ice increasing from Type I to Type II chondrule formation regions (Ebel & Grossman, 2000; (Alexander et al., 2008; Connolly & Huss, 2010; Grossman et al., 2012; Kita et al., 2010; Tenner et al., 2015).

Additionally, as briefly noted before, Type I chondrules formed within a range of oxygen fugacities from IW -6 to IW -2 and Type II from IW -2 to IW -1 (Tenner et al., 2015 and references therein). This increase of oxygen fugacity and dust/gas ratio from Type I to Type II chondrule formation regions is consistent with their petrology since Type I chondrules are usually composed of small subhedral FeO-poor olivine, low-Ca pyroxene, a glassy or microcrystalline mesostasis, and variable abundances of Fe,Ni-metal blebs. On the other hand, Type II chondrules contain larger euhedral olivine grains, little or no pyroxene, glassy mesostasis usually with quenched microcrystallites, and low amounts of metal-sulfide (Jones, 2012).

Moreover, it appears that Type II chondrules formed at faster cooling rates than type I chondrules (>~10 K/h; Jacquet et al., 2015) which could mean that the Type I chondrule formation mechanism lasted longer than Type II, or that the ambient gas temperature in the Type I chondrule forming region was hotter than the Type II forming region. Despite the fact that Type I chondrules have higher liquidus temperatures compared to Type II, a hotter ambient gas for Type I chondrules appears to be a more conservative option considering that chondrules are thought to have been heated at peak temperatures to times on the order of many minutes to hours (Connolly & Jones, 2016).

The ambient temperature, depending on the thermal profile of the solar nebula, is an important constraint for chondrules from OCs because, as mentioned, Type I and Type II chondrules from the main chondrule population were formed in the same region of the protoplanetary disk in terms of their oxygen isotope composition, and because Type I and Type II chondrules in OCs are present in quite similar proportions, 54% vs. 46% (Hezel et al., 2018), thus their chemical differentiation is probably the key to understanding their formation environment.

All the aforementioned characteristic and conditions (chemical composition, cooling rates, oxygen fugacity, petrography, dust enrichment) to form Type I and Type II chondrules from OCs could be envisioned considering that the protoplanetary disk midplane is expected to be richer in dust (including ice) as a natural result of the solar nebula collapse, which causes the temperatures closer to the midplane to be cooler than the surface temperatures of the disk, since dust opacity prevents the gas getting hotter due to irradiation from the protosun. For example, as calculated by Salmeron & Ireland (2012), the temperatures of the solar nebula at radial distances beyond 1 AU are always below 280K and increase close to 440 K at 0.4 AU (Mercury's orbit). The vertical temperature profile depends on whether the disk is passive or active, however at 1 AU it could go from 280K in the midplane up to 3000-5000K in the disk atmosphere (e.g. (Glassgold et al., 2004; Salmeron & Ireland, 2012; Walsh et al., 2013). In this line, Ciesla (2008) calculated that 1 My after refractory inclusions, which is the time after most chondrules were formed (Kita & Ushikubo, 2012) the temperature of the nebula at more than 1 AU is <300K.

Additionally, although a handful of Type I and Type II chondrules are as old as refractory inclusions (Bollard et al., 2017) most of them were formed between 1 and 3 My after first solids (e.g. Kita & Ushikubo, 2012). In fact, ^{26}Al isotopic measurements show that Type II chondrules formed contemporaneously or later than Type I chondrules, therefore the physicochemical conditions dependant on the thermal profile in the OCs chondrule forming region were established early in the solar nebula, probably after ~1 My of refractory inclusions.

Therefore, it appears that Type II chondrules formed closer to the midplane compare to Type I chondrules being formed further away. Consequently, since Type I and Type II

chondrules from OCs equilibrated with the same homogenous oxygen gas reservoir, and the physicochemical conditions necessary to explain their chemical and petrological characteristics correlates with a spatially vertical and radial thermal structure of the protoplanetary disk, it appears that the chondrule formation region of the main population of chondrules from OCs was chemically differentiated in both a vertical and radial fashion and that Type I and Type II chondrules, responding to this structure, form a chemical continuum. In this regard, (Miyazaki & Korenaga, 2017) explore the vertical physicochemical structure of the protoplanetary disk proposing different condensation fronts for elements of different volatility.

The chemical gaseous transition in terms of Fa mol% composition of chondrule olivine from OCs chondrules can be observed in figure 5.26 for all pristine olivine and, specifically, for olivines from the main population with Type I olivines plotting generally closer to the Type II chondrule olivine cluster with increasing FeO in their composition.

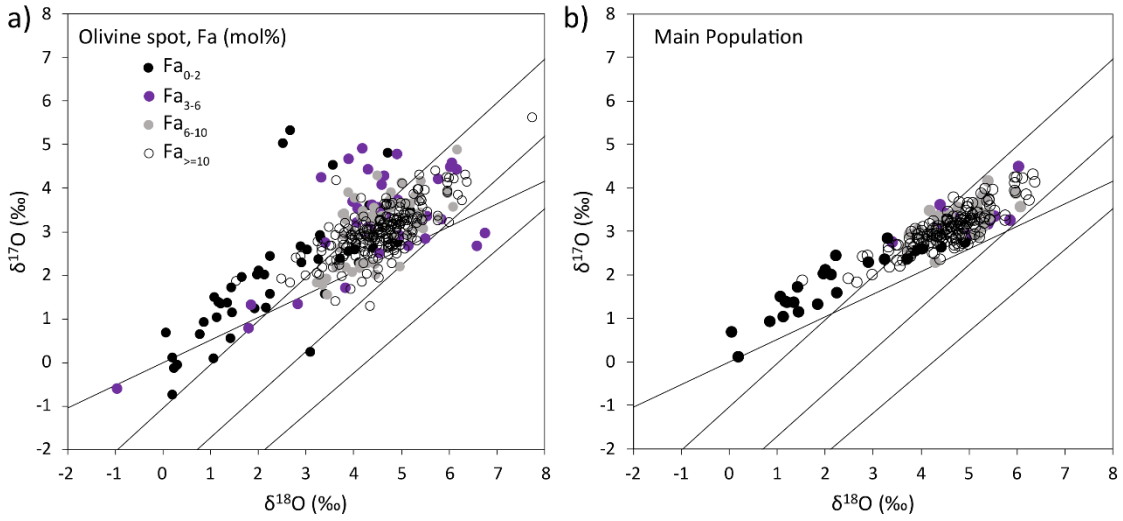

Figure 5.25. Triple oxygen isotope plot off a) all olivine and b) olivine from the main chondrule population of the most pristine samples studied here. For clarity, external errors are not shown for clarity.

An example of the physical conditions in the surroundings of a canonical T-Tauri star is shown in figure 5.27 for dust and gas (Walsh et al., 2013). The dust enrichment towards the midplane is clear from the top plots. The middle plots show the ambient gas temperature increasing from the midplane towards the disk atmosphere and the lower diagrams the temperature of the dust at different locations.

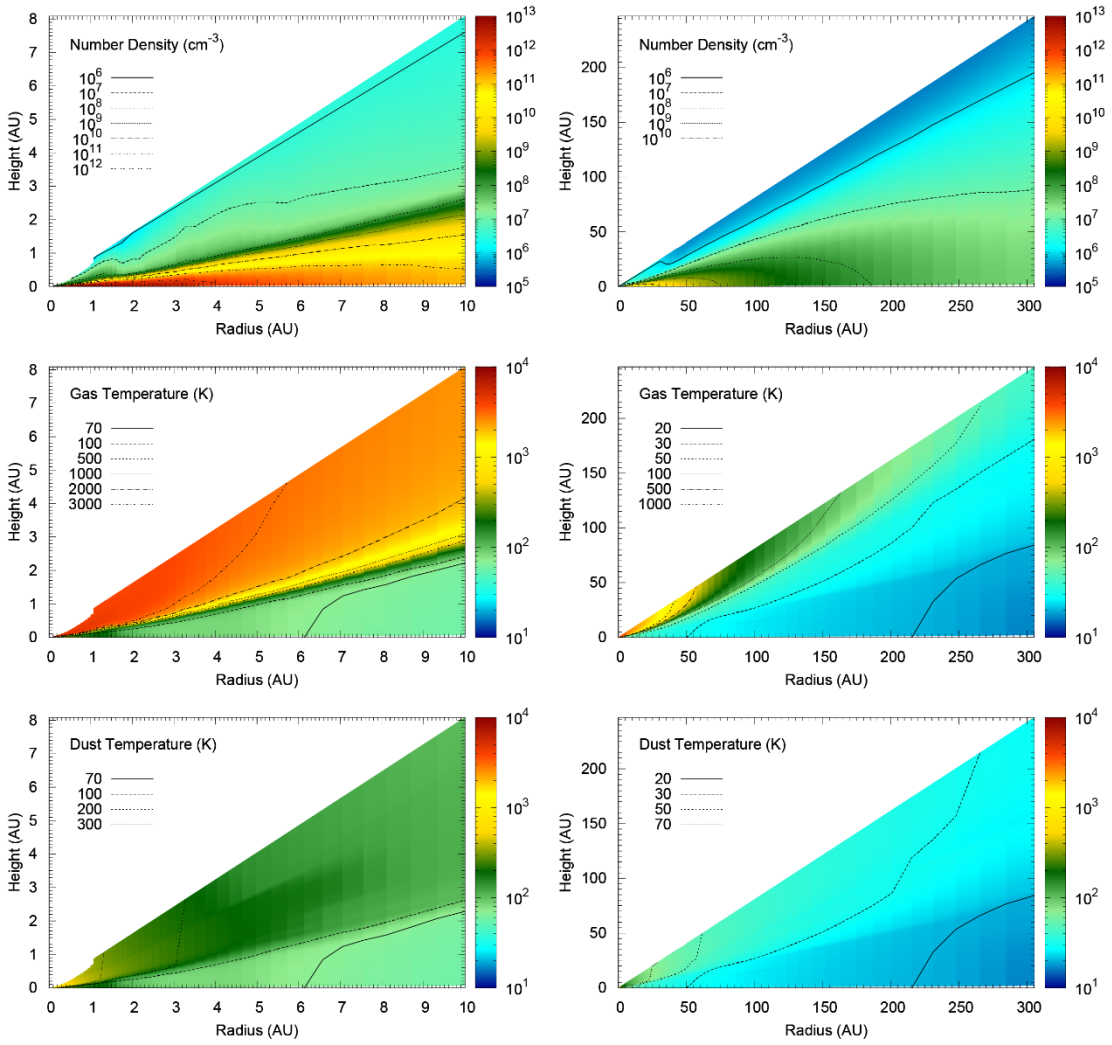

Figure 5.26. Physical model of a protoplanetary disk surrounding a typical T-Tauri star at different radial and vertical distances from the protostar and the midplane. Number density (top), gas temperature (middle) and dust temperature (bottom) as a function of disk radius and height up to maximum radii of r = 10 AU (left) and 305 AU (right). Obtained from Walsh et al. (2013).

Finally, as remarked in sections 5.5 and 5.7, if the primordial dust of the solar nebula is being thermally processed while infalling towards the central star in the earliest stage of the protosun accretion, then its more volatile components are going to be vaporised further away from the sun and at lower vertical distances from the midplane than the more refractory, enriching the surrounding gas in those elements. Therefore, the radial and vertical chemical stratification of the ambient gas argued above will then be a regional characteristic of the solar nebula and different condensation/evaporation lines (e.g. snow line) will exist from the very beginning. Some models place the snow line at 5 AU early in the solar system (Ciesla & Cuzzi, 2006). On one hand, first condensates (refractory inclusions, forsterite, and metal), started forming during this stage. On the other hand, the residual primitive dust associated to those regions will be fractionated as well. In other words, both ambient gas and primordial dust will be responding to the temperature profile (background), which can be modified locally by transient heating events.

When the star accretion rate decreases and the protosun enters into the T-Tauri star regime (cooler environment), and considering the geometry of the disk (Figure 5.27), the replenishment of primordial dust and its abundance increases with heliocentric distances. At this stage, when the disk was 2-4 My old the snow line is thought to have been located between 2-3 AU (Doyle et al., 2015; Ciesla & Cuzzi, 2006) roughly matching the current position of the main asteroid belt. An example of the snow line associated to the physical conditions of a T-Tauri star is shown in figure 5.28 after Walsh et al. (2013). The diagonal red band indicates a higher proportion of water in gas phase due to evaporation of water ice, consistent with the thermal profile of Figure 5.27.

With this schema in mind, and according to the formation environment of Type I and Type II chondrules from OCs, it is possible that chondrule precursors, in general, were processed in the upper skin layers of the disk (Hubbard & Ebel, 2015). This provides a strong constraint on the chondrule formation mechanism(s). In this regard, chondrule formation in disk-winds is a suitable option (Salmeron & Ireland, 2012).

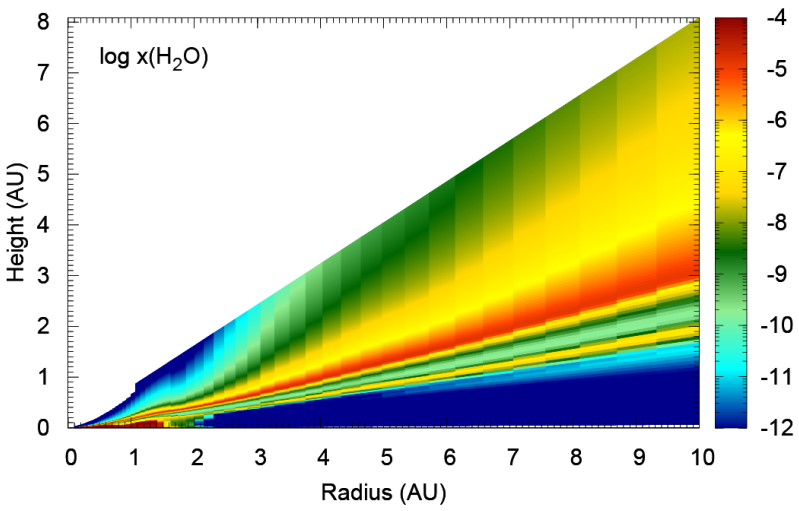

Figure 5.27. Fractional abundances of H_2O molecules in the gas phase as a function of disk radius and height up to a radius of 10 AU. Warm colors represent a higher amount of water in the gas phase.

Therefore, the different ingredients present at distinct orbital distances, broadly dependent on the background thermal gradient, will give birth to planetesimals, planetary embryos, and eventually, the current planets that are seen today. This conceptual model explains the general architecture of the solar system, however, star formation is a chaotic process and conditions are far from being constant, therefore some overlap is expected. Additionally, it appears that giant planet migration also played an important role in shaping the solar system (e.g. Walsh et al., 2011).

5.9. The oxygen isotope planetary reservoir of the inner solar system

In section 5.8 was mentioned that the oxygen isotope composition of Type I chondrule olivine is delimiting the borders of the main population sample distribution. This is more evident when examining figure 5.26a and 5.26b since most of the statistical outliers have a Type I olivine composition. On the other hand, Type II chondrule olivine forms a tight cluster close to $\delta^{18}O$ ~4.5‰ and $\delta^{17}O$ ~3.0‰ between the Y&R and PCM lines.

In this regard, the oxygen isotope composition of Type I and Type II chondrule olivine from OCs is very different to what occurs in carbonaceous chondrites where Type I chondrules are notably ^{16}O-rich relative to Type II chondrules although Type I chondrules with oxygen ratios similar to Type II chondrules have also been found but are much less common (Rudraswami et al., 2011; Ushikubo et al., 2012; Tenner et al., 2013, 2015, 2017; Schrader et al., 2014).

Assuming that the oxygen isotope composition of solar system materials can be explained in the context of the photochemical and self-shielding model, Type II chondrules from carbonaceous chondrites have usually been interpreted as a result of equilibration of ^{16}O-rich silicate precursors during chondrule formation in an environment with higher dust/gas ratio and the presence of $^{17,18}O$-rich water ice which increment both the oxygen fugacity of the ambient gas and the oxygen isotope composition of chondrules (e.g. (Connolly & Huss, 2010; Schrader et al., 2014; Tenner et al., 2015). The absence of this pattern in OC chondrules could be reflecting: 1) the lack of ^{16}O-rich primordial precursors on their chondrule formation region, 2) the equilibration with a long-lasting planetary-like oxygen reservoir usually explained as the mixture and homogenization of ^{16}O-rich solar and $^{17,18}O$-rich nebula water gas reservoirs or both.

In view of the homogeneity in oxygen isotopes among chondrules from OCs, it is not clear whether or not heavy ice water is responsible for both the oxygen isotopic composition and the FeO-content of Type I and Type II chondrule olivine. If this was the case, a natural consequence would be that Type II chondrules should be heavier in oxygen isotopes than Type I chondrules but the opposite is actually seen considering the mean values, although not resolvable, for Type I olivine is $\Delta^{17}O$ ~0.74‰ and $\Delta^{17}O$ ~0.66‰ for Type II olivine.

Additionally, as noted before, Type I chondrule olivine record more variability in $\Delta^{17}O$ values compare to Type II chondrule olivine for which the distribution is tighter both considering $\Delta^{17}O$ ratios and the Type II cluster on the triple oxygen plot. Moreover, what is still more intriguing is the fact that the highest $\Delta^{17}O$ compositions ($^{17,18}O$-richer) of this research are related to Type I chondrule olivines reaching a maximum of $\Delta^{17}O$ ~3.97‰ in a forsteritic grain (~Fa1, spot GRO_CH382_1) while the maximum in a Type II olivine was $\Delta^{17}O$ ~2.28‰ (~Fa11, spot MIL_CH472_2), both part of the 'statistical outliers'. Thus, if heavy water is influencing the oxygen isotope composition of OC chondrules, it appears to be affecting Type I chondrules to a higher extent than Type II chondrules. Given the above, the usual interpretation employed to explain the oxygen isotope differences among Type I and Type II chondrules from carbonaceous chondrites does not fit for H vs L vs LL OC chondrules.

In this regard, it has been pointed out by Krot et al. (2010) that, assuming a molecular cloud silicate dust or primordial dust with ^{16}O-rich composition ($\Delta^{17}O$ ~ -24‰) and posterior evolution towards higher $\Delta^{17}O$ planetary reservoir-like values with time is not clear considering the time frame required to mix and homogenised the solar and nebula water reservoirs, which is the preferred model to explain the planetary reservoir.

The latter is consistent with the previous discussion where the overlapping ages of refractory inclusions and chondrules from OC and carbonaceous chondrites and their oxygen isotope compositions suggest that the oxygen isotope gaseous reservoirs of the protoplanetary disk were spatially separated, possibly reflecting an overall radial gradient characterized by the availability of the main oxygen carrier species (CO, SiO, and H_2O).

Therefore, Krot et al. (2010) suggested that the primordial silicate dust, >99% amorphous dust of the interstellar medium (Nguyen et al., 2016), is on average ^{16}O-poor and close to $\Delta^{17}O$ ~0‰. Similar to Krot et al. (2010), to explain the oxygen isotope composition of Type I and Type II chondrules from OCs, a conclusion of this investigation is that instead of ^{16}O-rich and close to solar, the primordial dust average of the solar nebula had an oxygen isotope composition close to planetary. In this regard, it is proposed here that the gaseous planetary reservoir is a mixture of oxygen carriers dominated by SiO, which was established during the main collapse phase of the Sun-formation process at the earliest stages of disk evolution when temperatures were high enough to sublime presolar dust.

Furthermore, based on the results of this research and the meteoritical record, it is proposed that the expression of the planetary reservoir is recorded by the main population of chondrules accreted by OCs and that the average composition of the primordial dust is $\Delta^{17}O$ ~0.7‰. Particularly, Type II chondrules, apart from their oxygen isotope composition, are also chemically characterized by higher abundances of the rock-forming elements with moderately volatile elements closer to chondritic (Scott & Krot, 2014). Therefore, if chondrules are thermochemical sensors of the protoplanetary disk gas (e.g. Libourel & Portail, 2018) then the ambient gas in which Type II chondrules were formed was characterized by a signature closer to chondritic as a consequence of being formed closer to a dustier midplane. Then, based on Type II chondrules, the gaseous planetary reservoir proposed here accounts for both its oxygen isotope and chemical compositions.

Therefore, after removing statistical outliers at the 95% confidence interval, the mean $\delta^{18}O$ and $\delta^{17}O$ composition of Type II chondrules constraining the average composition of the gaseous planetary reservoir on the triple oxygen diagram is $\delta^{18}O = 4.64 \pm 0.15$‰ (SE, $\sigma_{95\%}$) and $\delta^{17}O = 3.03 \pm 0.10$‰ (SE, $\sigma_{95\%}$), with variabilities (2SD, $\sigma_{95\%}$) of 0.97‰ and 0.52‰ (2SD, $\sigma_{95\%}$), respectively. External errors are calculated by propagating the uncertainties at the 95% confidence interval of the laser fluorination and average internal error of San Carlos olivine data measured in the sessions where pristine samples were analyzed.

Chondrule oxygen isotope data from the literature is shown in figure 5.29 and it appears that a tendency from ^{16}O-richer compositions towards the composition of the planetary reservoir exists, which based on section 5.5 discussion, could indicate that chondrules with compositions similar to the planetary reservoir have been formed closer to it. This tendency is clearer for bulk chondrule composition data and it is highlighted by the red-dashed arrow.

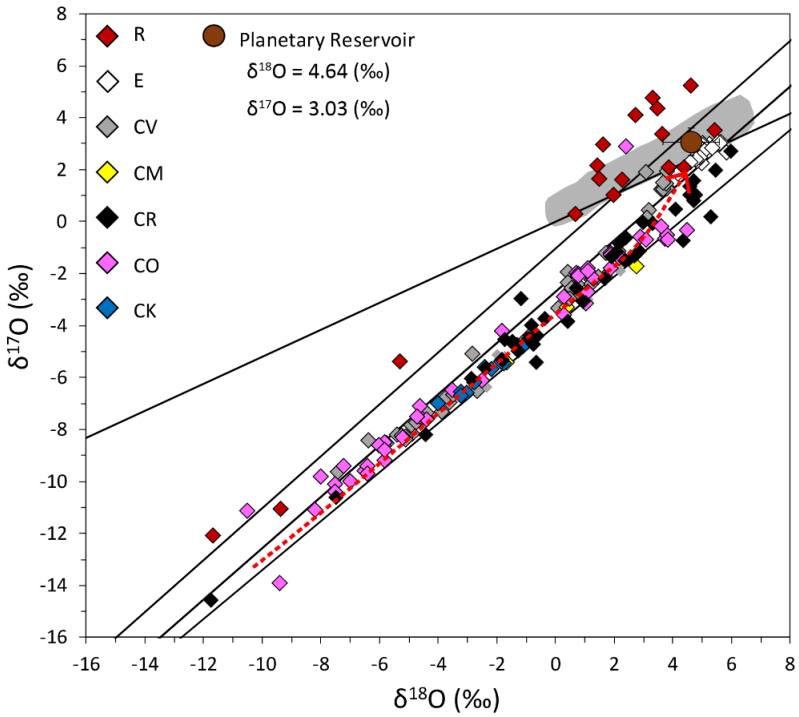

Figure 5.28. Triple oxygen isotope plot of the planetary reservoir gas composition and chondrule compositions from the literature. R: Miller et al., 2017 and Greenwood et al., 2000. E: Clayton and Mayeda, 1985. CV: Clayton et al., 1983; Rubin et al., 1990; Rudraswami et al., 2011. CM: Rowe et al., 1984. CR: Weisberg et al., 1993; Krot et al., 2006; Jones et al., 2004. CO: Jones et al., 2000; Tenner et al., 2013; Kunihiro et al., 2004. CK: Clayton and Mayeda, 1999. The grey area represents the main chondrule population for OCs reported here. The red-dashed arrow shows the transition from ^{16}O-richer reservoirs towards the planetary reservoir composition. Errors of the planetary reservoir are the 2SD ($\sigma_{95\%}$) variability.

Different lines of evidence are available in the literature that support the planetary reservoir proposed here. Some of this data has been presented in previous sections e.g. the time of formation and oxygen isotope composition of refractory inclusions and chondrules from OCs and other chondrite classes, and the chemical composition of OCs chondrules.

The case of refractory inclusions (CAIs) is particularly interesting since the ^{16}O-poorest compositions (Δ^{17}O ~-2‰ to ~0‰; (Clayton, 1993; Kawasaki et al., 2012; Simon et al., 2016; Aléon, 2018 and references therein) are usually associated to less refractory minerals in CAIs Wark-Lovering rims with a higher proportion of Si in their atomic structure e.g. Åkermanite (melilite), anorthite, and pyroxene. Additionally, FUN (fractionation and unidentified nuclear effects) CAIs, are thought to have been mass-fractionated due to melting and evaporation in a vacuum (<10^{-6} bar; Krot et al., 2010), and posteriorly equilibrated in a gas with a composition close to the planetary reservoir

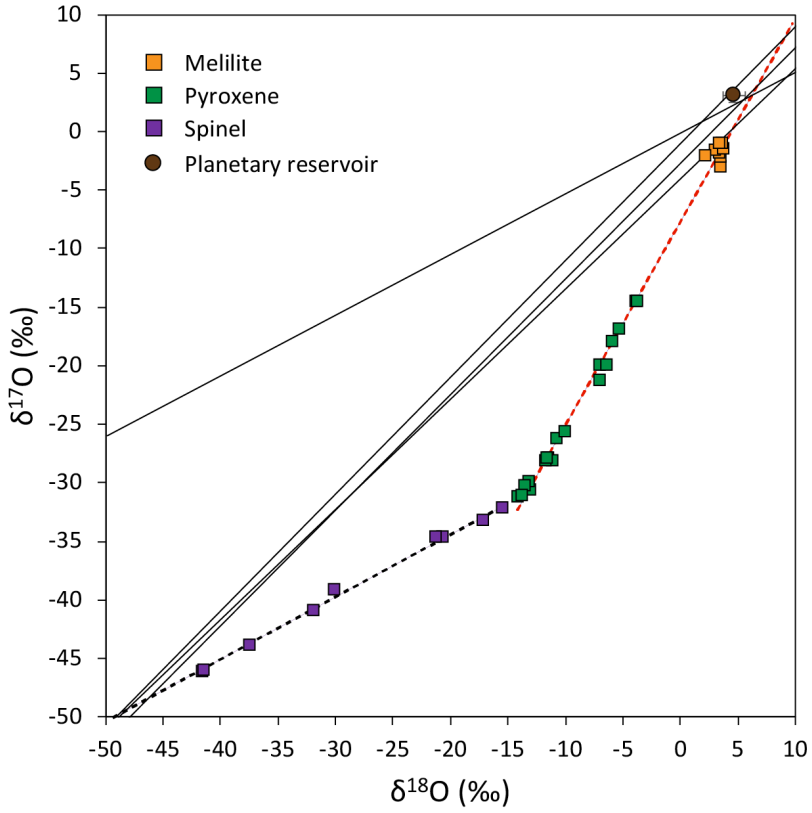

Figure 5.29. Oxygen isotopic compositions of individual phases from FUN CAIs. Data from Williams et al. (2017).

(Ireland, 1992; Krot et al., 2010; Williams et al., 2017). These trends can be observed in figure 5.30 which shows data from Williams et al. (2017).

The black-dashed line, parallel to the TF line, represents the isotope mass-fractionation effect associated with spinel ($\Delta^{17}O \sim -24‰$). After reaching a maximum, the FUN CAI melt starts forming pyroxene and finally melilite (Åkermanite) in a distinct physical and chemical regime, probably reflecting the characteristics of the proposed planetary reservoir (SiO) since the trend associated to the sequence pyroxene-melilite (red-dashed line) intersects, within uncertainties, the oxygen isotope composition of it.

In the same line, considering Type I chondrules of carbonaceous chondrites, Marrocchi & Chaussidon (2015) modelled the oxygen isotopic effects resulting during chondrule formation between precursor silicate dust and a gas enriched in SiO during the partial melting and evaporation of that dust. They found two main results: 1) consistency of their modelled results and the bulk-chondrule oxygen composition of the literature and 2) oxygen isotopic disequilibrium between chondrule pyroxene and olivine (Figure 5.31). It

is important to mention here that this disequilibrium is very small and not resolvable within SIMS errors in a single chondrule.

However, although it is not apparent from their rationale why they choose the values of $\delta^{18}O$ = 10‰ and $\delta^{17}O$ = 9‰ for the initial canonical gas composition, their results on figure 5.31 at 1600K, similar to FUN CAIs, show that this gas changes as a function of the degree of evaporation of CI-like dust having the oxygen isotope composition of the forsteritic precursors, which in this case are $\delta^{18}O$ of -15‰ (blue), -10‰ (red), -5‰ (green), and 0‰ (yellow), and the dust/gas ratio increases from the upper right to the lower left in each case (0.1 to 100 times). For instance, a precursor with initial composition of $\delta^{18}O$ = -15‰ on the CCAM line processed in a dust/gas ratio of 0.1 will generate a final product close to $\delta^{18}O$ ~ -7‰ and $\delta^{17}O$ ~ -10‰. Interestingly, the closest the precursor is to the TF line, the steeper the slope of the model.

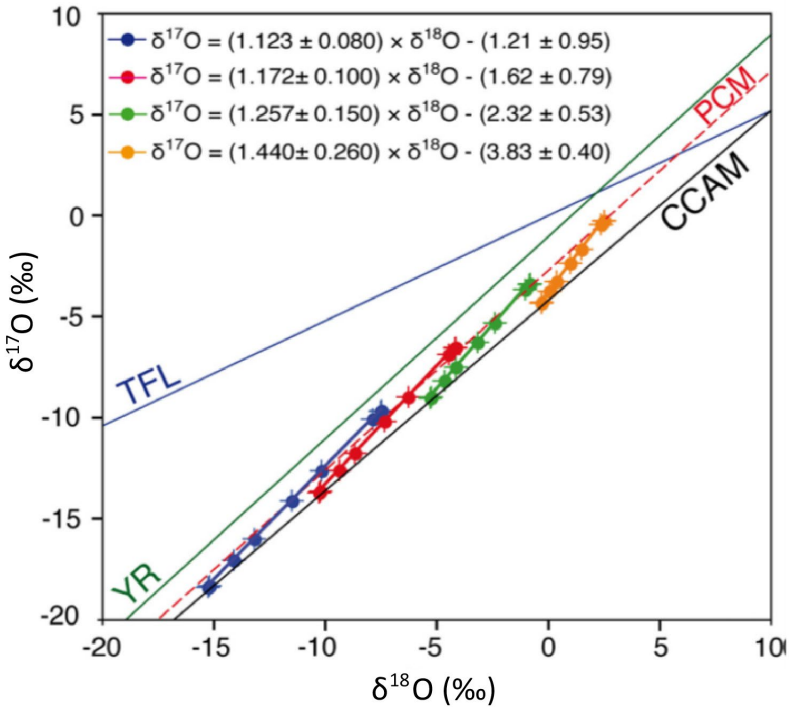

Figure 5.30. Triple oxygen isotope plot modified from Marrocchi and Chaussidon (2015) showing results of the model for gas-melt interactions at 1600K between chondrule precursors with different oxygen isotope compositions and an initial ambient gas at $\delta^{18}O$ = 10‰ and $\delta^{17}O$ = 9‰.

Assuming that the planetary reservoir was already established, the same model is used and the oxygen isotope composition of the initial gas is set to the ratios proposed here for the planetary reservoir, $\delta^{18}O$ = 4.64‰ and $\delta^{17}O$ = 3.03‰ (model and results in Supplementary Information). Similar results to Marrocchi & Chaussidon (2015) are obtained when changing the starting composition of precursor materials, but more interestingly, the isotopic composition of SiO_{gas} resulting from the vaporization of CI-like primordial dust whose average composition is that of the planetary reservoir falls on the zone where most forsteritic olivine (black circles) of the main chondrule population plots in the triple-oxygen diagram (Figure 5.32). Since forsterite shows no mass-fractionation with SiO gaseous molecule in the range of temperatures of chondrule formation (Javoy et al., 2012) then the mass-fractionation pattern observed relative to Type II chondrules in OCs is reflecting the interaction of a forsteritic melt and the isotopic composition of the SiO molecules of the planetary reservoir, and does not necessarily imply mass-fractionation due to evaporation and condensation processes of chondrule precursors invoked by Kita et al. (2010) during their formation.

This explanation could also be used for chondrules from enstatite and Rumuruti chondrites since this pattern is also observed in those chondrite classes. Moreover, by changing the oxygen isotope composition of chondrule precursors, the whole range of chondrule compositions for enstatite, ordinary, and Rumuruti chondrite chondrules is predicted. An example of the model is given in figure 5.32 where the Mg-rich precursor (red circle) was chosen to have an oxygen isotope composition of $\delta^{18}O$ = 6.00‰ and $\delta^{17}O$ = 3.20‰. Thus, when the dust/gas ratio increases from 0 to 200 times, trend shown by the arrows, the predicted composition of pyroxene, (green diamonds, enstatite chondrules) will evolve from $\delta^{18}O$ ~4.7‰ to ~5.8‰ in the direction of the precursor composition. The modeled pyroxene compositions match with the bulk-chondrule isotopic composition of pyroxene chondrules from enstatite chondrites (grey circles; Clayton et al., 1984).

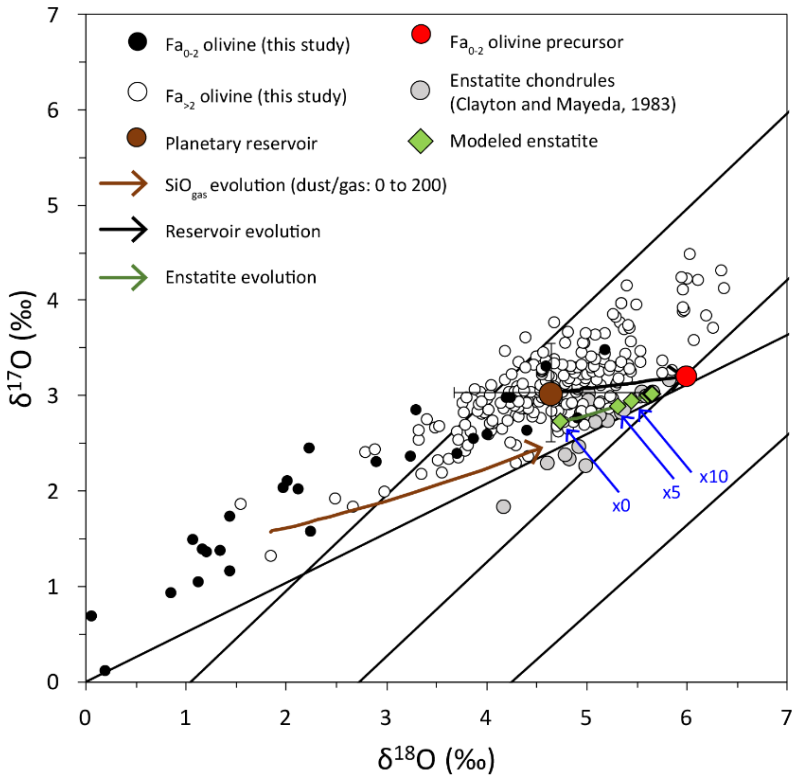

Figure 5.31. Triple oxygen isotope plot results of the model for gas-melt interactions at 1600K between forsteritic precursor with an oxygen isotope composition of $\delta^{18}O$ = 6.00‰ and $\delta^{17}O$ = 3.20‰ and the planetary reservoir gas at $\delta^{18}O$ = 4.64‰ and $\delta^{17}O$ = 3.03‰. Green diamonds reflect the composition of the enstatite produced when increasing the dust/gas ratio from 0 to 200 times solar. Blue arrows highlight different dust/gas ratios.

As pointed out by Marrocchi & Chaussidon, (2015), an advantage of this model, is that it requires lower dust enrichments compared to the high ratios proposed in the literature (up to dust/gas ratio > 10^6) since such high ratios are quite problematic from models of dust-grain dynamics in protoplanetary disks which allow concentration factors of less than 10 in the chondrule-forming regions (e.g. Hubbard et al., 2018). The existence of the proposed planetary reservoir from the earliest stages of disk evolution seems to be an appropriate solution for the inconsistencies pointed out by (Hubbard et al., 2018). For instance, from figure 5.32, when predicting the oxygen isotopic composition of chondrules from enstatite chondrites, the blue arrows indicate the dust/gas ratio needed to form pyroxene and is quite clear that after a dust/gas ratio of 5 to 10, the change in oxygen isotopic compositions of pyroxene is marginal. The same occurs when modeling chondrules from carbonaceous chondrites (Marrocchi & Chaussidon, 2015).

An important line of evidence supporting this reservoir conception is related to the crystalline grains found in Comet Wild-2 sampled by the Stardust mission (Wooden et al., 2017 and references therein). Krot et al. (2010) pointed out that the presence of refractory inclusion-like material together with the presence of olivine with oxygen isotope compositions close to the planetary reservoir, which are more likely to have been processed closer to the Sun than in the cometary formation region (~20 AU), suggests that a ^{16}O-poor reservoir (the planetary reservoir) was present from the earliest stages of the solar system evolution because at this stages the outward transport of material from the inner solar system is more efficient and energetic to reach such orbital distances (Krot et al. 2010 and references therein).

In addition to some cometary material, the bulk oxygen isotope composition of Earth, Moon, Mars, chondrites, achondrites, and iron meteorites, which some of them are thought to have accreted ~0.1 to 0.3 My after formation of refractory inclusions (Kruijer et al., 2014), have oxygen isotope compositions ranging close to planetary (Greenwood et al., 2017) compared to the full range of oxygen isotope compositions observed in the solar system. Moreover, it has been reported that some metallic meteorites have chondrule-like silicate inclusions embedded within them with a mean value of Δ^{17}O ~0.7‰ (McDermott et al., 2016). Therefore, it is possible that the limited variation of oxygen isotopes in planetary bodies of the solar system is reflecting variation around the planetary reservoir proposed here due to the addition or removal of ^{16}O-richer ^{16}O-poorer components.

In a galactic scale, it is unknown under what context the planetary reservoir could be related to the photochemical and self-shielding model (PSS) and what process(es) might be involved for its mean composition to be generated. Krot et al. (2010) argued that the average oxygen isotope composition of the primordial dust could have been inherited from galactic chemical evolution (GCE) or from the pollution of the protosolar molecular cloud by a massive star ejecta. However, Lugaro et al. (2012), assessing the cosmochemical mass-independent fractionation line of oxygen isotopes in the solar system, ruled out GCE as an explanation of it. Additionally, they also pointed out that a younger dust component compared to the gas of the solar system (star ejecta) is unlikely to explain the ^{16}O-poor composition (planetary) of the primordial dust.

In this regard, from infrared spectra data, it is known that >99% of silicates in the interstellar medium (ISM) are amorphous grains having FeO compositions < Fa10 and stoichiometries between olivine and pyroxene (Nguyen et al., 2016). This much lower degree of crystallinity compared to circumstellar outflows is attributed to amorphization during their residence in the ISM via grain destruction processes such as grain collisions, evaporation in SN shocks, sputtering by shocks and stellar winds, and exposure to cosmic galactic grains (Nguyen et al., 2016; Zinner, 2014). Therefore, it might be possible that the aforementioned galactic scale processes could be causing oxygen isotope homogenization of primordial silicates within the ISM. If this is the case, it could be possible that other stellar systems having terrestrial planets with oxygen isotope compositions similar to the planetary reservoir of the solar system exist.

Given the above, designing experiments or modelling on the amorphization of crystalline silicates to test the hypothesized consequences in their oxygen isotope composition appears to be the next step to understand the planetary reservoir at a galactic scale, its position in the triple-oxygen diagram, and the context with the PSS model of the solar system.

Finally, it is worth mentioning that since the volatility of the main oxygen-bearing molecules are different with CO being more volatile than H_2O, which is more volatile than SiO, the composition of the ambient gas in different locations of the solar nebula will depend on the relative proportions of the oxygen carriers and this proportions will change according to the thermal structure of the protoplanetary disk. In this view, the presence of the other species is guaranteed but will be diluted by the presence of the main one.

Therefore, if the Sun is enriched in highly volatile elements (Tc < 500K) compared to CI chondrites (Wang et al., 2018), which are usually accepted to represent the chemical composition of the primordial dust of the molecular cloud, but at the same the Sun and CI have practically the same composition in relatively more refractory elements, and because the Sun represents the average composition of the solar nebula, then the refractory composition of the Sun is simply reflecting the admixture of this primordial dust (CI-like) and, as pointed out by Ireland (2012), the enrichment of highly volatile elements in the Sun is indicative that these elements were mainly accreted in gaseous

phases. Then, forming ^{16}O-rich refractory inclusions at high temperatures in a gas of solar composition is trivial since volatile species like CO are enriched in such a gas, assuming that the photochemical and self-shielding model is correct since it predicts a ^{16}O-rich composition for CO molecules.

On the other hand, since primordial dust is depleted in volatile elements (e.g. C and O) compared to the Sun, the planetary reservoir envisioned here would be naturally ^{16}O-depleted yet dominated by rock-forming elements. Therefore, a mechanism to explain the planetary reservoir from mixing of solar and nebula water is not needed (e.g. Yurimoto & Kuramoto, 2004; Alexander et al., 2017). However, closer to the snow line H_2O might be playing an important role in oxidizing Fe^0 to Fe^{2+} making it available for olivine in an environment like the solar nebula. Therefore, the oxygen isotope compositions of solar system material can be explained considering these three discrete oxygen reservoir entities with CO, dominating close to the Sun at the highest ambient temperatures, SiO at lower ambient temperatures but also being constantly replenished at namely the primordial dust evaporation front due to the infalling molecular cloud, and H_2O enriched in the proximities of the snow line.

More research is needed to be done in order to further understand such a view of the planetary reservoir and its implications, however, this picture is promising considering the astrophysical context under which chondrules and, moreover, planets are thought to be formed (Salmeron & Ireland, 2012; Hubbard et al., 2018).

6. Conclusions

The results of this study may be summarized as follows:

- Through systematic in situ measurement of oxygen isotope composition of chondrule olivine from ordinary chondrites, and a robust statistical assessment, it has been proved for the first time that ordinary chondrite parent bodies from H, L, and LL groups sampled chondrules from the same main population of the protoplanetary disk. This population is characterised by a mean of $\Delta^{17}O = 0.74 \pm 0.10‰$ ($\sigma_{95\%}$) with a variability of 0.53‰ ($\sigma_{95\%}$). Therefore, this population was thermally processed in a gaseous oxygen isotope reservoir with a composition dominated by ~0.7‰.
- Although less frequent, chondrules with ^{16}O-poorer and ^{16}O-richer signatures but close to the shoulders of the main population are also present indicating that they could have been formed in adjacent oxygen isotope reservoirs and/or in a slightly perturbed main reservoir. In addition, distinctively lighter $\Delta^{17}O$ ratios relative to the main chondrule population have also been found in chondrules and olivine relicts. These signatures were acquired in reservoirs common to the formation region of chondrules from carbonaceous chondrites and refractory inclusions. This is the first time that refractory inclusion-like oxygen isotope compositions are found in chondrules from OCs.
- Based on the $\Delta^{17}O$ chondrule sample distribution and the statistical assessment it is suggested that the gaseous reservoirs of the inner solar system were chiefly controlled by the thermal structure of the protoplanetary disk with lighter compositions towards the Sun and heavier compositions probably closer to the snow line.
- The low probability of finding ^{16}O-rich signatures indicates that solid mixing between reservoirs was limited in the inner solar system. Moreover, since carbonaceous chondrites accreted at farther orbital distances than OC asteroids, it appears that the mechanism to transport chondrules to the accretion zone of carbonaceous chondrites was quite energetic, probably x- and/or disk-winds.

- The implications of such a view appear to be in conflict with some of the fundamental conditions previously used to highlight chondrule and chondrite formation, particularly, the chondrule-matrix complementarity. However, considering the robustness of the results presented here and the literature data, it is suggested that the chondrule-matrix complementarity needs at least to be revised and, probably, reconceptualized. In this regard, the geochemical affinities of the nucleosynthetic 'anomalies' and their partitioning associated to the main chondritic objects (chondrules, refractory inclusions, and matrix) and the thermal structure of the protoplanetary disk are essential. These compositions, associated with siderophile elements, e.g. Mo and Ru, appear to be the key since they are linked to a nucleosynthetic metal carrier within the matrix.
- Considering that OCs accreted one main chondrule population with a $\Delta^{17}O$ average composition lower, within uncertainties, than the whole-rock composition of H, L, and LL chondrites, the shift towards ^{16}O-poorer composition in bulk chondrites has to be related to the composition of the matrix, most likely $^{17,18}O$-rich water ice.
- Furthermore, when the thermal profile of the disk is considered, the bulk chemical and oxygen isotope compositions of EOCs correlate with their putative accretion locations, with H parent body or bodies agglomerating closer to the Sun than L and LL, in that order. Then an overall gradient in $\Delta^{17}O$ correlating to heliocentric distances is proposed for terrestrial planets and asteroids. This gradient has been proposed using Mo and Ru nucleosynthetic whole-rock compositions of solar system material which in the case of chondrites appears to be correlated to the matrix modal abundances.
- Given the above, it is suggested that the matrix proportion accreted at different heliocentric distances is the residual primordial dust available due to the thermal profile (geometry) of the protoplanetary disk. If this is the case, the apparent nucleosynthetic dichotomy (carbonaceous and non-carbonaceous meteorites), usually explained by the separation of nucleosynthetic reservoirs due to proto Jupiter formation, may not exist. In this regard, siderophile elements are more attractive than lithophile elements since partitioning of the latter among chondrite components are more difficult to assess.

- Owing to the conclusion that Type I and Type II chondrules from the main chondrule population were processed in the same oxygen isotope reservoir, and considering the physicochemical conditions needed to explain their different chemical compositions, it is suggested that the OC chondrule formation region was chemically differentiated in both a vertical and radial fashion, with Type II chondrules being processed relatively closer to the midplane than Type I chondrules, at cooler ambient temperatures.
- The above conclusion together with the previous suggestion that the oxygen isotope reservoirs of the inner solar system were controlled by the thermal gradient of the protoplanetary disk with ^{16}O-richer compositions towards the Sun and ^{16}O-poorer compositions probably closer to the snow line, are ground-breaking since it gives spatial meaning to one of the most enigmatic problems in cosmochemistry, chondrule formation, through the measurement of oxygen isotope which in turn has played a key role in meteoritics and cosmochemistry.
- Moreover, it is proposed that the radial and vertical chemical stratification of the ambient gas was a regional characteristic that was probably established early on and lasted until the gas was dissipated from the inner solar system. In this picture, it is possible that, in general, chondrule processing would have occurred in the upper layers of the disk. This would suppose an important constraint to chondrule formation models. In this regard, disk-winds appear to be a prospective mechanism.
- The Type I vs Type II long-lasting dichotomy conundrum, mainly observed in chondrules from OCs, has been explained here by proposing a change in the paradigm related to the oxygen isotope reservoirs of the solar system, particularly the so-called planetary reservoir. It is proposed that the gaseous oxygen isotope planetary reservoir is a discrete reservoir enriched in SiO_{gas} molecules and other rock-forming elements that was established early in the solar system evolution reflecting the average oxygen isotope composition of the primordial dust of the solar nebula.
- The planetary reservoir composition was recorded by the main population of chondrules from OCs. In particular, the $\delta^{17}O$ and $\delta^{18}O$ ratios of the planetary reservoir is calculated using data exclusively from Type II chondrules since they

account for both the chemical composition, enriched in rock-forming and the oxygen isotopes. Therefore, the average composition of this reservoir is $\delta^{18}O$ = 4.64 ± 0.15‰ ($\sigma_{95\%}$) and $\delta^{17}O$ = 3.03 ± 0.10‰ ($\sigma_{95\%}$), with variabilities of 0.97‰ and 0.52‰ ($\sigma_{95\%}$), respectively.

The aforementioned reservoir could be the answer to elucidate fundamental questions about chondrule formation and, moreover, planet formation, as a general process, since terrestrial planets in other stellar systems could be responding to similar physicochemical conditions and processes.

REFERENCES

Aléon, J. (2016). Oxygen isotopes in the early protoplanetary disk inferred from pyroxene in a classical type B CAI. *Earth and Planetary Science Letters*, *440*, 62–70. https://doi.org/10.1016/j.epsl.2016.02.007

Aléon, J. (2018). Closed system oxygen isotope redistribution in igneous CAIs upon spinel dissolution. *Earth and Planetary Science Letters*, *482*, 324–333. https://doi.org/10.1016/j.epsl.2017.11.027

Alexander, C. M. Od., Grossman, J. N., Ebel, D. S., & Ciesla, F. J. (2008). The Formation Conditions of Chondrules and Chondrites. *Science*, *320*(5883), 1617–1619. https://doi.org/10.1126/science.1156561

Alexander, Conel M. O'D. (2017). The origin of inner Solar System water. *Philosophical Transactions of the Royal Society A: Mathematical, Physical and Engineering Sciences*, *375*(2094), 20150384. https://doi.org/10.1098/rsta.2015.0384

Alexander, Conel M. O'D., Nittler, L. R., Davidson, J., & Ciesla, F. J. (2017). Measuring the level of interstellar inheritance in the solar protoplanetary disk. *Meteoritics & Planetary Science*, *52*(9), 1797–1821. https://doi.org/10.1111/maps.12891

Amelin, Y., & Ireland, T. R. (2013). Dating the Oldest Rocks and Minerals in the Solar System. *Elements*, *9*(1), 39–44. https://doi.org/10.2113/gselements.9.1.39

Amelin, Y., & Krot, A. (2007). Pb isotopic age of the Allende chondrules. *Meteoritics & Planetary Science*, *42*(7–8), 1321–1335. https://doi.org/10.1111/j.1945-5100.2007.tb00577.x

Amelin, Y., Krot, A. N., Hutcheon, I. D., & Ulyanov, A. A. (2002). Lead Isotopic Ages of Chondrules and Calcium-Aluminum–Rich Inclusions. *Science*, *297*.

Amelin, Yuri, Kaltenbach, A., Iizuka, T., Stirling, C. H., Ireland, T. R., Petaev, M., & Jacobsen, S. B. (2010). U–Pb chronology of the Solar System's oldest solids with variable 238U/235U. *Earth and Planetary Science Letters*, *300*(3–4), 343–350. https://doi.org/10.1016/j.epsl.2010.10.015

Ash, R. D., Rumble, D., Alexander, C. M. O., & MacPherson, G. J. (1998). Oxygen isotopes in isolated chondrules from the Tieschitz ordinary chondrite: initial compositions and differential parent body alteration. *LUNAR AND PLANETARY SCIENCE*, *29*.

Ávila, J. N., Ireland, T. R., Holden, P., Lanc, P., Schram, N., Latimore, A., … Williams, I. S. (In Review). HIGH-PRECISION OXYGEN ISOTOPE 1 MEASUREMENTS OF ZIRCON 2 REFERENCE MATERIALS WITH THE SHRIMP-SI. *Chemical Geology*.

Baertschi, P. (1976). ABSOLUTE 180 CONTENT OF STANDARD MEAN OCEAN WATER. *Earth and Planetary Science Letters*, *31*, 341–344.

Bischoff, A., Scott, E. R. D., Metzler, K., & Goodrich, C. A. (2006). Nature and Origins of Meteoritic Breccias. In *Meteorites and the Early Solar System II* (p. 34).

Bischoff, Addi, Vogel, N., & Roszjar, J. (2011). The Rumuruti chondrite group. *Chemie Der Erde - Geochemistry*, *71*(2), 101–133. https://doi.org/10.1016/j.chemer.2011.02.005

Blackburn, T., Alexander, C. M. O., Carlson, R., & Elkins-Tanton, L. T. (2017). The accretion and impact history of the ordinary chondrite parent bodies. *Geochimica et Cosmochimica Acta*, *200*, 201–217. https://doi.org/10.1016/j.gca.2016.11.038

Bland, P. A., Alard, O., Benedix, G. K., Kearsley, A. T., Menzies, O. N., Watt, L. E., & Rogers, N. W. (2005). Volatile fractionation in the early solar system and chondrule/matrix complementarity. *Proceedings of the National Academy of Sciences*, *102*(39), 13755–13760. https://doi.org/10.1073/pnas.0501885102

Bollard, J., Connelly, J. N., Whitehouse, M. J., Pringle, E. A., Bonal, L., Jørgensen, J. K., … Bizzarro, M. (2017). Early formation of planetary building blocks inferred from Pb isotopic ages of chondrules. *Science Advances*, *3*(8), e1700407. https://doi.org/10.1126/sciadv.1700407

Bonal, L., Quirico, E., Flandinet, L., & Montagnac, G. (2016). Thermal history of type 3 chondrites from the Antarctic meteorite collection determined by Raman spectroscopy of their polyaromatic carbonaceous matter. *Geochimica et Cosmochimica Acta*, *189*, 312–337. https://doi.org/10.1016/j.gca.2016.06.017

Bridges, J. C., & Ireland, T. R. (2015). OXYGEN ISOTOPE ANALYSES BY SHRIMP OF CHONDRULES IN HIGHLY UNEQUILIBRATED LL3 CHONDRITES (Vol. 46, pp. 1674–1675). Presented at the Lunar and Planetary Science Conference.

Bridges, J. C., Li, C., Franchi, I. A., Hutchison, R., Saxton, A. S., Pillinger, C. T., & Ouyang, Z. (1999). The relative effects of mineralogy and chondrule size on oxygen isotopic exchange in Bo Xian (LL3.9). *LUNAR AND PLANETARY SCIENCE*, *30*.

Bridges, John C, Franchi, I. A., Hutchison, R., Sexton, A. S., & Pillinger, C. T. (1998). Correlated mineralogy, chemical compositions, oxygen isotopic compositions and size of chondrules. *Earth and Planetary Science Letters*, *155*(3–4), 183–196. https://doi.org/10.1016/S0012-821X(97)00213-6

Budde, G., Burkhardt, C., Brennecka, G. A., Fischer-Gödde, M., Kruijer, T. S., & Kleine, T. (2016). Molybdenum isotopic evidence for the origin of chondrules and a distinct genetic heritage of carbonaceous and non-carbonaceous meteorites. *Earth and Planetary Science Letters*, *454*, 293–303. https://doi.org/10.1016/j.epsl.2016.09.020

Budde, G., Kleine, T., Kruijer, T. S., Burkhardt, C., & Metzler, K. (2016a). Tungsten isotopic constraints on the age and origin of chondrules. *Proceedings of the National Academy of Sciences*, *113*(11), 2886–2891. https://doi.org/10.1073/pnas.1524980113

Budde, G., Kleine, T., Kruijer, T. S., Burkhardt, C., & Metzler, K. (2016b). Tungsten isotopic constraints on the age and origin of chondrules. *Proceedings of the National Academy of Sciences*, *113*(11), 2886–2891. https://doi.org/10.1073/pnas.1524980113

Cameron, A. G. W. (1995). The first ten million years in the solar nebula. *Meteoritics*, *30*(2), 133–161. https://doi.org/10.1111/j.1945-5100.1995.tb01110.x

Chaumard, N., Defouilloy, C., & Kita, N. T. (2018). Oxygen isotope systematics of chondrules in the Murchison CM2 chondrite and implications for the CO-CM relationship. *Geochimica et Cosmochimica Acta*, *228*, 220–242. https://doi.org/10.1016/j.gca.2018.02.040

Chaussidon, M., Libourel, G., & Krot, A. N. (2008). Oxygen isotopic constraints on the origin of magnesian chondrules and on the gaseous reservoirs in the early Solar System. *Geochimica et Cosmochimica Acta*, *72*(7), 1924–1938. https://doi.org/10.1016/j.gca.2008.01.015

Choi, B.-G., McKeegan, K. D., Krot, A. N., & Wasson, J. T. (1998). Extreme oxygen-isotope compositions in magnetite from unequilibrated ordinary chondrites. *Nature*, *392*(6676), 577–579. https://doi.org/10.1038/33356

Ciesla, F. J. (2008). Radial transport in the solar nebula: Implications for moderately volatile element depletions in chondritic meteorites. *Meteoritics & Planetary Science*, *43*(4), 639–655. https://doi.org/10.1111/j.1945-5100.2008.tb00675.x

Ciesla, F. J., & Cuzzi, J. N. (2006). The Evolution of the Water Distribution in a Viscous Protoplanetary Disk. *Icarus*, *181*(1), 178–204. https://doi.org/10.1016/j.icarus.2005.11.009

Clayton, R. N. (1993). Oxygen Isotopes in Meteorites. *Ann. Rev. Earth Planet. Sci*, *21*, 15–149.

Clayton, R. N. (2003). Oxygen Isotopes in Meteorites. In *Treatise on Geochemistry* (Vol. 1, pp. 129–142). Elsevier.

Clayton, R. N., Grossman, L., & Mayeda, T. K. (1973). A Component of Primitive Nuclear Composition in Carbonaceous Meteorites. *Science*, *182*(4111), 485–488. https://doi.org/10.1126/science.182.4111.485

Clayton, R. N. (2002). Solar System: Self-shielding in the solar nebula. *Nature*, *415*(6874), 860–861. https://doi.org/10.1038/415860b

Clayton, R. N., Mayeda, T. K., Goswami, J. N., & Olsen, E. J. (1991). Oxygen isotope studies of ordinary chondrites. *Geochimica et Cosmochimica Acta*, *55*(8), 2317–2337.

Clayton, R. N., Mayeda, T. K., & Rubin, A. E. (1984). Oxygen isotopic compositions of enstatite chondrites and aubrites. *Journal of Geophysical Research*, *89*(S01), C245. https://doi.org/10.1029/JB089iS01p0C245

Connelly, J. N., Bizzarro, M., Krot, A. N., Nordlund, A., Wielandt, D., & Ivanova, M. A. (2012). The Absolute Chronology and Thermal Processing of Solids in the Solar Protoplanetary Disk. *Science*, *338*(6107), 651–655. https://doi.org/10.1126/science.1226919

Connolly, H. C., & Huss, G. R. (2010). Compositional evolution of the protoplanetary disk: Oxygen isotopes of type-II chondrules from CR2 chondrites. *Geochimica et Cosmochimica Acta*, *74*(8), 2473–2483. https://doi.org/10.1016/j.gca.2010.01.005

Connolly, H. C., & Jones, R. H. (2016). Chondrules: The canonical and noncanonical views: A Review of Chondrule Formation. *Journal of Geophysical Research: Planets*, *121*(10), 1885–1899. https://doi.org/10.1002/2016JE005113

Cuzzi, J. N., & Zahnle, K. J. (2004). Material Enhancement in Protoplanetary Nebulae by Particle Drift through Evaporation Fronts. *The Astrophysical Journal*, *614*(1), 490–496. https://doi.org/10.1086/423611

DeMeo, F. E., & Carry, B. (2014). Solar System evolution from compositional mapping of the asteroid belt. *Nature*, *505*(7485), 629–634. https://doi.org/10.1038/nature12908

Desch, S. J., Ciesla, F. J., Hood, L. L., & Nakamoto, T. (2005). Heating of chondritic materials in solar nebula shocks. In *Chondrites and the protoplanetary disk* (Vol. 341, p. 849).

Desch, S. J., & Connolly, H. C. (2002). A model of the thermal processing of particles in solar nebula shocks: Application to the cooling rates of chondrules. *Meteoritics & Planetary Science*, *37*, 183–207.

Desch, Steven J., Kalyaan, A., & Alexander, C. M. O. (2017). The Effect of Jupiter's Formation on the Distribution of Refractory Elements and Inclusions in Meteorites. *ArXiv:1710.03809 [Astro-Ph]*. Retrieved from http://arxiv.org/abs/1710.03809

Desch, Steven J., Morris, M. A., Connolly, H. C., & Boss, A. P. (2012). The importance of experiments: Constraints on chondrule formation models: Constraints on chondrule formation models. *Meteoritics & Planetary Science*, *47*(7), 1139–1156. https://doi.org/10.1111/j.1945-5100.2012.01357.x

Di Rocco, T., & Pack, A. (2015). Triple oxygen isotope exchange between chondrule melt and water vapor: An experimental study. *Geochimica et Cosmochimica Acta*, *164*, 17–34. https://doi.org/10.1016/j.gca.2015.04.038

Doyle, P. M., Jogo, K., Nagashima, K., Krot, A. N., Wakita, S., Ciesla, F. J., & Hutcheon, I. D. (2015). Early aqueous activity on the ordinary and carbonaceous chondrite parent bodies recorded by fayalite. *Nature Communications*, *6*(1). https://doi.org/10.1038/ncomms8444

Doyle, P. M., Krot, A. N., & Kaori, J. (2016). Aqueous alteration and accretion of chondrite parent bodies: when and where? *Elements*, *12*(5), 368–369. https://doi.org/10.2113/gselements.12.5.368

Ebel, D. S., & Grossman, L. (2000). Condensation in dust-enriched systems. *Geochimica et Cosmochimica Acta*, *64*(2), 339–366. https://doi.org/10.1016/S0016-7037(99)00284-7

Faure, G., & Mensing, T. M. (2007). *Introduction to planetary science: the geological perspective*. Dordrecht: Springer.

Fedkin, A. V., & Grossman, L. (2013). Vapor saturation of sodium: Key to unlocking the origin of chondrules. *Geochimica et Cosmochimica Acta*, *112*, 226–250. https://doi.org/10.1016/j.gca.2013.02.020

Fischer-Gödde, M., & Kleine, T. (2017). Ruthenium isotopic evidence for an inner Solar System origin of the late veneer. *Nature*, *541*(7638), 525–527. https://doi.org/10.1038/nature21045

Friedrich, J. M., Weisberg, M. K., Ebel, D. S., Biltz, A. E., Corbett, B. M., Iotzov, I. V., Wolman, M. D. (2015). Chondrule size and related physical properties: A compilation and evaluation of current data across all meteorite groups. *Chemie Der Erde - Geochemistry*, *75*(4), 419–443. https://doi.org/10.1016/j.chemer.2014.08.003

Friend, P., Hezel, D. C., & Mucerschi, D. (2016). The conditions of chondrule formation, Part II: Open system. *Geochimica et Cosmochimica Acta*, *173*, 198–209. https://doi.org/10.1016/j.gca.2015.10.026

Gerber, S., Burkhardt, C., Budde, G., Metzler, K., & Kleine, T. (2017). Mixing and Transport of Dust in the Early Solar Nebula as Inferred from Titanium Isotope Variations among Chondrules. *The Astrophysical Journal*, *841*(1), L17. https://doi.org/10.3847/2041-8213/aa72a2

Giletti, B. ., Semet, M. ., & Yund, R. . (1978). Studies in diffusion—III. Oxygen in feldspars: an ion microprobe determination. *Geochimica et Cosmochimica Acta*, *42*(1), 45–57. https://doi.org/10.1016/0016-7037(78)90215-6

Glassgold, A. E., Najita, J., & Igea, J. (2004). Heating Protoplanetary Disk Atmospheres. *The Astrophysical Journal*, *615*(2), 972–990. https://doi.org/10.1086/424509

Gounelle, M., Krot, A. N., Nagashima, K., & Kearsley, A. (2009). Extreme ^{16} O Enrichment in Calcium-Aluminum-rich Inclusions from the Isheyevo (CH/CB) Chondrite. *The Astrophysical Journal*, *698*(1), L18–L22. https://doi.org/10.1088/0004-637X/698/1/L18

Greenwood, J. P., Rubin, A. E., & Wasson, J. T. (2000). Oxygen isotopes in R-chondrite magnetite and olivine: links between R chondrites and ordinary chondrites. *Geochimica et Cosmochimica Acta*, *64*(22), 3897–3911. https://doi.org/10.1016/S0016-7037(00)00452-X

Greenwood, R. C., Burbine, T. H., Miller, M. F., & Franchi, I. A. (2017). Melting and differentiation of early-formed asteroids: The perspective from high precision oxygen isotope studies. *Chemie Der Erde*, *77*(1), 1–43. https://doi.org/10.1016/j.chemer.2016.09.005

Grossman, J. N., & Brearley, A. J. (2005). The onset of metamorphism in ordinary and carbonaceous chondrites. *Meteoritics & Planetary Science*, *40*(1), 87–122. https://doi.org/10.1111/j.1945-5100.2005.tb00366.x

Grossman, L., Beckett, J. R., Fedkin, A. V., Simon, S. B., & Ciesla, F. J. (2008). Redox Conditions in the Solar Nebula: Observational, Experimental, and Theoretical Constraints. *Reviews in Mineralogy and Geochemistry*, *68*(1), 93–140. https://doi.org/10.2138/rmg.2008.68.7

Grossman, L. (1972). Condensation in the primitive solar nebula. *Geochimica et Cosmochimica Acta*, *86*, 597–619.

Grossman, L., Fedkin, A. V., & Simon, S. B. (2012). Formation of the first oxidized iron in the solar system: Formation of the first oxidized iron in the solar system. *Meteoritics & Planetary Science*, *47*(12), 2160–2169. https://doi.org/10.1111/j.1945-5100.2012.01353.x

Hashizume, K., Takahata, N., Naraoka, H., & Sano, Y. (2011). Extreme oxygen isotope anomaly with a solar origin detected in meteoritic organics. *Nature Geoscience*, *4*(3), 165–168. https://doi.org/10.1038/ngeo1070

Henke, S., Gail, H. P., Trieloff, M., Schwarz, W. H., & Kleine, T. (2012). Thermal history modelling of the H chondrite parent body. *Astronomy & Astrophysics*, *545*, A135. https://doi.org/10.1051/0004-6361/201219100

Hertwig, A. (2017). Estimating Dust Enrichment and Water Ice Abundance in the Protoplanetary Disk from Oxygen Isotope Ratios and FeO-content of Type I Chondrules from CV chondrites. *Chondrules as Astrophysical Objects*, 2022.

Hewins, R. (1997). *Ann. Rev. Earth Planet. Sci*, *25*, 61–83.

Hewins, R. H., Connolly, H. C., Lofgren, G. E., & Libourel, G. (2005). Experimental Constraints on Chondrule Formation, *Chondrites and the Protoplanetary Disk*. *ASP Conference Series, Vol. ###, 2005*

Hezel, D. C., Harak, M., & Libourel, G. (2018). What we know about elemental bulk chondrule and matrix compositions: Presenting the ChondriteDB Database. *Chemie Der Erde*, *78*(1), 1–14. https://doi.org/10.1016/j.chemer.2017.05.003

Hezel, D. C., & Palme, H. (2007). The conditions of chondrule formation, Part I: Closed system. *Geochimica et Cosmochimica Acta*, *71*(16), 4092–4107. https://doi.org/10.1016/j.gca.2007.06.035

Hezel, D. C., Russell, S. S., Ross, A. J., & Kearsley, A. T. (2008). Modal abundances of CAIs: Implications for bulk chondrite element abundances and fractionations. *Meteoritics & Planetary Science*, *43*(11), 1879–1894. https://doi.org/10.1111/j.1945-5100.2008.tb00649.x

Hubbard, A., & Ebel, D. S. (2015). Semarkona: Lessons for chondrule and chondrite formation. *Icarus*, *245*, 32–37. https://doi.org/10.1016/j.icarus.2014.09.025

Hubbard, A., Mac Low, M. M., & Ebel, D. S. (2018). Dust concentration and chondrule formation. *ArXiv:1803.10047 [Astro-Ph]*. Retrieved from http://arxiv.org/abs/1803.10047

Huss, G. R., Rubin, A. E., & Grossman, J. N. (2006). Thermal Metamorphism in Chondrites. In *Meteorites and the Early Solar System II* (p. 20).

Huss, G. R., Alexander, C. M. O., Palme, H., Bland, P. A., & Wasson, J. T. (2005). Genetic relationships between chondrules, fine-grained rims, and interchondrule matrix. *Chondrites and the Protoplanetary Disk - ASP Conference Series Vol. 341*, *341*, 701–731.

Hutchison, R. (2004). *Meteorites: A Petrologic, Chemical and Isotopic Synthesis*. Cambridge University Press.

Ickert, R. B., Hiess, J., Williams, I. S., Holden, P., Ireland, T. R., Lanc, P., Clement, S. W. (2008). Determining high precision, in situ, oxygen isotope ratios with a SHRIMP II: Analyses of MPI-DING silicate-glass reference materials and zircon from contrasting granites. *Chemical Geology*, *257*(1–2), 114–128. https://doi.org/10.1016/j.chemgeo.2008.08.024

Ireland, T. R. (1992). Evidence for distillation in the formation of HAL and related hibonite inclusions. *Geochimica et Cosmochimica Acta*, *56*, 2503–2520.

Ireland, T. R. (2012). Oxygen isotope tracing of the Solar System. *Australian Journal of Earth Sciences*, *59*(2), 225–236. https://doi.org/10.1080/08120099.2012.620626

Ireland, T. R., Clement, S., Compston, W., Foster, J. J., Holden, P., Jenkins, B., … Williams, I. S. (2008). Development of SHRIMP. *Australian Journal of Earth Sciences*, *55*(6–7), 937–954. https://doi.org/10.1080/08120090802097427

Ireland, T. R., Schram, N., Holden, P., Lanc, P., Ávila, J., Armstrong, R., Compston, W. (2014). Charge-mode electrometer measurements of S-isotopic compositions on SHRIMP-SI. *International Journal of Mass Spectrometry*, *359*, 26–37. https://doi.org/10.1016/j.ijms.2013.12.020

Ireland, T. R., & Fegley, B. (2000). The Solar System's Earliest Chemistry: Systematics of Refractory Inclusions. *International Geology Review*, *42*(10), 865–894. https://doi.org/10.1080/00206810009465116

Ireland, T. R., Holden, P., Norman, M. D., & Clarke, J. (2006). Isotopic enhancements of ^{17}O and ^{18}O from solar wind particles in the lunar regolith. *Nature*, *440*(7085), 776–778. https://doi.org/10.1038/nature04611

Jacquet, E. (2014a). The quasi-universality of chondrule size as a constraint for chondrule formation models. *Icarus*, *232*, 176–186. https://doi.org/10.1016/j.icarus.2014.01.012

Jacquet, E. (2014b). Transport of solids in protoplanetary disks: Comparing meteorites and astrophysical models. *Comptes Rendus Geoscience*, *346*(1–2), 3–12. https://doi.org/10.1016/j.crte.2014.02.004

Jacquet, E., Alard, O., & Gounelle, M. (2015). Trace element geochemistry of ordinary chondrite chondrules: The type I/type II chondrule dichotomy. *Geochimica et Cosmochimica Acta*, *155*, 47–67. https://doi.org/10.1016/j.gca.2015.02.005

Jarosewich, E. (1990). Chemical analyses of meteorites - compilation of stony and iron meteorites.pdf. *Meteoritics*, *25*, 323–337.

Javoy, M., Balan, E., Méheut, M., Blanchard, M., & Lazzeri, M. (2012). First-principles investigation of equilibrium isotopic fractionation of O- and Si-isotopes between refractory solids and gases in the solar nebula. *Earth and Planetary Science Letters*, *319–320*, 118–127. https://doi.org/10.1016/j.epsl.2011.12.029

Johnson, B. C., Minton, D. A., Melosh, H. J., & Zuber, M. T. (2015). Impact jetting as the origin of chondrules. *Nature*, *517*(7534), 339–341. https://doi.org/10.1038/nature14105

Jones, R. H. (2012). Petrographic constraints on the diversity of chondrule reservoirs in the protoplanetary disk: Diversity of chondrule reservoirs. *Meteoritics & Planetary Science*, *47*(7), 1176–1190. https://doi.org/10.1111/j.1945-5100.2011.01327.x

Kawasaki, N., Sakamoto, N., & Yurimoto, H. (2012). Oxygen isotopic and chemical zoning of melilite crystals in a type A Ca-Al-rich inclusion of Efremovka CV3 chondrite: O-isotopes of melilite in a type A CAI from Efremovka. *Meteoritics & Planetary Science*, *47*(12), 2084–2093. https://doi.org/10.1111/maps.12033

Kita, N. T., Defouilloy, C., Goodrich, C. A., & Zolensky, M. E. (2017). Oxygen Isotope Reservoirs in the Protoplanetary Disk Inferred from Chondrules in Primitive Meteorites. *Chondrules as Astrophysical Objects*, 2022.

Kita, N. T., Tenner, T. J., Ushikubo, T., Hertwig, A., Chaumard, N., Defouilloy, C., Rudraswami, N. G. (2016). Chondrule Oxygen Isotope Systematics among Different Chondrite Groups: Variety of Isotope Reservoirs in the Protoplanetary Disk. *79th Annual Meeting of The Meteoritical Society*, *No. 6378*.

Kita, N. T., Kimura, M., Ushikubo, T., Valley, J. W., & Nyquist, L. E. (2008). Oxygen Isotope Systematics of Chondrules From the Least Equilibrated H. *39th Lunar and Planetary Science Conference*, *No. 1391*, 2059.

Kita, N. T., Nagahara, H., Tachibana, S., Tomomura, S., Spicuzza, M. J., Fournelle, J. H., & Valley, J. W. (2010). High precision SIMS oxygen three isotope study of chondrules in LL3 chondrites: Role of ambient gas during chondrule formation. *Geochimica et Cosmochimica Acta*, *74*(22), 6610–6635. https://doi.org/10.1016/j.gca.2010.08.011

Kita, N. T., & Ushikubo, T. (2012). Evolution of protoplanetary disk inferred from ^{26}Al chronology of individual chondrules: Disk evolution and ^{26}Al chronology of chondrules. *Meteoritics & Planetary Science*, *47*(7), 1108–1119. https://doi.org/10.1111/j.1945-5100.2011.01264.x

Kita, N. T., Yin, Q.-Z., MacPherson, G. J., Ushikubo, T., Jacobsen, B., Nagashima, K., … Jacobsen, S. B. (2013). ^{26} Al- ^{26} Mg isotope systematics of the first solids in the early solar system. *Meteoritics & Planetary Science*, *48*(8), 1383–1400. https://doi.org/10.1111/maps.12141

Kobayashi, S., Imai, H., & Yurimoto, H. (2003). New extreme 16O-rich reservoir in the early solar system. *Geochemical Journal*, *37*(6), 663–669. https://doi.org/10.2343/geochemj.37.663

Kööp, L., Davis, A. M., Nakashima, D., Park, C., Krot, A. N., Nagashima, K., … Kita, N. T. (2016). A link between oxygen, calcium and titanium isotopes in ^{26}Al-poor hibonite-rich CAIs from Murchison and implications for the heterogeneity of dust reservoirs in the solar nebula. *Geochimica et Cosmochimica Acta*, *189*, 70–95. https://doi.org/10.1016/j.gca.2016.05.014

Kööp, L., Nakashima, D., Heck, P. R., Kita, N. T., Tenner, T. J., Krot, A. N., Davis, A. M. (2018). A multielement isotopic study of refractory FUN and F CAIs: Mass-dependent and mass-independent isotope effects. *Geochimica et Cosmochimica Acta*, *221*, 296–317. https://doi.org/10.1016/j.gca.2017.04.029

Krot, A. N., & Nagashima, K. (2017). Constraints on mechanisms of chondrule formation from chondrule precursors and chronology of transient heating events in the protoplanetary disk. *Geochemical Journal*, *51*(1), 45–68. https://doi.org/10.2343/geochemj.2.0459

Krot, A. N., Nagashima, K., van Kooten, E. M. M., & Bizzarro, M. (2017). High-temperature rims around calcium–aluminum-rich inclusions from the CR, CB and CH carbonaceous chondrites. *Geochimica et Cosmochimica Acta*, *201*, 155–184. https://doi.org/10.1016/j.gca.2016.09.031

Krot, A. N., Nagashima, K., Ciesla, F. J., Meyer, B. S., Hutcheon, I. D., Davis, A. M., Huss, G. R., Scott, E. R. D. (2010). Oxygen Isotope Composition of the Sun and Mean Oxygen Isotopic Composition of the Protosolar Silicate Dust: Evidence from Refractory Inclusions. *The Astrophysical Journal* 713, no. 2: 1159–66.

Krot, A. N., Amelin, Y., Bland, P., Ciesla, F. J., Connelly, J., Davis, A. M., Yin, Q.-Z. (2009). Origin and chronology of chondritic components: A review. *Geochimica et Cosmochimica Acta*, *73*(17), 4963–4997. https://doi.org/10.1016/j.gca.2008.09.039

Krot, A. N., Keil, K., Scott, E. R. D., Goodrich, C. A., & Weisberg, M. K. (2014). Classification of Meteorites and Their Genetic Relationships. In *Treatise on Geochemistry* (pp. 1–63). Elsevier. https://doi.org/10.1016/B978-0-08-095975-7.00102-9

Kruijer, T. S., Touboul, M., Fischer-Godde, M., Bermingham, K. R., Walker, R. J., & Kleine, T. (2014). Protracted core formation and rapid accretion of protoplanets. *Science*, *344*(6188), 1150–1154. https://doi.org/10.1126/science.1251766

Libourel, G., & Chaussidon, M. (2011). Oxygen isotopic constraints on the origin of Mg-rich olivines from chondritic meteorites. *Earth and Planetary Science Letters*, *301*(1–2), 9–21. https://doi.org/10.1016/j.epsl.2010.11.009

Libourel, G., & Portail, M. (2018). Chondrules as direct thermochemical sensors of solar protoplanetary disk gas. *Science Advances*, *4*(7), eaar3321. https://doi.org/10.1126/sciadv.aar3321

Lodders, K. (2003). Solar System Abundances and Condensation Temperatures of the Elements. *The Astrophysical Journal*, *591*(2), 1220–1247. https://doi.org/10.1086/375492

Lugaro, M., Liffman, K., Ireland, T. R., & Maddison, S. T. (2012). Can Galactic Chemical Evolution Explain the Oxygen Isotopic Variations in the Solar System? *The Astrophysical Journal*, *759*(1), 51. https://doi.org/10.1088/0004-637X/759/1/51

Lyons, J. R., & Young, E. D. (2005). CO self-shielding as the origin of oxygen isotope anomalies in the early solar nebula. *Nature*, *435*(7040), 317–320. https://doi.org/10.1038/nature03557

MacPherson, G. J. (2014). Calcium–Aluminum-Rich Inclusions in Chondritic Meteorites. In *Treatise on Geochemistry* (pp. 139–179). Elsevier. https://doi.org/10.1016/B978-0-08-095975-7.00105-4

Marrocchi, Y., & Chaussidon, M. (2015). A systematic for oxygen isotopic variation in meteoritic chondrules. *Earth and Planetary Science Letters*, *430*, 308–315. https://doi.org/10.1016/j.epsl.2015.08.032

McCoy, T. J., & Nittler, L. R. (2014). Mercury. In *Treatise on Geochemistry* (pp. 119–126). Elsevier. https://doi.org/10.1016/B978-0-08-095975-7.00121-2

McCoy, T. J., Scott, E. R. D., Jones, R. H., Keil, K., & Taylor, G. J. (1991). Composition of chondrule silicates in LL3-5 chondrites and implications for their nebular history and parent body metamorphism. *Geochimica et Cosmochimica Acta*, *55*(2), 601–619. https://doi.org/10.1016/0016-7037(91)90015-W

McDermott, K. H., Greenwood, R. C., Scott, E. R. D., Franchi, I. A., & Anand, M. (2016). Oxygen isotope and petrological study of silicate inclusions in IIE iron meteorites and their relationship with H chondrites. *Geochimica et Cosmochimica Acta*, *173*, 97–113. https://doi.org/10.1016/j.gca.2015.10.014

McDougal, D., Nakashima, D., Tenner, T. J., Kita, N. T., Valley, J. W., & Noguchi, T. (2017). Intermineral oxygen three-isotope systematics of silicate minerals in equilibrated ordinary chondrites. *Meteoritics & Planetary Science*. https://doi.org/10.1111/maps.12932

McKeegan, K. D., Kallio, A. P. A., Heber, V. S., Jarzebinski, G., Mao, P. H., Coath, C. D., … Burnett, D. S. (2011). The Oxygen Isotopic Composition of the Sun Inferred from Captured Solar Wind. *Science*, *332*(6037), 1528–1532. https://doi.org/10.1126/science.1204636

McKibbin, S. J., Ireland, T. R., Holden, P., O'Neill, H. S. C., & Mallmann, G. (2016). Rapid cooling of planetesimal core-mantle reaction zones from Mn-Cr isotopes in pallasites. *Geochemical Perspectives Letters*, 68–77. https://doi.org/10.7185/geochemlet.1607

McNally, C. P., Hubbard, A., Mac Low, M.-M., Ebel, D. S., & D'Alessio, P. (2013). Mineral Processing By Short Circuits in Protoplanetary Disks. *The Astrophysical Journal*, *767*(1), L2. https://doi.org/10.1088/2041-8205/767/1/L2

Metzler, K., & Pack, A. (2016). Chemistry and oxygen isotopic composition of cluster chondrite clasts and their components in LL3 chondrites. *Meteoritics & Planetary Science*, *51*(2), 276–302. https://doi.org/10.1111/maps.12592

Metzler, K., Pack, A., & Hezel, D. C. (2017). Ordinary Chondrite Chondrules: Oxygen Isotope Variations. Chondrules and Protoplanetary Disk.

Miller, K. E., Lauretta, D. S., Connolly, H. C., Berger, E. L., Nagashima, K., & Domanik, K. (2017). Formation of unequilibrated R chondrite chondrules and opaque phases. *Geochimica et Cosmochimica Acta*, *209*, 24–50. https://doi.org/10.1016/j.gca.2017.04.009

Miyazaki, Y., & Korenaga, J. (2017). Effects of Chemistry on Vertical Dust Motion in Early Protoplanetary Disks. *The Astrophysical Journal*, *849*(1), 41. https://doi.org/10.3847/1538-4357/aa8cd1

Morbidelli, A., Lunine, J. I., O'Brien, D. P., Raymond, S. N., & Walsh, K. J. (2012). Building Terrestrial Planets. *Annual Review of Earth and Planetary Sciences*, *40*(1), 251–275. https://doi.org/10.1146/annurev-earth-042711-105319

Morris, M. A., & Desch, S. J. (2010). THERMAL HISTORIES OF CHONDRULES IN SOLAR NEBULA SHOCKS. *The Astrophysical Journal*, *722*(2), 1474–1494. https://doi.org/10.1088/0004-637X/722/2/1474

Nagahara, H., & Ozawa, K. (2012). The role of exchange reactions in oxygen isotope fractionation during CAI and chondrule formation: The role of oxygen isotope exchange reaction. *Meteoritics & Planetary Science*, *47*(7), 1209–1228. https://doi.org/10.1111/j.1945-5100.2012.01377.x

Nagashima, K., Krot, A. N., & Huss, G. R. (2015). Oxygen-isotope compositions of chondrule phenocrysts and matrix grains in Kakangari K-grouplet chondrite: Implication to a chondrule-matrix genetic relationship. *Geochimica et Cosmochimica Acta*, *151*, 49–67. https://doi.org/10.1016/j.gca.2014.12.012

Nguyen, A. N., Keller, L. P., & Messenger, S. (2016). MINERALOGY OF PRESOLAR SILICATE AND OXIDE GRAINS OF DIVERSE STELLAR ORIGINS. *The Astrophysical Journal*, *818*(1), 51. https://doi.org/10.3847/0004-637X/818/1/51

Olsen, M. B., Wielandt, D., Schiller, M., Van Kooten, E. M. M. E., & Bizzarro, M. (2016). Magnesium and ^{54}Cr isotope compositions of carbonaceous chondrite chondrules – Insights into early disk processes. *Geochimica et Cosmochimica Acta*, *191*, 118–138. https://doi.org/10.1016/j.gca.2016.07.011

Pack, A., Yurimoto, H., & Palme, H. (2004). Petrographic and oxygen-isotopic study of refractory forsterites from R-chondrite Dar al Gani 013 (R3.5-6), unequilibrated

ordinary and carbonaceous chondrites. *Geochimica et Cosmochimica Acta*, *68*(5), 1135–1157. https://doi.org/10.1016/j.gca.2003.07.014

Poole, G. M., Rehkämper, M., Coles, B. J., Goldberg, T., & Smith, C. L. (2017). Nucleosynthetic molybdenum isotope anomalies in iron meteorites – new evidence for thermal processing of solar nebula material. *Earth and Planetary Science Letters*, *473*, 215–226. https://doi.org/10.1016/j.epsl.2017.05.001

Pringle, E. A., Moynier, F., Beck, P., Paniello, R., & Hezel, D. C. (2017). The origin of volatile element depletion in early solar system material: Clues from Zn isotopes in chondrules. *Earth and Planetary Science Letters*, *468*, 62–71. https://doi.org/10.1016/j.epsl.2017.04.002

Rubin, A. E. (2010). Physical properties of chondrules in different chondrite groups: Implications for multiple melting events in dusty environments. *Geochimica et Cosmochimica Acta*, *74*(16), 4807–4828. https://doi.org/10.1016/j.gca.2010.05.018

Rudraswami, N. G., Ushikubo, T., Nakashima, D., & Kita, N. T. (2011). Oxygen isotope systematics of chondrules in the Allende CV3 chondrite: High precision ion microprobe studies. *Geochimica et Cosmochimica Acta*, *75*(23), 7596–7611. https://doi.org/10.1016/j.gca.2011.09.035

Russell, S. S., MacPherson, G. J., Leshin, L. A., & McKeegan, K. D. (2000a). ^{16}O enrichments in aluminum-rich chondrules from ordinary chondrites. *Earth and Planetary Science Letters*, *184*(1), 57–74. https://doi.org/10.1016/S0012-821X(00)00309-5

Ruzicka, A., Hiyagon, H., Hutson, M., & Floss, C. (2007). Relict olivine, chondrule recycling, and the evolution of nebular oxygen reservoirs. *Earth and Planetary Science Letters*, *257*(1–2), 274–289. https://doi.org/10.1016/j.epsl.2007.02.037

Ruzicka, A. (2012). Chondrule formation by repeated evaporative melting and condensation in collisional debris clouds around planetesimals: Chondrule formation in collisional debris clouds. *Meteoritics & Planetary Science*, *47*(12), 2218–2236. https://doi.org/10.1111/j.1945-5100.2012.01412.x

Ryerson, F. J., Durham, W. B., Cherniak, D. J., & Lanford, W. A. (1989). Oxygen diffusion in olivine: Effect of oxygen fugacity and implications for creep. *Journal of Geophysical Research: Solid Earth*, *94*(B4), 4105–4118. https://doi.org/10.1029/JB094iB04p04105

Sakamoto, N., Seto, Y., Itoh, S., Kuramoto, K., Fujino, K., Nagashima, K., … Yurimoto, H. (2007). Remnants of the Early Solar System Water Enriched in Heavy Oxygen Isotopes. *Science*, *317*(5835), 231–233. https://doi.org/10.1126/science.1142021

Salmeron, R., & Ireland, T. (2012). The role of protostellar jets in star formation and the evolution of the early solar system: Astrophysical and meteoritical perspectives:.

Meteoritics & Planetary Science, *47*(12), 1922–1940. https://doi.org/10.1111/maps.12029

Sanders, I. S., Scott, E. R. D., & Delaney, J. S. (2017). Origin of mass-independent oxygen isotope variation among ureilites: Clues from chondrites and primitive achondrites. *Meteoritics & Planetary Science*, *52*(4), 690–708. https://doi.org/10.1111/maps.12820

Sanders, I. S., & Scott, E. R. D. (2012). The origin of chondrules and chondrites: Debris from low-velocity impacts between molten planetesimals?: Origin of chondrules and chondrites. *Meteoritics & Planetary Science*, *47*(12), 2170–2192. https://doi.org/10.1111/maps.12002

Saxton, J. M., Lyon, I. C., & Turner, G. (1998). Oxygen isotopes in forsterite grains from Julesburg and Allende: Oxygen-16-rich material in an ordinary chondrite. *Meteoritics & Planetary Science*, *33*(5), 1017–1027. https://doi.org/10.1111/j.1945-5100.1998.tb01708.x

Schoene, B., Condon, D. J., Morgan, L., & McLean, N. (2013). Precision and Accuracy in Geochronology. *Elements*, *9*(1), 19–24. https://doi.org/10.2113/gselements.9.1.19

Schrader, D. L., Connolly, H. C., Lauretta, D. S., Nagashima, K., Huss, G. R., Davidson, J., & Domanik, K. J. (2013a). The formation and alteration of the Renazzo-like carbonaceous chondrites II: Linking O-isotope composition and oxidation state of chondrule olivine. *Geochimica et Cosmochimica Acta*, *101*, 302–327. https://doi.org/10.1016/j.gca.2012.09.045

Schrader, D. L., Connolly, H. C., Lauretta, D. S., Nagashima, K., Huss, G. R., Davidson, J., & Domanik, K. J. (2013). The formation and alteration of the Renazzo-like carbonaceous chondrites II: Linking O-isotope composition and oxidation state of chondrule olivine. *Geochimica et Cosmochimica Acta*, *101*, 302–327. https://doi.org/10.1016/j.gca.2012.09.045

Schrader, D. L., Nagashima, K., Krot, A. N., Ogliore, R. C., & Hellebrand, E. (2014). Variations in the O-isotope composition of gas during the formation of chondrules from the CR chondrites. *Geochimica et Cosmochimica Acta*, *132*, 50–74. https://doi.org/10.1016/j.gca.2014.01.034

Schrader, D. L., Nagashima, K., Krot, A. N., Ogliore, R. C., Yin, Q. Z., Amelin, Y., Kaltenbach, A. (2017). Distribution of 26 Al in the CR chondrite chondrule-forming region of the protoplanetary disk. *Geochimica et Cosmochimica Acta*, *201*, 275–302. https://doi.org/10.1016/j.gca.2016.06.023

Scicchitano, M. R. (2018). *Oxygen isotopes as tracers and stopwatches for rock-fluid interaction in the crust: New analytical and experimental developments*. The Australian National University.

Scott, E. R. D., & Krot, A. N. (2001). Oxygen isotopic compositions and origins of calcium-aluminum-rich inclusions and chondrules. *Meteoritics & Planetary Science*, *36*(10), 1307–1319. https://doi.org/10.1111/j.1945-5100.2001.tb01826.x

Scott, E. R. D., Krot, A. N., & Sanders, I. S. (2018). Isotopic Dichotomy among Meteorites and Its Bearing on the Protoplanetary Disk. *The Astrophysical Journal*, *854*(2), 164. https://doi.org/10.3847/1538-4357/aaa5a5

Scott, E. R. D., Rubin, A. E., Taylor, G. J., & Keil, K. (1984). Matrix material in type 3 chondrites-occurrence, heterogeneity and relationship with chondrules. *Geochimica et Cosmochimica Acta*, *48*(9), 1741–1757. https://doi.org/10.1016/0016-7037(84)90029-2

Scott, E. R. D., & Krot, A. N. (2014). Chondrites and Their Components. In *Treatise on Geochemistry* (pp. 65–137). Elsevier. https://doi.org/10.1016/B978-0-08-095975-7.00104-2

Sears, D., & Lyon, I. (1998). The oxygen isotopic properties of olivines in the Semarkona ordinary chondrite. *Meteoritics & Planetary Science*, *1032*, 1029–1032.

Sears, D. W. G., Lyon, I., Saxton, J., & Turner, G. (1998). The oxygen isotopic properties of olivines in the Semarkona ordinary chondrite. *Meteoritics & Planetary Science*, *33*(5), 1029–1032. https://doi.org/10.1111/j.1945-5100.1998.tb01709.x

Shu, F. H., Shang, H., & Lee, T. (1996). Toward an Astrophysical Theory of Chondrites. *Science*, *271*(5255), 1545–1552. https://doi.org/10.1126/science.271.5255.1545

Shukolyukov, A., & Lugmair, G. W. (2000). On the 53Mn Heterogeneity in the Early Solar System. In W. Benz, R. Kallenbach, & G. W. Lugmair (Eds.), *From Dust to Terrestrial Planets* (Vol. 9, pp. 225–236). Dordrecht: Springer Netherlands. https://doi.org/10.1007/978-94-011-4146-8_15

Simon, J. I., Matzel, J. E. P., Simon, S. B., Hutcheon, I. D., Ross, D. K., Weber, P. K., & Grossman, L. (2016). Oxygen isotopic variations in the outer margins and Wark–Lovering rims of refractory inclusions. *Geochimica et Cosmochimica Acta*, *186*, 242–276. https://doi.org/10.1016/j.gca.2016.04.025

Spencer, C. J., Kirkland, C. L., & Taylor, R. J. M. (2016). Strategies towards statistically robust interpretations of in situ U–Pb zircon geochronology. *Geoscience Frontiers*, *7*(4), 581–589. https://doi.org/10.1016/j.gsf.2015.11.006

Spergel, D. N., Verde, L., Peiris, H. V., Komatsu, E., Nolta, M. R., Bennett, C. L., Wright, E. L. (2003). First Year Wilkinson Microwave Anisotropy Probe (WMAP) Observations:

Determination of Cosmological Parameters. *The Astrophysical Journal Supplement Series*, *148*(1), 175–194. https://doi.org/10.1086/377226

Sugiura, N., & Fujiya, W. (2014). Correlated accretion ages and ε ^{54} Cr of meteorite parent bodies and the evolution of the solar nebula. *Meteoritics & Planetary Science*, *49*(5), 772–787. https://doi.org/10.1111/maps.12292

Symes, S. J. K., Sears, D. W. G., Akridge, D. G., Huang, S., & Benoit, P. H. (1998). The crystalline lunar spherules: Their formation and implications for the origin of meteoritic chondrules. *Meteoritics and Planetary Science*, *33*(1), 13–29.

Tachibana, S., & Huss, G. R. (2005). Sulfur isotope composition of putative primary troilite in chondrules from Bishunpur and Semarkona. *Geochimica et Cosmochimica Acta*, *69*(12), 3075–3097. https://doi.org/10.1016/j.gca.2004.06.025

Tachibana, S., Nagahara, H., Ozawa, K., Ikeda, Y., Nomura, R., Tatsumi, K., & Joh, Y. (2011). KINETIC CONDENSATION AND EVAPORATION OF METALLIC IRON AND IMPLICATIONS FOR METALLIC IRON DUST FORMATION. *The Astrophysical Journal*, *736*(1), 16. https://doi.org/10.1088/0004-637X/736/1/16

Tenner, T. J., Kimura, M., & Kita, N. T. (2017). Oxygen isotope characteristics of chondrules from the Yamato-82094 ungrouped carbonaceous chondrite: Further evidence for common O-isotope environments sampled among carbonaceous chondrites. *Meteoritics & Planetary Science*, *52*(2), 268–294. https://doi.org/10.1111/maps.12791

Tenner, T. J., Nakashima, D., Ushikubo, T., Kita, N. T., & Weisberg, M. K. (2015). Oxygen isotope ratios of FeO-poor chondrules in CR3 chondrites: Influence of dust enrichment and H 2 O during chondrule formation. *Geochimica et Cosmochimica Acta*, *148*, 228–250. https://doi.org/10.1016/j.gca.2014.09.025

Tenner, T. J., Ushikubo, T., Kurahashi, E., Kita, N. T., & Nagahara, H. (2013). Oxygen isotope systematics of chondrule phenocrysts from the CO3.0 chondrite Yamato 81020: Evidence for two distinct oxygen isotope reservoirs. *Geochimica et Cosmochimica*

Testi, L., Birnstiel, T., Ricci, L., Andrews, S., Blum, J., Carpenter, J., … Wilner, D. (2014). Dust Evolution in Protoplanetary Disks. *ArXiv:1402.1354 [Astro-Ph]*. https://doi.org/10.2458/azu_uapress_9780816531240-ch015

Ushikubo, T., Kimura, M., Kita, N. T., & Valley, J. W. (2012). Primordial oxygen isotope reservoirs of the solar nebula recorded in chondrules in Acfer 094 carbonaceous chondrite. *Geochimica et Cosmochimica Acta*, *90*, 242–264. https://doi.org/10.1016/j.gca.2012.05.010

Turner, M., Ireland, T. R., Hermann, J., Holden, P., Padrón-Navarta, J. A., Hauri, E. H., and Turner, S. Sensitive High Resolution Ion Microprobe – Stable Isotope (SHRIMP-SI)

Analysis of Water in Silicate Glasses and Nominally Anhydrous Reference Minerals (2015). *Journal of Analytical Atomic Spectrometry* 30, no. 8: 1706–22.

Ushikubo, T., Nakashima, D., Kimura, M., Tenner, T. J., & Kita, N. T. (2013). Contemporaneous formation of chondrules in distinct oxygen isotope reservoirs. *Geochimica et Cosmochimica Acta*, *109*, 280–295. https://doi.org/10.1016/j.gca.2013.01.045

Ushikubo, T., Tenner, T. J., Hiyagon, H., & Kita, N. T. (2017). A long duration of the 16 O-rich reservoir in the solar nebula, as recorded in fine-grained refractory inclusions from the least metamorphosed carbonaceous chondrites. *Geochimica et Cosmochimica Acta*, *201*, 103–122. https://doi.org/10.1016/j.gca.2016.08.032

Van Schmus, W. R., & Wood, J. A. (1967). A chemical-petrologic classification lot the chondritic meteorites. *Geochimica et Cosmochimica Acta*, *31*, 747–765.

Varela, M., Kurat, G., & Zinner, E. (2006). The primary liquid condensation model and the origin of barred olivine chondrules. *Icarus*, *184*(2), 344–364. https://doi.org/10.1016/j.icarus.2006.05.009

Vermeesch, P. (2012). On the visualisation of detrital age distributions. *Chemical Geology*, *312–313*, 190–194. https://doi.org/10.1016/j.chemgeo.2012.04.021

Vernazza, P., Zanda, B., Binzel, R. P., Hiroi, T., DeMeo, F. E., Birlan, M., Lockhart, M. (2014). MULTIPLE AND FAST: THE ACCRETION OF ORDINARY CHONDRITE PARENT BODIES. *The Astrophysical Journal*, *791*(2), 120. https://doi.org/10.1088/0004-637X/791/2/120

Villeneuve, J., Chaussidon, M., & Libourel, G. (2009). Homogeneous Distribution of 26Al in the Solar System from the Mg Isotopic Composition of Chondrules. *Science*, *325*(5943), 985–988. https://doi.org/10.1126/science.1173907

Walsh, C., Millar, T. J., & Nomura, H. (2013). Chemical Processes in Protoplanetary Disks. *The Astrophysical Journal*, *722*(2), 1607–1623. https://doi.org/10.1088/0004-637X/722/2/1607

Walsh, K. J., Morbidelli, A., Raymond, S. N., O'Brien, D. P., & Mandell, A. M. (2011). A low mass for Mars from Jupiter's early gas-driven migration. *Nature*, *475*(7355), 206–209. https://doi.org/10.1038/nature10201

Wang, H. S., Lineweaver, C. H., & Ireland, T. R. (2018). The Volatility Trend of Protosolar and Terrestrial Elemental Abundances. *ArXiv:1810.12741 [Astro-Ph]*. Retrieved from http://arxiv.org/abs/1810.12741

Wang, H., Weiss, B. P., Bai, X.-N., Downey, B. G., Wang, J., Wang, J., Zucolotto, M. E. (2017). Lifetime of the solar nebula constrained by meteorite paleomagnetism. *Science*, *355*(6325), 623–627. https://doi.org/10.1126/science.aaf5043

Warren, P. H. (2011). Stable-isotopic anomalies and the accretionary assemblage of the Earth and Mars: A subordinate role for carbonaceous chondrites. *Earth and Planetary Science Letters*, *311*(1–2), 93–100. https://doi.org/10.1016/j.epsl.2011.08.047

Weisberg, M. K., & Kimura, M. (2012). The unequilibrated enstatite chondrites. *Chemie Der Erde - Geochemistry*, *72*(2), 101–115. https://doi.org/10.1016/j.chemer.2012.04.003

Weisberg, Michael K., Ebel, D. S., Connolly, H. C., Kita, N. T., & Ushikubo, T. (2011). Petrology and oxygen isotope compositions of chondrules in E3 chondrites. *Geochimica et Cosmochimica Acta*, *75*(21), 6556–6569. https://doi.org/10.1016/j.gca.2011.08.040

Wendt, I., & Carl, C. (1991). The statistical distribution of the mean squared weighted deviation. *Chemical Geology: Isotope Geoscience Section*, *86*(4), 275–285. https://doi.org/10.1016/0168-9622(91)90010-T

Williams, C. D., Ushikubo, T., Bullock, E. S., Janney, P. E., Hines, R. R., Kita, N. T., Wadhwa, M. (2017). Thermal and chemical evolution in the early solar system as recorded by FUN CAIs: Part I – Petrology, mineral chemistry, and isotopic composition of Allende FUN CAI CMS-1. *Geochimica et Cosmochimica Acta*, *201*, 25–48. https://doi.org/10.1016/j.gca.2016.10.053

Wood, J. A. (1962). Chondrules and the Origin Of the Terrestrial Planets. *Nature*, *194*, 127.

Wooden, D. H., Ishii, H. A., & Zolensky, M. E. (2017). Cometary dust: the diversity of primitive refractory grains. *Philosophical Transactions of the Royal Society A: Mathematical, Physical and Engineering Sciences*, *375*(2097), 20160260. https://doi.org/10.1098/rsta.2016.0260

Young, E. D., Russell, S. S. (1998). Oxygen Reservoirs in the Early Solar Nebula Inferred from an Allende CAI. *Science* 282, no. 5388: 452–55.

Yurimoto, H., & Kuramoto, K. (2004). Molecular Cloud Origin for the Oxygen Isotope Heterogeneity in the Solar System. *Science*, *305*(5691), 1763–1766. https://doi.org/10.1126/science.1100989

Yurimoto, H., Kuramoto, K., Krot, A. N., Scott, E. R. D., Cuzzi, J. N., Thiemens, M. H., & Lyons, J. R. (2006). Origin and Evolution of Oxygen Isotopic Compositions of the Solar System. In *Meteorites and the Early Solar System II*.

Yurimoto, Hisayoshi, Kuramoto, K., Krot, A. N., Scott, E. R., Cuzzi, J. N., Thiemens, M. H., & Lyons, J. R. (2007). Origin and evolution of oxygen isotopic compositions of the solar system. *Protostars and Planets V*, *1*, 849–862.

Zanda, B., Hewins, R., Bourotdenise, M., Bland, P., & Albarede, F. (2006). Formation of solar nebula reservoirs by mixing chondritic components. *Earth and Planetary Science Letters*, *248*(3–4), 650–660. https://doi.org/10.1016/j.epsl.2006.05.016

Zinner, E. (2014). Presolar Grains. In *Treatise on Geochemistry* (pp. 181–213). Elsevier. https://doi.org/10.1016/B978-0-08-095975-7.00101-7

APPENDIX

Calculation method for evaporation-driven gas-melt interaction model.

The details of the calculation method for the determination of $\delta^i O_{pyroxene}$ ratios (where *i* is either atomic number 17 or 18) has been described by Marrocchi and Chaussidon (2015) and will be briefly described here.

The most important concept of this model is that it considers the oxygen isotope variation of Mg-rich chondrules as the result of open-system gas–melt interactions between the chondrule precursor silicate dust and a SiO-enriched gas in the protoplanetary disk.

The gas enrichment in SiO results from partial melting and evaporation of silicate dust. Then the Si and O molar contents of the evolved composition of the initial gas can be written as:

$$[Si]_{gas} = [Si]_{initial\ gas} + R \times [Si]_{dust} \quad (1)$$

$$[O]_{gas} = [O]_{initial\ gas} + R \times [O]_{dust} \quad (2)$$

$$\delta^i O_{gas} = \frac{\delta^i O_{initial\ gas} \times [O]_{initial\ gas} + R \times \delta^i O_{dust} \times [O]_{dust}}{[O]_{gas}} \quad (3)$$

Where $[Si]_{gas}$ and $[O]_{gas}$, $[Si]_{initial\ gas}$ and $[O]_{initial\ gas}$, and $[Si]_{dust}$ and $[O]_{dust}$ are the molar contents of in the evolved gas, initial gas, and precursor dust, respectively; R is the dust/gas ratio and $\delta^i O_x$ is to the oxygen isotope composition of each component (where *x*: gas, initial gas, and precursor dust).

In a high-temperature gas of the solar nebula, most of the oxygen is associated to CO (Lodders, 2003). However, when the R ratio increases, SiO becomes an important oxygen-bearing molecule in the gas. The fraction of oxygen carried by SiO in the gas is defined as:

$$f_{SiO} = \frac{[SiO]}{[SiO]+[CO]} \quad (4)$$

With [SiO] and [CO] the molar contents of the gas in SiO and CO, respectively. Using f_{SiO}, the oxygen isotope composition of the gas can be written as:

$$\delta^i O_{gas} = f_{SiO} \times \delta^i O_{SiO\ gas} + (1 - f_{SiO}) \times \delta^i O_{CO\ gas} \quad (5)$$

or

$$\delta^{i}O_{SiO\ gas} = \delta^{i}O_{gas} - (1 - f_{SiO})\ x\ \Delta^{i}O_{CO-SiO} \quad (6)$$

where $\Delta^{i}O_{CO-SiO}$ is the equilibrium oxygen isotopic fractionation between CO and SiO. The SiO_2 content of the melt is controlled by the partial dissolution of precursor olivines and the interaction of the melt with the SiO-rich. Therefore the reaction can be written as (Tissandier et al., 2002):

$$SiO_{(gas)} + \frac{1}{2}O_{2(gas)} = SiO_{2(melt)} \quad (7)$$

$$Mg_2SiO_{4(olivine)} + SiO_{2(melt)} = Mg_2Si_2O_{6(melt)} = Mg_2Si_2O_{6(pyroxene)} \quad (8)$$

Therefore the oxygen isotope composition of pyroxene is:

$$\delta^{i}O_{pyroxene} = \frac{2}{3}\ \delta^{i}O_{precursor\ olivine} + \frac{1}{3}\ (\Delta^{i}O_{pyroxene\text{-}SiO} + \delta^{i}O_{SiO}) \quad (9)$$

where

$$\delta^{i}O_{SiO} = \frac{\delta^{i}O_{initial\ gas}\ x\ [O]_{initial\ gas} + R\ x\ \delta^{i}O_{dust}\ x\ [O]_{dust}}{[O]_{gas}} - \frac{\Delta^{i}O_{CO\text{-}SiO}}{1+[SiO]/[CO]} \quad (10)$$

For the calculations, it was assumed that the precursors or initial dust had chemical compositions of CI chondrites and that the initial gas was solar (Lodders, 2003). Therefore, $[Si]_{dust} = [Si]_{initial\ gas} = 1 \times 10^6$, $[O]_{dust} = 7.55 \times 10^6$, $[O]_{initial\ gas} = 1.41 \times 10^7$, $[C]_{dust} = 7.72 \times 10^5$ and $[C]_{initial\ gas} = 7.08 \times 10^6$). The $\Delta^{i}O_{CO-SiO}$ and $\Delta^{i}O_{pyroxene-SiO}$ values are temperature-dependent fractionation factors obtained from Javoy et al. (2012).

As mentioned in the discussions, the only difference between the model calculated here compare to the model of Marrocchi and Chaussidon (2015) is that the initial gas values are $\delta^{18}O = 4.64‰$ and $\delta^{17}O = 3.03‰$, the oxygen isotope composition of the planetary reservoir proposed by this study. The initial composition of the olivine precursor is $\delta^{18}O = 6.00‰$ and $\delta^{17}O = 3.20‰$, which predicts the compositional range of bulk chondrules (pyroxene chondrules) from enstatite chondrites. Table 1 shows the results at different temperatures, although figure 5.32 shows the model results at 1600K.

Table 1. Result of model calculations for gas-melt interactions between olivine and gas

R	SiO/CO	f_{SiO}	$\delta^{18}O_{neb}$	$\delta^{18}O_{SiO}$	$\delta^{18}O_{pyroxene}$	$\Delta^{18}O_{px\text{-}ol}$	$\delta^{17}O_{neb}$	$\delta^{17}O_{SiO}$	$\delta^{17}O_{pyroxene}$	$\Delta^{17}O_{px\text{-}ol}$
T=1500K										
0	0.14	0.12	4.64	1.49	4.64	-1.36	3.03	1.39	2.67	-0.53
1	0.25	0.20	5.11	2.25	4.90	-1.10	3.09	1.60	2.74	-0.46
5	0.55	0.35	5.63	3.31	5.25	-0.75	3.15	1.94	2.86	-0.34
10	0.74	0.43	5.79	3.72	5.39	-0.61	3.17	2.10	2.91	-0.29
50	1.12	0.53	5.95	4.25	5.57	-0.43	3.19	2.31	2.98	-0.22
100	1.20	0.55	5.98	4.34	5.59	-0.41	3.20	2.35	2.99	-0.21
200	1.24	0.55	5.99	4.38	5.61	-0.39	3.20	2.36	3.00	-0.20
1000	1.28	0.56	6.00	4.42	5.62	-0.38	3.20	2.38	3.00	-0.20
2000	1.29	0.56	6.00	4.43	5.62	-0.38	3.20	2.38	3.00	-0.20
T=1600K										
0	0.14	0.12	4.64	1.84	4.74	-1.26	3.03	1.58	2.73	-0.47
1	0.25	0.20	5.11	2.57	4.99	-1.01	3.09	1.77	2.79	-0.41
5	0.55	0.35	5.63	3.57	5.32	-0.68	3.15	2.08	2.89	-0.31
10	0.74	0.43	5.79	3.96	5.45	-0.55	3.17	2.22	2.94	-0.26
50	1.12	0.53	5.95	4.44	5.61	-0.39	3.19	2.41	3.00	-0.20
100	1.20	0.55	5.98	4.52	5.64	-0.36	3.20	2.44	3.01	-0.19
200	1.24	0.55	5.99	4.57	5.65	-0.35	3.20	2.46	3.02	-0.18
1000	1.28	0.56	6.00	4.60	5.66	-0.34	3.20	2.47	3.03	-0.17
2000	1.29	0.56	6.00	4.61	5.66	-0.34	3.20	2.48	3.03	-0.17
T=1700K										
0	0.14	0.12	4.64	2.15	4.83	-1.17	3.03	1.73	2.77	-0.43
1	0.25	0.20	5.11	2.85	5.06	-0.94	3.09	1.91	2.83	-0.37
5	0.55	0.35	5.63	3.79	5.38	-0.62	3.15	2.20	2.93	-0.27
10	0.74	0.43	5.79	4.15	5.50	-0.50	3.17	2.32	2.97	-0.23
50	1.12	0.53	5.95	4.61	5.65	-0.35	3.19	2.49	3.02	-0.18
100	1.20	0.55	5.98	4.68	5.67	-0.33	3.20	2.52	3.03	-0.17
200	1.24	0.55	5.99	4.72	5.69	-0.31	3.20	2.54	3.04	-0.16
1000	1.28	0.56	6.00	4.75	5.70	-0.30	3.20	2.55	3.04	-0.16
2000	1.29	0.56	6.00	4.76	5.70	-0.30	3.20	2.55	3.04	-0.16
T=1800K										
0	0.14	0.12	4.64	2.40	4.90	-1.10	3.03	1.87	2.81	-0.39
1	0.25	0.20	5.11	3.08	5.13	-0.87	3.09	2.03	2.86	-0.34
5	0.55	0.35	5.63	3.98	5.43	-0.57	3.15	2.30	2.95	-0.25
10	0.74	0.43	5.79	4.32	5.54	-0.46	3.17	2.41	2.99	-0.21
50	1.12	0.53	5.95	4.74	5.68	-0.32	3.19	2.57	3.04	-0.16
100	1.20	0.55	5.98	4.81	5.71	-0.29	3.20	2.59	3.05	-0.15
200	1.24	0.55	5.99	4.85	5.72	-0.28	3.20	2.61	3.05	-0.15
1000	1.28	0.56	6.00	4.88	5.73	-0.27	3.20	2.62	3.06	-0.14
2000	1.29	0.56	6.00	4.88	5.73	-0.27	3.20	2.62	3.06	-0.14

The initials conditions are: $\delta^{18}O$ = 6.00‰ and $\delta^{17}O$ = 3.20‰ for olivine precursor and $\delta^{18}O$ = 4.64‰ and $\delta^{17}O$ = 3.03‰. Other parameters and calculation method are same as in Marrocchi and Chaussidon (2015). R: dust/gas ratio; f_{SiO}: fraction of oxygen in the gas carried by SiO; $\delta^{17,18}O_{neb}$: $\delta^{17,18}O$ ratio of the gas that equilibrated with the olivine precursor; $\delta^{17,18}O_{SiO}$: $\delta^{17,18}O$ ratio of the SiO molecule in the gas; $\delta^{17,18}O_{pyroxene}$: calculated $\delta^{17,18}O$ ratio of the pyroxene; $\Delta^{17,18}O = \delta^{17,18}O_{olivine\ precursor} - \delta^{17,18}O_{pyroxene}$.